

EXPERIMENTAL AND NUMERICAL INVESTIGATION OF PRESSURE
SWIRL ATOMIZERS

A THESIS SUBMITTED TO
THE GRADUATE SCHOOL OF NATURAL AND APPLIED SCIENCES
OF
MIDDLE EAST TECHNICAL UNIVERSITY

BY

BÜLENT SÜMER

IN PARTIAL FULFILLMENT OF THE REQUIREMENTS
FOR
THE DEGREE OF DOCTOR OF PHILOSOPHY
IN
AEROSPACE ENGINEERING

FEBRUARY 2014

Approval of the thesis:

**EXPERIMENTAL AND NUMERICAL INVESTIGATION OF PRESSURE
SWIRL ATOMIZERS**

submitted by **BÜLENT SÜMER** in partial fulfillment of the requirements for the degree of **Doctor of Philosophy in Aerospace Engineering Department, Middle East Technical University** by,

Prof. Dr. Canan ÖZGEN
Dean, Graduate School of **Natural and Applied Sciences**

Prof. Dr. Ozan TEKİNALP
Head of Department, **Aerospace Engineering**

Prof. Dr. İsmail H. TUNCER
Supervisor, **Aerospace Engineering Department, METU**

Assoc. Prof. Dr. Oğuz UZOL
Co-supervisor, **Aerospace Engineering Department, METU**

Examining Committee Members:

Prof. Dr. Yusuf ÖZYÖRÜK
Aerospace Engineering Department, METU

Prof. Dr. İsmail H. TUNCER
Aerospace Engineering Department, METU

Prof. Dr. Haluk AKSEL
Mechanical Engineering Department, METU

Prof. Dr. Abdullah ULAŞ
Mechanical Engineering Department, METU

Assist. Prof. Dr. Sıtkı USLU
Mechanical Engineering Department, TOBB ETÜ

Date:

I hereby declare that all information in this document has been obtained and presented in accordance with academic rules and ethical conduct. I also declare that, as required by these rules and conduct, I have fully cited and referenced all material and results that are not original to this work.

Name, Last Name: BÜLENT SÜMER

Signature :

ABSTRACT

EXPERIMENTAL AND NUMERICAL INVESTIGATION OF PRESSURE SWIRL ATOMIZERS

SÜMER, BÜLENT

Ph.D., Department of Aerospace Engineering

Supervisor : Prof. Dr. İsmail H. TUNCER

Co-Supervisor : Assoc. Prof. Dr. Oğuz UZOL

February 2014, 223 pages

In this study, unsteady flows inside a pressure swirl atomizer are investigated using experimental and numerical techniques. High Speed Shadowgraphy Technique is used in order to visualize the flow structures inside the atomizer and the resulting spray at high temporal and spatial resolutions. The images of the air core inside the pressure swirl atomizer and the resulting spray formations are captured at four different water flow rates. Then, the time variation of the air core diameter at different axial locations of the atomizer is found using the image processing tool developed. The corresponding mean spray cone angles are similarly obtained. The analysis reveals the unsteady features of the air core and the macroscopic properties of the spray. Microscopic properties of the spray are determined using a two component Phase Doppler Particle Analyzer. Sauter mean diameter distributions of the resulting water droplets and the velocity distributions for two different droplet size classes are obtained as a function of flow rate through the atomizer. Unsteady, two-phase flow fields within the pressure swirl atomizer are computed using a computational fluid dynamics tool based on the volume of fluid method. Two dimensional axisymmetric swirl and three dimensional numerical simulations are performed to analyze the unsteady flows inside the atomizer. The vortex structures inside the pressure swirl atomizer and the axial variation of core diameter are investigated. As a result of the experimental and numerical studies, it is found that the air core diameter and spray cone angle are not much sensitive to the flow rate. The experimental and numerical studies show that, the low frequency

oscillations observed in the velocity field are associated with the dynamics of the vortical structures within the water region, while the high frequency oscillations are associated with the dynamics of the vortical structures at the head end of the air core.

Keywords: Pressure Swirl Atomizer, Aircore, High Speed Shadowgraphy Technique, Phase Doppler Particle Analyzer, Computational Fluid Dynamics, Volume of Fluid Method

ÖZ

BASINÇLI GİRDAP TİPİ PÜSKÜRTEÇLERİN DENEYSSEL VE SAYISAL OLARAK İNCELENMESİ

SÜMER, BÜLENT

Doktora, Havacılık ve Uzay Mühendisliği Bölümü

Tez Yöneticisi : Prof. Dr. İsmail H. TUNCER

Ortak Tez Yöneticisi : Doç. Dr. Oğuz UZOL

Şubat 2014 , 223 sayfa

Bu çalışmada basınçlı girdap tipi bir püskürteç içindeki zamana bağlı akışlar deneysel ve sayısal teknikler kullanılarak incelenmiştir. Basınçlı girdap tipi püskürtecin içindeki akışın ve oluşan spreyn zaman ve uzayda yüksek çözünürlükte gözlemlenebilmesi için Yüksek Hızlı Gölge Görüntüleme Tekniği kullanılmıştır. Basınçlı girdap tipi püskürtecin içindeki hava çekirdeğinin ve ortaya çıkan spreyn görüntüleri dört farklı su debisi için yakalanmıştır. Daha sonra, değişik eksenel lokasyonlardaki hava çekirdeği çapının zamana bağlı değişimi, geliştirilen görüntü işleme aracı kullanılarak bulunmuştur. Denk gelen ortalama spreyn koni açısı değerleride benzer şekilde elde edilmiştir. İncelemeler hava çekirdeğinin durağan olmayan özelliklerini ve spreyn makroskopik özelliklerini meydana çıkarmıştır. Spreyn mikroskopik özellikleri ise iki elamanlı Faz Doppler Parçacık Analizcisi kullanılarak belirlenmiştir. Ortaya çıkan su zerrelerinin Sauter ortalama çap dağılımları ve iki farklı zerre büyüklüğü sınıfı için hız dağılımları püskürteç içinden geçen su debisinin fonksiyonu olarak elde edilmiştir. Basınçlı girdap tipi püskürteç içindeki zamana bağlı iki fazlı akış sonlu hacim yöntemi tabanlı bir hesaplamalı akışkanlar dinamiği aracı kullanılarak hesaplanmıştır. Püskürteç içindeki zamana bağlı akışların incelenebilmesi için, İki boyutlu, eksenel simetrik döngülü ve üç boyutlu sayısal simülasyonlar gerçekleştirilmiştir. Basınçlı girdap tipi püskürteç içindeki girdap yapıları ve hava çekirdeği çapının eksenel değişimi incelenmiştir. Deneysel ve sayısal çalışmalar sonucunda, hava çekirdeği çap-

pının ve sprej koni açısının debiye fazla duyarlı olmadığı bulunmuştur. Deneysel ve sayısal çalışmalar, hız alanı içinde gözlenen düşük frekanslı salınımların su bölgesi içindeki girdap yapıları ile ilişkili olduğunu, diğer taraftan, hız alanı içinde gözlenen yüksek frekanslı salınımların hava çekirdeğinin kafa kısmında oluşan girdap yapıları ile ilişkili olduğunu göstermiştir.

Anahtar Kelimeler: Basıncılı Girdap Tipi Püskürteç, Yüksek Hızlı Gölge Görüntüleme Tekniğı, Faz Doppler Parçacık Analizcisi, Hesaplamalı Akışkanlar Dinamiğı, Akışkan Hacmi Metodu

To my family...

ACKNOWLEDGMENTS

I would like to express my appreciation to my supervisor Prof. Dr. İsmail H. Tuncer for his prompt responses to my submitted work, understanding and guidance throughout the study. I am grateful to Assoc. Prof. Dr. Oğuz Uzol for his support and encouragement.

I wish to thank Dr. Nejdet Erkan for his invaluable support and discussions on the subject.

I would like to thank to my thesis committee members, Prof. Dr Yusuf Özyörük and Prof. Dr. Haluk Aksel, for their interest on the subject and for their valuable comments.

I would like to thank to my brother, Dr. Bilsay Sümer, for his support and to my colleague, Mr. Bora Yazıcı, for discussions regarding different aspects of this study.

Finally, I would like to thank to my wife, Özlem Sümer, for her understanding, patience and support.

The present research has been supported by TÜBİTAK-SAGE under the project IBTA funded by the Republic of Turkey, Ministry of Development.

TABLE OF CONTENTS

ABSTRACT	v
ÖZ	vii
ACKNOWLEDGMENTS	x
TABLE OF CONTENTS	xi
LIST OF TABLES	xvii
LIST OF FIGURES	xviii
CHAPTERS	
1 INTRODUCTION	1
1.1 Background to the Research	1
1.2 Research Problem	5
1.3 Literature Survey	7
1.3.1 Introduction	7
1.3.2 Inviscid Flow Through the Pressure Swirl Atomizer	7
1.3.3 Flow Through the Pressure Swirl Atomizer-Experimental and Numerical Research	11
1.3.4 Pressure Swirl Atomizer - Dynamic Element in Liquid Propellant Rocket Thrust Chambers	25

1.3.5	Characterization of the Resulting Spray	30
1.4	Research on Pressure Swirl Atomizers - Why it is needed . .	39
1.5	Methodology	40
1.5.1	Outline of the Thesis	41
1.5.2	Definitions	42
2	EXPERIMENTAL INVESTIGATION	45
2.1	Introduction	45
2.2	Experimental Facility	45
2.3	Pressure Swirl Atomizer	46
2.4	Experimental Methodology	48
2.4.1	High Speed Shadowgraphy System	48
2.4.1.1	Image Capturing and Processing . . .	51
2.4.1.2	Image Processing Tool	54
2.4.1.3	From Pixel Coordinates to Physical Coordinates	55
2.4.2	Phase Doppler Anemometry Technique	57
2.4.2.1	Optical Alignment	62
2.4.2.2	Optical and Processor Setup	63
2.5	Experimental Results-High Speed Shadowgraphy System . .	64
2.5.1	Formation of the Air Core and the Hollow Cone Spray	64
2.5.2	Visualization and Qualitative Characterization of Air Core	68

	2.5.2.1	Precession Movement of the Air Core Cap	69
	2.5.2.2	Wave Forms on the Air Core	70
	2.5.3	Quantitative Analysis of the Air Core Diameter . . .	73
	2.5.3.1	Calculation of the Air Core Diameter . . .	73
	2.5.3.2	Comparison of Results	78
	2.5.3.3	Frequency Domain Analysis of the Air Core Diameter	78
	2.5.3.4	Mode Shapes of the Air Core Diameter	83
2.6		Experimental Results-Characterization of the Hollow Cone Spray	91
	2.6.1	Spray Cone Angle	91
	2.6.2	Microscopic Properties of the Hollow Cone Spray .	94
3		NUMERICAL INVESTIGATION	103
	3.1	Introduction	103
	3.2	Numerical Methodology	103
	3.2.1	Governing Differential Equations	104
	3.2.2	Solution Methodology	106
	3.2.2.1	Volume of Fluid Method	107
	3.3	Computational Domain Geometry Sensitivity and Grid Sen- sitivity Study	108
	3.3.1	Computational Domain Geometry Sensitivity Study	109
	3.3.1.1	Introduction	109

	3.3.1.2	Simulation Results	111
	3.3.1.3	Conclusion	117
	3.3.2	Grid Sensitivity Study	118
	3.3.2.1	Introduction	118
	3.3.2.2	Simulation Results	119
	3.3.2.3	Conclusion	125
3.4		Two Dimensional Axis-Symmetric Swirl Simulation Results	126
	3.4.1	Introduction	126
	3.4.2	Flow Through the Pressure Swirl Atomizer	126
	3.4.3	Vortex Dynamics	134
	3.4.3.1	Vortex Structures in the Water Region	135
	3.4.3.2	The Stagnation Region at the Head End of the Atomizer	138
	3.4.3.3	Vortex Structures in the Air Core	142
	3.4.4	Analysis of the Air Core Diameter	147
	3.4.5	Comparison of Results	149
3.5		Three Dimensional Flow Simulations	153
	3.5.1	Introduction	153
	3.5.2	Flow Through the Pressure Swirl Atomizer	154
	3.5.3	Vortex Dynamics	163
	3.5.4	Analysis of the Air Core Diameter	167
	3.5.5	Comparison of Results	169

4	CONCLUSIONS AND RECOMMENDATIONS	171
	REFERENCES	175
APPENDICES		
A	TIME HISTORY OF AIRCORE DIAMETER FOR DIFFERENT OPERATING POINTS	183
A.1	Q=2.0 lt/min	184
A.2	Q=3.18 lt/min	186
A.3	Q=4.0 lt/min	188
A.4	Q=5.0 lt/min	190
B	FREQUENCY SPECTRUM OF AIRCORE DIAMETER FOR DIFFERENT OPERATING POINTS	193
B.1	Q=2.0 lt/min	194
B.2	Q=3.18 lt/min	196
B.3	Q=4.0 lt/min	198
B.4	Q=5.0 lt/min	200
C	MODE SHAPES OF AIRCORE FOR DIFFERENT OPERATING POINTS	203
C.1	Q=2.0 lt/min	204
C.2	Q=3.18 lt/min	206
C.3	Q=4.0 lt/min	208
C.4	Q=5.0 lt/min	210
D	TIME HISTORY OF AIRCORE DIAMETER- 2D AXISYMMETRIC SWIRL NUMERICAL SIMULATIONS	213

E	FREQUENCY SPECTRUM OF AIRCORE DIAMETER- 2D AX- ISYMMETRIC SWIRL NUMERICAL SIMULATIONS	217
	CURRICULUM VITAE	221

LIST OF TABLES

TABLES

Table 2.1	High speed camera settings for spray and air core.	49
Table 2.2	Beam waist, fringe spacing, limits of measurable velocity and diameter	63
Table 2.3	Axial coordinates of the stations.	74
Table 2.4	Mean air core diameter and the corresponding standard deviations. .	77
Table 2.5	Comparison of air core diameter at swirl chamber and mid nozzle. .	78
Table 2.6	The reconstruction ratio for POD approximations.	86
Table 3.1	Values for horizontal and vertical dimensions and the resulting number of elements for each grid.	110
Table 3.2	Calculated mean air core diameters at four different axial locations. .	121
Table 3.3	Predicted mean axial velocities, corresponding standard deviations and the frequency peaks at designated probe points	146
Table 3.4	Comparison of air core diameters at designated stations	150

LIST OF FIGURES

FIGURES

Figure 1.1	The main elements of a thrust chamber assembly.	2
Figure 1.2	The classification of pressure atomizers.	3
Figure 1.3	A typical bi-propellant coaxial pressure swirl injector design.	4
Figure 1.4	Flow through the pressure swirl atomizer and hollow cone spray.	6
Figure 1.5	Flow through the pressure swirl atomizer.	8
Figure 1.6	Passage fullness ratio versus discharge coefficient.	10
Figure 1.7	Photograph of air core inside the pressure swirl atomizer [14].	12
Figure 1.8	Comparison of discharge coefficient measurements with inviscid theory predictions and experimental correlations [19].	15
Figure 1.9	Mean film thickness at the orifice [21].	17
Figure 1.10	Variation of film thickness at the exit, spray cone angle and discharge coefficient with D_s/D_o [24].	18
Figure 1.11	Variation of film thickness and velocities at the nozzle exit [25].	19
Figure 1.12	Air core on a fully developed cylindrical swirl atomizer [36].	23
Figure 1.13	Effect of extra swirl chamber length on the air core [39].	24
Figure 1.14	Response function for Bazarov's atomizer [44].	28
Figure 1.15	Image of the air core diameter.	29
Figure 1.16	Properties of the spray [47].	31
Figure 1.17	Images of the spray formed by a coaxial injector [60].	35
Figure 1.18	Stationary and pulsating sprays [67].	37
Figure 1.19	Hierarchy in Injector Experiments.	41

Figure 1.20 The main parts of a pressure swirl atomizer.	42
Figure 2.1 Single element atmospheric cold flow facility.	46
Figure 2.2 The internal geometry of the pressure swirl atomizer.	47
Figure 2.3 Plexiglas pressure swirl atomizer on the experimental facility.	47
Figure 2.4 High Speed Shadowgraphy System.	48
Figure 2.5 LED and the collimating optics.	50
Figure 2.6 Diffuser screen and the images with and without diffuser screen.	50
Figure 2.7 Images of the air core inside the atomizer (left) and the resulting hollow cone spray (right).	51
Figure 2.8 Conversion of RGB image to gray scale image	52
Figure 2.9 Application of various edge detectors to gray scale image.	53
Figure 2.10 Sobel edge detector weighted central difference operators.	53
Figure 2.11 The sample image after application of Sobel edge detector.	54
Figure 2.12 The change of normalized intensity along a line at $x=200$ pixel.	55
Figure 2.13 Calibration images, fine needle and ruler.	56
Figure 2.14 Schematic of phase Doppler anemometry system.	57
Figure 2.15 Transmitter and receiver optics positioned on three-axis traverse.	59
Figure 2.16 The fiberoptic transmitter probe and its elements.	60
Figure 2.17 Probe volume, fringes and the diameter of the measurement volume.	61
Figure 2.18 Electrical signal and application of filters.	62
Figure 2.19 Formation of the air core and the hollow cone spray.	65
Figure 2.20 Flow rate versus pressure drop.	66
Figure 2.21 Air core and spray at different flow rates.	67
Figure 2.22 Pressure drop and mass flow rate.	68
Figure 2.23 Mushroom cap of the air core and tip of the cap.	69
Figure 2.24 Precession movement of the air core cap.	69

Figure 2.25 Cavitation waves at the head end of the atomizer (3.18 lt/min water).	71
Figure 2.26 Free surface waves (3.18 lt/min water).	72
Figure 2.27 Rotational waves (3.18 lt/min water).	72
Figure 2.28 Stations for the air core diameter calculations.	73
Figure 2.29 Time history of air core diameter at designated stations.	75
Figure 2.30 Mean air core diameter and the corresponding standard deviations.	76
Figure 2.31 Frequency spectrum of the air core diameter at designated stations.	80
Figure 2.32 Air core diameter data as a three dimensional surface for different operating points.	85
Figure 2.33 Singular values.	86
Figure 2.34 First mode shape of the air core (Q=2.0 lt/min) , isometric view (a) and side view (b) .	87
Figure 2.35 First four mode shapes, Q=2.0 lt/min.	88
Figure 2.36 First four mode shapes, Q=3.18 lt/min.	89
Figure 2.37 First four mode shapes, Q=4.0 lt/min.	89
Figure 2.38 First four mode shapes, Q=5.0 lt/min.	90
Figure 2.39 Hollow cone spray for different flow rates.	91
Figure 2.40 Schematic for the spray cone angle calculation.	92
Figure 2.41 Edges of the spray (Q=3.18 lt/min).	92
Figure 2.42 Coordinate system and the measurement locations.	94
Figure 2.43 Diameter histograms at designated locations.	95
Figure 2.44 Contour plots of Sauter mean diameter for different flow rates.	96
Figure 2.45 Velocity histograms at designated locations.	97
Figure 2.46 Mean and RMS x-velocity contours [m/s] and streamlines originated from a line at x=16 ($d < 10 \mu\text{m}$).	98
Figure 2.47 Mean and RMS x-velocity contours [m/s] and streamlines originated from a line at x=16 ($d > 100 \mu\text{m}$).	99

Figure 2.48 Mean and RMS y-velocity contours [m/s] and streamlines originated from a line at $x=16$ ($d<10\mu\text{m}$).	100
Figure 2.49 Mean and RMS y-velocity contours [m/s] and streamlines originated from a line at $x=16$ ($d>100\mu\text{m}$).	100
Figure 3.1 Overview of iterative time advancement scheme.	107
Figure 3.2 Computational domain for AXS numerical simulations.	109
Figure 3.3 Grids for different computational domains.	110
Figure 3.4 Initial computational domain, contours of volume fraction of air (GRID1B).	111
Figure 3.5 Evolution of air volume fraction with time (GRID1B).	112
Figure 3.6 Evolution of axial velocity and swirl velocity on Probe1.	113
Figure 3.7 Mean volume fraction contours of air.	114
Figure 3.8 Mean axial velocity contours [m/s].	115
Figure 3.9 Mean axial velocities and corresponding standard deviations along designated stations.	115
Figure 3.10 Mean swirl velocity contours [m/s].	116
Figure 3.11 Mean swirl velocities and corresponding standard deviations along designated stations.	117
Figure 3.12 Computational domains used in grid sensitivity study.	118
Figure 3.13 Evolution of air volume fraction contours for GRID2, GRID3 and GRID4.	119
Figure 3.14 Mean volume fraction contours of air.	120
Figure 3.15 Mean volume fraction contours of air at the head end of the atomizer.	121
Figure 3.16 Mean static pressure contours [bars].	122
Figure 3.17 Mean axial velocity contours [m/s].	122
Figure 3.18 Mean swirl velocity contours [m/s].	123
Figure 3.19 Mean axial velocities and corresponding standard deviations along designated stations.	124

Figure 3.20 Mean swirl velocities and corresponding standard deviations along designated stations.	125
Figure 3.21 Mean Volume fraction contours of air.	126
Figure 3.22 Mean volume fractions at designated stations.	127
Figure 3.23 Contours of volume fraction of air together with in plane velocity vectors.	128
Figure 3.24 Mean axial velocity contours [m/s].	128
Figure 3.25 Mean axial velocities and corresponding standard deviations along designated stations.	130
Figure 3.26 Mean swirl velocity contours [m/s].	131
Figure 3.27 Mean swirl velocities and corresponding standard deviations along designated stations.	132
Figure 3.28 Mean radial velocity contours [m/s].	133
Figure 3.29 Vortex structures inside the pressure swirl atomizer.	134
Figure 3.30 Evolution of the corner vortices near the swirl chamber wall.	136
Figure 3.31 Time history of axial velocity and frequency domain representation of axial velocity signal.	137
Figure 3.32 Stagnation region, water and air flows.	138
Figure 3.33 Stagnation region, volume fraction contours of air and in plane velocity vectors.	139
Figure 3.34 Time history of air core diameter and frequency domain representation of air core diameter signal along a station at $x=0.2$ mm.	140
Figure 3.35 Time history of axial, radial and swirl velocity and frequency domain representation of velocity signals.	141
Figure 3.36 Vortex structures in the air core.	142
Figure 3.37 Vortex structures at four different regions of the air core.	143
Figure 3.38 Evolution of the vortices in the air core.	144
Figure 3.39 Time history of axial velocity and frequency domain representation of axial velocity signal.	145
Figure 3.40 Time history of air core diameter at designated stations.	147

Figure 3.41 Frequency spectrum of air core diameter.	148
Figure 3.42 Mean air core diameter and standard deviations.	149
Figure 3.43 Comparison of frequency spectrum of air core diameter at designated stations, experiment and AXS numerical simulations.	151
Figure 3.44 The geometry of the solution domain and computational grid for 3D flow simulations.	153
Figure 3.45 Initial volume fractions contours of air.	154
Figure 3.46 Evolution of the volume fractions contours of air.	155
Figure 3.47 Mean volume fraction contours of air.	156
Figure 3.48 Mean axial velocity contours.	157
Figure 3.49 Periodic boundaries and three different planes.	157
Figure 3.50 Comparison of mean axial velocities at three different planes	158
Figure 3.51 Comparison of 3D mean axial velocities and the corresponding standard deviations (theta=90 plane) and 2D-AXS mean axial velocities and the corresponding standard deviations.	159
Figure 3.52 Comparison of mean swirl velocities at three different planes. . . .	160
Figure 3.53 Comparison of 3D mean swirl velocities and the corresponding standard deviations (theta=90 plane) and AXS mean swirl velocities and the corresponding standard deviations.	161
Figure 3.54 Vortices in the water region and air core vortex as visualized by Q-isosurfaces.	164
Figure 3.55 Contours of volume fraction and in plane velocity vectors (theta=90). 165	
Figure 3.56 Isosurfaces of volume fraction of air	166
Figure 3.57 Time history of air core diameter at designated stations (theta=90). 167	
Figure 3.58 Frequency domain representation of air core diameter at designated stations (theta=90).	168
Figure 3.59 Mean air core diameter and standard deviations predicted by numerical simulations.	169
Figure 3.60 Comparison of mean air core diameter data-3D numerical simulations and experiment.	170

Figure A.1	Time history of the aircore diameter, Stations 1-10.	184
Figure A.2	Time history of the aircore diameter, Stations 11-20.	185
Figure A.3	Time history of the aircore diameter, Stations 1-10.	186
Figure A.4	Time history of the aircore diameter, Stations 11-20.	187
Figure A.5	Time history of the aircore diameter, Stations 1-10.	188
Figure A.6	Time history of the aircore diameter, Stations 11-20.	189
Figure A.7	Time history of the aircore diameter, Stations 1-10.	190
Figure A.8	Time history of the aircore diameter, Stations 11-20.	191
Figure B.1	Frequency spectrum of the aircore diameter, Stations 1-10.	194
Figure B.2	Frequency spectrum of the aircore diameter, Stations 11-20.	195
Figure B.3	Frequency spectrum of the aircore diameter, Stations 1-10.	196
Figure B.4	Frequency spectrum of the aircore diameter, Stations 11-20.	197
Figure B.5	Frequency spectrum of the aircore diameter, Stations 1-10.	198
Figure B.6	Frequency spectrum of the aircore diameter, Stations 11-20.	199
Figure B.7	Frequency spectrum of the aircore diameter, Stations 1-10.	200
Figure B.8	Frequency spectrum of the aircore diameter, Stations 11-20.	201
Figure C.1	Mode shapes of the aircore, Modes1-10.	204
Figure C.2	Mode shapes of the aircore, Modes11-20.	205
Figure C.3	Mode shapes of the aircore, Modes1-10.	206
Figure C.4	Mode shapes of the aircore, Modes11-20.	207
Figure C.5	Mode shapes of the aircore, Modes1-10.	208
Figure C.6	Mode shapes of the aircore, Modes11-20.	209
Figure C.7	Mode shapes of the aircore, Modes1-10.	210
Figure C.8	Mode shapes of the aircore, Modes11-20.	211
Figure D.1	Time history of the aircore diameter, Stations 1-10.	214

Figure D.2 Time history of the aircore diameter, Stations 11-20. 215

Figure E.1 Frequency spectrum of the aircore diameter, Stations 1-10. 218

Figure E.2 Frequency spectrum of the aircore diameter, Stations 11-20. 219

CHAPTER 1

INTRODUCTION

Combustion systems installed on aerial and launch vehicles make use of liquid fuels because of their high volumetric efficiencies. Combustion systems using liquid fuels rely on effective atomization to increase the specific surface area of the fuel and thereby achieve high rates of mixing and evaporation. The vaporization of the fuel droplet is necessary before it burns and it is strongly dependent on the surface area of the droplet. In most of the combustion systems, the reduction in mean fuel drop size leads to higher volumetric heat release rates, easier ignition, and a wider burning range [1]. Therefore, the transformation of bulk liquid into sprays and other physical dispersions of small particles in a gaseous atmosphere are important in the combustion process. Sprays can be produced in many different ways. Essentially, all that is needed is a high relative velocity between the liquid to be atomized and the surrounding gas. The process of atomization is one in which a liquid jet or sheet is disintegrated by a suitable type of energy. A device used for liquid atomization is most frequently called an atomizer. The atomizer can be an independent device or part of a complex device such as a bi-propellant liquid propellant rocket injector or a diesel injector [2].

1.1 Background to the Research

Liquid rocket engines have been widely used in missile and launch vehicle applications. These type of engines have the highest demonstrated performance of any chemical rocket propulsion system. They have the advantage of thrust modulation

and re-usability over the solid propellant rocket engines. In bi-propellant rocket engines, liquid fuel and oxidizer are stored in separate tanks and they are fed into the thrust chamber assembly where they mix and react chemically. The resulting hot gases are then accelerated through a converging diverging nozzle to generate thrust. In general, the thrust chamber assembly consists of a welded one piece injector assembly, and a regeneratively cooled thrust chamber structure. The injector assembly features oxidizer inlet, oxidizer dome/manifold, fuel manifold and bi-propellant injector elements, number of which primarily depends on the thrust level of the Liquid Rocket Engine. The main elements of a thrust chamber assembly is shown in Figure 1.1

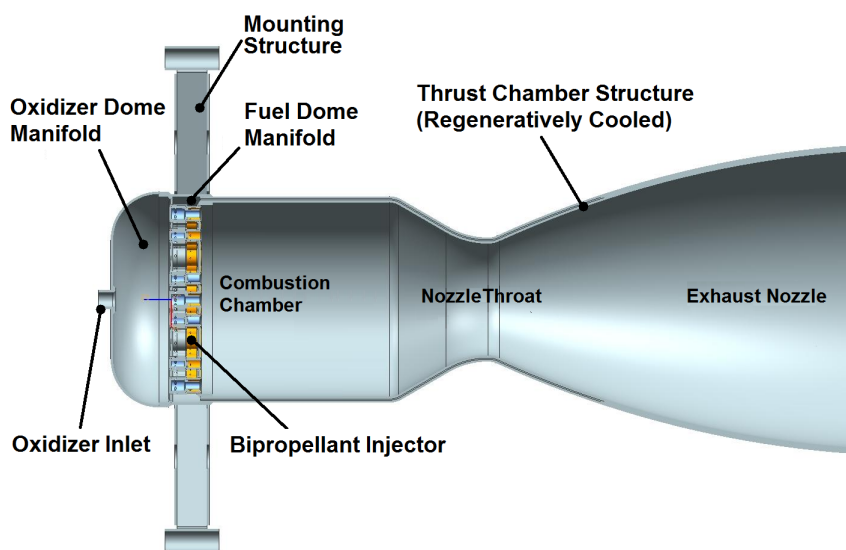


Figure 1.1: The main elements of a thrust chamber assembly.

The combustion process takes place in the thrust chamber and injectors are the main elements that define the combustion efficiency, stability and heat transfer characteristics. The injector is solely responsible for propellant atomization and combustible mixture formation. The performance of the thrust chamber assembly is dependent on the injector design. Inadequate mixing of propellants or deficiency in atomization may lead to a poor performing thrust chamber [3].

The injector design also affects the stability characteristics of the thrust chamber. An injector design may be fine tuned to minimize the coupling between the fluid mechan-

ics/acoustics of the chamber and the combustion process to impede the combustion instability. Wide margins of acoustic stability were achieved in Russian liquid rocket engines even at very high thrust chamber pressures by the use of acoustically tuned injectors, whose internal cavities serve as acoustic resonators [4].

The most often used method for liquid atomization and mixing formation in liquid rocket engines is the conversion of potential energy in the form of pressure drop to kinetic energy of the propellants by use of the pressure atomizers. Pressure atomizers rely on the conversion of pressure to kinetic energy to achieve a high relative velocity between the liquid and the surrounding gas. The energy efficiency of such injectors is low, since the major part of the energy is consumed in increasing the liquid velocity rather than overcoming surface tension [5]. General classification of pressure atomizers is given in Figure 1.2.

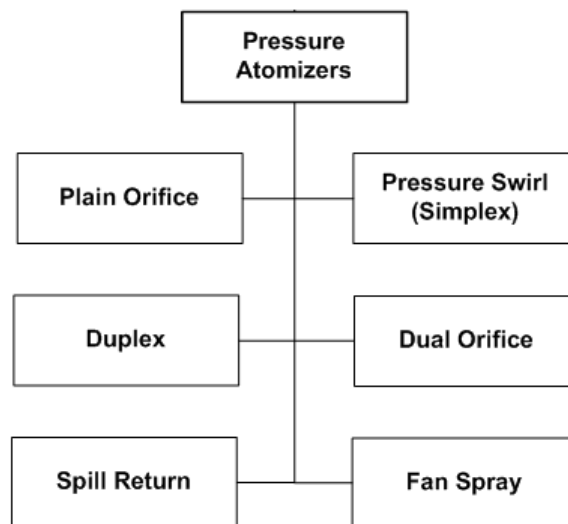


Figure 1.2: The classification of pressure atomizers.

Liquid rocket engines, which use unlike impinging, like impinging or shower head injectors, utilize plain orifice atomizers. Like and Unlike Impinging type elements are widely used in liquid rocket thrust chambers that are designed in the U.S.A. The F1 engine of the Apollo Space Vehicle utilized impinging type elements with cryogenic-storable combination of Liquid Oxygen and RP-1. However, this propellant combi-

nation with impinging type elements led to combustion instability problems. During the first test of the engine at rated thrust, the engine got a spontaneous instability which destroyed the engine. Within a period of one year, they had eleven catastrophic failures because of the combustion instability which resulted in the initiation of the so called, "Program Go". In the "Program Go" the causes of the instabilities were investigated [6]. The investigations mainly concentrated on impinging type of injectors and baffles to suppress the combustion instabilities.

On the other hand, the Russian engines that use the same cryogenic-storable formulation and utilizes bi-propellant pressure swirl type injection elements have minor combustion instability problems [7]. All three stages of the Soyuz Space Vehicle use liquid propellant engines that utilize bi-propellant swirl type injectors. A typical bi-propellant pressure swirl injector is shown in Figure 1.3, which has an inner oxidizer atomizer and a fuel atomizer at the periphery.

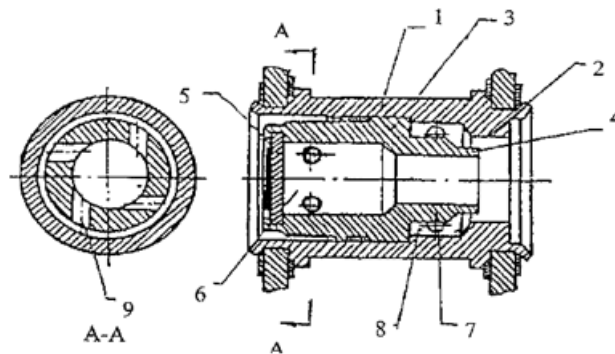


Figure 1.3: A typical bi-propellant coaxial pressure swirl injector design.

Bi-propellant swirl injector has a hollow casing (1) with a nozzle (2) which serves as a fuel atomizer in this case. The hollow insert (3) with the nozzle (4) and flared-out bottom (5), which serves as an oxidizer atomizer, are brazed into the fuel atomizer. The flared bottom (5) and the insert (3) forms the swirl chamber of the oxidizer atomizer (6) which is connected to the oxidizer delivery manifold through the tangential passages (9). The insert (3) and the casing (1) form a peripheral vortex chamber for the fuel which is connected to its delivery manifold through its tangential passages (7).

Pressure swirl atomizers are found to be the inexpensive and the most reliable type of atomizer for fuel injection due to its superior atomization characteristics and relatively simple geometry. The atomization characteristics of swirl atomizers offer a significant advantage in throttling and give high thrust per atomizer. The swirl atomizers are less sensitive to manufacturing processes, chocking and cavitation when compared to plain orifice atomizers. They also have self tuning capability with variable flow resistance under transient conditions which improves the engine start up operations. The pressure swirl atomizers, in general, produce a hollow cone spray without the presence of liquid jet along the axis of the atomizer. This property of the hollow cone spray has the advantage of recirculating the hot combustion products to the atomizer exit to stabilize the flame and protecting the wall of the injector plate from excessive heat in liquid rocket engines [8] .

1.2 Research Problem

Despite of the geometric simplicity of the pressure swirl atomizer, the hydrodynamic processes occurring within the nozzle are highly complex. The formation of the air core and the resulting unsteady phenomena are the most interesting features of this kind of atomizer. Liquid enters the atomizer through the tangential inlet ports and moves like a free vortex inside the atomizer, resulting in high velocity and low pressure along the axis of the atomizer. As mass flow rate through the atomizer increases, the velocity of the liquid at the center increases and the pressure along the axis of the atomizer falls below the ambient pressure. An airflow forms from the ambient medium into the atomizer by depleting the liquid along the axis and a liquid vortex with a free surface is formed within the atomizer. The radius of the free surface changes from a minimum at the base of the swirl chamber to a larger value at the exit of the nozzle. A thinner liquid film exits through the nozzle and eventually breaks up into fine droplets forming a hollow cone spray as shown in 1.4.

The formation of the air core within the atomizer makes the flow inside the atomizer a free surface flow whose numerical treatment calls for special methods to track the liquid/gas interface. On the other hand, the formation of the air core reduces the mass flow rate through the exit nozzle and in turn reduces the discharge coefficient of

the atomizer. The liquid goes out of the atomizer as a liquid film which affects the atomization characteristic of the atomizer profoundly.

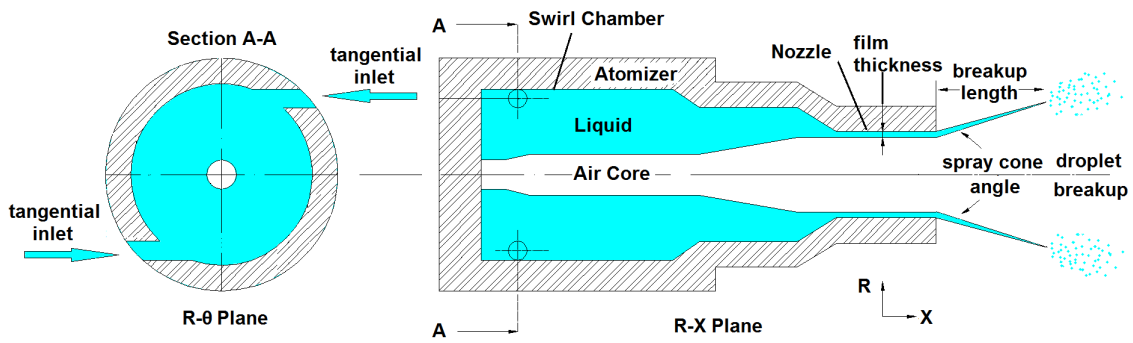


Figure 1.4: Flow through the pressure swirl atomizer and hollow cone spray.

The main objective of this thesis is to study the formation of the air core inside the pressure swirl atomizer and the resulting hollow cone spray. Unsteady flows inside pressure swirl atomizers are investigated experimentally with a High Speed Shadowgraphy System. It provides large amount of transient and fine resolved air core diameter data, which is then used to investigate highly transient two-phase fluid flow physics with statistical methods. Furthermore, detailed numerical investigation of the unsteady flow inside the atomizer is performed using Computational Fluid Dynamics (CFD) Tools. The macroscopic and microscopic properties of the resulting hollow cone spray are investigated using High Speed Shadowgraphy and Phase Doppler Anemometry techniques respectively.

1.3 Literature Survey

1.3.1 Introduction

Pressure swirl atomizers are used in many different fields, yet the main interest of the present study is their usage in combustion systems, especially on the liquid propellant rocket engine combustors. The survey of the literature will be widened to include previous work on chemical engineering field in order to evaluate the significance of the research accomplished on that area from the point of view of the current study.

The research on the pressure swirl atomizer can be handled in two branches for which the analysis methods differ significantly. The first branch deals with the flow inside the atomizer and its steady and dynamic characteristics, while the second branch deals with the properties of the resulting hollow cone spray. With the mentioned classification in mind, the literature will firstly be surveyed for the previous work related with the inner atomizer flows and secondly the previous work related with the characterization of the resulting spray.

1.3.2 Inviscid Flow Through the Pressure Swirl Atomizer

The highly complex hydrodynamic processes that occur within the swirl atomizer direct researchers to use simplified models. In the earlier analytical studies, the flow inside the swirl atomizer is treated as steady, incompressible, inviscid flow [9], [10], [11]. The theory proposed by Abramovich [9] and Taylor [10] and later by Giffen [11] concentrated on the same equations and assumptions with a minor difference on the parameters used to formulate the problem [12]. Due to its historical and practical importance the inviscid theory of swirl atomizer as proposed by Abramovich [9] will be discussed in this section.

A swirl atomizer consists of three main elements; tangential inlet passages, swirl chamber and the nozzle. The flow enters to the swirl chamber from the tangential inlet passages with a velocity V_{in} . The inlet velocity has only tangential component if the tangential inlets are normal to the R-X plane as shown in Figure 1.5. U_A , U_T and U_R are the axial, tangential and radial velocity components of the liquid film.

The change in the free surface radius is directly related to the change in the velocity components. If the gas cavity assumed to be stationary then pressure on the liquid surface is equal to the combustion chamber pressure.

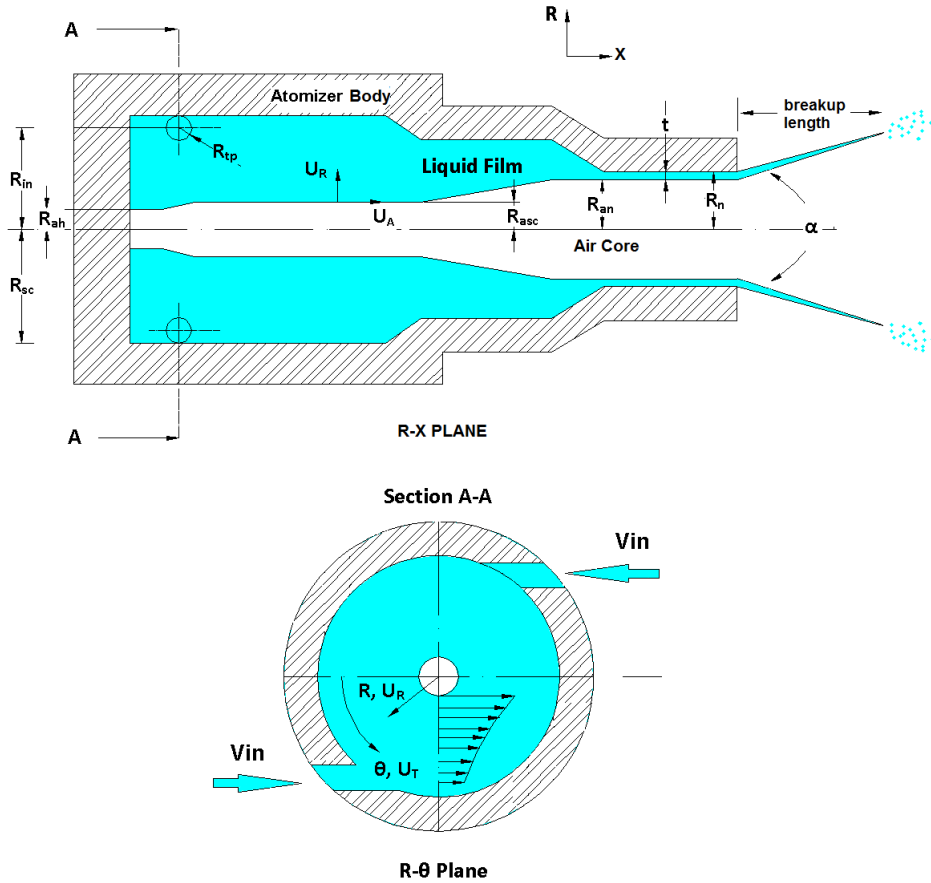


Figure 1.5: Flow through the pressure swirl atomizer.

Abramovich [9] treated the flow inside the pressure swirl atomizer as a steady, incompressible, inviscid flow and used the continuity equation and Bernoulli's equation together with the angular momentum equation to solve the flow problem inside the atomizer. He defines the coefficient of passage fullness (ϵ), as the ratio of the area of the liquid film at the nozzle A_{nf} to the area of the nozzle A_n as follows;

$$\epsilon = \frac{A_{nf}}{A_n} = \frac{\pi(R_n^2 - R_{an}^2)}{\pi R_n^2} = 1 - \frac{R_{an}^2}{R_n^2} \quad (1.1)$$

Where R_{an} is the radius of the air core at the nozzle and R_n is the radius of the nozzle. Abramovich [9] finds the mass flow rate through atomizer as;

$$\dot{m} = \frac{\epsilon}{\sqrt{1 + \frac{A^2 \epsilon^2}{1-\epsilon}}} \rho_f A_n \sqrt{P_f - P_c} \quad (1.2)$$

where A is the geometric characteristic parameter of the atomizer, ρ is the density of the liquid, A_n is the area of the nozzle, P_f is the pressure of the fluid at the inlet of the atomizer and P_c is the combustion chamber pressure, which reduces to ambient pressure at ambient conditions.

The discharge coefficient, which relates the actual flow rate to the maximum flow rate through the nozzle, shows itself as the first term on the left hand side of Equation 1.2. The discharge coefficient is a function of the geometric characteristic parameter of the atomizer (A) and the coefficient of passage fullness (ϵ) and can be written as follows;

$$\mu = \frac{\epsilon}{\sqrt{1 + \frac{A^2 \epsilon^2}{1-\epsilon}}} \quad (1.3)$$

For different values of the geometric characteristic parameter, the discharge coefficient can be plotted as a function of the passage fullness ratio as shown in Figure 1.6. For each value of the geometric characteristic parameter (A), there exist a certain passage fullness value which makes the discharge coefficient maximum. This is in accordance with the principle of maximum flow [9] which states that the diameter of the air core will be such that the mass flow rate through the atomizer will be a maximum.

In mathematical terms the principle of maximum flow can be stated as;

$$\frac{d\dot{m}}{d\epsilon} = \frac{d\mu}{d\epsilon} = 0 \quad (1.4)$$

Solution of Equation 1.4 leads to definitions of geometric parameter and the discharge coefficient as a function of the passage fullness ratio only as follows

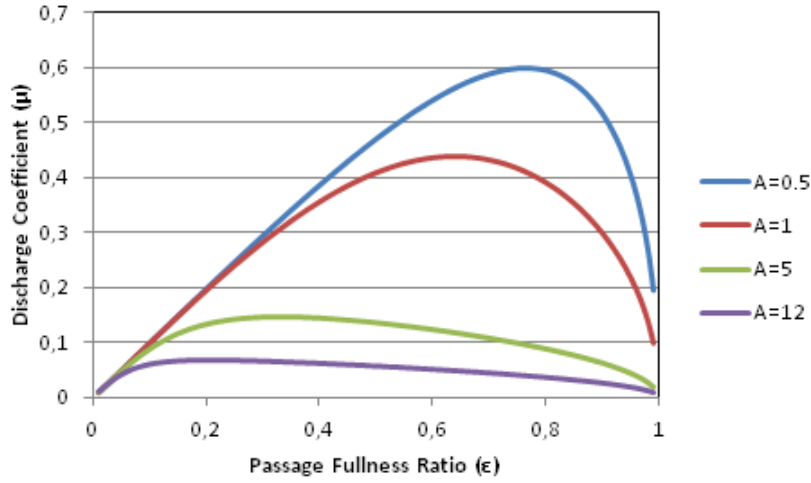


Figure 1.6: Passage fullness ratio versus discharge coefficient.

$$A = \frac{(1 - \epsilon) \sqrt{2}}{\epsilon \sqrt{\epsilon}} \quad (1.5)$$

$$\mu = \epsilon \sqrt{\frac{\epsilon}{2 - \epsilon}} \quad (1.6)$$

The spray cone angle can be calculated as the ratio of the tangential velocity of the liquid film at mean radius ($r_m = (r_{an} + r_n)/2$), to the axial velocity of the liquid at the nozzle. The calculated value can be written as a function of the passage fullness coefficient as follows

$$\tan\left(\frac{\alpha}{2}\right) = \frac{2 \sqrt{2}(1 - \epsilon)}{\sqrt{\epsilon}(1 + \sqrt{1 - \epsilon})} \quad (1.7)$$

Equations 1.5, 1.6 and 1.7 are very useful in that they easily correlate the mass flow rate to the atomizer geometry. Once the spray angle is determined based on the design considerations, one can calculate the coefficient of passage fullness using equation 1.7. The geometric parameter of the atomizer and the discharge coefficient are then determined using equations 1.5 and 1.6, respectively.

The mass flow rate of the propellant through the atomizer, the density of the propel-

lant, the combustion chamber pressure (P_c) and the pressure of the propellant at the manifold (P_f) are known from a priori performance analysis of the liquid rocket engine. Using the known values above one can calculate the area of the atomizer nozzle from Equation 1.2.

Giffen and Muraszew [11] compared their inviscid analysis results with the experiments and observed significant differences. They arrived to conclusion that the theoretical results should be regarded as indicating trends rather than giving numerical values.

Khavkin [13] reviewed the theories of other Russian researchers on swirl atomizer flows and concluded that none of them has any advantage over Abramovich's theory. On the other hand Khavkin points out that deviation of the discharge coefficient between tested and calculated according to Abramovich's theory reach two, even three times. Khavkin [13] related the discrepancy in discharge coefficient to F/V ratio, where F is the inner surface area of the atomizer and V is the inner volume of the atomizer, and to viscous losses. He points out that for F/V values less than 0.5 frictional losses are not effective and start to be effective for larger values of F/V . He pointed out that the viscous losses do not solely depend on the size and geometry but also on the physical properties of the liquid, like the viscosity and the surface tension. He also commented that although the Equation 1.7 is simple, the deviation of the calculated spray cone angle values are large when compared to the experimental data.

The treatment of the flow inside the atomizer as steady, inviscid, incompressible flow together with the employment of principle of maximum flow leads to very basic equations which can be used in conceptual design of pressure swirl atomizers, but more complicated treatment is needed to obtain high fidelity results.

1.3.3 Flow Through the Pressure Swirl Atomizer-Experimental and Numerical Research

Som and Mukherjee [14] performed theoretical and experimental studies to investigate the effect of non-dimensional geometrical parameters on the air core diameter. They established theoretical relations by using the laminar boundary layer equations

for steady motion of a viscous axis-symmetric liquid flow through the swirl atomizer by assuming a free vortex potential core exists. They used direct photographic technique and simple cathetometer to measure the air core diameter. A sample photograph, which was taken by Som and Mukherjee is shown in Figure 1.7

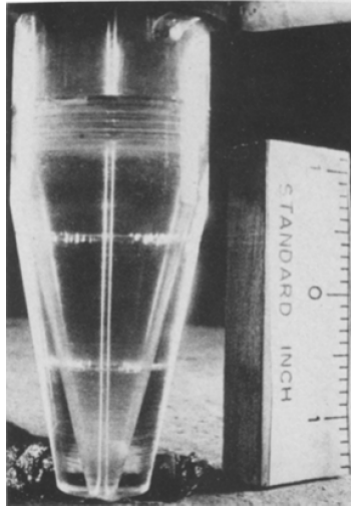


Figure 1.7: Photograph of air core inside the pressure swirl atomizer [14].

They found that;

- For any nozzle the air core radius is a direct function of Reynolds number at the inlet to the nozzle only at its lower range then remains constant,
- For any fixed values of inlet Reynolds number to the nozzle, length to diameter ratio of the swirl chamber and swirl chamber convergence angle, the ratio of air core diameter to nozzle diameter increases with an increase in the nozzle to swirl chamber diameter ratio
- For fixed values of nozzle to swirl chamber diameter ratio and length to diameter ratio of the swirl chamber the ratio of air core diameter to nozzle diameter increases with an increase in swirl chamber convergence angle.
- For fixed values of nozzle to swirl chamber diameter ratio and swirl chamber convergence angle, the ratio of air core to nozzle diameter increases with the decrease in length to diameter ratio of the swirl chamber.

In his following works, Som [15], [16] extends his theoretical formulation based on laminar boundary layer equations to take into account non-Newtonian liquids. The experimental observations of the air core forming within a Perspex atomizers are obtained using photographic technique which utilizes a telescopic eye piece. The experimental observations revealed the formation of the air core which started as a depletion of the fluid at the exit of the nozzle. After the initiation of the air core, it remained stable and they did not observe any fluctuations on the air core. Som suspected of occurrence of hydrodynamic instabilities of the swirling boundary layer yet does not resolve those instabilities either with his theoretical formulations or the conducted experiments.

Rizk and Lefebvre [17] examined the influences of main dimensions and operating conditions of swirl atomizers on the thickness of the annular liquid film at the nozzle of the atomizer using analytical methods. In their analytical treatment of the flow inside the pressure swirl atomizer, they consider a small element of the liquid film in the nozzle and assume that only pressure and viscous forces act on this element and under steady flow conditions these forces balance each other. With this way they found an analytical expression for the average velocity at the nozzle and expression for the spray cone angle. Taking into account also the work of Giffen and Muraszew [11] they find an analytical expression for the liquid film thickness as follows;

$$t^2 = \frac{1560FN\mu (1 + X)}{\rho^{0.5}d_o\Delta P^{0.5} (1 - X)^2} \quad (1.8)$$

where t is the liquid film thickness, d_o is the diameter of the nozzle, FN is the flow number, μ is the viscosity of the liquid, ρ is the density of the liquid, ΔP is the pressure drop across the atomizer and X is ratio of the air core area to nozzle area and given by;

$$X = \frac{(d_o - 2t)^2}{d_o^2} \quad (1.9)$$

Since X is also a function of film thickness (t) at the exit of the nozzle of Equations 1.8 and 1.9 needs to be solved iteratively.

They used equation 1.8 to calculate the film thickness for different nozzle dimensions

and operating conditions, using the measured flow rates and compared their results with experiments. The calculated film thickness values for different injection pressures follows the general trend of the experimental curves, yet deviation from the experimentally measured values are high at some cases.

They also suggested an expression for the discharge coefficient as a function of geometrical parameters of the atomizer as follows;

$$C_D = 0.35 \left(\frac{A_p}{D_s d_o} \right)^{0.5} \left(\frac{D_s}{d_o} \right)^{0.25} \quad (1.10)$$

where A_p is the area of the tangential inlet passages, D_s is the diameter of the swirl chamber and d_o is the diameter of the nozzle.

Based on their analytical expression, Rizk and Lefebvre [17] concluded that;

- an increase in pressure drop across the injector leads to thinner film thickness,
- an increase in the inlet area leads to thicker film thickness,
- a decrease in swirl chamber diameter leads to thicker film thickness,
- effects of both orifice and swirl chamber lengths on film thickness are quite small.

Suyari and Lefebvre [18] derived a new equation for the liquid film thickness by equating equation 1.9 to the discharge coefficient equation proposed by Giffen and Muraszew [11] as follows;

$$0.09 \left[\frac{A_p}{D_s d_o} \right] \left[\frac{D_s}{d_o} \right]^{0.5} = \frac{(1 - X)^3}{1 + X} \quad (1.11)$$

They also derived an expression for the film thickness at the exit of the atomizer as follows;

$$t = 3.66 \left[\frac{d_o \dot{m}_L \mu_L}{\rho_L \Delta P} \right]^{0.25} \quad (1.12)$$

where d_o is the nozzle exit diameter, t is the liquid film thickness at the nozzle exit, ρ_L is the density of the liquid, μ_L is the dynamic viscosity of the liquid, ΔP is the pressure drop across the atomizer, \dot{m} is the mass flow rate across the atomizer.

They measured the liquid film thickness at the exit of a simplex atomizer by using an electrical conductance method and compared the results of the experiments with the ones obtained using equation 1.11. They concluded that the best fit between the measured values of liquid film thickness and the various equations for calculating film thickness is provided by equation 1.11 and the film thickness is over predicted by equation 1.8 and 1.12.

Ballester and Dopazo [19] investigated experimentally the influence of pressure swirl atomizer dimensions and injection conditions on discharge coefficient and spray angle. They compare their test results on discharge coefficient with the available correlations and inviscid theory. The comparison of the measurements of discharge coefficient with the experimental correlations and inviscid theory is given in Figure 1.8.

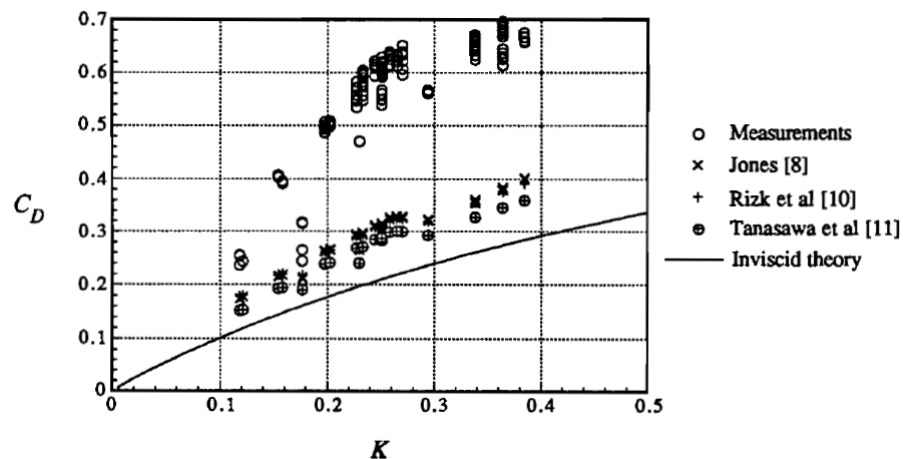


Figure 1.8: Comparison of discharge coefficient measurements with inviscid theory predictions and experimental correlations [19].

They stated that the measured discharge coefficients deviates considerably from the ones calculated using the inviscid theory and published experimental correlations. They related this deviation to the size of the atomizers, which is small in their case. They attributed the differences in the behavior of small size atomizers to the significant role of viscous effects.

Chinn et. al. [20] used the Computational Fluid Dynamics (CFD) package FLUENT to investigate the flow inside a pressure swirl atomizer and compared their results with the experimental work of others. This work is among the initial efforts to identify the flow field inside a pressure swirl atomizer using CFD techniques. They assumed that the flow field is axis-symmetric and laminar. They proposed a computational technique in which the air core boundary was replaced by a solid surface at which slip was allowed. They did not solve for the shape of the air core interface rather they estimate it based on some flow solutions in the atomizer in the absence of air core. They identified Taylor-Gortler type vortices within the swirl chamber adjacent to wall, and stated that the this time dependent vortices impede them from having a converged solution field.

One of the early attempts to track the air core interface within the atomizer is the work of Jeng et al. [21] in which a computational model based on Arbitrary-Lagrangian-Eulerian method with finite volume formulation was employed for tracking of the air core interface. In order to validate the numerical study, experiments were conducted on large scale Plexiglas pressure swirl atomizers. They used Charge Coupled Device (CCD) cameras to visualize the liquid sheet thickness and spray cone angle. They predicted the mean sheet thickness at the nozzle and spray cone angle for atomizers having different geometric characteristic parameters using the established model and they compared their results with the experiments and analytical studies. The mean sheet thickness at the nozzle for different values of geometric characteristic parameter of the atomizer is given in Figure 1.9.

Cooper et. al.[22] measured the axial and tangential velocity components within pressure swirl atomizers by using Laser Doppler Anemometer Technique and compared their results with the result of CFD computations. The atomizers have conical, curved and square convergence geometries form swirl chamber to nozzle. They pointed out that the LDA measurements confirmed the Gortler type wall vortices on the swirl chamber adjacent to wall predicted by CFD computations. They identified recirculation in the main body of the swirl chamber flow as well as the standing and travelling waves on the air core.

Datta and Som [23] numerically investigated the flow inside a swirl atomizer. They

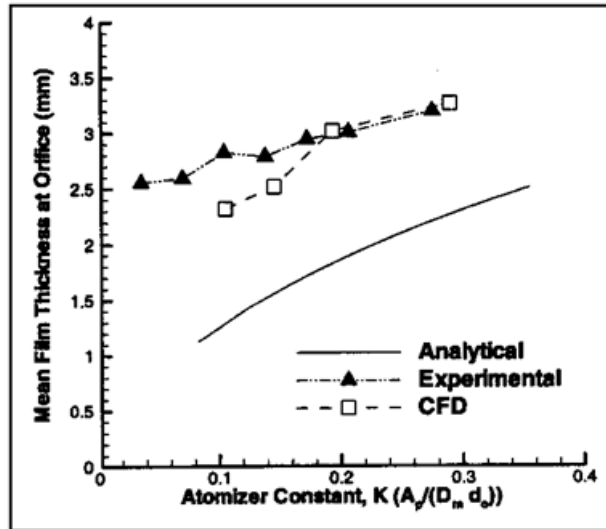


Figure 1.9: Mean film thickness at the orifice [21].

claimed that the flow inside the nozzle becomes axis symmetric provided that the entry of the liquid is made through a number of tangential passages placed symmetrically around the periphery at the base of the swirl chamber. They employed an explicit finite difference computing technique to solve the resulting set of equations for both phases. They considered the liquid flow as turbulent and employed standard k-w turbulence model. The air core flow was considered as laminar. The work of Datta and Som [23] was in contrast with the findings of other researchers in that they did not find the bulging of the liquid at the entrance of the nozzle of the atomizer with their simulations.

Sakman et.al.[24] numerically investigated the effect of changes in geometry of a pressure swirl atomizer on its performance. They used the same computational model used in Jeng et al. [21]. They investigate the effect on length to diameter ratio of the swirl chamber (L_s/D_s), length to diameter ratio of the nozzle (L_o/D_o) and swirl chamber diameter to nozzle diameter ratio (D_s/D_o) on the film thickness at the nozzle exit, spray cone angle and discharge coefficient. They kept the mass flow rate through the nozzle constant for all cases and covered a range of (L_s/D_s) from 0.1 to 1.5, L_o/D_o from 0.2 to 2 and a range of D_s/D_o from 3.5 to 6.5. They found out that D_s/D_o had the biggest influence on performance parameters among the three non dimensional

parameter studied. The variation of film thickness at the exit, spray cone angle and discharge coefficient with D_s/D_o are given in Figure 1.10.

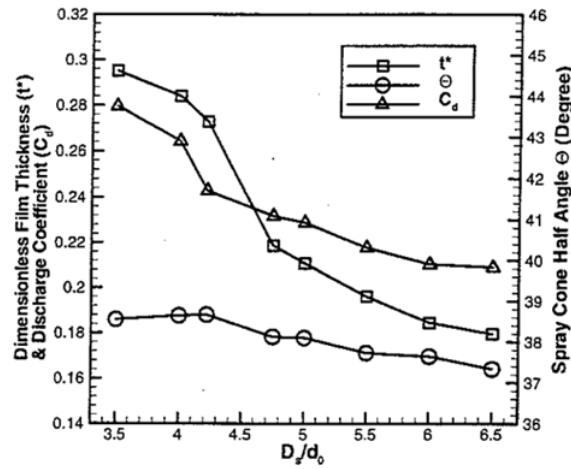


Figure 1.10: Variation of film thickness at the exit, spray cone angle and discharge coefficient with D_s/D_o [24].

Nonnenmacher and Piesche [25] used FLUENT software to calculate the flow inside a helical pressure swirl atomizer. They neglected the gradients of the flow in circumferential direction and modeled the flow through the atomizer as a two dimensional axisymmetric flow. They solved the momentum equation in the circumferential direction in order to determine the axial and radial gradients. They added a computational area after the nozzle exit to prevent the boundary conditions located downstream influencing the calculated flow inside the atomizer. They tracked the air core interface using the volume of fluid method. They compared their numerical results with experimental results. The film thickness and the liquid velocities at the exit of the atomizer that was predicted by FLUENT simulations agree well with the results of experimental measurements as shown in Figure 1.11.

Dash et. al. [26] analyzed experimentally and numerically the flow inside conical and cylindrical pressure swirl atomizers. For the conical pressure swirl atomizer, they carried out experiments using water with Plexiglas nozzles and photographed the resulting air core. They stated that it is necessary to use a high speed camera to capture the instantaneous formation of air core since development of the air core is very rapid. Based on their observations of the air core within the pressure swirl atomizer using

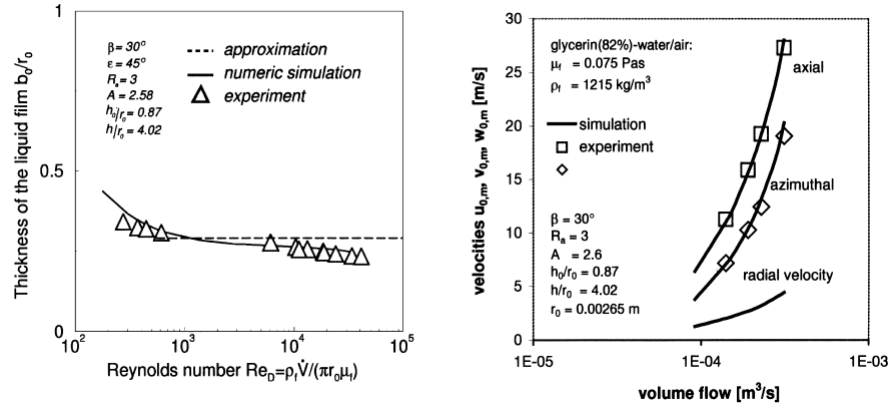


Figure 1.11: Variation of film thickness and velocities at the nozzle exit [25].

photographic technique, they assumed that the flow is steady and the air core is nearly axis-symmetric and performed two dimensional numerical simulations. They used finite volume method for the solution of the governing equations for incompressible viscous flows and Volume of Fluid Method (VOF) to simulate the free surface effects. They extended the actual domain 7 mm downstream and 8 mm in radial direction away from the nozzle exit.

Although the Reynolds number at the inlet passages are below the critical Reynolds number, they performed laminar flow simulations. They stated that the turbulence did not play an important role due to the stabilizing effect of the streamline curvature [26].

Maatje et.al.[27] performed unsteady axis-symmetric flow simulations in a large and small pressure swirl atomizers using both COMET and FLUENT flow solvers. They figured out that the air core interface is unsteady, with the waves generated at swirl chamber head end. They stated that the two dimensional simulations enabled them to understand the details of the flow, and they found three dimensional simulations necessary to understand the details of the flow. Although they pointed the unsteadiness of the air core interface and location at which the waves are generated, they did not identify the source of the unsteadiness.

Cooper and Yule[28] presented the images of waves on the air core/liquid interface of a pressure swirl atomizer. They used modular Perspex atomizer in which they can

change the number of inlet ports, length of the swirl chamber and outlet ports independently. They used high speed cameras to visualize the air core inside the atomizer. They identified three types of waves; namely, helical, low frequency stationary waves and random ripples whose frequencies increased and wavelengths decreased with flow rate.

Von Lavante et. al.[29] numerically investigated the flow inside the pressure swirl atomizers using COMET and FLUENT. They considered and investigated the unsteady behavior of pressure swirl atomizers by performing both 2D axis-symmetric and 3D simulations. Both 2D axis-symmetric and 3D simulations showed that the flow at the air core interface was unsteady and the liquid flow gave rise to hydrodynamic instabilities that result in the formation of Gortler vortices.

Halder et. al.[30] experimentally investigated the initiation of air core in a pressure swirl atomizer to determine the influences of nozzle geometry and nozzle flow parameters on the size of the fully developed air core. They fabricated a number of simplex atomizers with different geometrical properties from Perspex and visualize the formation of the air core with a camera. One of the pressure swirl atomizers that they investigated experimentally (nozzle identification number 21) had also been studied by Dash et.al. [26]. They specified the flow rate through the atomizer, from the point of similarity, as the Reynolds number inlet to the nozzle defined based on the diameter of the inlet passages and flow velocity at the inlet passage. They claimed that the air core was stable at the swirl chamber. They identified the bulging of the liquid at the entrance of the nozzle.

Donjat et.al.[31] experimentally investigated the air core oscillations and performed a 3D simulation of the flow inside the atomizer using FLUENT software. They used a modular atomizer design which consists of a swirler cup and the nozzle. They performed Laser Induced Fluorescence visualizations to examine the structure of the internal flow. They performed LDA measurements inside the atomizer at different axial locations which gave the radial profiles of the axial and tangential velocity components. They characterize the air core oscillations with a laser beam and photo detector arrangement. They found out two dominant frequencies from their Fourier analysis of the data. They stated that the lowest one was due to the precession movement of

the air core due to the inlet jet diffusion and the second one is due to the rotating double helix wave.

Shaikh et.al.[32] performed unsteady laminar CFD simulations to predict the internal flow of a pressure swirl atomizer using FLUENT. They performed both 2D axis symmetric simulations with swirl and 3D simulations and used velocity inlet and pressure outlet boundary conditions. They used volume of fluid method with geo-reconstruct scheme to track the air core interface. By looking at the cell Reynolds number contour plot they argued that the flow is turbulent at microscopic level but the rotational effect stabilizes the overall flow and suppress turbulence. Shaikh et.al.[32] measured the axial velocity within the atomizer using Phase Doppler Particle Analyzer (PDPA) and they commented that the computational results are in good agreement with the experimental data. Although they claimed that they performed 2D axis symmetric simulations, they did not give the results of these simulations. The velocity contour plots are of a single time instant rather than average values. The unsteady oscillations at the air core are also not quantified.

Madsen et.al.[33] used FLUENT software to simulate the flow through a large scale atomizer. They simulated the two phase flow with VOF method using a laminar flow assumption, VOF method using LES approach and two fluid Euler/Euler method using laminar flow assumption. They attempted to use standard, RNG and realizable $k-\epsilon$ turbulence models of the FLUENT software but they stated that these turbulent models were unable to predict the air core inside atomizer. They performed three dimensional numerical simulations with two different grids which consisted of 300,000 and 550,000 elements. They refined the mesh around the fluid interface when the solution is near steady state and this refinement nearly doubles the number of elements in each grid. They compared their simulation results with experiment and concluded that the VOF method assuming laminar flow gives the best results for the cases considered.

Zong and Yang[34] investigated numerically the cryogenic fluid flow inside a pressure swirl atomizer. They solved the Favre-filtered conservation equations of mass, momentum, and energy and used Large Eddy Simulation (LES) technique to achieve turbulence closure. They performed axis symmetric numerical solutions and noted that

this approach could capture the salient features of swirl injector dynamics though it lacks vortex-stretching mechanism. They modeled the tangential inlet passage as a slit on the atomizer and specified mass flow rate and temperature on the inlet boundary. They applied non-reflecting type boundary conditions at the exit boundaries. They obtained the mean flow properties by taking time average of instantaneous quantities. They gave the temporal evolution of the temperature fields and stated that there exist a primary vortex shedding due to Kelvin-Helmholtz instability of the mixing layer. They monitored the pressure at six different locations in the computational domain and obtained the power spectral densities of pressure fluctuations.

Park and Heister[35] developed a fully nonlinear boundary element method model to simulate the flow inside a pressure swirl atomizer and the resulting spray. They utilized an axis-symmetric boundary element formulation in which they superimposed a potential vortex to the bulk flow to simulate the swirl. They conducted parametric studies to assess the influence of atomizer geometry and flow characteristics on film thickness and spray angle produced by the atomizer.

Halder and Som[36] numerically and experimentally investigated the air core diameter, discharge coefficient and spray cone angle of a cylindrical pressure swirl atomizer. They numerically solved conservation equations for mass and momentum along with the volume fraction of the liquid phase by the finite volume method in an implicit scheme. The number of control volumes that they used in their computations was between 45000 to 180000. They compared their numerical analysis results with the tests that they performed. They photographed the air core and spray cone angle with a wide angle lens camera and scanned and magnified the images to obtain the air core diameter. They performed steady numerical simulations whereas the images that they recorded during experiments showed unsteady character of the air core as shown in Figure 1.12.

Morad and Eslami [37] experimentally investigated the inner and outer atomizers of a liquid/liquid swirl injector. They observed that the discharge coefficient for the inner atomizer has a sharp drop and reached an asymptote as the injection pressure increases, however the discharge coefficient for the outer atomizer showed a smooth drop and reached an asymptote. They also performed axis symmetric CFD simula-

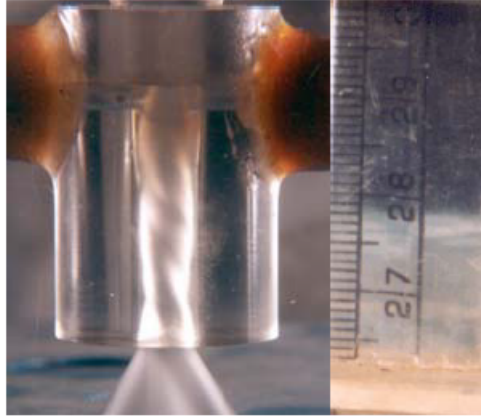


Figure 1.12: Air core on a fully developed cylindrical swirl atomizer [36].

tions of the inner atomizer. They encountered some fluctuations and they misleadingly showed air vortices at the exit of the nozzle as the reason for this unsteadiness.

Hinckel et.al. [38] numerically investigated the internal flow through a pressure swirl atomizer by using the ANSYS CFX package. They solved Reynolds Averaged Navier-Stokes equations with $k-\epsilon$ turbulence model. They used VOF method to track the air core interface. Using CFD they analyzed the effects of geometric characteristic of the atomizer and the ratio of radius of tangential passage to the swirl arm on the flow through the atomizer and compared their results with the inviscid solution of Abramovich [9] and solution of Khavkin [13].

Kim et.al. [39] experimentally investigated the formation of the air core and liquid film thickness in a pressure swirl atomizer. Keeping in mind possible usage of the air core inside the pressure swirl atomizer as an acoustic resonator [4], they construct their atomizer model such that the swirl chamber length can be adjusted easily. They visualized the flow inside the atomizer using a high speed camera and they measured the air core diameter at the nozzle of the atomizer using electrical conductance method. They conducted experiments on water under constant injector pressure drops of 2,4,6,8 and 10 bars. They reported that as they increased the swirl chamber length, after a certain value the air core becomes unstable and seemed to be a rotating double helix shape (Figure 1.13).

Kim et.al.[39] postulated that the instability of the air core in a helical shape is due

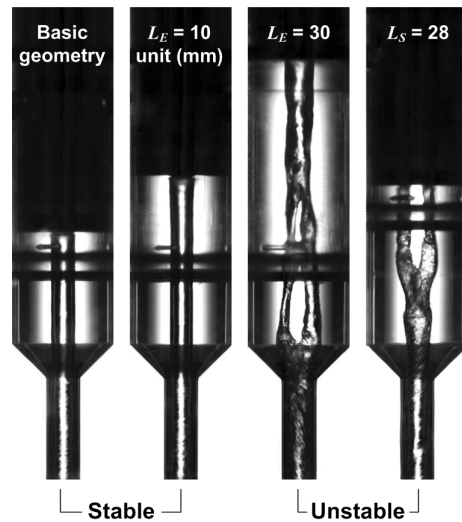


Figure 1.13: Effect of extra swirl chamber length on the air core [39].

to viscous effects, geometric parameters of the atomizer and inlet Reynolds number and called for more research to understand the phenomena. Without pointing out the actual reason for the instabilities they proposed to have a back hole at the base of the swirl chamber to suppress the instabilities. This action indeed solved the air core break up phenomena.

Moon et. al.[40] measured the liquid film thickness inside a pressure swirl atomizer for direct injection gasoline engines using photographic techniques. They used the MATLAB image processing toolbox and Canny method to detect the edges of the air core. They captured and analyzed fifty images to reduce the possible error from shot-to-shot variations. They performed experiments in different injection pressures and they reached to the conclusion that the injection pressure does not have an influence on the liquid film thickness as opposed to other researchers. They compared the measured film thickness values that they measured with ones obtained by the equations of [18] and [39] and proposed a new equation for the film thickness for high pressure swirl atomizers.

Fu et. al.[41] used electrical conductance method to measure the liquid film thickness in an open-end pressure swirl atomizer. The unsteady behavior of the air core showed itself in their film thickness measurements, and they stated that the gas liquid interface in the annular liquid flow varies quickly. Based on their measurements, which

were restricted to two measurement locations due to their measurement method, they calculated the average film thickness values and compared their results with the ones obtained by using the equations of [17] and [18]. They also used a flow pulsation generator to fluctuate the pressure at the inlet. They stated that the fluctuations on the film thickness are closely related to the pressure fluctuations at the inlet of the atomizer. They found that at low fluctuation frequencies, the liquid film variations at the nozzle follows the variation of pressure but at high frequencies there is a phase lag between two frequencies.

1.3.4 Pressure Swirl Atomizer - Dynamic Element in Liquid Propellant Rocket Thrust Chambers

The fundamental processes of injection, atomization, vaporization, and mixing in liquid rocket engines, are the cause of various instability mechanisms, such as hydrodynamic waves on the liquid surface, acoustic fluctuations bouncing back and forth in the combustor and injector tubes, Kelvin-Helmholtz instabilities associated with the liquid breakup process, the unsteady recirculation zone at various locations in the system, and so forth . These instabilities may couple with the heat-release process and could result in combustion instabilities. Injectors dictate to a large extent the characteristics of these processes and play a vital role in the entire system. The dynamic characteristics of injectors are of great importance to the performance of the whole combustion system [42].

The various studies surveyed in the previous section investigated the flow inside pressure swirl atomizer. The main outcome of the survey is the identification of the oscillations on the air core-liquid interface. The identification of these kind of oscillations generally attributed to the work of Cooper and Yule [28] who saw these oscillations in their tests with a large scale pressure swirl atomizer that works on water. The free oscillation phenomenon inside the pressure swirl atomizer was also reported by many researchers following Cooper and Yule [28]. However, the Russian researchers have the knowledge that pressure swirl type atomizers have dynamic character and the origin of these knowledge goes back to the beginning of eighties. However they approached the problem in a different way and postulated that a source of pressure

fluctuations should present to have dynamic response from the atomizer. Bazarov devised a linear theory on the swirl atomizer dynamics and outlined the theory in his book printed in 1979 [43]. Bazarov identified the combustion chamber and the propellant feed line as the two major source for intense pressure fluctuations and characterized the dynamic behavior of the atomizer by the response function defined by;

$$\Pi_{inj} = \frac{\frac{\dot{m}'_n}{\dot{m}_n}}{\frac{\Delta P'_{inj}}{\Delta P_{inj}}} \quad (1.13)$$

In order to predict the fluctuating mass and pressure components, Bazarov assumed that the disturbances are small and linearizes the inviscid, incompressible flow equations and find expressions for the fluctuating components. Bazarov calculated the response function for the tangential inlet passages, swirl chamber, and nozzle and using the assumption of linearity he defined the total response of the atomizer as the product of responses of different parts of the atomizer as follows;

$$\Pi_{inj} = \left(\frac{R_v}{r_{he}}\right)^2 \frac{\Pi_t \Pi_{vn} \Pi_n}{1 + 2\Pi_t(\Pi_{v2} + \Pi_{v3})} \quad (1.14)$$

Based on Bazarov's main hypothesis that either the flow disturbances at the delivery line or the flow disturbance at the combustion chamber causes the fluctuating fluid flow inside the atomizer, Maksud[44] described how the flow disturbances occur inside the atomizer from the perspective of the terms in Equation 1.13. He stated that a flow disturbance at the delivery line causes a perturbation at the tangential inlets, which results in a fluctuating inlet mass flow rate and pressure drop across the inlets. He then postulated that the fluctuating inlet mass flow rate causes a free surface deflection at the atomizer head end which results in a fluctuating pressure across liquid body at the injector head end. Then he stated that the flow disturbance created at the head end propagates downstream which is viewed by the observer as a surface wave and it eventually reaches the nozzle exit which results in the mass flow rate fluctuation.

He also described the oscillating mass flow rate and pressure drop phenomena by

considering the gaseous core. This time he proposed that a disturbance which may result from combustion chamber propagates in the gaseous core to the atomizer head end and originates a surface wave which causes a variable nozzle exit mass flow rate at the nozzle exit. He also postulated that the created surface wave causes a pressure drop at the head end which means a variable resistance at the entrance of the swirl chamber which causes a fluctuating mass flow rate and hence pressure drop across the tangential inlets.

After identifying the main reasons for the free surface deflection at the atomizer head end as either the fluctuating mass flow into the atomizer or the combustion chamber fluctuations, Maksud[44] systematically went over the Bazarov's theory and stated that two different waves may present within a pressure swirl atomizer. The first of these waves is the surface waves which are the result of the periodic free surface deflection at the atomizer head end and the second is the vorticity waves which are the result of periodic fluctuation of circumferential velocity at different radial layers of the fluid.

He also plotted the response function for the atomizer that is used by Bazarov based on Equation 1.13 as shown in Figure 1.14

Huo et.al. [42] extended the work of Zong et. al.[34] in order to investigate the effect of external forcing on the dynamics of swirl atomizer using numerical methods. An external forcing was imposed by pulsating the mass flow rate at selected frequencies at the tangential inlet of the atomizer. The external forcing gives an oscillation magnitude of 15% of the mean mass flow rate and frequencies in the range of 0.55-14kHz. From the analysis of the free oscillating flow they found that the 0.55 kHz mode is closely related to the longitudinal wave of hydrodynamic instability within the liquid film. They investigated the temporal evaluation of temperature fields from their simulation results at forcing frequencies from 0.55kHz to 14kHz and commented that low frequency forcing (0.55 kHz and 1 kHz) affect the flow field significantly and high frequency forcing does not show any significant influence on the flow dynamics. Huo et.al.[42] used the phase "free oscillating flow" and calculated the frequencies associated with it and used those frequencies when exciting the flow. This was to our knowledge first study which made a connection between the free oscillating flow and

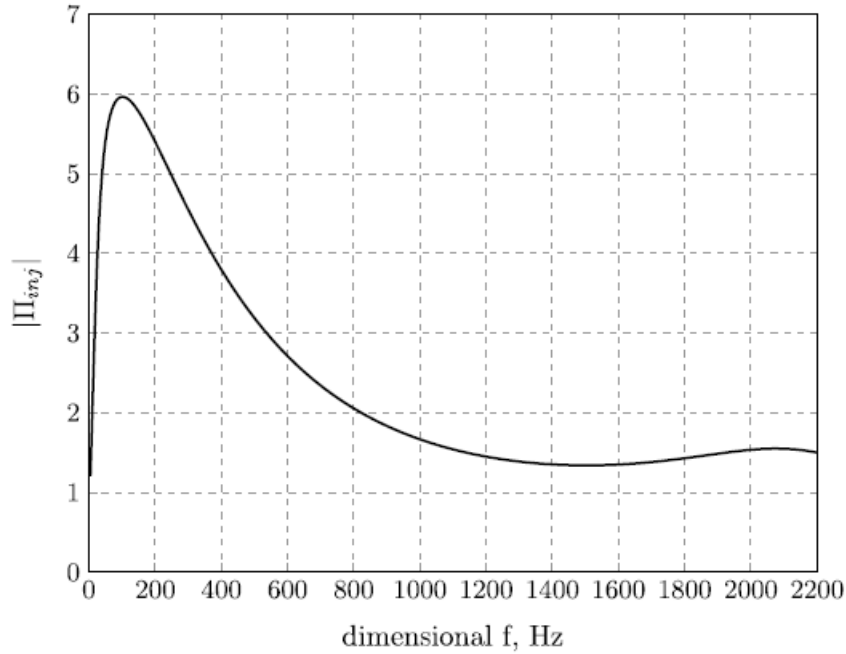


Figure 1.14: Response function for Bazarov’s atomizer [44].

the atomizer dynamics.

In order to study the flow through a pressure swirl atomizer experimentally under pulsating inlet flow conditions, researchers used devices called pulsators, which creates harmonic pressure pulsations at the tangential inlet ports. Bazarov [2007] introduced two types of pulsators, namely; hydro-mechanical pulsators and inertial pulsators.

Khil et.al.[45] used a hydromechanical pulsator to study the dynamic behavior of swirl atomizer. The hydromechanical pulsator can achieve pulsation frequencies up to 300Hz.

Ahn et.al.[46] built a hydromechanical pulsator that can produce periodic pressure fluctuations up to 700 Hz. and investigated both the flow inside the pressure swirl atomizer and resulting spray using high speed photography. They observed air core diameter fluctuations in both swirl chamber and nozzle. They noted that for low pulsation frequencies the air core diameter changed as much as 15 % of the mean value, yet the change in the air core diameter decreases for high pulsation frequencies. They also stated that the frequency determined from the images of the oscillating air

core diameter match the frequency of the oscillating manifold pressure measured by pressure a transducer, as well as the frequency of the pulsator. An image of the air core inside the pressure swirl atomizer as captured by Ahn et.al. [46] is shown in Figure 1.15, unfortunately head end portion of the atomizer is not recognizable. Two red lines with green tips shows the boundaries of the air core for air core diameter calculations.

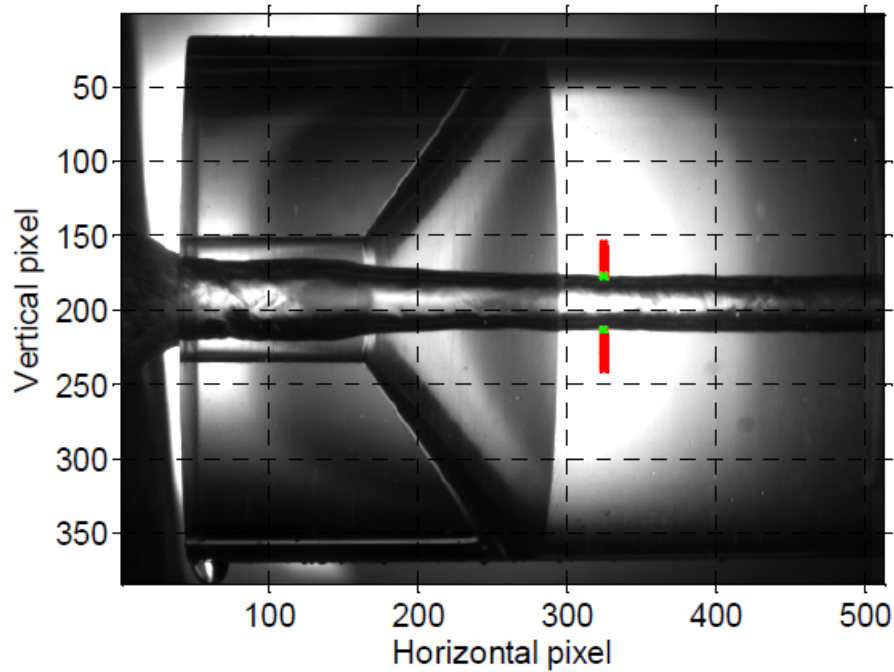


Figure 1.15: Image of the air core diameter.

The work of Huo et.al. [42] is unique in that the results of simulations for the free oscillating flow are compared with the forced oscillating flow inside the pressure swirl atomizer. The recent experimental investigations accomplished by Khil et. al.[45] and Ahn et.al.[46] reinforces the findings of Huo et.al.[42] that the forcing frequencies closer to the frequencies associated with the hydrodynamic instability within the liquid flow inside the pressure swirl atomizer have the dominant effect on the flow dynamics.

The survey accomplished in this section reveals that the characterization of the hydrodynamic oscillations that occur in pressure swirl atomizer is a significant task. The atomizer designer should be aware of such oscillations and the corresponding

frequencies and should have the ability to change or suppress them as needed. On the other hand this kind of information is also important in design of different parts of a Liquid Propellant Rocket Engine. For instance the turbo pump designer should make a budget of possible external forcing on the propellant lines and leave a safety margin between the forcing frequencies and the frequency of the hydrodynamic oscillations that occur in pressure swirl atomizers. The same argument is also true for combustion chamber designer.

In the next section the survey is extended so that it includes the literature on pressure swirl atomizer sprays.

1.3.5 Characterization of the Resulting Spray

The purpose in using liquid atomizers in combustion systems is to form a spray thereby increasing the surface area for the liquid and prepare for the subsequent combustion process. As surveyed in the previous sections the liquid film thickness at the exit of the injector has a profound effect on the spray formation. It is closely related to the resulted drop size distribution and spray cone angle and mixing efficiency. The low frequency hydrodynamic stabilities of the liquid film have the potential to couple with the heat release process and may lead to system failures [42].

An image of a spray produced by a pressure swirl atomizer together with the properties of the spray that has to be characterized is given in Figure 1.15. Bachalo[47] pointed out that one or two diagnostic techniques may be insufficient to characterize the atomization and spray process.

A simple classification of spray properties may be accomplished by considering the scale of the spray property that needs to be characterized. In general spray properties is classified as macroscopic and microscopic properties. The spray cone angle and breakup length of a spray are generally pronounced as macroscopic properties, on the other hand size and velocity distribution of droplets are pronounced as microscopic spray properties of the spray [2].

The main goal of a designer is to design atomizers that can provide sufficient atomization and mixing of the propellants in all operating conditions. For the rated mass

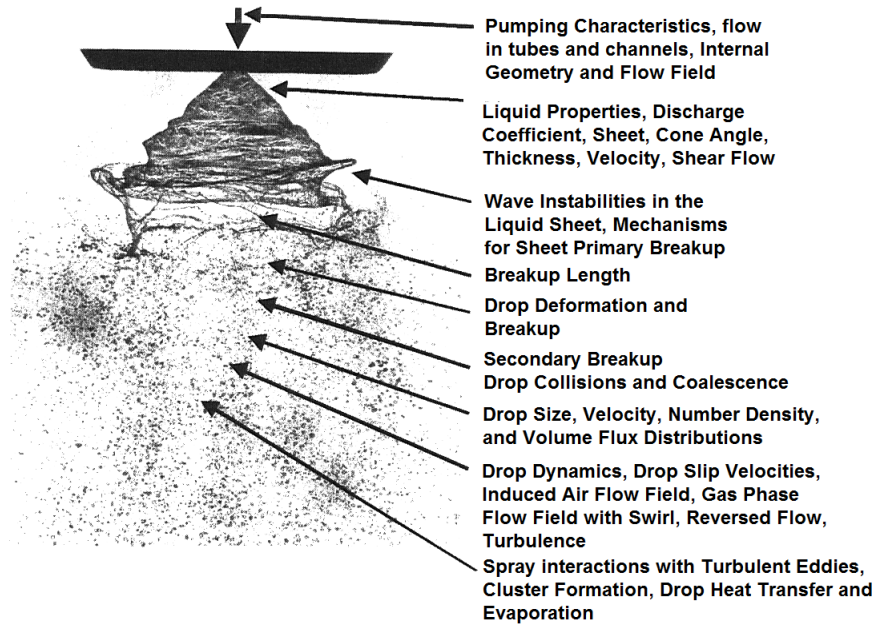


Figure 1.16: Properties of the spray [47].

flow rate, design goals may include a specific spray cone angle, breakup length, mixing efficiency and droplet size and velocity distribution at the vicinity of the breakup location. The information of spray cone angle, breakup length and the droplet size and velocity distribution is an important prerequisite for numerical spray combustion simulations since they are used to determine not only the spray boundaries but also the boundary conditions.

Ortman and Lefebvre[48] experimentally investigate the fuel distributions obtained from various types of pressure swirl atomizers using patternators. They defined the term; equivalent spray cone angle, which is based on the angle between the centers of mass in the left and right hand lobes of the spray. They investigated influence of fuel injection pressure and ambient nitrogen gas pressure on equivalent spray angle and on the radial fuel distribution for set of commercial simplex atomizers. They found that;

- when the fuel is injected to ambient conditions the equivalent spray cone angle first increases to a maximum value and then decreases with increasing fuel injection pressure,

- when the fuel is injected into a pressurized nitrogen environment, the equivalent spray cone angle starts from a peak value, which decreases with increasing nitrogen pressure, and decreases with increasing fuel injection pressure,
- for a fixed fuel injection pressure the equivalent spray cone angle decreases to a certain value as the nitrogen pressure increases and then remains constant.

Wang and Lefebvre[49] studied the factors governing the atomization process in pressure swirl atomizers. They conducted extensive measurements of drop sizes on six simple nozzles of different sizes and spray cone angles by using the laser diffraction method. They used their results to devise an equation for mean drop size. They subdivided the process of atomization in pressure swirl atomizers into two main stages. The first stage represents the generation of surface instabilities due to the combined effect of hydrodynamic and aerodynamic forces. The second stage is the conversion of surface protuberances to ligaments and then drops. Wang and Lefebvre [49] proposed the following equation for the Sauter mean diameter (SMD) of droplets;

$$SMD = A \left(\frac{\sigma^{0.5} \mu_L}{\rho_A^{0.5} \Delta P_L} \right)^x (t \cos \theta)^{1-1.5x} + B \left(\frac{\sigma \rho_L}{\rho_A \Delta P_L} \right)^y (t \cos \theta)^{1-y} \quad (1.15)$$

And by analyzing the experimental results they proposed the following values for the constant; $x=0.5$, $y=2.5$, $A=4.52$ and $B=0.39$.

Li et.al.[50] experimentally investigated the hollow cone spray from a pressure swirl atomizer and measured the droplet size and velocity distributions using a Phase Doppler Particle Analyzer (PDPA). They measured the spray properties at a location close to the break up location which they deduced from photographs of the spray. They used maximum entropy principle to predict the measured distributions. They concluded that predicted size distributions using the maximum entropy principle agrees well with the measurements, on the other hand the predicted velocity distributions shows large deviation from the measured ones.

Hautmann[51] characterized sprays from liquid-gas coaxial injectors. They used photographic technique to visually inspect the character of sprays, a patternation systems to measure the mass flux distribution, and Phase Doppler Particle Analyzer (PDPA) to measure the velocity and size distribution of spray droplets.

Dorfner et.al. [52] investigated the effects of surface tension and viscosity on the liquid sprays formed by pressure swirl atomizers using Phase Doppler Anemometer Technique. The results of the investigations showed that;

- an increase in surface tension results in an increase of both, number Sauter mean diameter.
- an increase in fluid viscosity yields to an increase of the resultant mean diameters.
- for a fixed fuel injection pressure the equivalent spray cone angle decreases to a certain value as the nitrogen pressure increases and then remains constant.

They stated that empirical equation proposed by Wang and Lefebvre [49] (Equation 1.15) yields good agreement for liquids with low viscosity and low surface tensions. On the other hand, they stated that Equation 1.15 yields smaller Sauter mean diameters for highly viscous liquids.

Ramamurthi and Tharakan [53] carried out experiments to determine the shape, surface texture and wave formation characteristics of the swirled sheets formed by pressure swirl atomizers. They used water as the working fluid and cameras to visualize the swirled sheets. They identified the regimes of tulip-shaped and conical sheet depending on the Reynolds number and Weber Number. They pointed out that the swirled liquid sheets disintegrate by wave motion when the liquid phase Weber number is greater than 150.

Ramamurthi and Patnaik [54] investigated the non-uniformity of hollow cone sprays experimentally for different values of surface roughness of the swirl atomizer nozzles. They took photographs of the resulting sprays and use mechanical patternators to study the uniformity of hollow cone sprays. They found that,

- the non-uniformity of the hollow cone spray enhances as the surface roughness of the nozzle increases,
- the discharge coefficient decreases as the surface roughness increases,
- the surface roughness has no significant effect on the spray cone angle.

Santolaya et.al [55] visualized the disintegration of the liquid film using a CCD camera and a stroboscopic light source. They obtained the microscopic properties of the spray by using a two component PDPA. They obtained velocity distribution at different axial locations for different size classes. They found that small droplets present along the axis and large droplets present at the edges of the spray.

Khavkin [56] proposed a theory to explain regimes of secondary break up phenomena in sprays formed by pressure swirl atomizers. He stated that in pressure swirl atomizer sprays a regime of secondary break up exists due to the stretching motion of centrifugal and viscous forces. Khavkin [56] pointed out that the existence of secondary breakup phenomena depends on the working parameters and liquids to be atomized. He stated that water and water solutions cannot be used for the investigation of the phenomena of secondary atomization.

Han et.al [57] experimentally investigated the effect of recess on the spray characteristics of liquid-liquid swirl coaxial injectors. They utilized back light stroboscopic photography technique to measure the macroscopic properties like, the spray cone angle, breakup length and drop formation length. They used PDPA to measure the diameter of around 10000 droplets at two different locations and calculated the SMD of the droplets.

Park et.al [58] investigated the effect of temperature on hollow cone spray properties. They used photographic technique to measure the spray cone angle, mechanical patternator to measure the volumetric distribution of the spray and laser diffraction technique to obtain the SMD of droplets. They stated that the SMD of droplets is influenced by kinematic viscosity in low temperature range while it is more influenced by surface tension in the high temperature range.

Yon and Blaisot [59] presented an image processing technique that can be used for sizing of the droplets and has the advantage of analysis of droplet shapes and measurement of non spherical droplets. They stated the two main limitation of the problem as the unfocused droplet characterization and partial/total overlapping projection of the droplet images.

Kim et.al [60] investigated the effect of injection and recess conditions on the spray

characteristics of a coaxial injector. They observed the spray patterns and measured the macroscopic properties of the spray using photographic images (Figure 1.17). They took sixty images for one experimental case. They used PDPA to measure the diameter of around 10000 droplets and calculated the SMD of the droplets. They utilized mechanical patternators to measure the mass distribution and mixing efficiency of the injectors.

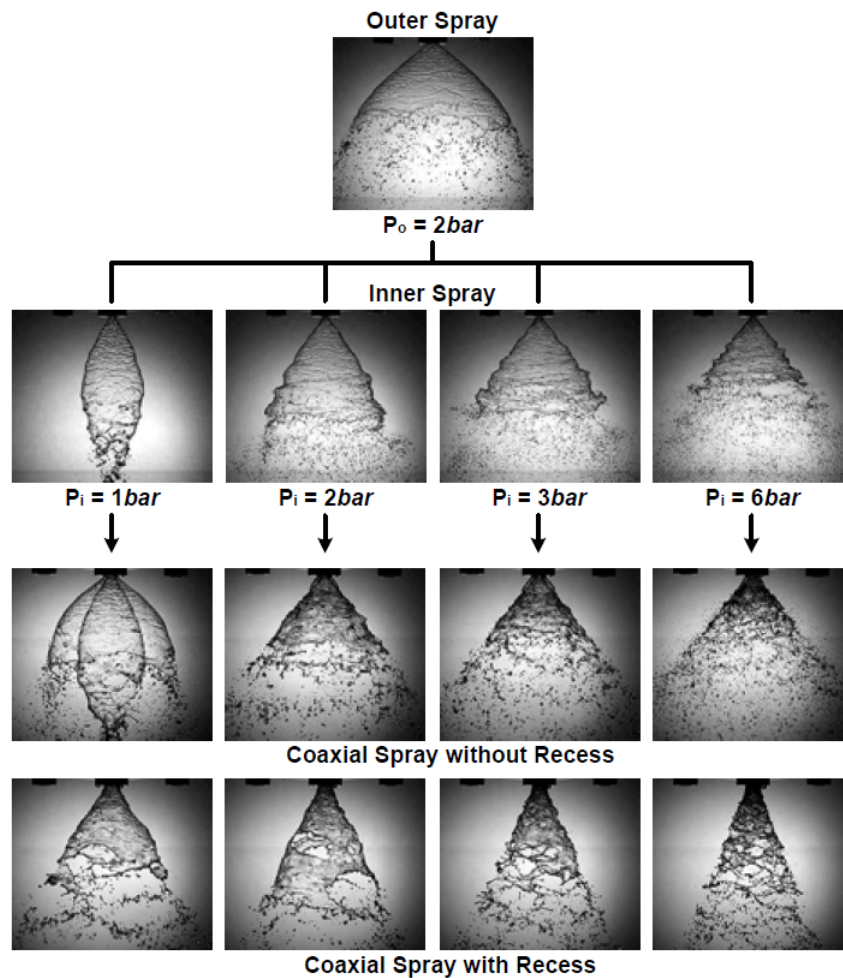


Figure 1.17: Images of the spray formed by a coaxial injector [60].

Park et.al. [61] investigated the characteristics of a hollow cone spray formed by a pressure swirl atomizer at fuel temperatures and fuel pressures in the range of 0.2-10 MPa and 253-313 K respectively. They identified a transitional instability at low temperature which results in a pulsating hollow cone spray. They explained the transi-

tional instability as results of the breakdown of the air core inside the atomizer. They used kerosene based aviation fuels as working fluids. They used photographic techniques to visualize both the air core and the resulting hollow cone sprays and laser diffraction technique to measure the size of droplets.

Kim et.al [62] conducted experiments to investigate the effect of injection conditions and ambient pressure on the spray shape, spray cone angle and breakup length. They used water as working fluid and measured the spray cone angle and break up length using the images of the spray taken by indirect photography.

Marchione et.al [63] investigated the behavior of a JETA-1 spray produced by a commercial pressure swirl atomizer. They analyzed the fluctuating behavior of the spray and spray cone angle using the images captured by a high speed camera.

Yang et.al. [64] theoretically and experimentally investigated the spray characteristics of a gas-liquid swirl coaxial injector. They used a measurement system consists of a light sheet illuminator and a high speed camera to obtain the images of the spray. They used an image analysis tool, which has temporal and spatial statistics ability, to calculate mean diameters, size distribution and velocity of droplets. They established a theoretical model to correlate experimental observations.

Reddy and Mishra [65] investigated spray behavior of a pressure swirl atomizer in transition regime. They studied the change in the spray pattern from a collapsed hollow cone spray to a developing hollow cone spray by increasing the working pressure of the pressure swirl atomizer. They visualized the spray cone angle by using a CCD camera with the help of a laser sheet produced by a 100mW laser. Then they processed the time averaged images and find the edges of the spray using Sobel's algorithm in order to calculate the spray cone angle. They used mechanical patternators to obtain the volumetric distribution of the spray. In addition they used the laser diffraction technique to obtain the axial and radial distributions of average drop sizes.

Karnawat and Kushari [66] studied the spray formed by a twin fluid pressure swirl atomizer. They used a 25mW He-Ne laser source and a set of optics for planar illumination of the spray and visualized the spray by using a CCD camera at a rate of 10 frames per second (fps). They analyzed the images using an image analysis code

written in MATLAB in order to obtain spray cone angle and breakup length. They used laser diffraction technique to measure the average droplet diameters.

Im and Yoon [67] studied the effect of chamber pressure on the self pulsation characteristics of a gas-liquid swirl coaxial injector. At each chamber pressure they evaluated the spray patterns which are visualized by using a digital camera and stroboscope. The images of stationary and pulsating sprays are shown in Figure 1.18. They also used a He-Ne laser and a photo detector in order to quantify the spray oscillation frequency based on the idea that laser beam attenuates greater in dense portions when compared to sparse portions of the spray.

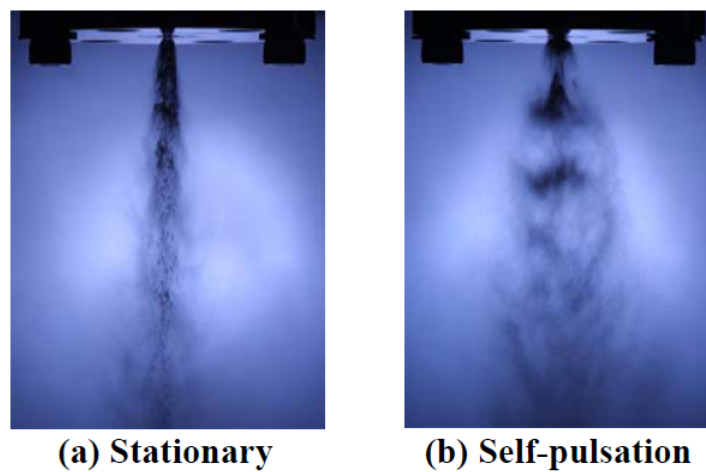


Figure 1.18: Stationary and pulsating sprays [67].

Kenny et.al [68] investigated the exit film thickness at the nozzle of a pressure swirl atomizer and the resulting hollow cone spray by using shadowgraph techniques. In their tests they operated the pressure swirl atomizer at a constant mass flow rate of 0.09 kg/s and varied the chamber back pressure ranging from 1 bar to 48 bars. They found that the film thickness at the exit of the injector increases and the spray cone angle decreases with increasing chamber back pressure.

Eberhart et.al. [69] characterized the hollow cone spray formed by a pressure swirl atomizer. They visualized the spray using a DSLR camera and used two different illumination techniques. They calculated the spray cone angle and the breakup length

by post processing the obtained images by using an image processing tool. They used a two component PDPA system to measure the diameter and velocity of the droplets. They found that small droplets with negative velocity are accumulated at the axis of the atomizer. They commented that the finding is key indication of a known swirl injection phenomena in which a recirculation region within the hollow cone spray forms as a result of the pressure difference between the inner and outer faces of the cone.

Santoloya et.al. [70] investigated a hollow cone spray using Phase Doppler Particle Analyzer. They evaluated the liquid volume fluxes for different size classes using a generalized integral method. They determined the two phase mean velocity fields and evaluated the liquid volume fluxes and total flow rates for all droplets and size classes.

Belhadeh et.al [71] developed an Eulerian model to investigate the liquid sheet atomization from a pressure swirl atomizer. They used volume of fluid method to track the interface and Reynolds Stress model is used for turbulence. They derived the Sauter mean diameter from the mean liquid mass fraction. They also performed experiments using PDPA and compared their numerical results with the measurements. The results obtained using the proposed Eulerian model are able to capture the general trend of the experiments in terms of mean velocity and Sauter mean distribution.

The survey on the spray characterization shows that,

- Prediction of spray cone angle may based on simple inviscid theories as given in the first section of this survey or on experiments,
- The breakup length may be obtained using theories on sheet breakup, numerical simulations or from experiments,
- It is hard to deduce the microscopic properties of the spray using theoretical or numerical approaches. The mostly accepted way to obtain such properties of the spray is experimentation.

1.4 Research on Pressure Swirl Atomizers - Why it is needed

As it is mentioned in Section 1.1. many different kinds of injectors can be used in a liquid rocket engine with the same propellant combination, and the choice can affect the performance and stability of the engine. In the case of F-1 engine, this choice had been made based on historical reasons. However, when the problem of combustion instability occurred, it needed huge amount of manpower and long time to identify the actual problem. The investigation of the inner flow through the atomizer and the resulting spray characteristics is a necessary prerequisite to understand the complex physics involved in the liquid rocket engine combustion process. Such an investigation results in detailed information about the characteristics of the injectors which can be used in the combustion chamber design to improve the performance and to reduce the likeliness to undergo combustion instabilities.

An extensive survey of the literature on the pressure swirl type atomizers was given in Section 1.3. In the earlier analytical studies, the flow inside the swirl atomizer was treated as a steady, incompressible, inviscid flow. In the recent experimental and numerical studies the formation of air core inside the atomizer, the effect of various flow parameters and geometrical parameters on the air core and the resulting spray characteristics are investigated. Moreover, the surface waves on the gas-liquid interface are identified and the resulting unsteady flow behavior is studied. With the recent developments of measurement systems and computational tools including hardware and software, the researches on pressure swirl atomizers still continue and provide new insights into the flow through the atomizers and the phenomena of atomization.

The research on the pressure swirl atomizers have been carried out by several researchers working in different disciplines. In most cases the research on the flow through the swirl atomizer is separated from the research on the resulting spray characteristics. The use of high speed photography techniques are rare for the investigation of both steady and dynamic characteristics of the atomizer. The quality of the gathered images are questionable and the image processing methods are not fully defined. The dynamics of the air core inside the pressure swirl atomizer is still a mystery; even though the existence of waves on the air core are known, the mechanisms for the formation of the surface waves are still not well understood.

In addition, numerical and experimental investigations lack fine resolution of the problem and the amount of data gathered from the analysis is generally low which is inadequate to achieve satisfactory conclusions.

In the present study we investigate the air core inside the pressure swirl atomizer using High Speed Shadowgraphy technique. High speed cameras are used to capture the images at high frame rates up to 20000 frame per second (fps). Pressure swirl atomizers are manufactured carefully and back light illumination is used to illuminate the pressure swirl atomizers in order to have clear images of the air core within the atomizer. An image processing tool is developed in order to analyze the images of the air core diameter quantitatively. Statistical methods are used to understand the behavior of the air core at different operating conditions of the atomizer. The unsteady two-phase flow field inside the atomizer is also investigated using CFD tools to gain a better understanding of the inner flow field . In addition the microscopic properties of the resulting hollow cone spray is obtained for different operating conditions.

1.5 Methodology

The investigation of pressure swirl atomizers has a crucial importance on the design of Liquid Rocket Engines (LRE), since it is the key enabling technology for development of thrust chambers. The general trend in the design of LRE thrust chambers shows an increase in sub-scale efforts. The general hierarchy in injector experiments is shown in Figure 1.20.

The experimental investigation is performed on the single element atmospheric cold flow facility of TUBITAK-SAGE. High Speed Shadowgraphy System is used to visualize the air core inside the pressure swirl atomizer and the resulting hollow cone spray. Two high-speed cameras are used in sync mode for the visualization. One camera records the flow inside the pressure swirl atomizer while the other one records the resulting hollow cone spray. The formation of the air core inside the pressure swirl atomizer is visualized by High Speed Shadowgraphy System. The temporal and spatial properties of the air core diameter is studied by using an image processing tool. The macroscopic properties of the spray, like the spray cone angle and break up length

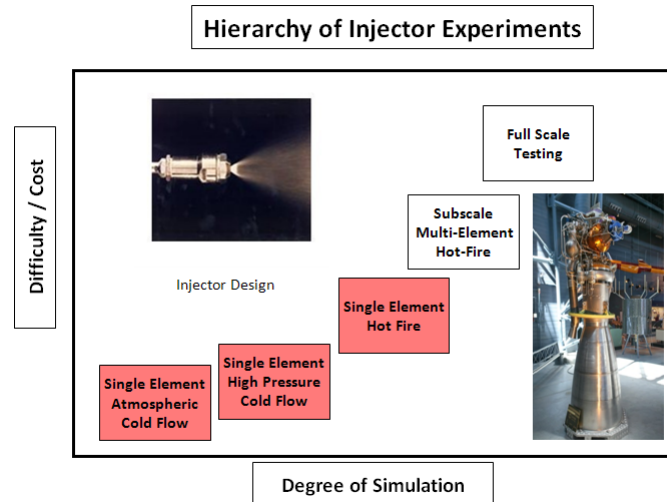


Figure 1.19: Hierarchy in Injector Experiments.

are also obtained using the images captured with High Speed Shadowgraphy System. The mean droplet diameters and the droplet size and velocity distributions of the resulting hollow cone spray are investigated using a Phase Doppler Particle Analyzer (PDPA).

Two-phase flow fields within the pressure swirl atomizer are computed using commercially available ANSYS-FLUENT software. Three dimensional (3D) and two dimensional axis-symmetric swirl (2D-AXS) flow simulations are performed.

1.5.1 Outline of the Thesis

In Chapter 1, a brief introduction to the liquid rocket injectors and pressure swirl atomizers are presented and the research problem is identified. The relevant background information and survey of literature are presented. The need for further research is attained and the methodology of the present study is introduced. The key and controversial terms are defined at the end of the chapter.

In Chapter 2 the experimental investigation of the flow inside the pressure swirl atomizer and the characterization of the resulting hollow cone spray are presented.

In Chapter 3 the numerical investigation of the flow inside the pressure swirl atomizer using two dimensional axisymmetric swirl and three dimensional numerical approaches are presented.

In Chapter 4 conclusions to the present study are given.

1.5.2 Definitions

In general, the definitions adopted by researchers are not uniform, so key and controversial terms are defined in this section.

Tangential Inlet Ports, Swirl Chamber, Convergence Section and Nozzle of a Pressure Swirl Atomizer

During the investigation of the flow through pressure swirl atomizers, different parts of the atomizer will often be referenced. The terminology that will be used in the present study is due to Bazarov [8]. In general, a pressure swirl atomizer is composed of four main sections as shown in Figure 1.20

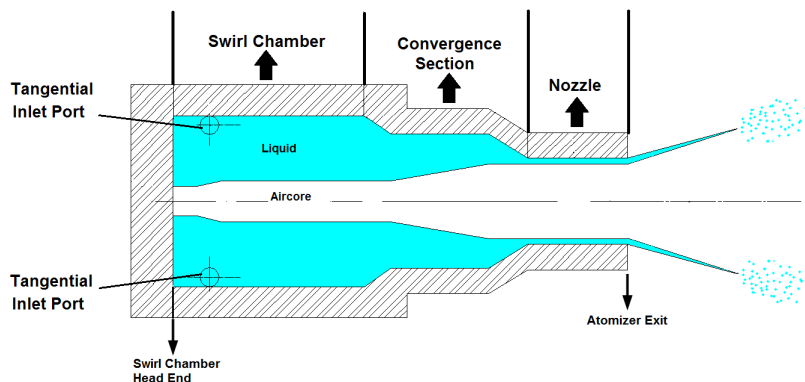


Figure 1.20: The main parts of a pressure swirl atomizer.

Tangential inlet ports are tangentially drilled holes, which starts outside of the atomizer and ends inside. The swirl chamber is the part of the atomizer where the tangential inlet ports are opened. The convergence section is the part between the swirl chamber and the nozzle. The nozzle is the final part of the atomizer where liquid goes out of the atomizer at the atomizer exit.

Geometric Characteristic Parameter

Geometric characteristic parameter of the atomizer (A) is a dimensionless parameter defined by Equation 1.16:

$$A = \frac{A_n}{A_{tp}} \cdot \frac{R_{in}}{R_n} \quad (1.16)$$

where R_n is the radius of the nozzle, A_{tp} is the area of the tangential flow passages, R_{in} is the distance from the atomizer axis to the axis of tangential passages, and A_n is the nozzle area. For a circular nozzle, the geometric characteristic parameter (A) of a pressure swirl atomizer can be written as;

$$A = \frac{\pi \cdot R_{in} \cdot R_n}{A_{tp}} \quad (1.17)$$

CHAPTER 2

EXPERIMENTAL INVESTIGATION

2.1 Introduction

The flow phenomena inside the pressure swirl atomizer and the resulting spray was investigated using different methods by several researchers as outlined in the previous chapter. Simplified analytical models were used in earlier studies due to the complex nature of the problem. The use of experimental methods to investigate the flow through the pressure swirl atomizer and the resulting spray formation has become widespread in recent years. In the present chapter, the experimental investigation of the flow through the pressure swirl atomizer and the resulting spray formation is presented. The chapter is arranged in six main sections. In the first section the information about the experimental facility is given. The pressure swirl atomizer, which is investigated in the present study, is introduced in the second section. Experimental methodology is given in the third section. The details of the data processing and reduction are given in the fourth section. The results of the experiments, that are performed using the High Speed Shadowgraphy System is given in the fifth section. In the last section the experimental results related with the characterization of the hollow cone spray are given in detail.

2.2 Experimental Facility

The experiments are performed on the single element atmospheric cold flow experimental facility of TUBITAK-SAGE. A general view of the single element cold flow

experimental facility is shown in Figure 2.1.

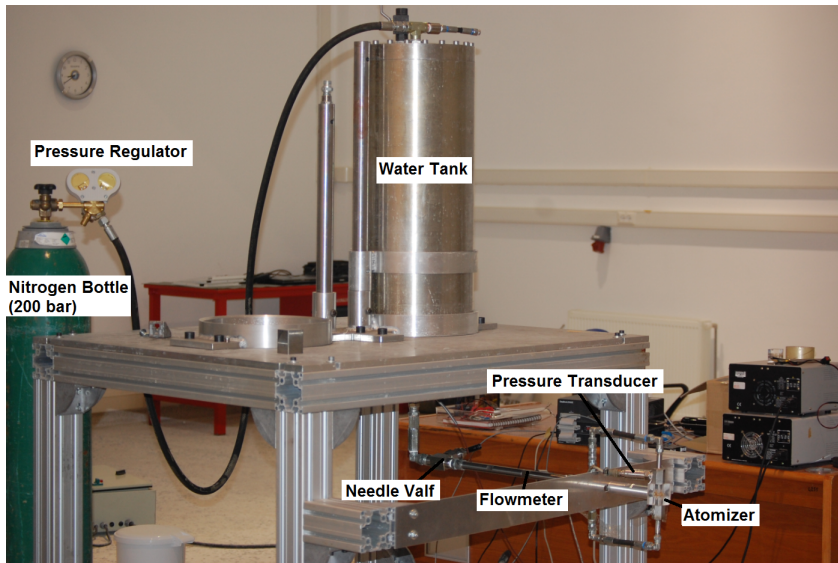


Figure 2.1: Single element atmospheric cold flow facility.

The experimental facility consists of a 40 liters water tank which can stand pressures up to 200 bars. A high pressure nitrogen cylinder and a gas pressure regulator are used to pressurize the water tank. An electro-pneumatically controlled, normally closed valve present at the exit of the water tank. The water flow rate is controlled by using a needle valve just after the normally closed valve. There exists a turbine type flow meter (S-Meter type DN10) at the main water line to measure the volume flow rate of water. Main line from the water tank branches into two after the flow meter and water is fed into the atomizer from two tangential inlet passages. Both branches are equipped with pressure transducer to check whether the flow rates are identical. The temperature of the water is measured before each test and it is in between 10 °C and 20 °C.

2.3 Pressure Swirl Atomizer

The internal geometry of the pressure swirl atomizer, which is studied in the present study, is given in Figure 2.2. The atomizer, whose geometrical properties are given in Figure 2.2, was studied previously by Dash et. al. [26] using numerical and experi-

mental techniques.

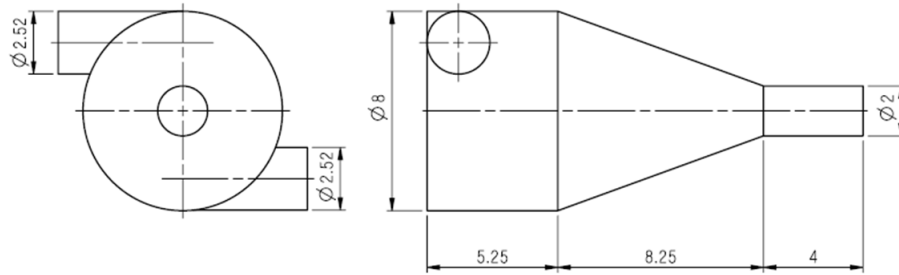


Figure 2.2: The internal geometry of the pressure swirl atomizer.

The total length of the atomizer is 17.5 mm and the length of the nozzle is 4 mm. The diameter of the swirl chamber and the nozzle of the atomizer are 8 mm and 2 mm, respectively. Water is fed through two tangential inlet passages; whose diameters are 2.52 mm.

Atomizers are manufactured from Plexiglas material which allows the use of photographic techniques to visualize the flow inside the atomizer. A Plexiglas pressure swirl atomizer which is mounted on the experimental facility is shown in Figure 2.3.

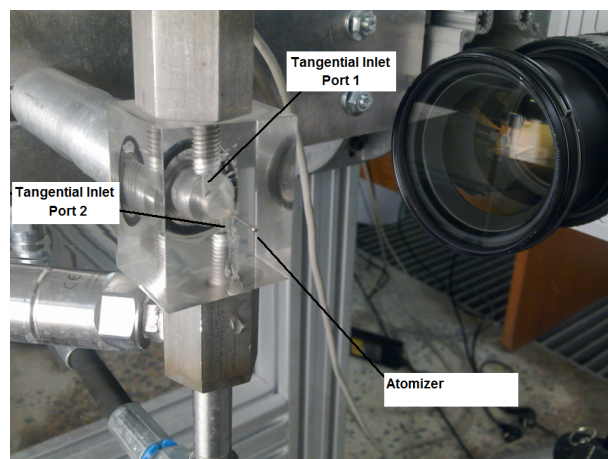


Figure 2.3: Plexiglas pressure swirl atomizer on the experimental facility.

2.4 Experimental Methodology

2.4.1 High Speed Shadowgraphy System

The literature survey reveals that both the numerical and experimental methods can be used to study the flow through the pressure swirl atomizer. Experimental methods generally focused on measuring the air core diameter or the liquid film thickness. In order to measure the air core diameter or the liquid film thickness, the electrical conductance method ([18], [39], [41]) and the photographic method ([14], [15], [16], [26], [40]) are mostly used in previous studies. The electrical conductance method uses a pair of probes in order to measure locally the conductance which is a function of the thickness of the film between the probes. In theory it is possible to take measurement at each location of interest as long as the necessary probes are installed on the test item, but in practical applications only one probe is used at location of interest [41]. If an optical access is available, photographic techniques can be used to visualize the air core and it is possible to study the major characteristics of the flow at any location by processing the photographic images [40].

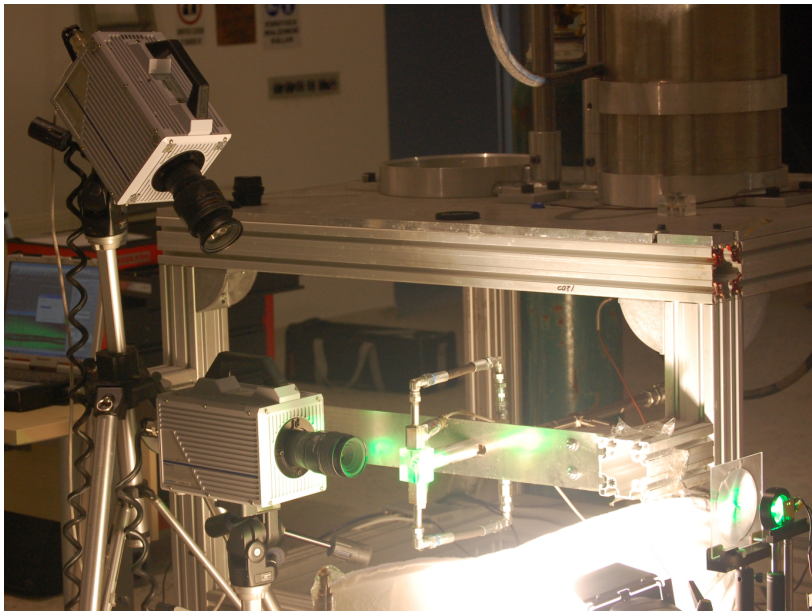


Figure 2.4: High Speed Shadowgraphy System.

A High Speed Shadowgraph system is used to visualize the air core inside the pressure swirl atomizer and the resulting hollow cone spray. Two high-speed RGB CMOS cameras (Photron SA 1.1) are used in sync mode for the visualization. One camera (Camera2), equipped with a 60 mm 1:2.8 D macro lens, records the flow inside the pressure swirl atomizer and the other one (Camera1), equipped with a 24-85 mm 1:2.8-4d lens records the resulting hollow cone spray.

The high speed camera setting for air core diameter and spray cone angle measurements are tabulated in

Table 2.1: High speed camera settings for spray and air core.

Parameter	Setting	
	Camera1	Camera2
Exposure time [microsecond]	10	10
Image recording rate (fps)	20000	20000
Recording duration [milisecond]	500	500
Image width [pixel]	576	768
Image height [pixel]	464	368

The High Speed Shadowgraph System as installed on the test facility is shown in Figure 2.4. Light sources and the cameras are aligned at the opposite sides. The back light illumination of the spray is obtained with two halogen lamps and a diffuser screen. The back light illumination of the atomizer is achieved by using high power light emitting diode (CBT-120, Luminus Devices) whose light intensity can be adjusted. The peak luminous flux of the light emitting diode (LED) is about 2100 lm at maximum continuous drive condition (18 amperes), whereas, a smaller drive condition (4 amperes) is sufficient to illuminate the atomizer in the present study.

A set of collimating optics, a condenser lens ($f=30$ mm) and a Fresnel lens ($f=100$ mm), delivers the green light from LED to the atomizer as shown in Figure 2.5.

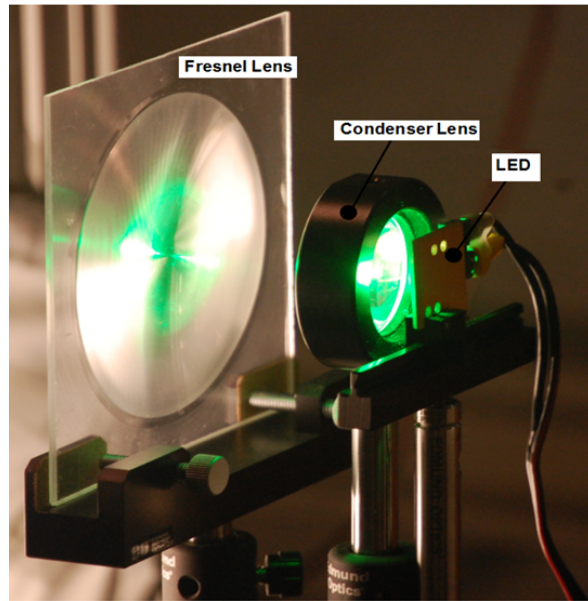


Figure 2.5: LED and the collimating optics.

The last element of the optical arrangement for the illumination of the pressure swirl atomizer is a diffuser screen, which is installed on the side wall of the atomizer. Since the inner walls of the atomizer are concave, the collimated monochromatic light coming from the Fresnel lens is diffused in order to achieve sufficient illumination. The diffuser screen is shown in Figure 2.6 together with the images obtained without and with using the diffuser screen.

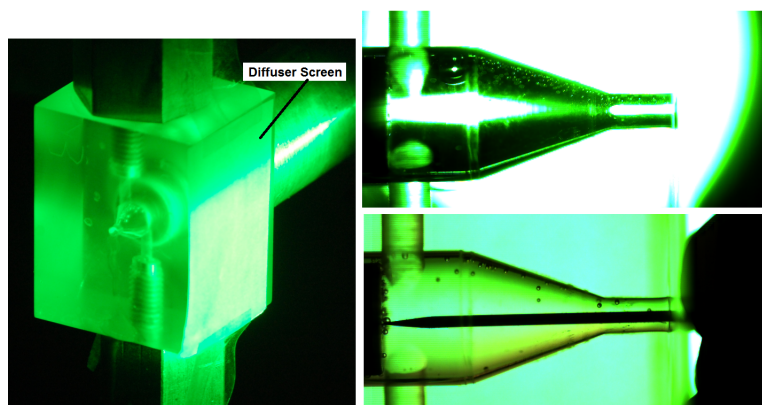


Figure 2.6: Diffuser screen and the images with and without diffuser screen.

The resolution for both high speed CMOS cameras is a function of the frame rate at which the images are collected. The cameras have a resolution of 1024x1024 pixels at 5400 frame per second (fps) and they can go up to 675000 fps for a resolution of 64x16 pixels. After adjusting the frame rate and supplying the sufficient illumination to have images at the specified frame rate, the High Speed Shadowgraphy system is ready to capture movies. The captured movies stored at camera memory and then they are transferred to a computer. It takes about one hour to save a 0.5 second movie file sampled at 20 kHz. The movie files are then converted to image files using Photron Fastcam Viewer.

2.4.1.1 Image Capturing and Processing

The captured images of the air core inside a pressure swirl atomizer and the resulting spray are shown in Figure 2.7 for illustration. Water flows through the atomizer and a hollow cone spray is formed.

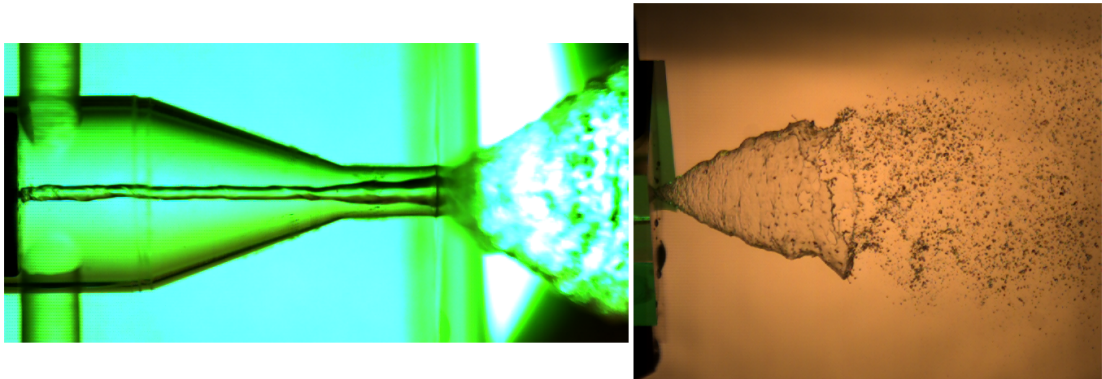


Figure 2.7: Images of the air core inside the atomizer (left) and the resulting hollow cone spray (right).

The sample images, which show the air core inside the atomizer and the hollow cone spray, has one distinct property. The edges of the interfaces are easily discerned due to high density gradients, and shows themselves as darker regions at the center of the atomizer and at the spray boundaries. The diameter of the air core at any location within the atomizer can be obtained by detecting the edges and measuring the distance

between two edges. Similarly the distance between spray boundaries can be found at any downstream location from the atomizer exit and the spray cone angle can be determined.

Edge detection is a low level operation used in image processing and computer vision applications. The main goal of edge detection is to locate and identify sharp discontinuities from an image. These discontinuities are due to abrupt changes in pixel intensity which characterizes boundaries of objects in a scene. Edges give boundaries between different regions in the image [72]. These object boundaries are the first step in many of computer vision algorithms like edge based face recognition, edge based obstacle detection, edge based target recognition, image compression etc. So the edge detectors are required for extracting the edges.

In order to use the edge detection operators efficiently, the RGB images obtained using the high speed cameras are first converted to gray scale images. A sample RGB image and the gray scale image are shown together in Figure 2.8. After this conversion an appropriate edge detector is applied to the gray scale image in order to find the edges. The results of applying various edge detectors are given in Figure 2.9.

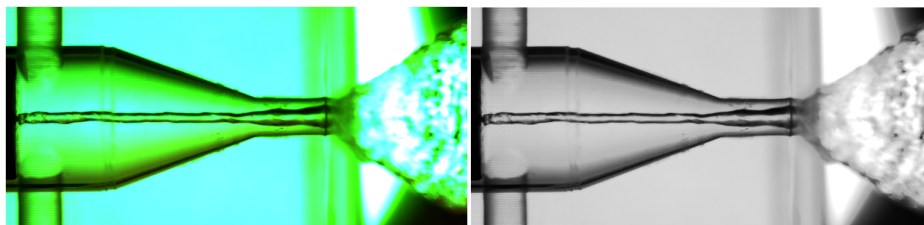


Figure 2.8: Conversion of RGB image to gray scale image

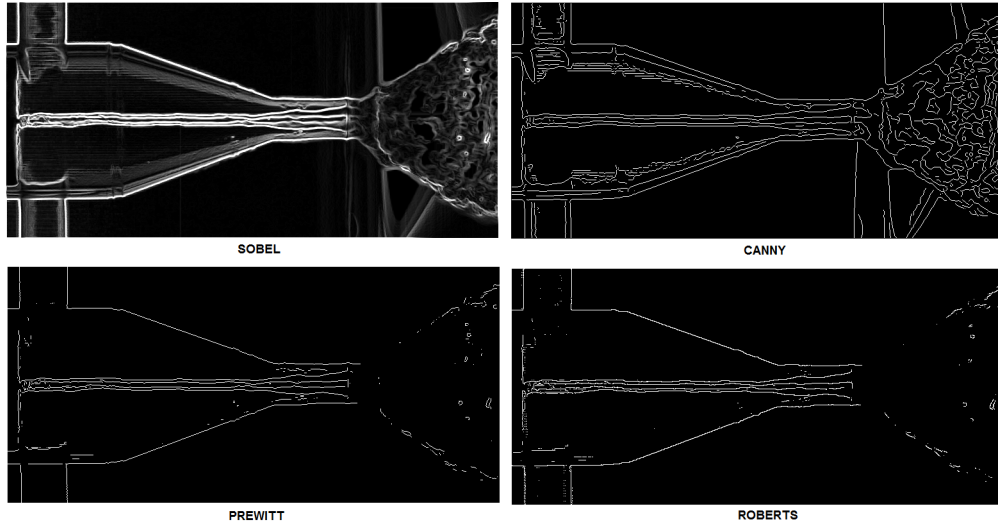


Figure 2.9: Application of various edge detectors to gray scale image.

In the present study, the Sobel edge detector is used in order to identify and locate the sharp discontinuities in the captured images. The Sobel operator performs a two dimensional spatial gradient measurement on the captured images. The Sobel edge detector uses weighted central difference operators in order to estimate the intensity gradients in horizontal and vertical directions. Weighted central difference operators in x (W_x) and y directions (W_y) of Sobel edge detector are given as follows;

$$\begin{array}{ccc}
 \begin{bmatrix} -1 & 0 & +1 \\ -2 & 0 & +2 \\ -1 & 0 & +1 \end{bmatrix} & & \begin{bmatrix} +1 & +2 & +1 \\ 0 & 0 & 0 \\ -1 & -2 & -1 \end{bmatrix} \\
 W_x & & W_y
 \end{array}$$

Figure 2.10: Sobel edge detector weighted central difference operators.

If we define original image as S , then the operators (W_x and W_y) are applied separately to the image to produce measurements of gradient component in each orientation (G_x and G_y) as follows;

$$G_x = W_x * S, G_y = W_y * S \quad (2.1)$$

where * in equation 2.1 denotes the two dimensional convolution operation. The magnitude of the gradient can then be obtained as follows;

$$G = \sqrt{G_x^2 + G_y^2} \quad (2.2)$$

which gives the edges of the original image based on the Sobel operator.

2.4.1.2 Image Processing Tool

An image processing program is developed in MATLAB to process the obtained images. The image processing consists of converting the RGB image to gray scale image, subtracting the background image and increasing the intensity, if necessary, and finding the edges using Sobel edge detector as shown in Figure 2.11

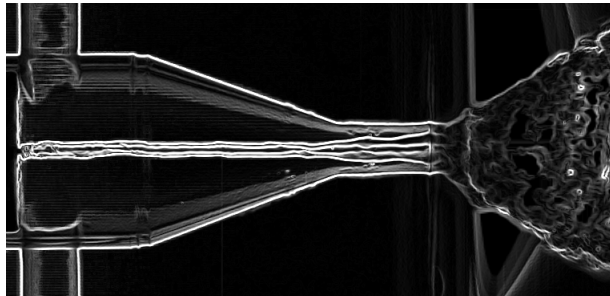


Figure 2.11: The sample image after application of Sobel edge detector.

The image shown in Figure 2.11 can then be used to find the air core diameter at any axial location within the atomizer. The axial location of interest and a line perpendicular to the atomizer axis at that location is defined as an input to the image processing program. The program computes the intensity values along the line and searches for the peak intensity values in Figure 2.12.

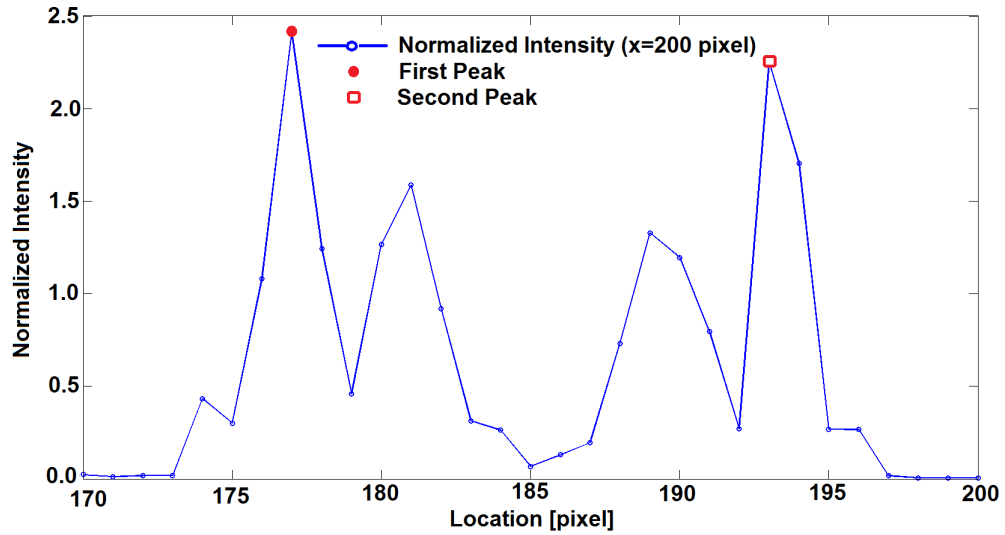


Figure 2.12: The change of normalized intensity along a line at x=200 pixel.

For the image shown in Figure 2.11 the first intensity peak is at 177 pixels and the second peak is at 193 pixels for the axial location of interest. The distance between two intensity peaks is determined as 16 pixels, which is the air core diameter at the location of interest. The uncertainty level for the air core diameter measurements is ± 1 pixel.

2.4.1.3 From Pixel Coordinates to Physical Coordinates

A fine needle is used when taking the calibration image of the atomizer. The diameter of the fine needle is measured using a Mitutoyo PV-5000 series profile projector with a resolution of $1 \mu\text{m}$ and a measurement uncertainty of $2 \mu\text{m}$. Before each test, the fine needle is inserted into the atomizer and a calibration image is captured. The diameter of the fine needle is determined with the image processing program in pixels. The uncertainty related to the measurement of the diameter of fine needle with the image processing program can be neglected due to the sharp edge of the fine needle. The known diameter of the fine needle is then used to determine a conversion factor from pixel coordinates to physical coordinates. Similarly a fine ruler is used to convert from pixel coordinates to physical coordinates outside of the atomizer. Calibration

images that are captured for the measurements within the atomizer and outside of the atomizer are given in Figure 2.13.

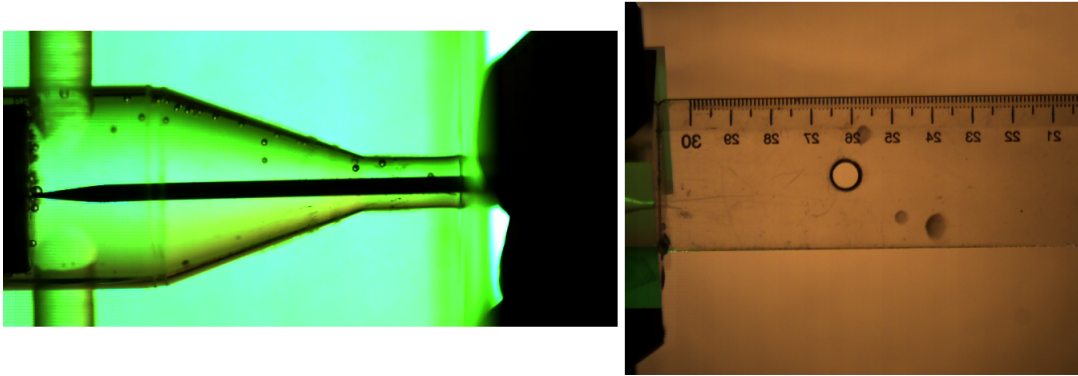


Figure 2.13: Calibration images, fine needle and ruler.

The effective image areas for Camera1 (spray measurement) and Camera2 (air core measurement) are 576x464 pixels (115x92mm) and 768x368 pixels (28x13 mm), respectively.

2.4.2 Phase Doppler Anemometry Technique

Phase Doppler anemometry (PDA) is a non-intrusive technique for the sizing of spherical particles. The PDA technique measures the velocity of the particles based on the laser Doppler anemometry technique, in addition it has the ability to measure the size of particles. The phase Doppler principle is first reported by Durst [73], who showed that the method can be applied to velocity measurements of reflecting and refracting particles. Later Bachalo [74] used the phase Doppler principle to develop a viable technique for drop size and velocity measurements.

A schematic of the phase Doppler anemometry system, showing the major components, is given in Figure 2.14.

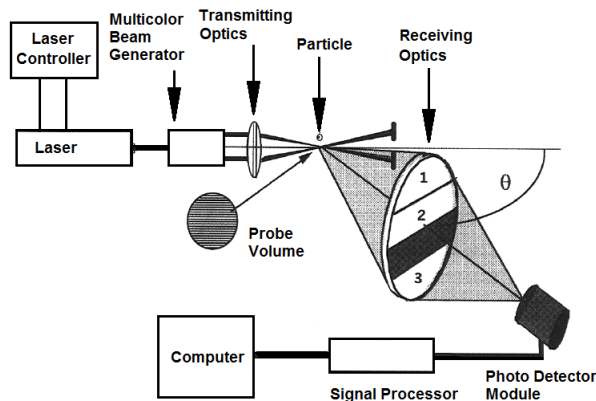


Figure 2.14: Schematic of phase Doppler anemometry system.

In PDA technique, interference patterns are produced at the crossing volume of two laser beams. The interference patterns are a series of light and dark fringes. As the particle moves through the measurement volume, it scatters light as it crosses a bright fringe, and scatters no light as it crosses a dark fringe. This results in a fluctuating pattern of scattered light intensity with a frequency proportional to the particle velocity. This frequency is known as the Doppler shift frequency, which is identical in all spatial directions. In addition to its capability of measuring particle velocities, the PDA technique can also determine the diameter of particles. When viewed from two separate spatial locations the scattered signals exhibit a phase shift

whose magnitude depends on factors including the angle at which light is scattered to each photo detector, the index of refraction of the material of the spherical particle, and parameters such as the light wavelength and the beam intersection angle. The phase shift measured in the Doppler signal obtained from the same particle using two closely spaced photo detectors varies linearly with the particle diameter. The PDA technique makes use of the phase shift measured in Doppler signal to determine the diameter of the particles. In principle, the measurement of particle size requires that the particle entering the measurement volume be spherical, and the diameters of amorphous particles cannot be measured using the phase Doppler method.

The PDA system have a transmitter package consists of a laser, a multicolor beam generator and a transmitter. In the most general case of three components PDA, the multicolor beam generator separates the beam coming from the laser into green, blue and violet laser beams and split each beam into two beams of preferably same power. The beams are carried to the transmitter optics by using fiber optic cables and they go into the transmitting optics as two parallel beams. Then the parallel beams are deflected by the transmitting optics and caused to intersect at a point. The beam crossover volume is called the probe volume.

The receiver package of the PDA system consists of a receiver optics which collects the light scattered by droplets within the probe volume and focused it onto a pinhole. Light which passed to pinhole is directed by mirrors to photo detectors. The mirrors are adjusted so that the light from different well-defined areas of the receiver lens is directed to individual photo detectors through fiber optic cables. The photo-detector module contains the photo detectors, which are extremely sensitive detectors of light in the ultraviolet, visible, and near-infrared ranges of the electromagnetic spectrum. Photo detectors generate electrical signals which represent incoming optical signals. The signal processor receives and processes analog burst signals from the photo detectors and sends the results to computer.

A two-component phase Doppler particle analyzer (PDPA; TSI Inc.) is used to study the microscopic properties of the hollow cone spray developed by the pressure swirl atomizer. The transmitter optics and the receiver optics are positioned on a three-axis remote-controlled traverse system as shown in Figure 2.15.

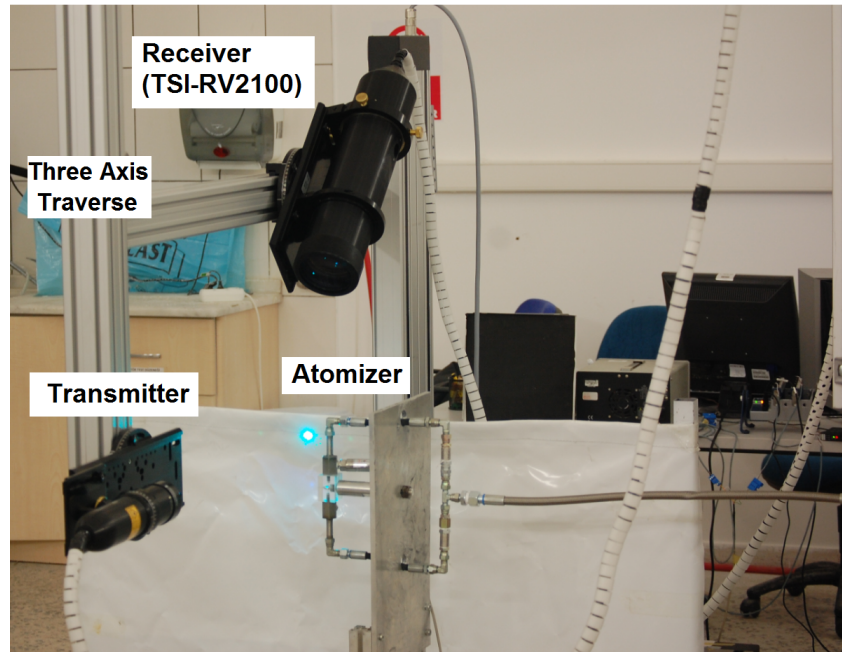


Figure 2.15: Transmitter and receiver optics positioned on three-axis traverse.

The transmitter package of the PDPA has an Ar-Ion laser (Coherent Innova 70-5) which has a maximum power output of 5 Watts at multiline blue/green. The multiline laser beam goes into the multicolor beam generator (Fiberlight). The laser and the Fiberlight is arranged inline such that the multicolor laser, which is generated by the laser goes into the Fiberlight.

The Fiberlight takes the multiline laser beam and separate it to green ($\lambda=514.5$ nm) and blue ($\lambda=488$ nm) beams . Both blue and green laser beams are further split into two laser beams (shifted and unshifted beams) by a set of optics that are positioned within the Fiberlight.

The shifted and unshifted beams are transmitted from Fiberlight to the fiberoptic cables by using Aerometrics type couplers. These couplers contains the necessary optics to focus the laser beam to the tips of the fiberoptic cables. The laser beams are then transferred to the transmitter through fiber optic cables. The transmitter contains lenses to collimate the laser beams coming from the fiber optic cables, a beam expander to expand the beams if necessary and a focusing lens to deflect the beams

such that they intersect to form the probe volume as shown in Figure 2.16.

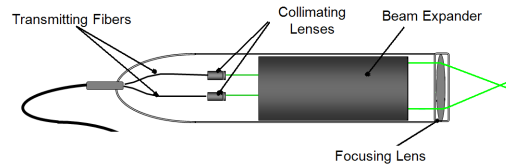


Figure 2.16: The fiberoptic transmitter probe and its elements.

The crossing of two laser beams results in an interference pattern of dark and bright fringes and forms the probe volume (measurement volume). This bright and dark fringes are basically the regions where the intensity of the crossing beams have maximum and minimum intensity. A schematic representation of the probe volume, fringes and the effective diameter of the measurement volume (shown with red dashed circle) are given in Figure 2.17. The particles that pass outside the effective diameter (or beam waist diameter) will scatter light but the intensity of the scattered light is so low that it would not produce a signal that can be processed to get a reliable velocity measurement. The two-component PDPA system, which is used in the present study crosses two sets of laser beams. The axial velocity and the diameter of the particle is measured using the probe volume, that is formed by crossing the green laser beams, by Channel 1 of the processor. The radial velocity of the particle is measured using the probe volume, that is formed by crossing the blue laser beams, by Channel 2 of the processor.

The intensity of the laser beams has Gaussian nature, which leads to the brighter fringes as one moves towards the center of the probe volume.

As a spherical particle passes through the probe volume it scatters light in all directions. The receiver package of the PDPA consist all necessary optical and electronic elements to collect the scattered light, convert them to electrical signals and extract information from these signals. The light scattered by the particle is collected by the receiver. The receiver has a lens assembly which collects the light scattered by droplets and focused it onto a multi mode fiber. The multi mode fibers transmits the light to the photo detectors. The photo detectors, which are contained in the photo

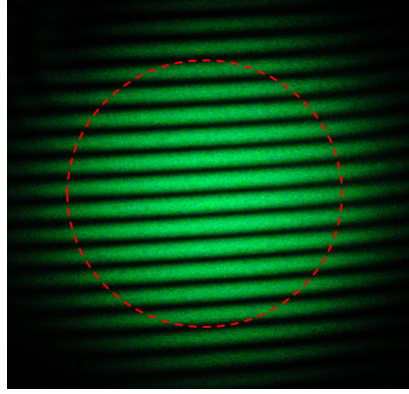


Figure 2.17: Probe volume, fringes and the diameter of the measurement volume.

detector module (PDM), converts the light transmitted by the multi mode fibers into electrical signals (voltage). The photo detectors that are used in the present study are photomultiplier tubes (PMT) which are extremely sensitive detectors of light. The PDM sends the electrical signals to the FSA signal processor. The FSA signal processor receives these signals and extracts information such as frequency, phase, burst transit time and burst arrival time from these signals and sends it to a computer.

The electrical signal from the photo detector at high light flux has generally the following components;

- a low frequency component (pedestal) caused by the particle passing through the Gaussian beam waist,
- Doppler frequency, superimposed on the pedestal and oscillates at the fringe crossing frequency,
- wide bandwidth noise generated in the PMT and downstream electronics.
- optical shift to enable velocity measurements in both directions.

The FSA signal processor removes the unnecessary components of the signal. The incoming signal is first high-pass filtered to remove the low frequency portion of the signal due to the Gaussian nature of the laser beams. After removing the pedestal, the signal is mixed with another signal whose frequency can range from 0-40 MHz.

The difference signal is then passed through to a selectable series of bandpass filters. This process of mixing is often called downmixing. After downmixing, the signals are passed through a user selectable series of bandpass filters. Passing the signals through the bandpass filters helps improve the Signal to Noise Ratio (SNR) of the signals by eliminating noise. The signal frequencies are then measured using the signal processor to calculate the velocity components. The pure electrical signal that is transmitted to FSA signal processor and the same signal after the application of high pass and low pass filters are given in Figure 2.18.

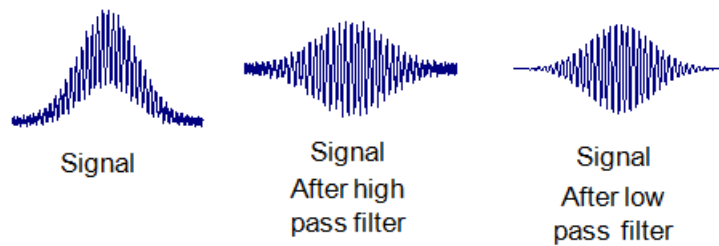


Figure 2.18: Electrical signal and application of filters.

The spacing between the scattered fringes contains the information about the size of the particle. In order to measure the spatial frequency a minimum of two detectors is required. In the current phase Doppler system, three separate detectors are used and two independent measurements of size are obtained using these detectors. The spatial frequency is measured as a phase shift between the two electrical signals resulting from the scattered light. This phase shift is used to calculate the size of the particle.

2.4.2.1 Optical Alignment

Accuracy of the data, which is obtained using the PDPA, significantly depend on the optical alignment. There are a couple of optical alignment issues that has to be done precisely before performing the experiments.

The first step in the optical alignment is to make the laser and Fiberlight inline so that all the beam goes out from the laser goes into the Fiberlight without any loss. The second step is to align the beam steering mirror and dispersion prism inside the

Fiberlight such that the split laser beams goes out of the small openings at the top of the Fiberlight and at least the beams of same colors have the same power rating. This alignment is performed by using alignment mask and a laser power meter to ensure that each beam is at the center of the alignment mask, and beams of same color have the same power, respectively. The third step is the process of focusing the laser beam to the tip of the fiberoptic cable. This alignment is performed using the Aerometric type couplers, which has the necessary optical arrangement for focusing the laser beam to the tip of the fiber optic cable. A power meter is used to measure the power levels of the beams going out from the couplers.

2.4.2.2 Optical and Processor Setup

In the present study, the receiver and transmitter are positioned on a 3-axis traverse in a 43° forward scatter configuration. The focal length of the focusing lens is 500 mm with a beam separation of 20 mm and laser beam diameter of 1.77 mm. The focal lengths of the receiver front lens and receiver back lens are 500 mm and 370 mm, respectively. The bragg cell frequency is 20 Mhz and the refractive index of the water is taken as 1.33. The PMT voltage at Channel 1 and Channel 2 is 390 and 350 V, respectively. The burst threshold is kept constant at 30 mV for both channels and the band pass filter is in the range 1-10 Mhz. The resulting beam waist, fringe spacing, the limits of the velocity and diameter that can be measured using the optical setup are given in Table 2.2 for both measurement channels. Each run continues until 30000 valid measurements are obtained using the PDPA system.

Table 2.2: Beam waist, fringe spacing, limits of measurable velocity and diameter

	Channel Number	
	1	2
Beam Waist [μm]	185	175
Fringe Spacing [μs]	12.86	12.20
Minimum Measurable Velocity [m/s]	-38.60	-36.61
Maximum Measurable Velocity [m/s]	77.19	73.21
Minimum Measurable Diameter [μm]	1.23	-
Maximum Measurable Diameter [μm]	514.5	-

2.5 Experimental Results-High Speed Shadowgraphy System

The flow through the pressure swirl atomizer and the resulting hollow cone spray are visualized with two high speed cameras in sync. The images, that are obtained from the cameras, are processed using the developed image processing tool and the air core diameter is obtained. In this section the results of the experimental investigation, which is performed using High Speed Shadowgraphy system are given.

2.5.1 Formation of the Air Core and the Hollow Cone Spray

The High Speed Shadowgraphy setup is used to visualize the formation of the air core within the atomizer and the hollow cone spray. Initially the atomizer is filled with water and the needle valve is opened from closed position to fully opened position, while the high speed cameras are recording. The air core formation within the atomizer and spray formation are shown with nine images in Figure 2.19. Each image showed the atomizer on the left and spray on the right. The sampling period of the images shown in Figure 2.19 is 7.5 milliseconds (ms) and a fully developed spray is formed at about 60 ms. The flow rate through the atomizer increases from Image 1 up to Image 9 at which the needle valve is at the fully opened position.

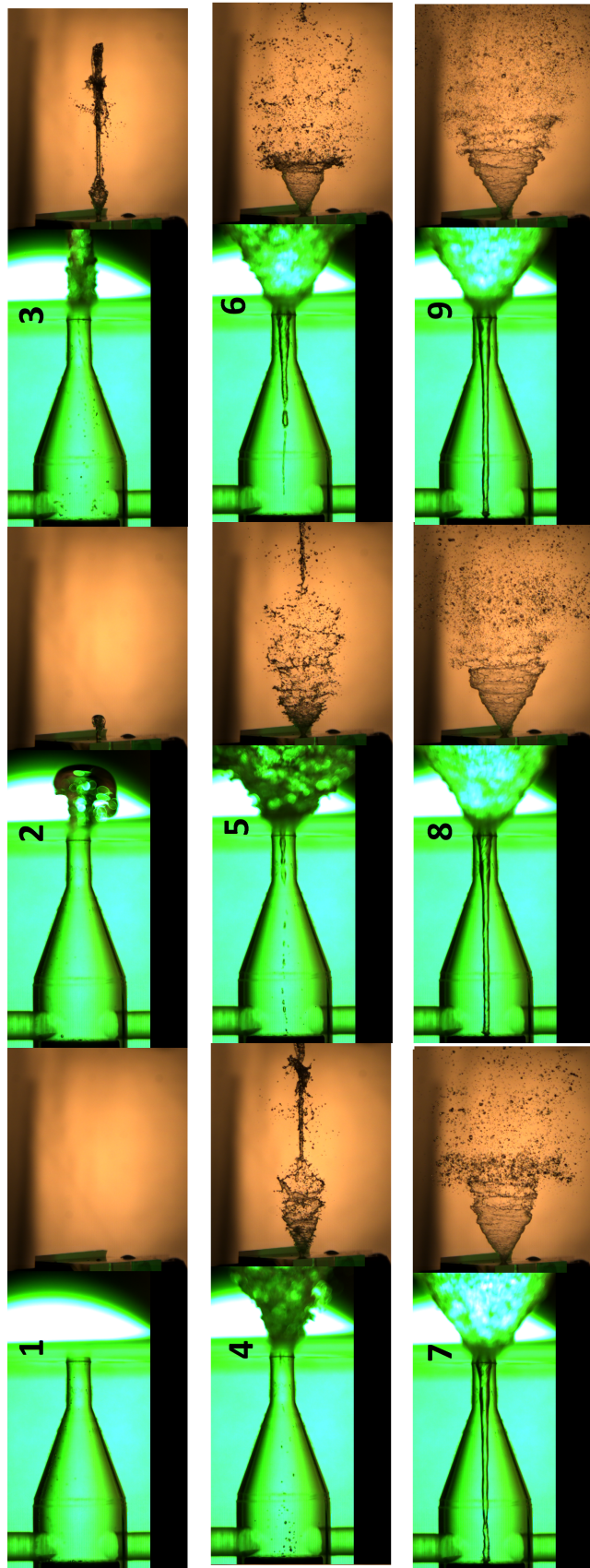


Figure 2.19: Formation of the air core and the hollow cone spray.

Although, the flow is a swirling flow, at low flow rates the swirl strength is too weak for the formation of air core inside the atomizer. The formation of the air core within the atomizer starts with the depletion of the water at the nozzle of the atomizer (image 4) and the formation of the full air core takes about 20 ms.

On the other hand some stages of the spray development can also be identified by investigation of Figure 2.19. At low flow rates, at which the air core is not present inside the atomizer and the atomizer runs full, the spray is like a distorted pencil (Image1-Image3) . As the flow rate increases, which in turn increased the swirl strength, an air core starts to appear within the atomizer (Image4-Image9), meanwhile the spray evolved to an onion shaped (image4) and then to a tulip shaped (image 9) hollow cone spray.

In order to see the effect of different operating conditions on the air core, the flow rate through the atomizer is increased by adjusting the needle valve. The flow rate through the atomizer is plotted against the pressure drop across the atomizer and shown in Figure 2.20.

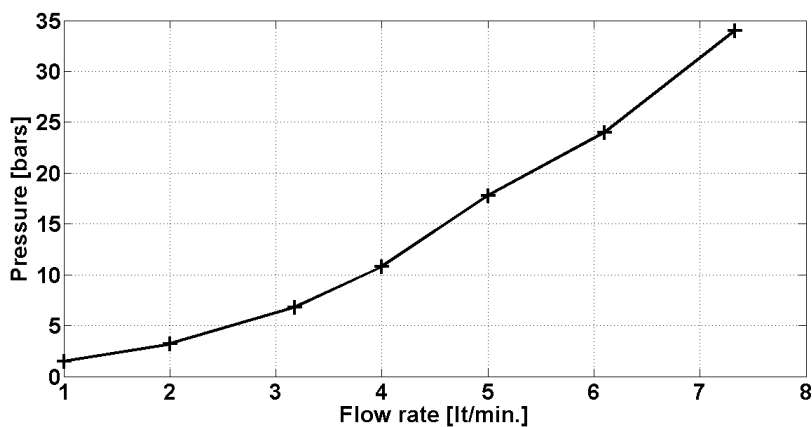


Figure 2.20: Flow rate versus pressure drop.

The formation of the air core is rapid and it occurs at a flow rate (Q) smaller than 1 lt /min. An air core present inside of the atomizer at all flow rates higher than 1 lt/min. On the other hand, the shape of the hollow cone spray is different at different flow rates as shown in Figure 2.21. At Q=1 lt/min , the hollow cone spray is at the tulip

stage with a smooth film and the atomization is rather coarse. As the flow rate across the atomizer increases the atomization becomes finer.

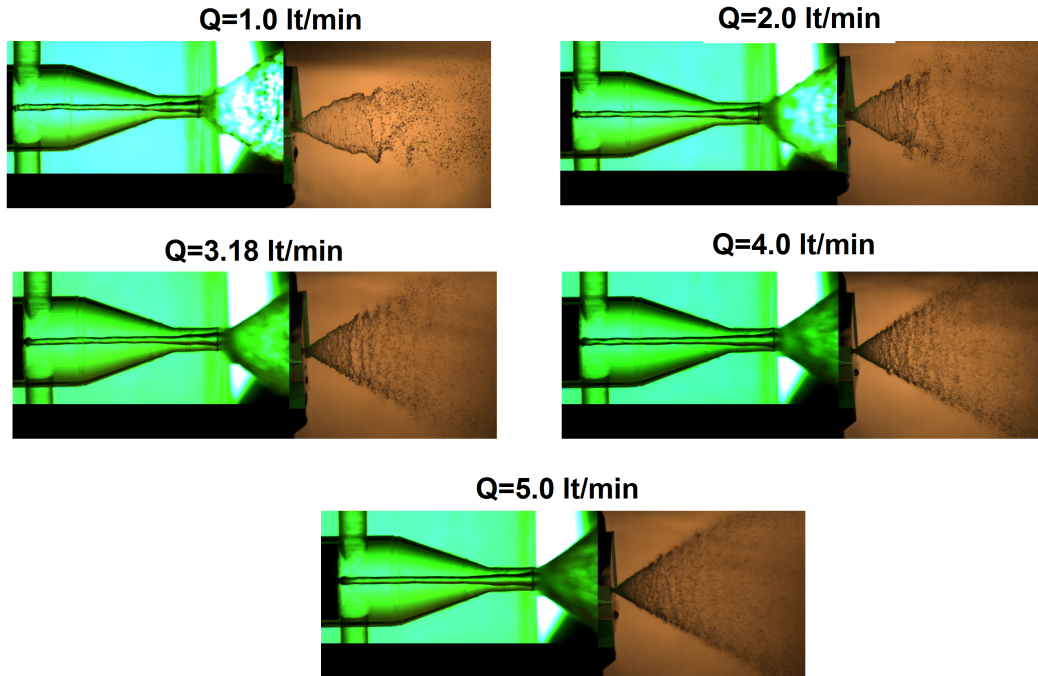


Figure 2.21: Air core and spray at different flow rates.

As the flow rate through the atomizer increases the pressure drop across the atomizer increases accordingly. Four operating points are considered for further calculations. The flow rate through the atomizer for these operating points are 2.0 lt/min, 3.18 lt/min, 4 lt/min and 5 lt/min and the corresponding pressure drop values are 3.2 bars, 6.8 bars, 10.8 bars and 17.8 bars, respectively. The operating point at which the flow rate equals to 3.18 lt/s was investigated previously by Dash et. al. [26] using both experimental and numerical techniques. The mass flow rate and pressure drop values are given together in Figure 2.22 for the mass flow rate of 3.18 lt/min. For this operating point, the images of flow through the atomizer and the resulting spray is captured between 55.5 and 56 seconds using the high speed camera.

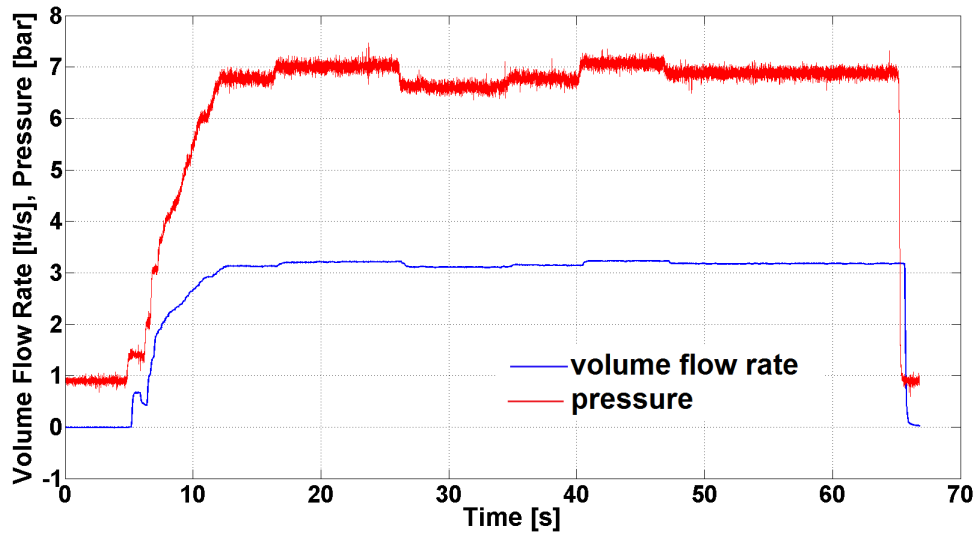


Figure 2.22: Pressure drop and mass flow rate.

2.5.2 Visualization and Qualitative Characterization of Air Core

The formation of the air core inside the atomizer depended on the swirl strength. At sufficiently high flow rates, an air core is present inside the atomizer, which oscillates even in the absence of external forcing on the mass flow rate. These kind of oscillations has been reported previously by several researchers based on their experimental and/or numerical investigations ([27], [28], [29], [31], [39]). The air core inside the pressure swirl atomizer resembles a drilling bit. At the head end of the atomizer, the air core ends with a shape like a mushroom cap as shown in Figure 2.23. Surface waves as well as cavitation and rotational waves on the air core surface are identified. The air core diameter is minimum at the head end of the swirl chamber and it is almost constant along the swirl chamber up to a location close to the nozzle inlet where it starts growing in size. The air core diameter is not constant along nozzle and attains its maximum value at the nozzle exit.

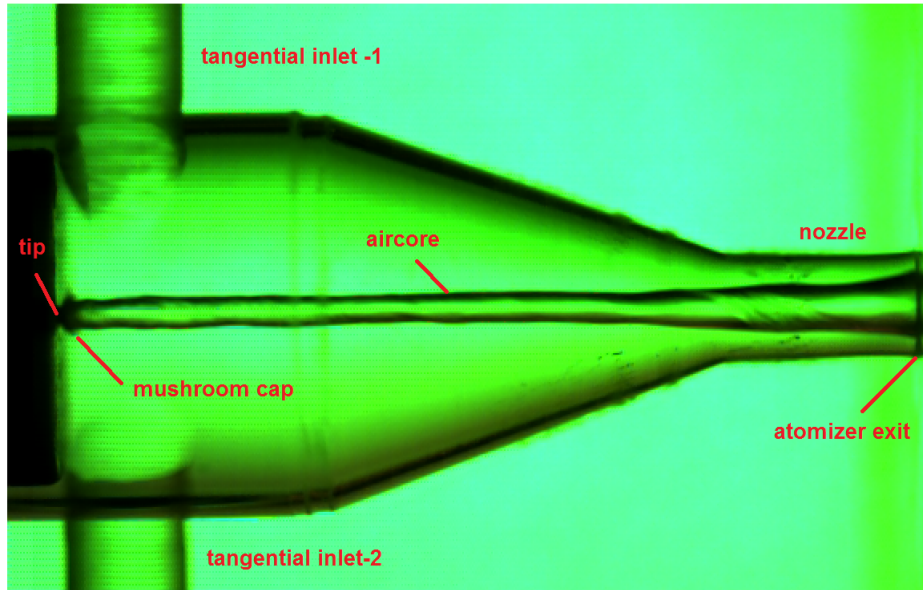


Figure 2.23: Mushroom cap of the air core and tip of the cap.

2.5.2.1 Precession Movement of the Air Core Cap

It is observed that the air core rotates using the tip of the mushroom cap as a pivot point. In some cases the rotation is also accompanied by a precession movement of the air core cap as shown in Figure 2.24 at which the direction of the translation is shown with a red arrow. Translation in the opposite direction is also observed for the atomizer studied in this study. The vertical displacement of the cap tip is below 1 mm, yet the vertical displacement changes the air core shape near the head end effectively.

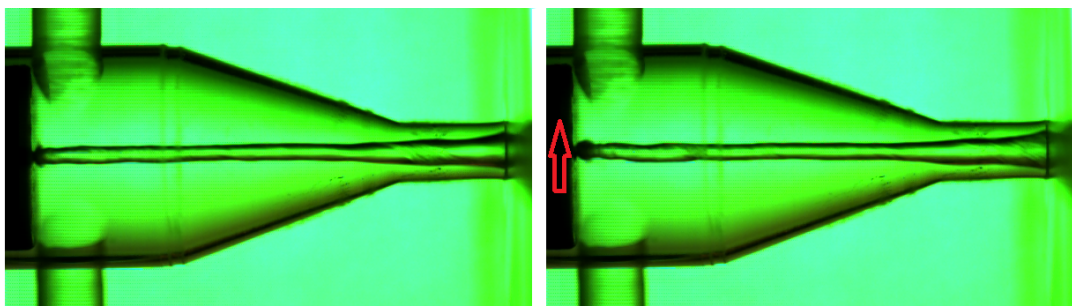


Figure 2.24: Precession movement of the air core cap.

2.5.2.2 Wave Forms on the Air Core

Three types of wave forms are identified in the water-air interface based on the visual investigation of the images captured by the high speed camera.

Cavitation Waves

The first type of wave forms, identified on the air core, are the cavitation waves which are originated from the head end of the atomizer. The onset of the cavitation wave is shown on the first three images of the first column of Figure 2.25 for a water flow rate of 3.18 lt/min.

The pressure swirl atomizer may be prone to cavitation at the air core near the head end, due to the fluctuations observed on the air core at this location. The fluctuations may create high local velocities and as a result local pressures below the vapor pressure of water, which may lead to cavitation.

The shape of the mushroom cap changes and a wave forms with a front at $x=50$ pixel as shown in the first image ($t=0.0$ ms), then the wave front very rapidly travels approximately to $x=75$ pixel in 0.05 ms and then approximately to $x=100$ pixel in 0.1 ms. The cavitation wave does not travel further in most of the occasions and the wave front does not go beyond 150 pixel. A periodic pattern is difficult to capture by just looking at the images, but a high frequency wave phenomena specific to the locations close to the head end is identified.

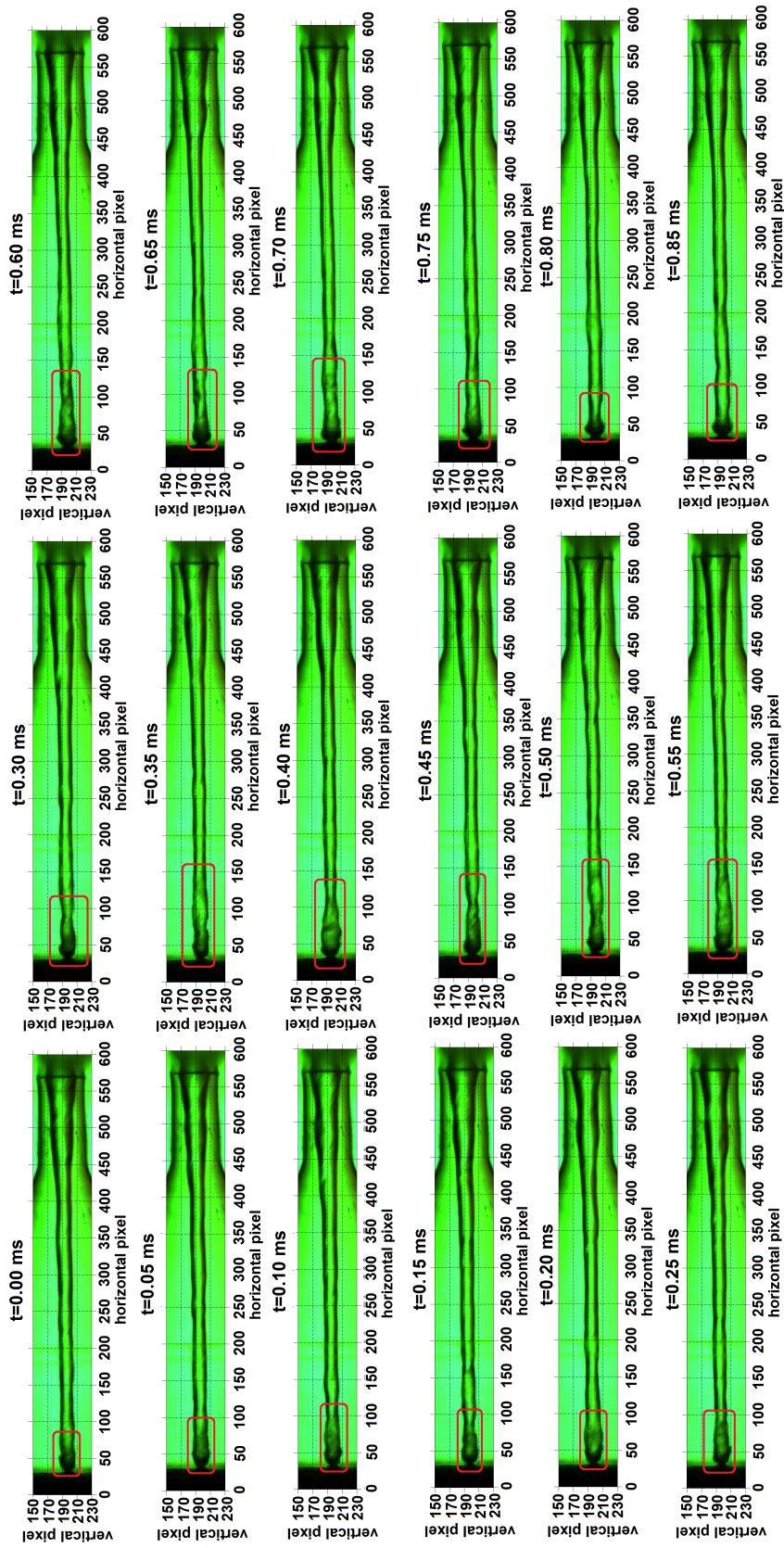


Figure 2.25: Cavitation waves at the head end of the atomizer (3.18 lt/min water).

Surface Waves

The second type of waves, that are identified on the air core interface, are the free surface waves, which are shown in Figure 2.26. Both short and long waves are identified at the swirl chamber and the nozzle.

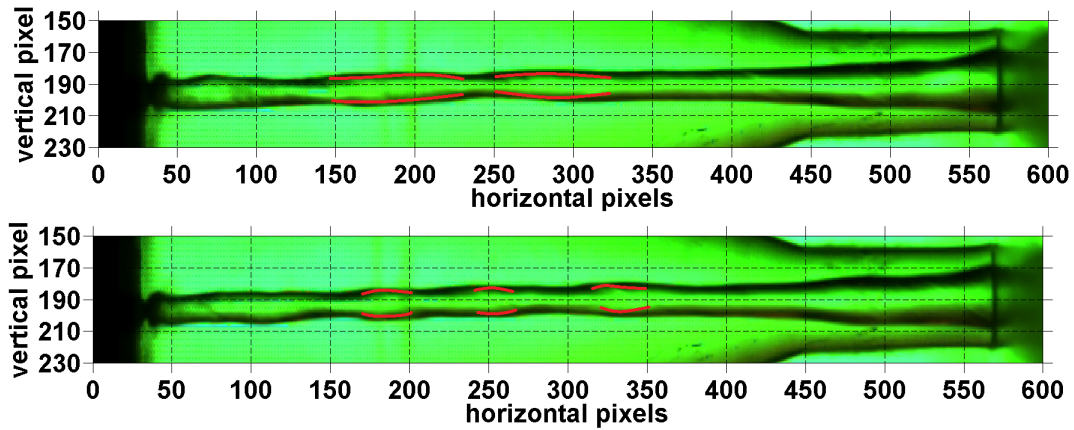


Figure 2.26: Free surface waves (3.18 lt/min water).

Rotational Waves

The third type of waves, that are identified at the air core interface, are the rotational waves. This kind of waves are identified on the air core both at the swirl chamber and at the nozzle but their appearance is quite different as shown in Figure 2.27.

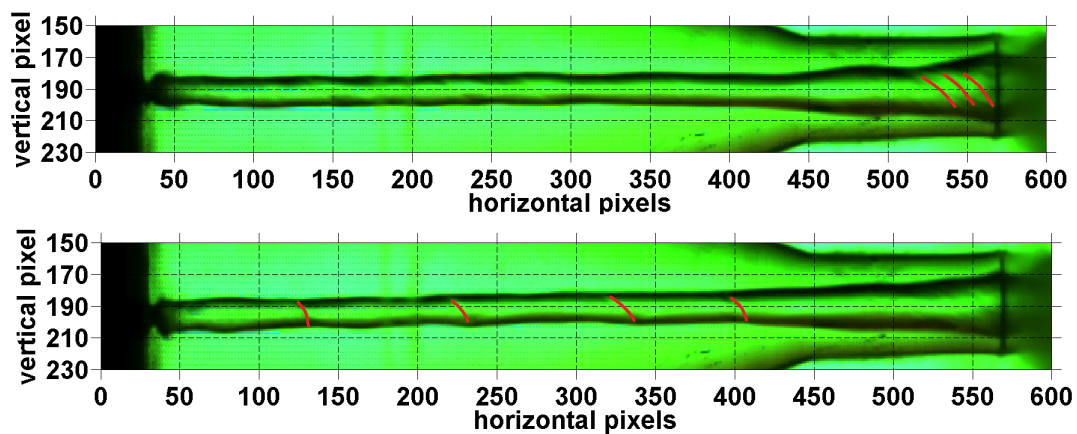


Figure 2.27: Rotational waves (3.18 lt/min water).

The combination of three type of waves is also possible at the air core interface. The common feature of all waves is that they changed the air core diameter considerably, so an analysis of the air core diameter should give some insight to the wave phenomena at the air core.

2.5.3 Quantitative Analysis of the Air Core Diameter

In this section the quantitative values of the air core diameter are obtained using the developed image processing tool, details of which was given in Section 3.2.3. It is possible to obtain time dependent air core diameter value at any axial location inside the atomizer. The air core diameter is calculated at twenty different sections along the atomizer and time domain representation of the air core diameter at each location is obtained. Using the time domain representations, the amplitude spectrum of the air core diameter signals are obtained using Fast Fourier Transform (FFT) Algorithm. In the final section the modes of the air core diameter are calculated using the POD technique.

2.5.3.1 Calculation of the Air Core Diameter

The axial locations (Stations), at which the air core diameter is calculated, are given in Figure 2.28 and the axial coordinates of the Stations are given in Table 2.3.

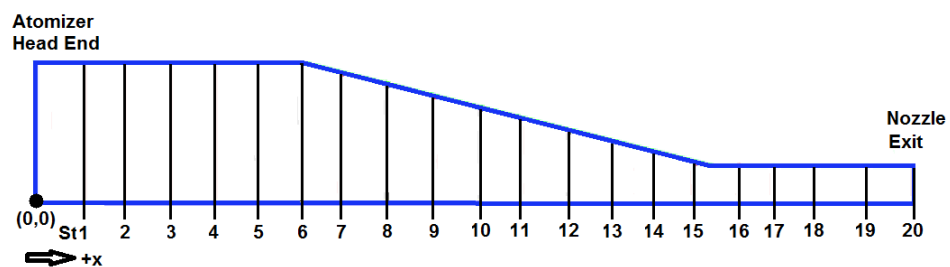


Figure 2.28: Stations for the air core diameter calculations.

Table 2.3: Axial coordinates of the stations.

Station Number	Axial Location [mm]	Station Number	Axial Location [mm]
1	1.109	11	9.625
2	1.195	12	10.500
3	2.625	13	11.375
4	3.500	14	12.250
5	4.375	15	13.125
6	5.250	16	14.000
7	6.125	17	14.875
8	7.000	18	15.500
9	7.875	19	16.625
10	8.750	20	17.500

The air core diameter is calculated at 20 different stations along the atomizer. The first station is only 1.109 mm away from the atomizer head end and starting with St3, the distance between the two stations is kept constant at 0.875 mm up to mid nozzle (St18). The last station (St20) is at the exit of the atomizer.

The time history of air core diameter is given in Figure 2.29 for six different stations. The first station is at the head end of the atomizer. Station 4 is at the swirl chamber, Station 8 and Station 12 are at the convergence section, Station 18 is at the mid nozzle and Station 20 is at the nozzle exit. The time history of air core diameter at other stations are given in Appendix A.

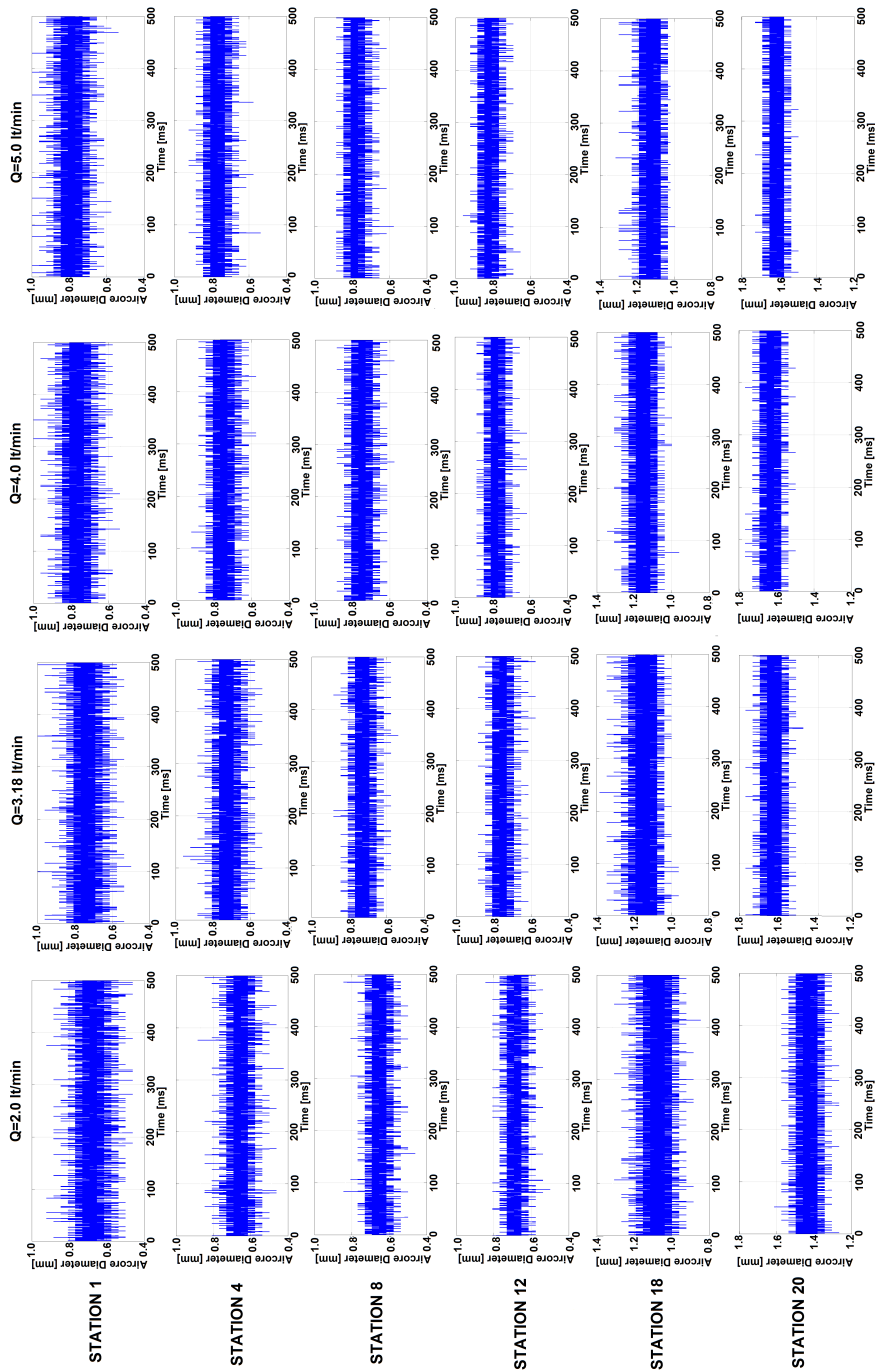


Figure 2.29: Time history of air core diameter at designated stations.

The mean air core diameter at the head end is observed to be zero as explained in the previous section. A mushroom cap is identified at the head end of the atomizer with a pivot point and the air core diameter is zero at that location. The shape of the air core based on the calculated mean air core diameter values for different operating points is given on the left of Figure 2.30 and the standard deviation from the mean air core diameter at each station is given on the right of Figure 2.30. The values for the mean air core diameter (ACD) at each station and the corresponding standard deviation (SD) values are also tabulated at Table 2.6.

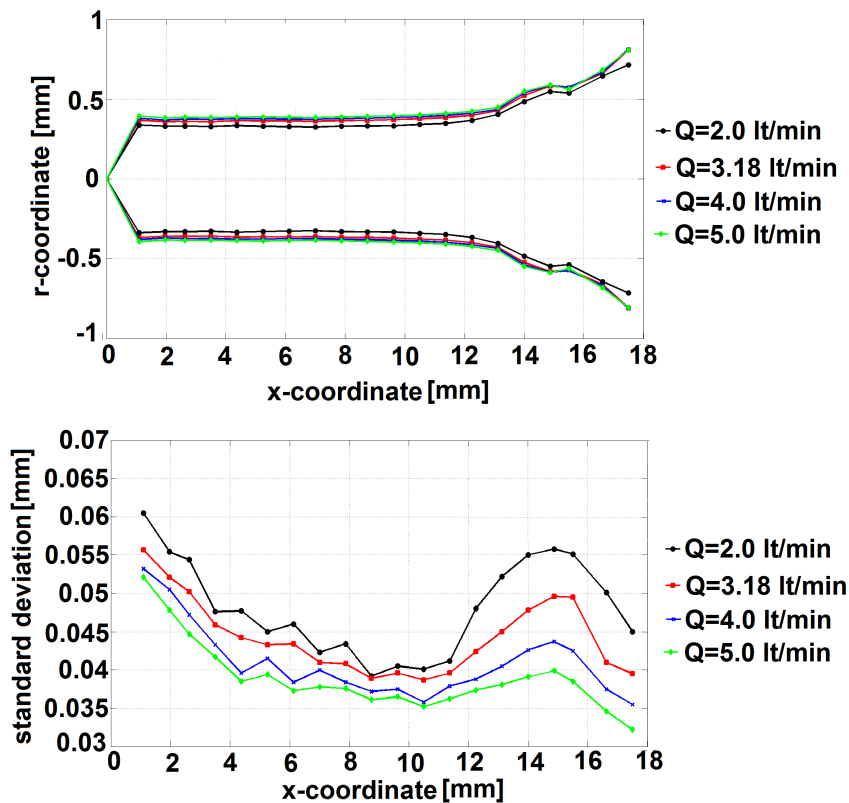


Figure 2.30: Mean air core diameter and the corresponding standard deviations.

The shape of the air core along the axis of the atomizer is almost identical for all operating conditions. The calculated mean air core diameters are almost constant between Station 1 ($x=1.09$ mm) and Station 12 ($x=10.5$ mm) for each operating condition and the air core diameters differ slightly. The mean air core diameters for $Q=2.0$ lt/min case are relatively small when compared to the ones at other operating points. The

Table 2.4: Mean air core diameter and the corresponding standard deviations.

Station	P=3.2 bars		P=6.8 bars		P=10.8 bars		P=17.8 bars	
	ACD	SD	ACD	SD	ACD	SD	ACD	SD
1	0.6735	0.0605	0.7355	0.0557	0.7612	0.0532	0.7870	0.0521
4	0.6567	0.0476	0.7186	0.0459	0.7478	0.0433	0.7684	0.0417
8	0.6500	0.0423	0.7212	0.0410	0.7470	0.0400	0.7689	0.0378
12	0.6812	0.0401	0.7528	0.0387	0.7780	0.0358	0.8017	0.0352
18	1.0751	0.0551	1.1401	0.0495	1.1489	0.0425	1.1239	0.0385
20	1.4303	0.0450	1.6119	0.0395	1.6272	0.0355	1.6134	0.0322

calculated air core diameter is 0.6735 mm for Q=2.0 lt/min bar case and increase to 0.7870 mm for Q=5.0 lt/min case at Station1. At station 12 the mean air core diameter is calculated as 0.6812 mm for Q=2.0 lt/min case and 0.8017 for Q=5.0 lt/min case. After Station 12 the calculated air core diameter values increase gradually up to Station 18 (x=15.5 mm) at which a decrease in the air core diameter is identified. After Station 18 the mean air core diameter continue to increase and has its maximum value at the exit of the atomizer for each operating condition. Although the mass flow rate at Q=5.0 lt/min case is 2.5 times higher than the Q=2.0 lt/min case the increase in the air core diameter is limited.

The standard deviation from the mean is higher for the Q=2.0 lt/min case and decrease with increasing flow rate at each axial location along the atomizer. The standard deviation values from the mean is maximum at the head end of the atomizer and decrease up to Station 12 (x=10.5 mm) for each operating condition. Starting with the Station 13 (x=11.375 mm) the standard deviation values increase up to Station 17 (x=14.875 mm) for all cases. The standard deviation values then decrease gradually up to the nozzle exit.

2.5.3.2 Comparison of Results

The mean air core diameter values at the swirl chamber and mid nozzle obtained in the present study are further compared with the available experimental results of Dash et. al. [26] for 3.18 lt/min flow condition. Dash et. al. [26] give single air core diameter for the whole swirl chamber. In the present study we calculate the air core diameter at different stations along the swirl chamber. So a mean air core diameter value for the swirl chamber is calculated based on the calculated air core diameter values at Stations 1-6 for comparison. The calculated mean air core diameter value at Station 18 gives the air core diameter at the mid nozzle and used directly for comparison. The comparison of the results of the present study with the results of Dash et. al. [26] are given in Table 2.5.

Table 2.5: Comparison of air core diameter at swirl chamber and mid nozzle.

	Air Core Diameter [mm]	
	Swirl Chamber	Mid Nozzle
Present Study	0.72	1.14
Dash et.al. [26]	0.67	1.15
% Difference	6.9	0.9

The air core diameter values obtained at the swirl chamber and nozzle in the present study are in good agreement with the results of Dash et. al. [26] for 3.18 lt/min. operating condition.

2.5.3.3 Frequency Domain Analysis of the Air Core Diameter

In order to analyze the time domain air core diameter data with respect to frequency, the time domain data is converted to frequency domain by using the fast Fourier transform (FFT) algorithm. The time histories of air core diameter at different stations are transformed into frequency domain using FFT in order to investigate how much of the air core diameter signal lies within each frequency band over a range of frequencies. The sampling frequency for the air core diameter signal is 20 kHz. Before applying

the FFT to the air core diameter signal, the signal is subtracted from its mean and it is windowed with Hanning window. The application of Hanning window forces the input signal to start and end at zero to mimic a periodic signal. FFT is applied to the air core diameter data using the function called *fft* in MATLAB. The frequency domain representation of the air core diameter data are given in Figure 2.31 for the stations whose time domain representations were given previously in Figure 2.29. The frequency spectrum of diameter at other stations were given in Appendix B.

The frequency spectrum of the air core diameter signal reveals two dominant frequency ranges, which depends on the axial location of the Station along which the air core diameter is calculated, as well as the operating point of the atomizer. Two range of dominant frequencies are identified at stations close to the head end for all operating points as shown in Figure 2.31 (Stations 1 and Station 4). The first one reveals a low frequency phenomena with dominant frequencies between 0-670 Hz. The second frequency range reveals a high frequency phenomena with dominant frequencies changing with the operating point of the atomizer.

Q=2.0 lt/min operating point

At Station 1, a dominant low frequency range is identified between 0-620 Hz and a dominant high frequency range is identified between 2600-5000 Hz. The amplitude of the low frequency oscillations are higher than the high frequency ones for Station 1. At Station 4, a dominant low frequency range is identified between 0-400 Hz and a dominant high frequency range is identified between 2000-4300 Hz. However for this station the amplitude of the high frequency oscillations are higher than the low frequency ones. As one moves from head end to nozzle entrance, at Station 8 and Station 12, similar dominant low frequency and high frequency ranges are identified but the amplitude of the high frequency oscillations decreases approximately half of the amplitude of the low frequency oscillations. At Station 18 several dominant frequencies are identified between 0-4500 Hz with comparable amplitude. At the exit of the atomizer, a dominant low frequency peak at 238 Hz is identified.

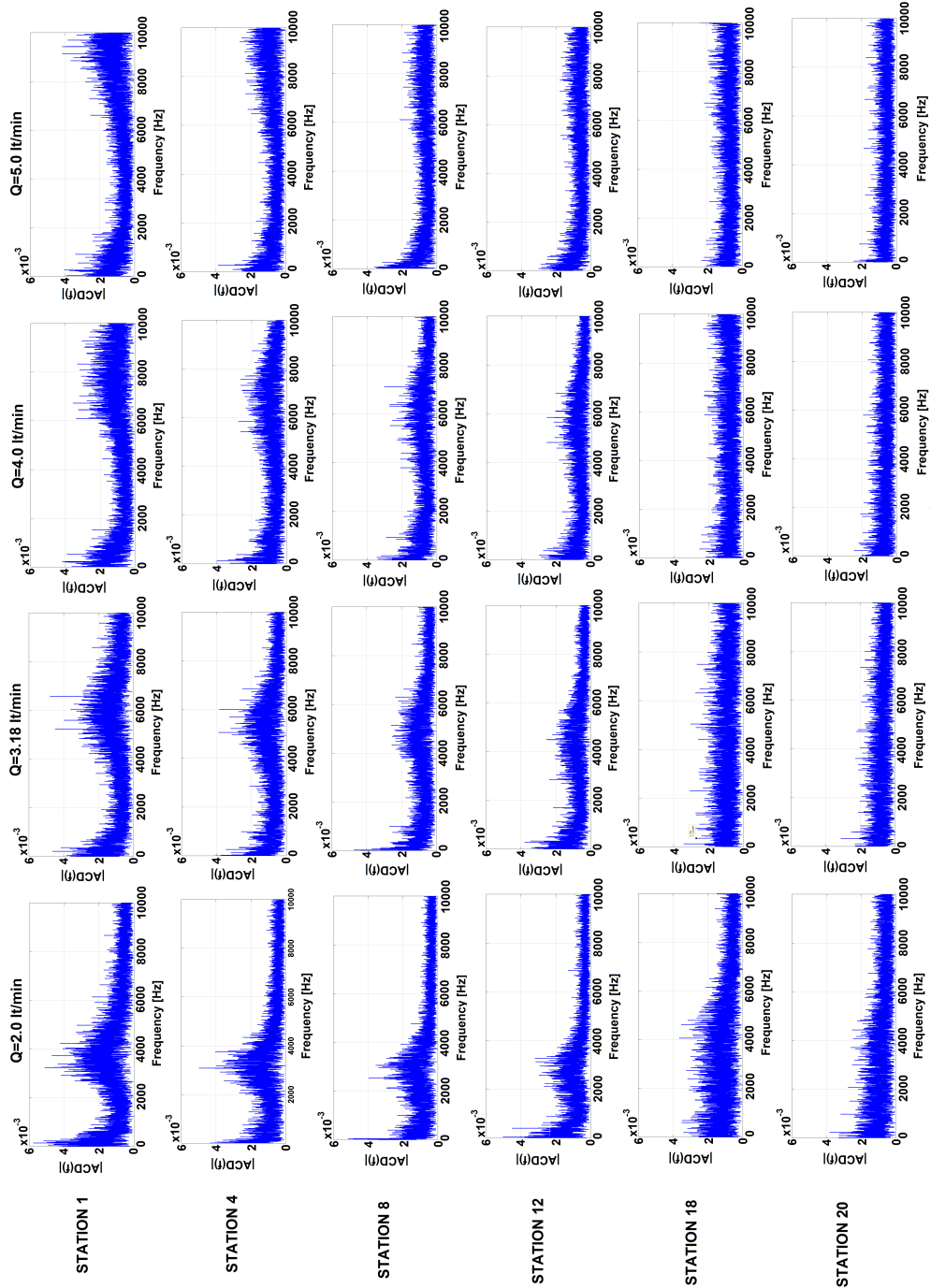


Figure 2.31: Frequency spectrum of the air core diameter at designated stations.

Q=3.18 lt/min operating point

At Station 1, a dominant low frequency range is identified between 58-620 Hz and a dominant high frequency range is identified between 4500-6700 Hz. At Station 4, a dominant low frequency range is identified between 28-332 Hz and a dominant high frequency range is identified between 5000-6000 Hz. The amplitude of the low frequency oscillations are similar to the high frequency ones for Station 1 and Station 4. As one moved from head end to nozzle entrance, at Station 8 and Station 12, similar dominant low frequency and high frequency ranges are identified but the amplitude of the high frequency oscillations decrease approximately half of the amplitude of the low frequency oscillations. At Station 18 several dominant frequencies are identified between 0-8000 Hz with comparable amplitude. At the exit of the atomizer, a dominant low frequency peak at 332 Hz is identified.

Q=4.0 lt/min operating point

At Station 1, a dominant low frequency range is identified between 32-680 Hz and a dominant high frequency range is identified between 6000-9000 Hz. At Station 4, a dominant low frequency range is identified between 28-390 Hz and a dominant high frequency range is identified between 5400-7700 Hz. The amplitude of the low frequency oscillations are similar to the high frequency ones for Station 1, whereas the amplitude of the high frequency oscillations are about half of the low frequency ones. As one moved from head end to nozzle entrance, at Station 8, similar dominant low frequency and high frequency ranges are identified but the amplitude of the high frequency oscillations are comparable to the low frequency ones. At Station 12 a dominant low frequency range is identified between 36-518 Hz and a dominant high frequency range is identified between 4500-6800 Hz with the amplitude of high frequency ones are smaller than the low frequency ones. At Station 18 and at the exit of the atomizer, several dominant frequencies are identified between 0-9000 Hz with comparable amplitude.

Q=5.0 lt/min operating point

At Station 1, a dominant low frequency range is identified between 50-908 Hz and a dominant high frequency range is identified between 8000-10000 Hz. At Station

4, a dominant low frequency range is identified between 90-450 Hz and a dominant high frequency range is identified between 6500-10000 Hz. The amplitude of the low frequency oscillations are similar to the high frequency ones for Station 1, whereas the amplitude of the high frequency oscillations are about half of the low frequency ones. As one moved from head end to nozzle entrance, at Station 8 and Station 12, similar dominant low frequency and high frequency ranges are identified and the amplitude of the high frequency oscillations are about half of the low frequency ones. At Station 18 and at the exit of the atomizer several dominant frequencies are identified between 0-9000 Hz with comparable amplitude.

In this section the frequency domain representations of the air core diameter signal is investigated for different operating points of the atomizer. The frequency domain representation of the air core diameter reveals dominant low and high frequency ranges. The amplitude of the dominant low frequency peaks and dominant low frequency peaks are comparable at stations close to the head end of the atomizer. For constant water flow rate, the amplitude of the high frequency peaks decreases as one moves from head end of the atomizer to inlet of the atomizer, which shows that the high frequency phenomena is specific to locations close to the head end of the atomizer.

2.5.3.4 Mode Shapes of the Air Core Diameter

Proper Orthogonal Decomposition (POD), also known as the Karhunen-Loeve Decomposition, is an optimal procedure for extracting a basis for a modal decomposition from a set of observations of possibly correlated variables. Among all possible decompositions of a random field, the POD is the most efficient in the sense that for a given number of modes, the projection on the subspace used for modeling the random field will on average contain the most reconstruction information possible [75]. The basis extraction is defined in such a way that the first principal component has the largest possible reconstruction information content, and each succeeding component in turn has the highest reconstruction information possible under the constraint that it has to be orthogonal to the preceding components. The applications of the POD procedure are widespread in fields like fluid mechanics [76],[77],[78] image processing [79] and structural dynamics [80].

A complete review of POD theory can be found in Liang et.al. [81] and numerous other references and is not given here in detail. Rather, the priority is given on Singular Value Decomposition (SVD), which is an extension of the eigenvalue decomposition for the case of non-square matrices. POD can be realized using the SVD, which uses the singular value decomposition to find the basis vectors satisfying the POD requirement in the sample space [81]. The SVD of the matrix A can be written in the form;

$$A = U\Sigma V^T \quad (2.3)$$

where U is an $N \times N$ orthogonal matrix, V is an $m \times m$ orthogonal matrix and Σ is an $N \times m$ matrix with all elements zero except along the diagonal. The diagonal elements of Σ consist of $r = \min(N, m)$ positive numbers, σ , which are arranged in decreasing order. The σ 's are unique and called the singular values of matrix and these values quantify the importance of the basis vectors in capturing the information present in the data [80].

An optimal order k approximation to matrix A can be calculated as follows

$$A_k = U \Sigma_k V^T \quad (2.4)$$

where for any $k < r$ the matrix Σ_k obtained by setting $\sigma_{k+1} = \sigma_{k+2} = \dots = \sigma_r = 0$. The approximation given with Equation 2.4 is optimal since there is no other order k matrix present closer to matrix A in the Frobenius norm [82].

The ratio of the reconstructive information of the snapshots captured by the first k POD basis vectors to the total reconstruction can be defined by Equation 3.3. The reconstruction ratio gives an indication of the magnitude of the missing information in the approximations, based on the property of the Frobenius norm of matrix A .

$$\varepsilon_{POD}(k) = \frac{\sum_{i=1}^k \sigma_i^2(A)}{\sum_{i=1}^r \sigma_i^2(A)} \quad (2.5)$$

where k is the order number of the approximation, r is the maximum number of singular values and σ_i is the i^{th} singular value [77].

Sirovich introduced [77] an intrinsic dimension (d_{kl}) of the space predicted by the POD procedure. He defined the intrinsic dimension as the number of actual modes required so that the captured reconstructive information is at least 90% of the total and that no neglected mode contains more than 1% of the reconstructive information contained in the principle orthogonal mode.

Later Marquez et.al. [80] used the reconstruction ratio to determine the truncation degree of the selected POD basis vectors. They commented that order of the POD approximation has to be determined such that $\varepsilon = 0.99$.

The POD is particularly useful in extracting the standing wave components [83]. In the present study we use the POD as a post-processing tool to extract modes, that upon summation, approximate the behavior of the air core diameter from unsteady air core diameter data. The air core diameter is calculated at twenty different stations along the axis of the atomizer for each operating point in the previous section. The calculations are performed using 10000 images, that are captured by the high speed camera at a frame rate of 20 kHz. The air core diameter data is arranged in a matrix A_{Nm} ($N=10000$ and $m=20$) such that the element A_{ij} is the air core diameter calculated at

j^{th} station at the i^{th} time instant.

The air core diameter data is shown in Figure 2.32 as three dimensional surfaces for each operating point.

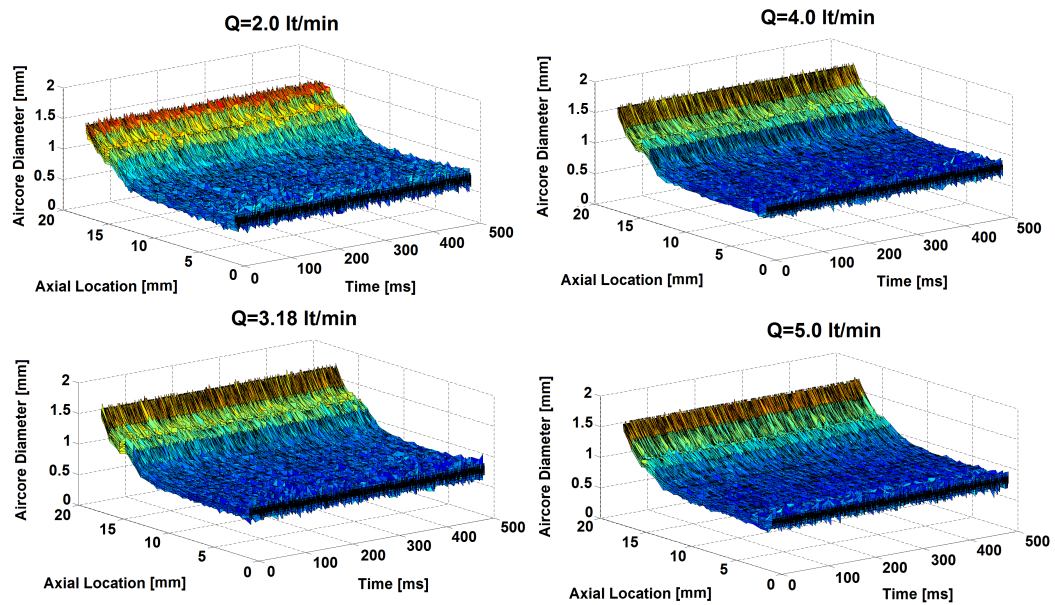


Figure 2.32: Air core diameter data as a three dimensional surface for different operating points.

The singular value decomposition of the matrix A is calculated using a MATLAB program and U , V and Σ matrices are obtained. The order r approximation to matrix A can then be calculated using Equation 3.4. The singular values, which are the diagonal elements of the Σ matrix, are plotted in logarithmic scale in Figure 2.33. The first singular values are 372, 405, 414 and 416 for $Q=2.0$ lt/min, $Q=3.18$ lt/min, $Q=4.0$ lt/min and $Q=5.0$ lt/min operating points, respectively. The second singular values are about two order of magnitude smaller than the first singular values for each operating point, which shows the dominant effect of the first singular value on reconstructing the air core diameter data.

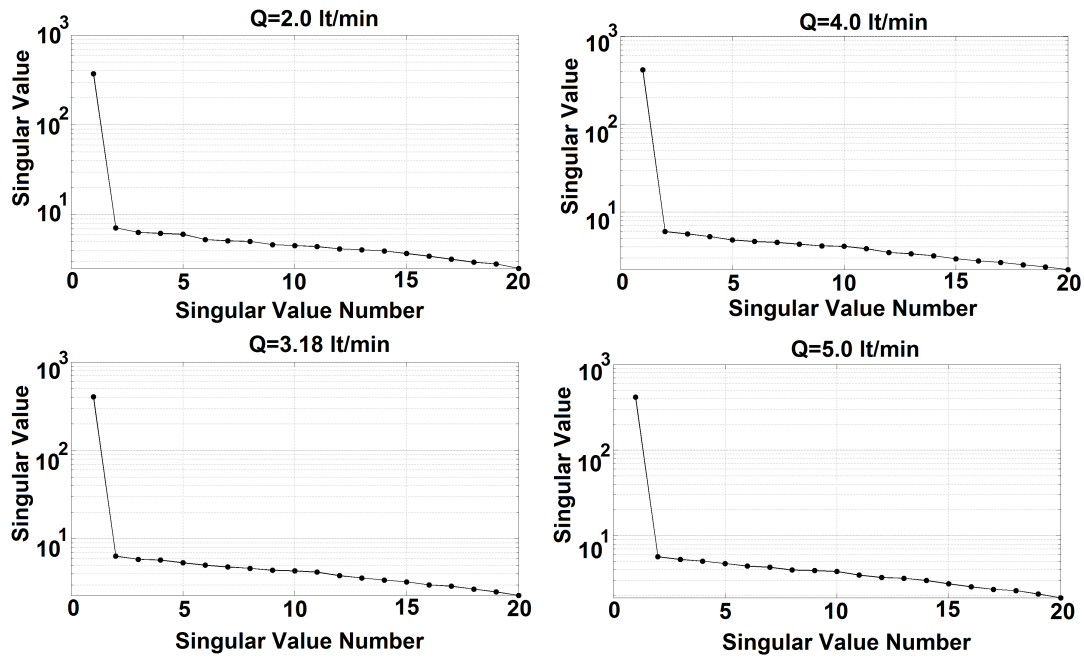


Figure 2.33: Singular values.

The percent reconstruction ratio values for the $Q=2.0$ lt/min operating point, which are calculated using Equation 3.5, are given in Table 2.6. The reconstructive information of the first mode is the highest and contain much of the information regarding the air core diameter data. The remaining modes has some information, but summing up first 10 modes to have an order 10 approximation to air core diameter data increases the percent reconstructive ratio only from 99.70 to 99.90.

Table 2.6: The reconstruction ratio for POD approximations.

Order of the POD approximation	Percent reconstruction ratio (% ϵ)
1	99.70
5	99.82
10	99.90
15	99.96
20	100

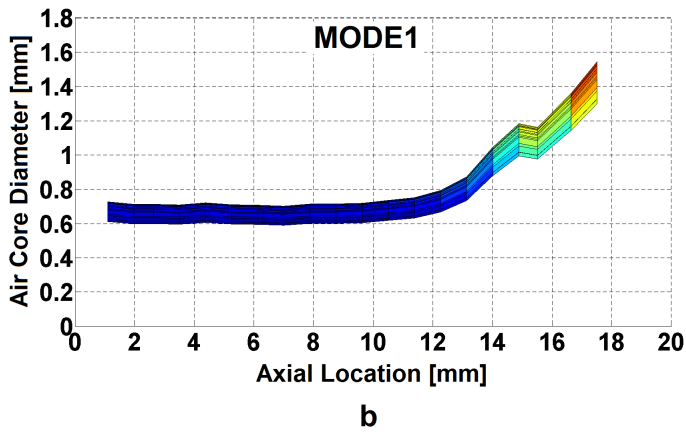
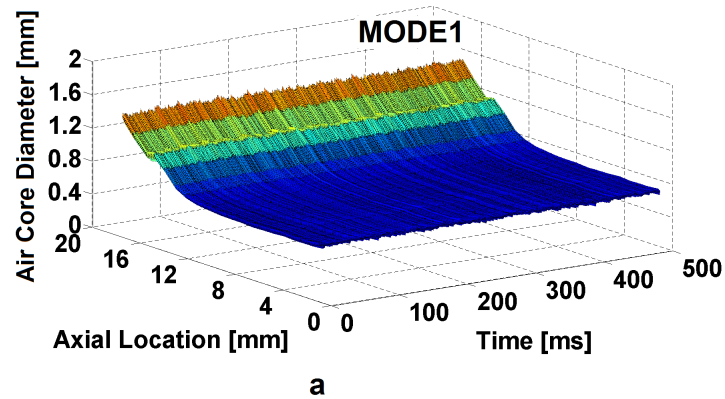


Figure 2.34: First mode shape of the air core ($Q=2.0$ lt/min) , isometric view (a) and side view (b) .

Order 1 approximation to air core diameter data, which is also the first mode shape of the air core, is given in Figure 2.34-a for $Q=2.0$ lt/min operating point. For the sake of clarity the side view of the surface representing the mode shape is also shown in Figure 2.34-b. The side view shows the shape of the first mode shape for a total of 10000 time instants.

The first four mode shapes of the air core diameter are given in Figure 2.35 for $Q=2.0$ lt/min operating condition. The first mode shape has the highest reconstructive content and gives the shape of the air core along the axis of the atomizer. The thickness of the first mode shape is almost constant all along the atomizer and does not contain any node points (locations where the thickness of the mode shape fall below 0.01 mm), which may be an indication of a traveling wave along the air core. As the order of the

mode shape increases node points come on to screen and their number increases. The second mode shape contains one node point at Station 5. For the second mode shape, the constant thickness segment between Station 8 and Station 13 may also be an indication of a traveling wave whose amplitude increases as one approaches to the nozzle part (expansion section at mid nozzle). The second mode shape in that sense is a result of combination of standing and stationary waves. The third mode shape contains one node point at Station 8 and an almost constant thickness segment between Station 9 and Station 13 mm. The thickness of the mode shape decreases at Station 15 and has a peak at station 17 where an expansion is identified. The fourth mode shape contains a total of four node points at Stations 5, 10, 12 and 16.

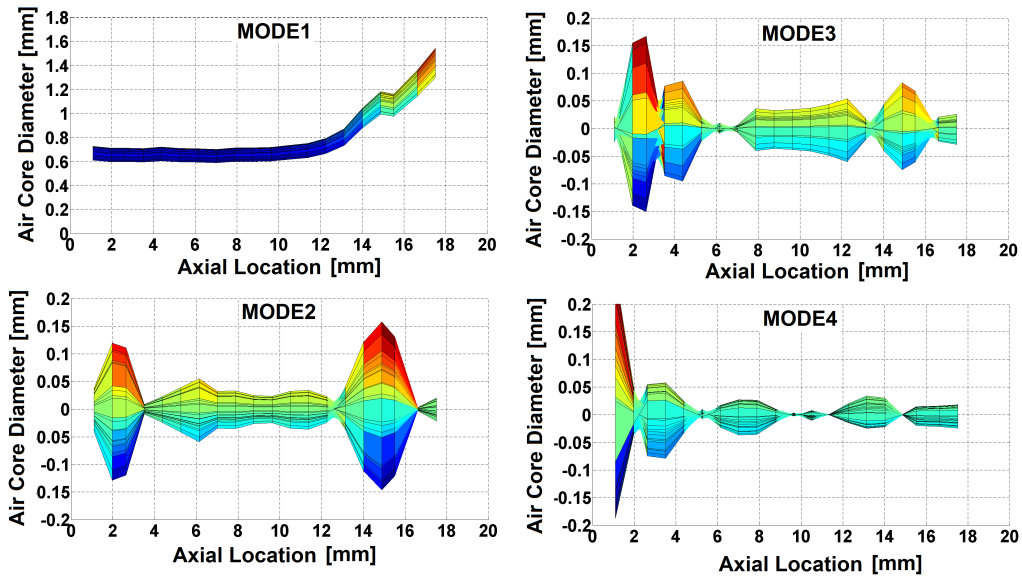


Figure 2.35: First four mode shapes, $Q=2.0$ lt/min.

The first four mode shapes of the air core diameter are given in Figure 2.36 for $Q=3.18$ lt/min operating condition. Increasing the water flow rate from 2.0 lt/min to 3.18 lt/min does not affect the first four mode shapes significantly.

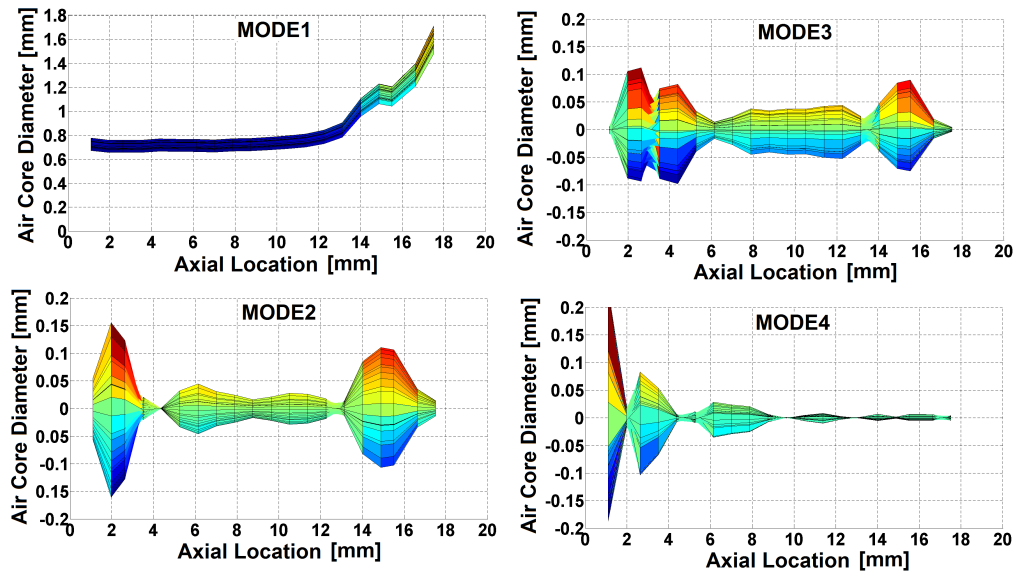


Figure 2.36: First four mode shapes, $Q=3.18$ lt/min.

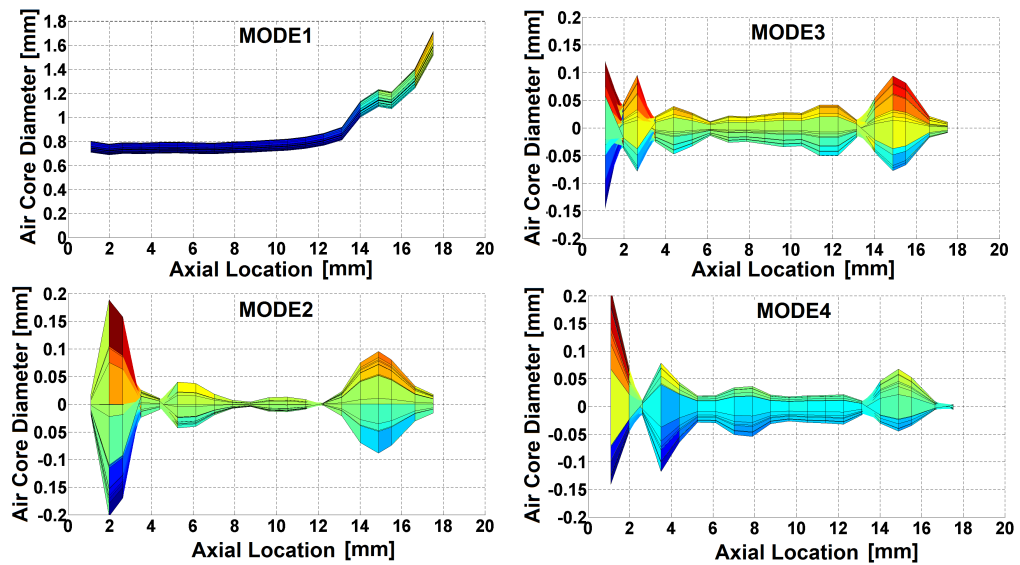


Figure 2.37: First four mode shapes, $Q=4.0$ lt/min.

The first four mode shapes of the air core diameter are given in Figure 2.37 and Figure 2.38 for $Q=4.0$ lt/min and $Q=5.0$ lt/min operating conditions, respectively. Although the first and third mode shapes does not affected by the increase in the water flow rate,

the second mode shape changes significantly when compared to the second mode shapes of the low flow rate operating points.

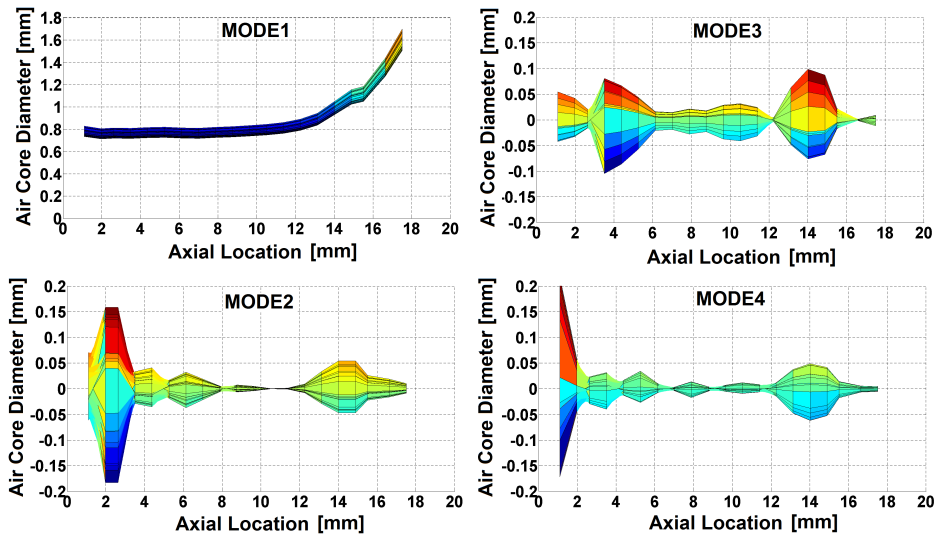


Figure 2.38: First four mode shapes, $Q=5.0$ lt/min.

The higher order modes shapes are given in Appendix C for all operating conditions. As the order of the mode shape increases the number of node points increases, the amplitude decreases and constant amplitude portions in the mode shapes vanish. The summation of twenty modes shapes gives the original air core diameter data for each operating condition.

In this section we identify the mode shapes of the air core diameter using POD based analysis. We calculate the first mode shape, which possesses the largest reconstruction information content and the higher order components, which has the highest reconstruction information possible under the constraint that they has to be orthogonal to the proceeding components. Each mode shape give a possible oscillation mode of the air core, which is difficult to deduce from the original data itself.

2.6 Experimental Results-Characterization of the Hollow Cone Spray

The presence of the air core inside the pressure swirl atomizers results in hollow cone sprays. In hollow cone sprays, most of the droplets are concentrated at the outer edge of the spray. In this section, the hollow cone spray, which formed by the pressure swirl atomizer, is characterized for flow rates of $Q=3.18$ lt/min, $Q=4.0$ lt/min and $Q=5.0$ lt/min. The hollow cone spray for different flow rates of water are shown in Figure 2.39.

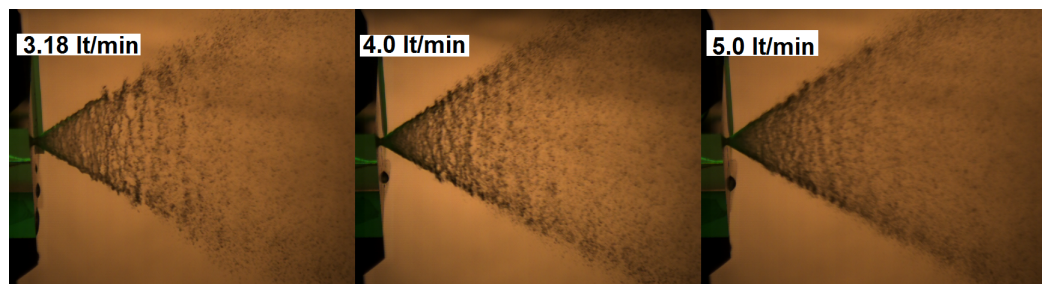


Figure 2.39: Hollow cone spray for different flow rates.

The spray cone angle of the resulting sprays are found using the developed image processing tool, whose details were given in the previous section. The microscopic properties of the hollow cone sprays are attained using the PDPA.

2.6.1 Spray Cone Angle

The schematic for the spray cone angle calculation is given in Figure 2.40. In order to calculate the spray cone angle, the distance between the edges of the spray (Y) is measured at a distance (X) from the exit of the atomizer.

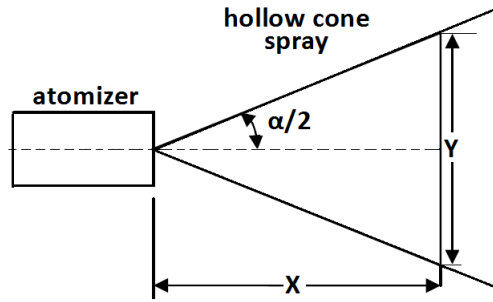


Figure 2.40: Schematic for the spray cone angle calculation.

The distance between the edges of the spray is measured using the captured images and the developed image processing tool. The sample image showing the edges of the spray are given in Figure 2.41.

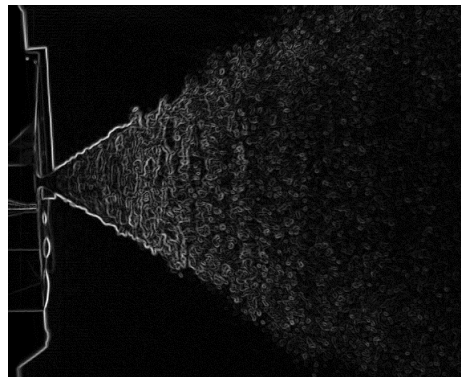


Figure 2.41: Edges of the spray (Q=3.18 lt/min).

Once the distance between the edges (Y) of the spray is obtained, the spray cone angle is calculated using the following equation;

$$\alpha = 2 \tan^{-1} \left(\frac{Y/2}{X} \right) \quad (2.6)$$

The spray cone angle is calculated with the explained methodology for each image, then the mean spray cone angle is calculated by taking the arithmetic average of the calculated spray cone angle values. The mean cone angles are calculated as 64.4

degree, 64.1 degree and 65 degree for water flow rates of 3.18 lt/min, 4.0 lt/min and 5.0 lt/min, respectively.

The measured spray cone angle in the present study differs only 5 degrees from the findings of Dash et. al. [26].

2.6.2 Microscopic Properties of the Hollow Cone Spray

The microscopic properties of the spray are measured with the two-component PDPA system. The measurements are performed for $Q=2.0$ lt/min, $Q=3.18$ lt/min and $Q=4.0$ lt/min operating points. The coordinate system and the measurement locations are shown in Figure 2.42 along with the hollow cone spray. The origin of the coordinate frame ($x=0$, $y=0$) is at the center of the atomizer exit. The first axial measurement location is 16 mm downstream of the atomizer exit. There are ten axial measurement locations and the distance between each location is 5 mm. At each axial location, y locations are also traversed at 3 mm intervals and the spray properties are measured at 115 different measurement locations for three different operating points.

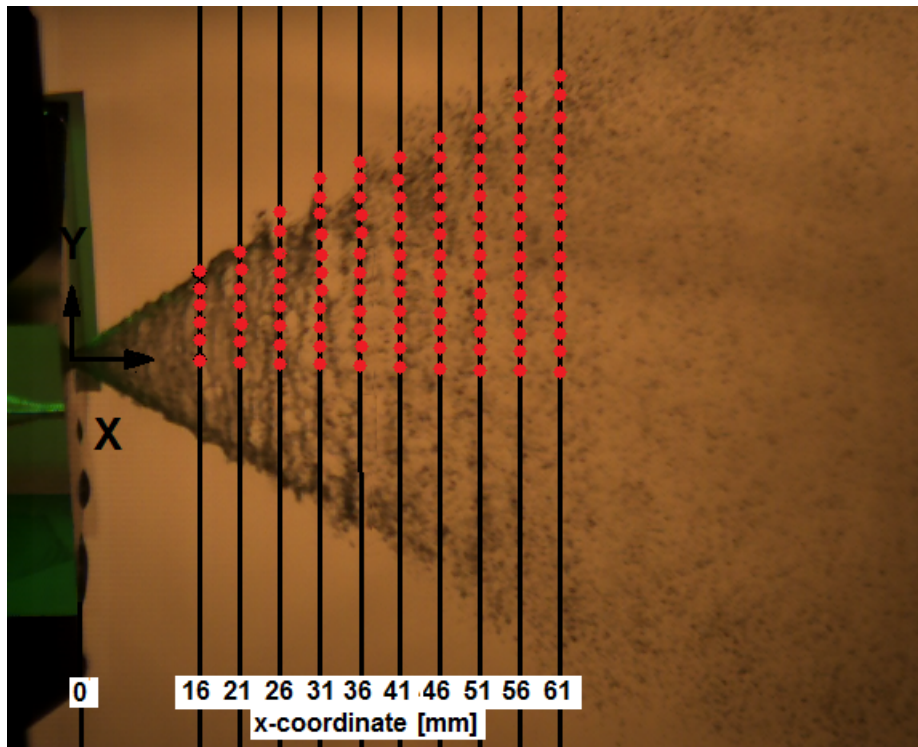


Figure 2.42: Coordinate system and the measurement locations.

At each measurement point, the properties of the water droplets passing through the probe volume are measured with the PDPA system. The diameter histograms at measurement locations ($x=16$ mm, $y=0$ mm) and ($x=16$ mm, $y=12$ mm) are given together in Figure 2.43.

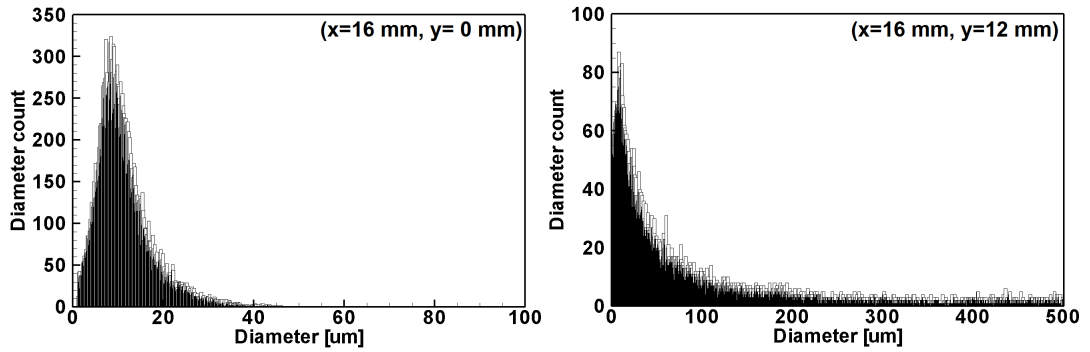


Figure 2.43: Diameter histograms at designated locations.

The histograms given in Figure 2.43 gives the diameter of each water droplet passing through the probe volume. In spray analysis, it is customary to define the droplet diameter at a measurement location with their mean. The basic definition for the mean droplet size is the number mean ($D[1,0]$) defined as follows

$$D[1, 0] = \frac{\sum d}{n} \quad (2.7)$$

where d is the diameter of each water droplet and n is the number of droplets. The nomenclature $D[1,0]$ comes from the fact that the numerator terms are to the diameter power of one (d^1) and there are no diameter terms on the denominator (d^0).

The mean definitions like the Sauter mean definition, is frequently used in spray analysis. Sauter mean diameter definition introduces the concept of moment means and it does not require the number of particles information to calculate the mean diameter. The Sauter mean diameter is defined as follows;

$$D[3, 2] = \frac{\sum d^3}{\sum d^2} \quad (2.8)$$

where $D(3,2)$ is the Sauter mean diameter (SMD) and d is the diameter of each water droplet.

The Sauter mean diameters calculated at location $(x=16, y=0)$ and location $(x=16, y=12)$

are 24 and 331, respectively. At location $(x=16,y=0)$, which is at the x axis, the small water droplets are frequent and the Sauter mean diameter is small. At location $(x=16,y=12)$, which is close to the liquid jet, the large diameters are frequent and the Sauter mean diameter is large.

The Sauter mean diameter distributions are shown together in Figure 2.44 as contour plots for water flow rates of 3.18 lt/min, 4.00 lt/min and 5.00 lt/min.

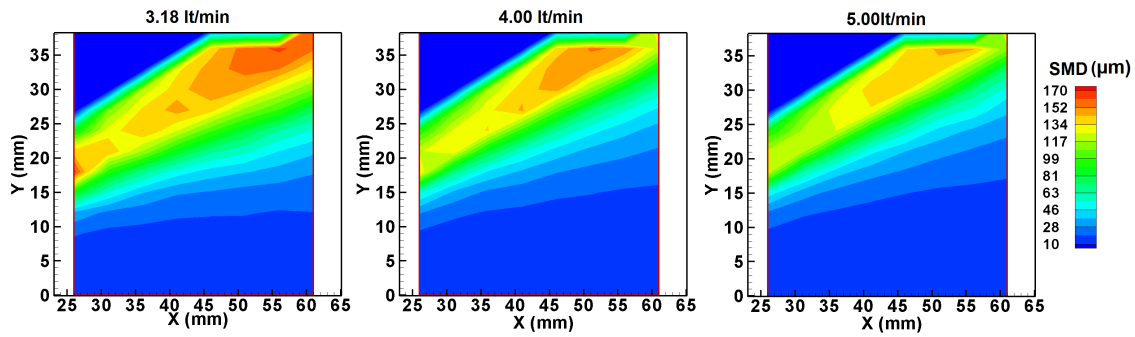


Figure 2.44: Contour plots of Sauter mean diameter for different flow rates.

The SMD contours reveals that at each axial location the SMD increases with the y-coordinate and it has a maximum value at the liquid jet and then decreases again away from the liquid jet for each flow rate. This is the case for almost all hollow cone sprays at quiescent air. The small water droplets concentrate on regions near the x-axis and the bigger droplets follows the liquid jet.

The x-velocity (V_x) and y-velocity (V_y) histograms at measurement locations $(x=16$ mm, $y=0$ mm) and $(x=16$ mm, $y=12$ mm) are given together in Figure 2.45.

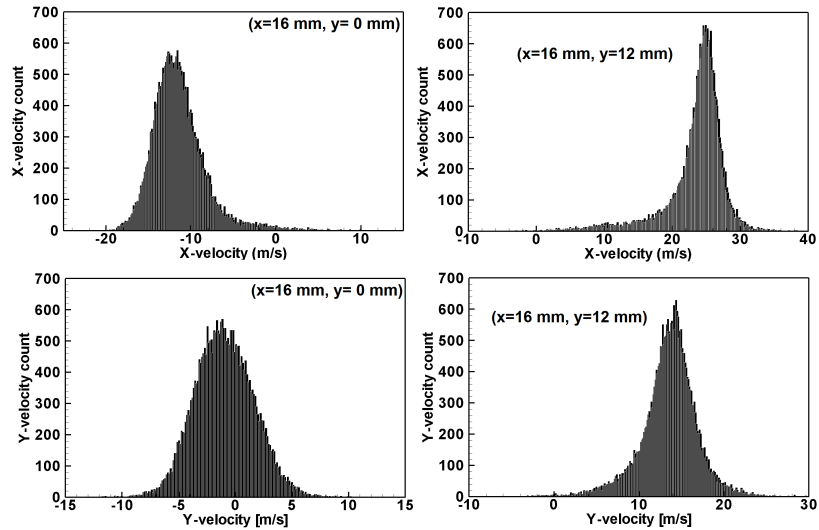


Figure 2.45: Velocity histograms at designated locations.

The mean V_x is measured as -11.3 mm at location $(x=16 \text{ mm}, y=0 \text{ mm})$ and it is measured as 23.36 at location $(x=16, y=12)$. The mean V_y is measured as -6.98 mm at location $(x=16 \text{ mm}, y=0 \text{ mm})$ and it is measured as 13.56 at location $(x=16, y=12)$. The mean velocity at the same axial location changes sign as the y -coordinate increases. The SMD values also change considerably depending on the y -coordinate along the same axial location.

The properties of the hollow cone spray are investigated for different droplet size classes, which gives a better understanding of the flow field within the spray. The first size class involves the water droplets whose diameter is smaller than $10 \mu\text{m}$ and the second size class the involves the water droplets whose diameter is greater than $100 \mu\text{m}$. The water droplets with diameter smaller than $10 \mu\text{m}$ generally follows the air flow.

The mean and RMS x -velocity contours for droplets, whose diameter is smaller than $10 \mu\text{m}$, are shown in Figure 2.46 for three different water flow rates. The streamlines shown in the figure are originated from a line at $x=16 \text{ mm}$.

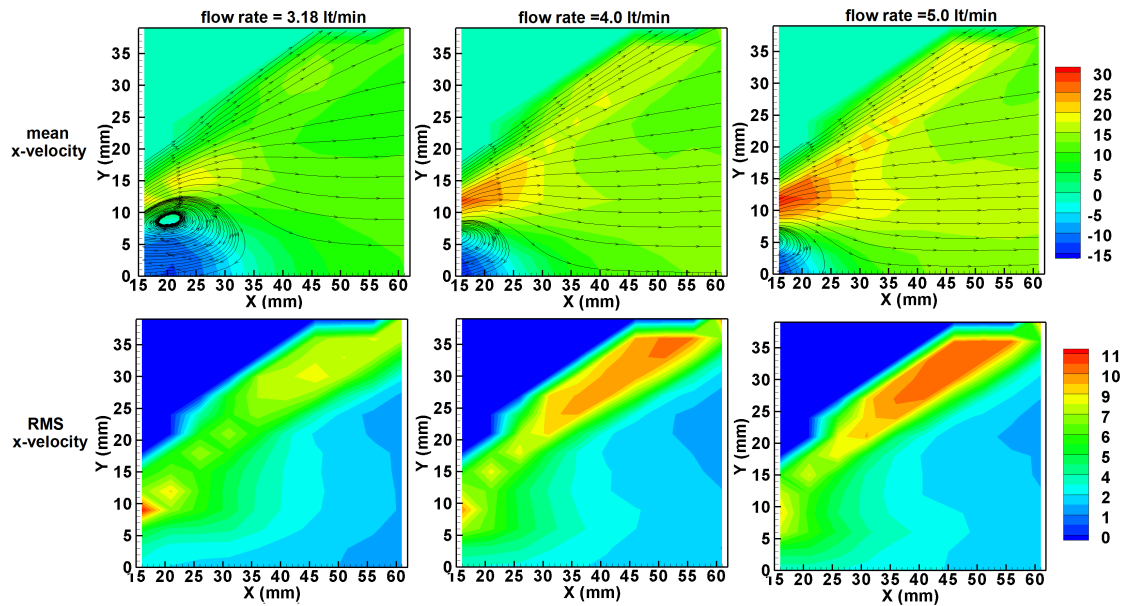


Figure 2.46: Mean and RMS x-velocity contours [m/s] and streamlines originated from a line at $x=16$ ($d < 10 \mu\text{m}$).

The measurements reveals a vortex close to the atomizer outlet near the spray axis for all three water flow rates. As the flow rate increases the mean velocity of the droplets increases and the identified vortex travels down to atomizers exit. At locations close to the x- axis, small droplets ($d < 10 \mu\text{m}$) are present and these small droplets move with the air flow in those locations. The mean velocity of the water droplets increases with the water flow rate. For each operating condition, the mean velocity of the droplets at the spray boundary decreases with increasing x-coordinate.

The RMS x-velocity contours shows that the x-velocity of the droplets, whose diameter smaller than $10 \mu\text{m}$, fluctuates. The fluctuation is maximum near the vortex region for $Q=3.18$ lt/min operating point and it is maximum at the spray boundaries for $Q=4.0$ lt/min and $Q=5.0$ lt/min operating points.

The mean and RMS x-velocity contours for droplets, whose diameter is greater than $100 \mu\text{m}$, are shown in Figure 2.47 for three different water flow rates. The streamlines shown in the figure are originated from a line at $x=16$ mm.

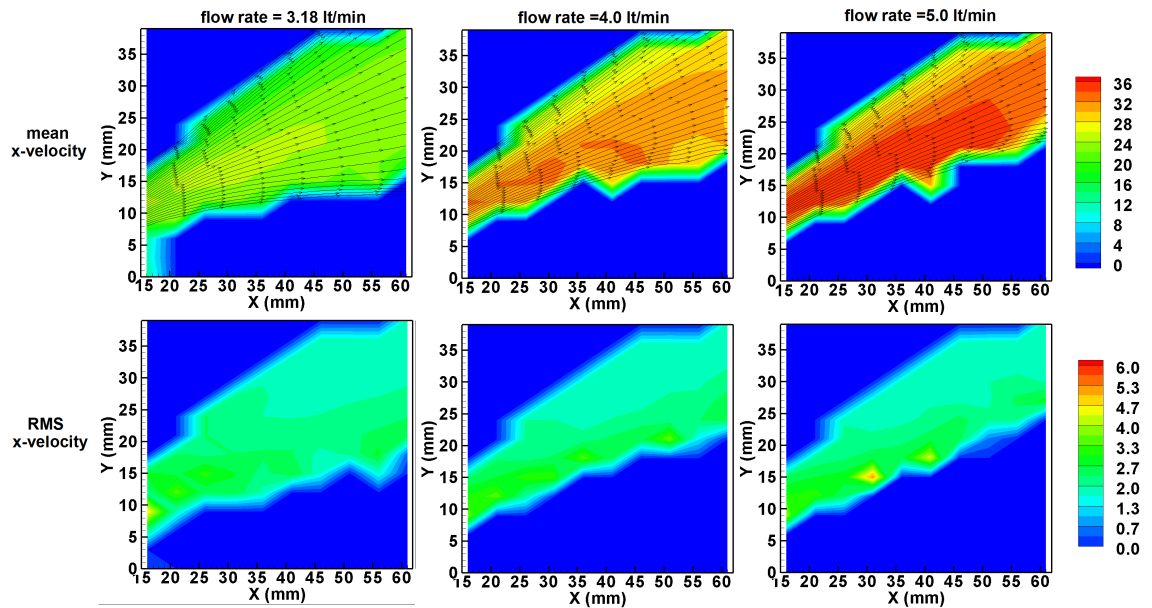


Figure 2.47: Mean and RMS x-velocity contours [m/s] and streamlines originated from a line at $x=16$ ($d>100\mu\text{m}$).

The water droplets with diameter greater than $100\mu\text{m}$ follows the spray boundaries. The mean x-velocity is zero at small y-locations since there are no droplets with diameter greater than $100\mu\text{m}$ at those locations. However for $Q=3.18$ lt/min operating point, water droplets with diameter greater than $100\mu\text{m}$ is measured at $x=16$ close to the axis. The mean x-velocity of the droplets with diameter greater than $100\mu\text{m}$ increases as the flow rate of the atomizer increases. It is apparent that as the water flow rate increases the droplets, whose diameter greater than $100\mu\text{m}$ tend to follow straight paths and the mean x-velocity of the water droplets increases with the water flow rate.

The mean and RMS y-velocity contours for droplets, whose diameter is smaller than $10\mu\text{m}$, are shown in Figure 2.48 and the mean and RMS y-velocity contours for droplets, whose diameter is greater than $100\mu\text{m}$, are shown in Figure 2.49 for three different water flow rates. The streamlines shown in the figure are originated from a line at $x=16$ mm.

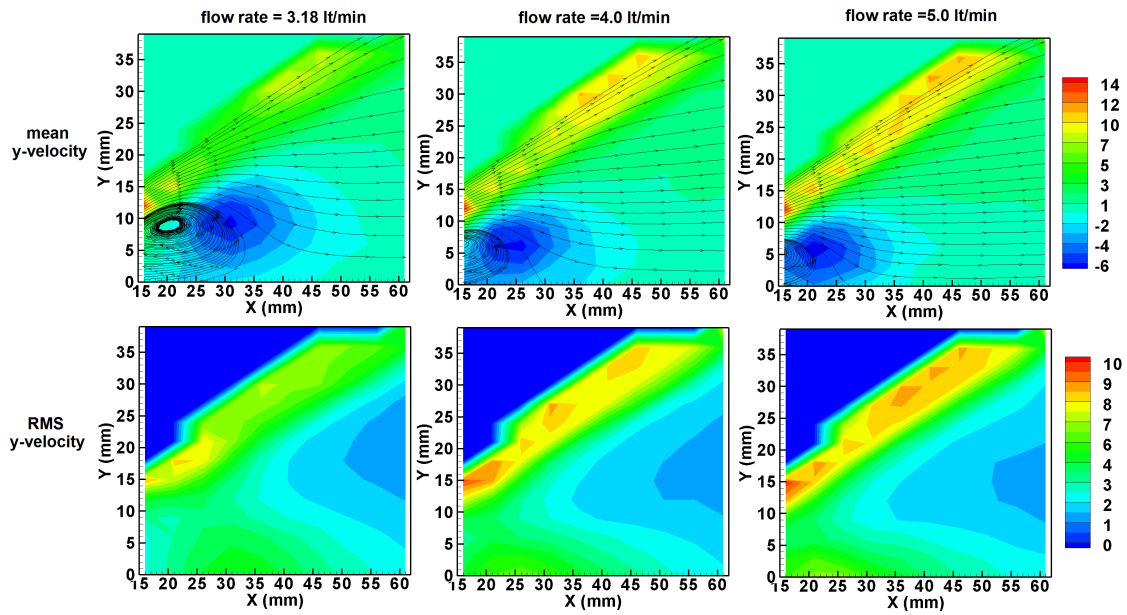


Figure 2.48: Mean and RMS y-velocity contours [m/s] and streamlines originated from a line at $x=16$ ($d < 10\mu\text{m}$).

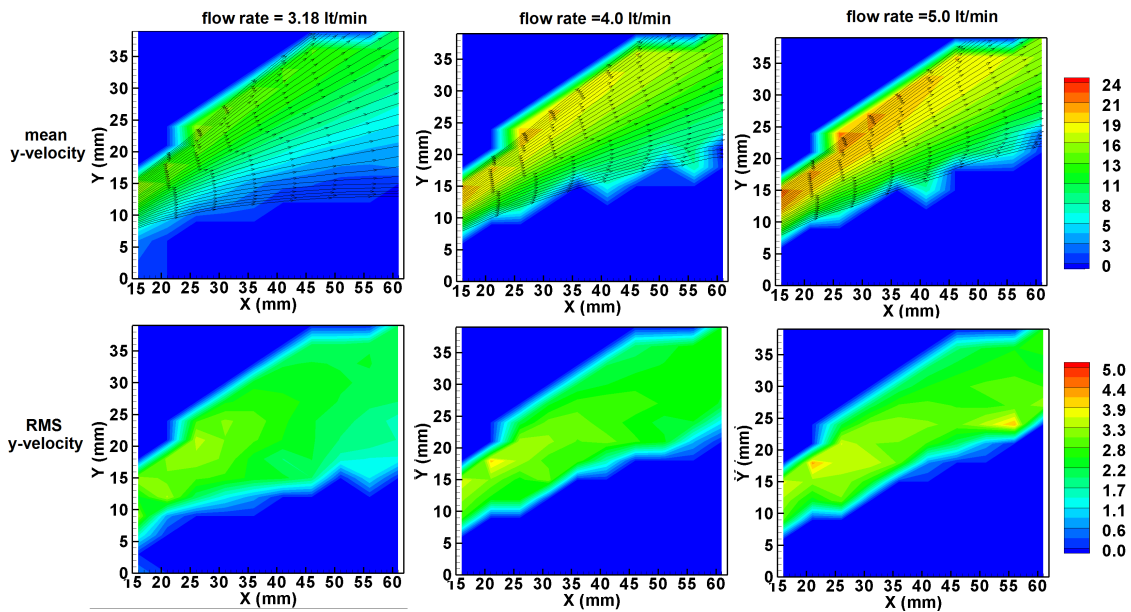


Figure 2.49: Mean and RMS y-velocity contours [m/s] and streamlines originated from a line at $x=16$ ($d > 100\mu\text{m}$).

Mean y-velocity contours of water droplets, whose diameter is smaller than $100\mu\text{m}$,

reveals water droplets with negative y-velocities close to the vortex region. The minimum mean y-velocity is -6.3 m/s, -6.3 m/s and -7.0 m/s for Q=3.18 lt/min, Q=4.0 lt/min and Q=5.0 lt/min operating points, respectively. The maximum y-velocity of the water droplets, whose diameter smaller than 10 μm , is at x=16 mm for all operating points. The maximum mean y-velocity is 12.8 m/s, 13.6 m/s and 13.7 m/s for Q=3.18 lt/min, Q=4.0 lt/min and Q=5.0 lt/min operating points, respectively. The fluctuations in the mean y-velocity of droplets, whose diameter is smaller than 10 μm , are maximum near the spray boundaries for all operating points.

Mean y-velocity of water droplets, whose diameter is greater than 100 μm , increases with the water flow rate. The maximum mean y-velocity of water droplets, whose diameter is greater than 100 μm , is 16.3 m/s, 20.3 m/s and 22.1 m/s for Q=3.18 lt/min, Q=4.0 lt/min and Q=5.0 lt/min operating points, respectively. The fluctuations in the y-velocity is maximum at the outer spray boundaries for all operating points of the atomizer.

CHAPTER 3

NUMERICAL INVESTIGATION

3.1 Introduction

In this chapter the pressure swirl atomizer, which was investigated using experimental methods in the previous chapter, will be investigated using computational fluid dynamic tools. The unsteady two-phase flow through the pressure swirl atomizer is investigated using commercially available ANSYS-FLUENT software in order to have a better understanding of the flow field. The problem is complicated with the presence of the air core inside atomizer, which calls for the usage of interface kinematic algorithms. The present chapter is arranged in four sections. In the first section (Numerical Methodology), the governing differential equations and the numerical solution methodology are given. In the second section the computational domain sensitivity study and grid sensitivity study are presented. The results of the axis-symmetric swirl (2D-AXS) numerical simulations are given in the third section and the results of the three dimensional numerical simulations are given in the fourth section.

3.2 Numerical Methodology

In general, the flow through the pressure swirl atomizers are numerically studied by using finite volume method ([20], [21], [25], [26], [34], [36], [38]) by adapting the necessary algorithms to capture or track the gas/liquid interface near the air core. The numerical studies implementing methods such as finite difference method [23] and boundary element method [35] exist but their usage is limited.

The challenging issue in numerical analysis of pressure swirl atomizer flows is the presence of the air core inside the atomizer. The flow inside the atomizer can be treated as a free surface flow where a well-defined interface is present between two immiscible fluids. The solution of the flow problem inside the pressure swirl atomizer calls out numerical solution methods of incompressible Navier-Stokes equations with interfaces. A numerical solution algorithm to solve the Navier-Stokes equations together with a solution algorithm, which describes the shape and location of the interface and evolves them with time, is required to handle the flow problem. In addition, the physical processes, which are specific to and localized at fluid interfaces, need to be modeled.

3.2.1 Governing Differential Equations

Free surface flows, in which a well-defined interface with two immiscible fluids are present, can be described by one set of governing equations with the assumption that fluids move with the local center of mass. Unsteady, laminar, incompressible Navier-Stokes equations, which are solved throughout the domain and shared by all the phases can be written as;

$$\frac{\partial \rho}{\partial t} + \nabla \cdot (\rho \mathbf{V}) = 0 \quad (3.1)$$

$$\frac{\partial}{\partial t}(\rho \vec{V}) + \nabla \cdot (\rho \vec{V} \vec{V}) = -\nabla(P) + \nabla \cdot [\mu(\nabla \vec{V} + \nabla \vec{V}^T)] + \rho \vec{g} + \vec{F} \quad (3.2)$$

The momentum equation given in Equation 3.2 contains a singular interface term (F) in order to take into account the surface tension which acts only at the interface. The momentum equation is then valid for the whole computational domain including the interfaces where the material properties change abruptly.

In Equations 3.1 and 3.2 velocity is treated as a mass-averaged variable and defined as follows;

$$v = \frac{\alpha_a \rho_a v_a + \alpha_w \rho_w v_w}{\rho} \quad (3.3)$$

where α is the volume fraction, ρ is the density and v is the velocity. The subscript "a" denotes air and subscript "w" denotes water. The density and viscosity are defined as follows;

$$\rho = \alpha_a \rho_a + (1 - \alpha_a) \rho_w \quad (3.4)$$

$$\mu = \alpha_a \mu_a + (1 - \alpha_a) \mu_w \quad (3.5)$$

where α_w and α_a are the volume fractions of water and air respectively, which are linked with the following constraint;

$$\alpha_a + \alpha_w = 1 \quad (3.6)$$

An additional equation is needed in order to locate and evolve the interface with time. The capturing of the interface between the air and water is governed by the advection equation as follows;

$$\frac{\partial}{\partial t}(\alpha_a \rho_a) + \nabla(\alpha_a \rho_a \vec{v}_a) = 0 \quad (3.7)$$

Where v_a is the velocity of air at the interface. The solution of Equation 3.7 does not give the exact position of the interface, rather, it gives the boundaries of a transition region where $0 < \alpha_a < 1$. In capturing methods, the knowledge of volume fraction allows one set of model equations to apply everywhere in the domain. Away from the interface the equations reduce to ones for water or air alone, and within the interface they contain approximate discrete delta functions for interfacial terms.

3.2.2 Solution Methodology

In the present study, the governing equations for two phase flow are solved using ANSYS-FLUENT commercial software package. The physical domain is discretized using the finite volumes whose shape depends on the dimensions of the problem. Finite volume formulation is used for the solution of the discretized governing equations, such that the integral conservation laws are enforced in each of the control volumes defined by the computational grid.

Unsteady, laminar, Navier-Stokes equations are solved for incompressible phases using the pressure based coupled algorithm, which solves a coupled system of momentum and pressure based continuity equations. The pressure based coupled algorithm of ANSYS-FLUENT employs the projection method to solve the governing equations. In the projection method, a pressure correction equation, which is derived from the continuity and momentum equations, is solved in order to obtain a continuous velocity field. The coupled nonlinear equations are solved iteratively until the solution converges. The iterative time advancement scheme of ANSYS-FLUENT is used to solve the unsteady flow. In the iterative time advancement scheme, all the equations are solved iteratively for a given time step until the convergence criteria are met. Therefore, in order to advance the solution for one time step, it is necessary to perform a number of outer iterations. The number of outer iterations performed in the present study is kept constant at 20 for all performed numerical simulations.

An overview of the iterative time advancement scheme with pressure based coupled algorithm is given in Figure 3.1

The transport equations are first converted to discretized equations and these equations are solved for each cell and the solution variables are stored at the cell centers. A linearized set of equations are obtained for each cell and these equations are solved using a Gauss-Seidel linear equation solver in conjunction with an algebraic multi-grid solver. Second order upwind scheme was used for the solution of momentum equations in the present study . A first order implicit time integration was used for the solution of the momentum and pressure based continuity equations.

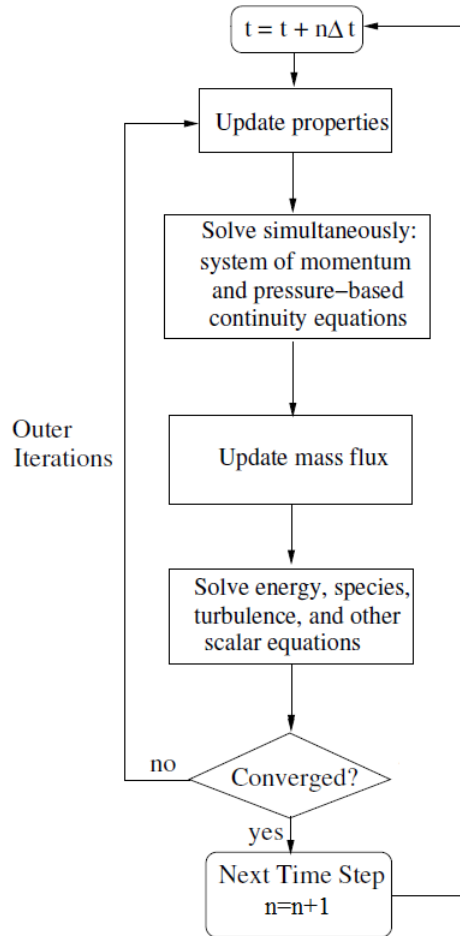


Figure 3.1: Overview of iterative time advancement scheme.

3.2.2.1 Volume of Fluid Method

The Volume of Fluid (VOF) method is the most widely known volume tracking method. The method is attributed to the work of Hirt and Nichols [84] and the usage of VOF methods in solving free surface flows is widespread. The VOF formulation in ANSYS-FLUENT is generally used to compute a time dependent solution where two or more immiscible liquids are present. For two phase flows one additional flow variable is added to the solution algorithm. The additional variable is the volume fraction of one liquid and the volume fraction of the remaining fluid is calculated from the fact that the sum of volume fractions add to unity (Equation 3.6).

The explicit scheme is used for the time discretization and the standard finite differ-

ence interpolation schemes are applied to the volume fraction values that computed at the previous time step as follows;

$$\frac{\alpha_a^{n+1}\rho_a^{n+1} - \alpha_a^n\rho_a^n}{\Delta t} + \sum_f (\rho_a)V_f^n \alpha_{a,f}^n = 0 \quad (3.8)$$

where $n+1$ is the current time step, n is the previous time step, $\alpha_{a,f}$ is the face value of the air volume fraction and U_f is the volume flux through the face based on normal velocity. High Resolution Interface Capturing (HRIC) scheme is used in order to interpolate the face fluxes [85].

Surface Tension

In order to take into account the surface tension along each phase, ANSYS-FLUENT uses Continuum Surface Force (CSF) model [86]. The addition of surface tension to the VOF calculation with the CSF model results in a source term in the momentum equation. Using the CSF model the source term in the momentum equation could be written as follows;

$$F = \sigma_{ij} \frac{\rho \kappa_i \nabla \alpha_i}{\frac{1}{2}(\rho_w + \rho_a)} \quad (3.9)$$

where σ_{ij} is the surface tension, ρ is the volume averaged density, κ_i is the surface curvature, α_i is the volume fraction, ρ_a and ρ_w are the density of air and water, respectively.

3.3 Computational Domain Geometry Sensitivity and Grid Sensitivity Study

In this section 2D-AXS numerical simulations are performed with different grids in order to investigate the effect of computational domain geometry and grid resolution on the simulation results. The flow properties are investigated using contour plots of flow variables, velocity distributions along the axial stations and probe points. The same stations, which was used to present the air core diameter values in the previous chapter, are used in this chapter to represent the results.

3.3.1 Computational Domain Geometry Sensitivity Study

3.3.1.1 Introduction

In 2D-AXS flow simulations, all three velocity components are considered in the solution of conservation of momentum equations in axial, radial and tangential directions with the assumption of zero velocity gradients in tangential direction. The solution domain for AXS flow simulations, which is extended from the nozzle exit in both horizontal and vertical directions, and one of the computational grids used in AXS flow simulations are shown together in Figure 3.2 along with the boundary conditions.

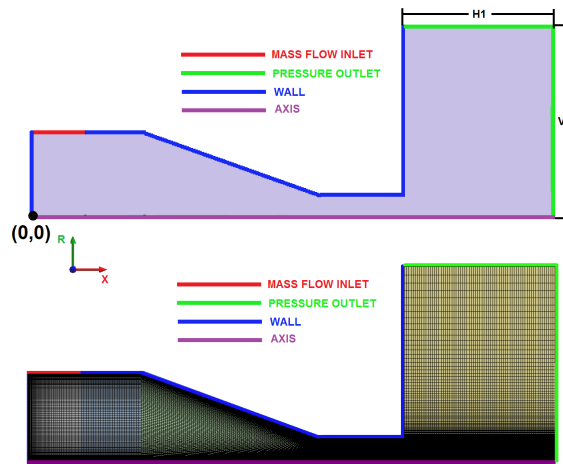


Figure 3.2: Computational domain for AXS numerical simulations.

In AXS flow simulations the 3D inlet boundary conditions are implemented by setting the radial velocity component such that the mass flow rate is satisfied. In addition, the tangential velocity component is set to the mean velocity in the tangential inlet port to ensure that same angular momentum enters the swirl chamber [26]. The mass flow inlet boundary condition is applied to a line which extends 2.49 mm from the head end of the swirl chamber (Figure 3.2). Mass flow rate of 0.053 kg/s is defined at the inlet boundary along a direction vector of $-0.1572\mathbf{j}+0.9866\mathbf{k}$, where \mathbf{j} and \mathbf{k} are the unit vectors along radial and tangential directions respectively. No-slip boundary condition is applied at the wall boundaries and the pressure outlet boundary condition

is applied at the outer boundaries.

In order to investigate the size of computational domain geometry on simulation results, three different computational domains are formed by changing the horizontal dimension (H1) and vertical dimension (V1) shown in Figure 3.2. The values for the horizontal dimension (H1) and vertical dimension (V1) are given in Table 3.1. The resulting grids are shown in Figure 3.3

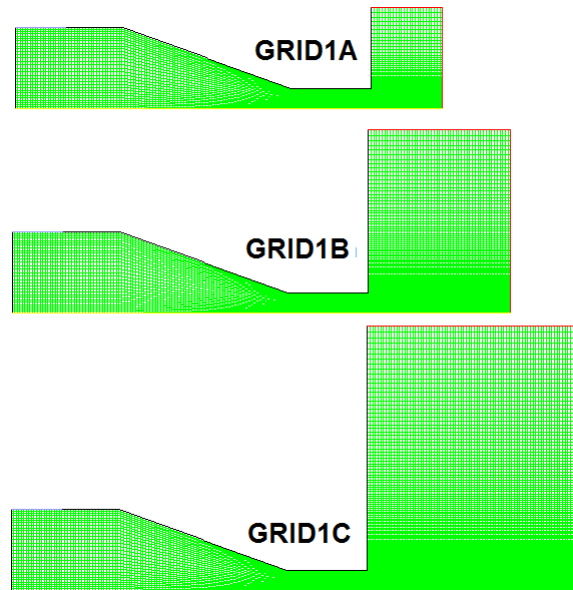


Figure 3.3: Grids for different computational domains.

Grids shown in Figure 3.3 have the same number of elements inside the atomizer but the resulting total number of elements is different as shown in Table 3.1. The dimensions that leads to GRID1B was used by Dash et.al. [26] in their computations.

Table 3.1: Values for horizontal and vertical dimensions and the resulting number of elements for each grid.

GRID	H1 [mm]	V1 [mm]	Number of Elements
GRID1A	3.5	4	5720
GRID1B	7	8	9620
GRID1C	10.5	12	15100

The results of the AXS flow simulations with GRID1A, GRID1B and GRID1C will be investigated and compared in the following section.

3.3.1.2 Simulation Results

Unsteady AXS laminar flow simulations are performed with GRID1A, GRID1B and GRID1C using the pressure based solver. The solutions are initialized such that air is present inside the atomizer and a mass flow rate of 0.053 kg/s water was defined at the mass flow inlet boundary through the direction vector of $-0.1572j+0.9866k$. Initial volume fraction contours of air are shown in Figure 3.4 for GRID1B. Initially the atomizer is full of air ($\alpha_a=1$) except for the inlet section at which the volume fraction of the air is always 0.

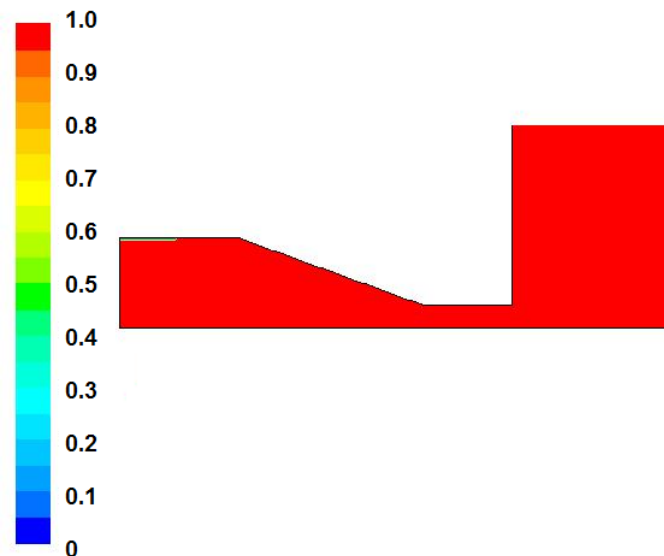


Figure 3.4: Initial computational domain, contours of volume fraction of air (GRID1B).

The solutions are second order accurate in space, first order accurate in time and the fixed time step for the calculations is 1 micro-seconds (μs). The iterative time advancement scheme is used in which all the equations are solved iteratively for a given time step until the convergence criteria are met. Advancing the solution by one time step requires outer equations whose number is limited to 20 in present simulations.

At about 8 milliseconds (ms) water flows out of the atomizer for all grids and the simulations were carried on for additional 12 ms. The evolution of the volume fraction of water with time is shown in Figure 3.5 for GRID1B.

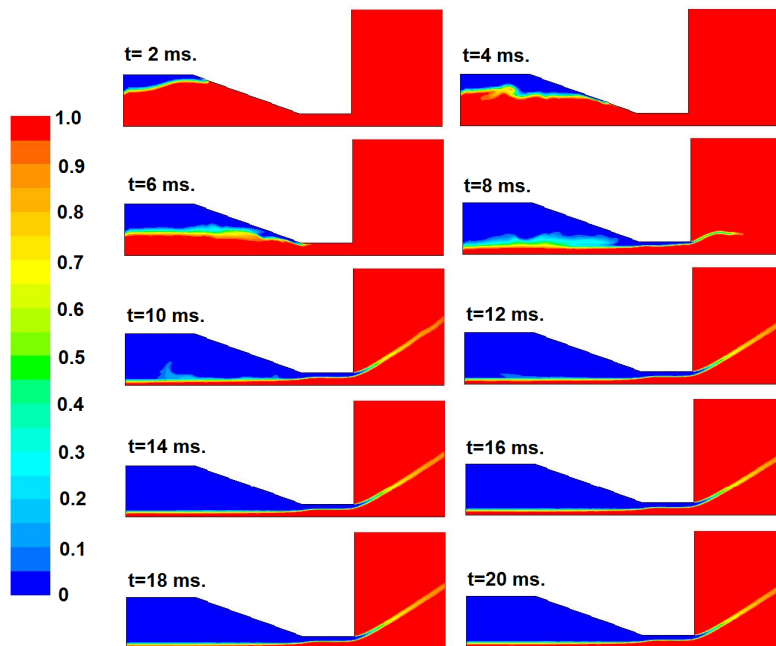


Figure 3.5: Evolution of air volume fraction with time (GRID1B).

An air core formed near the atomizer axis whose diameter is minimum at the head end of the atomizer. The air core diameter is nearly constant along the swirl chamber and increased to a larger value starting from the nozzle inlet.

The time histories of axial and swirl velocities at Probe1 ($x=17.5$ mm, $r=0.8$ mm) are given in Figure 3.6 for GRID1A, GRID1B and GRID1C. At Probe 1 the axial and swirl velocity predictions does not differ up to 19.2 ms. After 19.2 ms axial velocities and swirl velocities, which are predicted at Probe1, starts to oscillate.

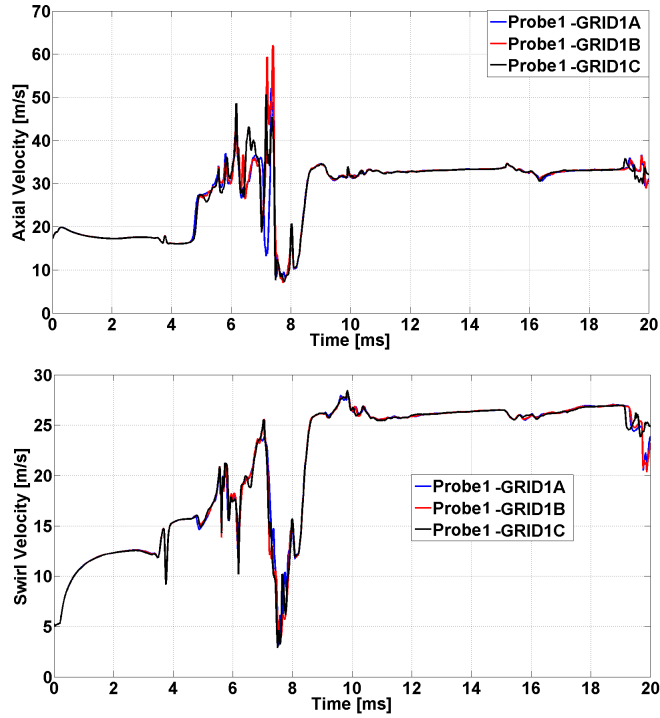


Figure 3.6: Evolution of axial velocity and swirl velocity on Probe1.

In order to investigate the oscillatory behavior of the flow and the effect of computational domain geometry on the predictions, the simulations are continued for an additional 100 ms. A fixed time step size of $1 \mu\text{s}$ is used, which resulted in a total of 120000 time steps and 2.4 million iterations for each grid. The mean volume fraction contours for GRID1A, GRID1B and GRID1C are shown together in Figure 3.7.

The volume fraction is one when the corresponding phase is air and the volume fraction is zero when the corresponding phase is water. The volume fraction value makes a transition from 0 to 1 along the interface. In order to obtain a quantitative value for the air core diameter, the radial location at which the volume fraction value is less than 0.5 is searched along the interface and the first three radial locations at which the volume fraction value is larger than 0.5 is marked. The average of the three radial locations is calculated together with an average volume fraction value. The calculated average radial location value is then used as an approximation to the air core diameter at the axial location of interest. The mean air core diameter that is predicted using

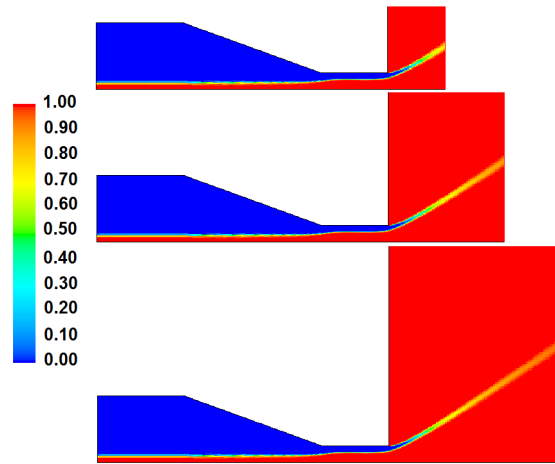


Figure 3.7: Mean volume fraction contours of air.

GRID1A, GRID1B and GRID1C are same regardless of the axial location. A constant mean air core diameter of 0.62 mm is predicted by all three grids up to $x=8.75$ mm at which an air core diameter of 0.57 mm is predicted. The air core diameter increases gradually from 0.57 mm at $x=8.75$ mm to 1.17 mm at $x=14.8$ mm and stay constant up to $x=16.6$ mm. At the exit of the atomizer all three grids predicts an air core diameter of 1.33 mm.

The mean axial velocity contours for GRID1A, GRID1B and GRID1C are shown together in Figure 3.8. The mean axial velocity of the water increased from swirl chamber to the exit of the atomizer and axial velocity is maximum at the exit of the atomizer. The flow solver predicts a maximum axial velocity 36.09 m/s for GRID1A and 36.15 m/s for GRID1B and GRID1C. The mean axial velocity of the air flow into the atomizer increases from -12.4 m/s at the nozzle exit to -51.3 m/s at an axial location of about 8-10.5 mm away from the head end. The reason for such a high suction velocity at that part of the nozzle is the coarse grid resolution. The structured mesh topology within the swirl chamber results in squeezed cells in the convergent part which changes the direction of the water flow locally, reduce the air core and effective flow area of the air. The mean axial velocity distributions for GRID1A, GRID1B and GRID1C are shown together in Figure 3.9 for six different stations. The errors bars in Figure 3.9 represents the standard deviation from the mean axial velocity for each grid.

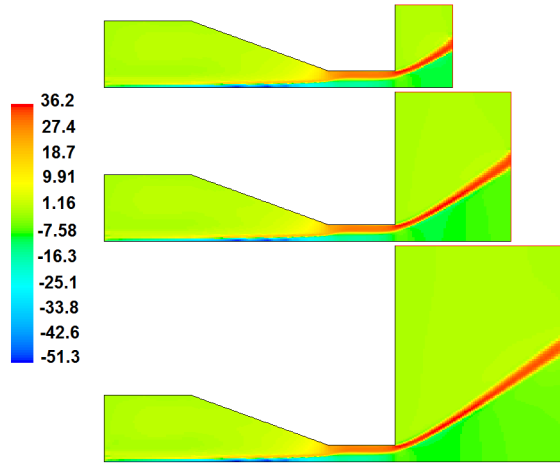


Figure 3.8: Mean axial velocity contours [m/s].

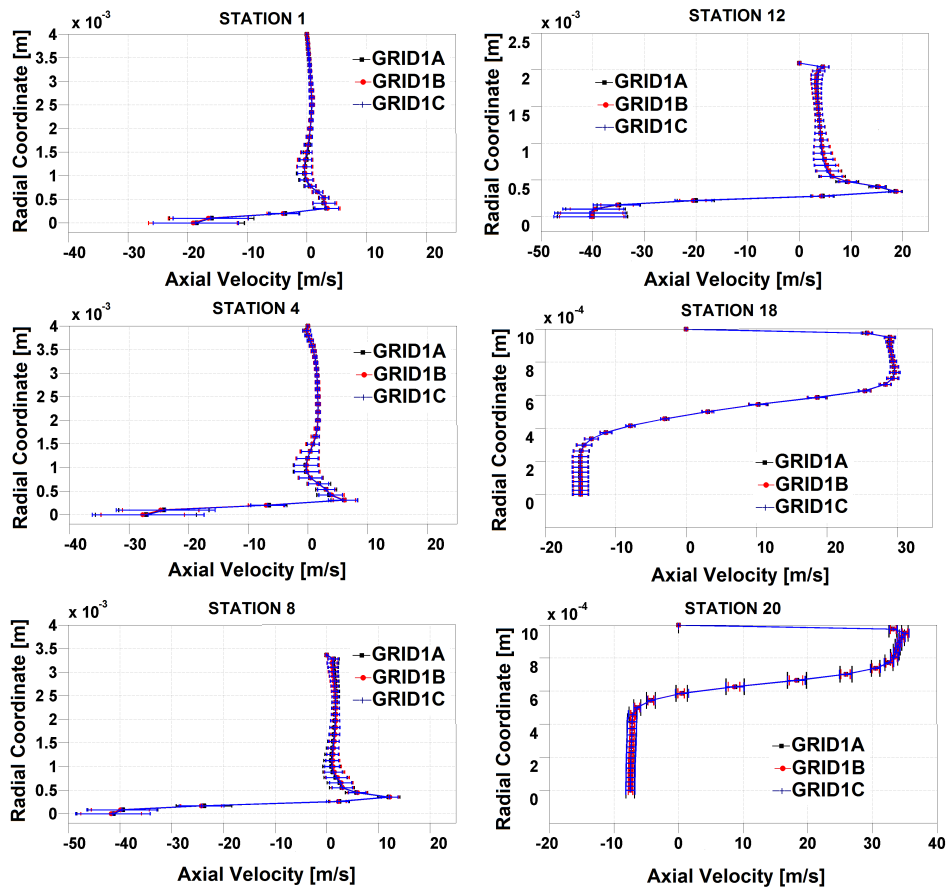


Figure 3.9: Mean axial velocities and corresponding standard deviations along designated stations.

The standard deviation from the mean axial velocity is maximum in radial locations inside the air core for Stations 1, 4, 8, 12 and 18. The standard deviation from the mean is almost constant along the radial direction at Station 20. The mean axial velocities and the standard deviations from the mean axial velocity do not change considerably with the computational domain geometry.

The mean swirl velocity contours for GRID1A, GRID1B and GRID1C are shown together in Figure 3.10.

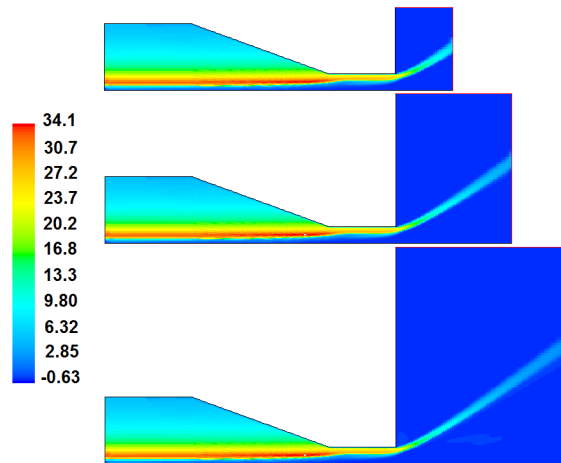


Figure 3.10: Mean swirl velocity contours [m/s].

The swirl velocity is minimum near the mass flow inlet boundary condition and attains a maximum value of 34 m/s near the air core for all three grids. The swirl velocity distribution resembles a free vortex, with the exception that a finite velocity is predicted due to the formation of the air core along the axis of the atomizer.

The mean swirl velocity distributions for GRID1A, GRID1B and GRID1C are shown together in Figure 3.11 for six different stations. The errors bars in Figure 3.11 represents the standard deviation from the mean swirl velocity for each grid. The standard deviation from the mean swirl is maximum in radial locations inside the air core for Stations 1, 4, 8 and 12. The standard deviation from the mean is maximum in the water region for Station 18 and Station 20. The mean swirl velocities and the standard deviations from the mean swirl velocity do not change considerably with the computational domain geometry.

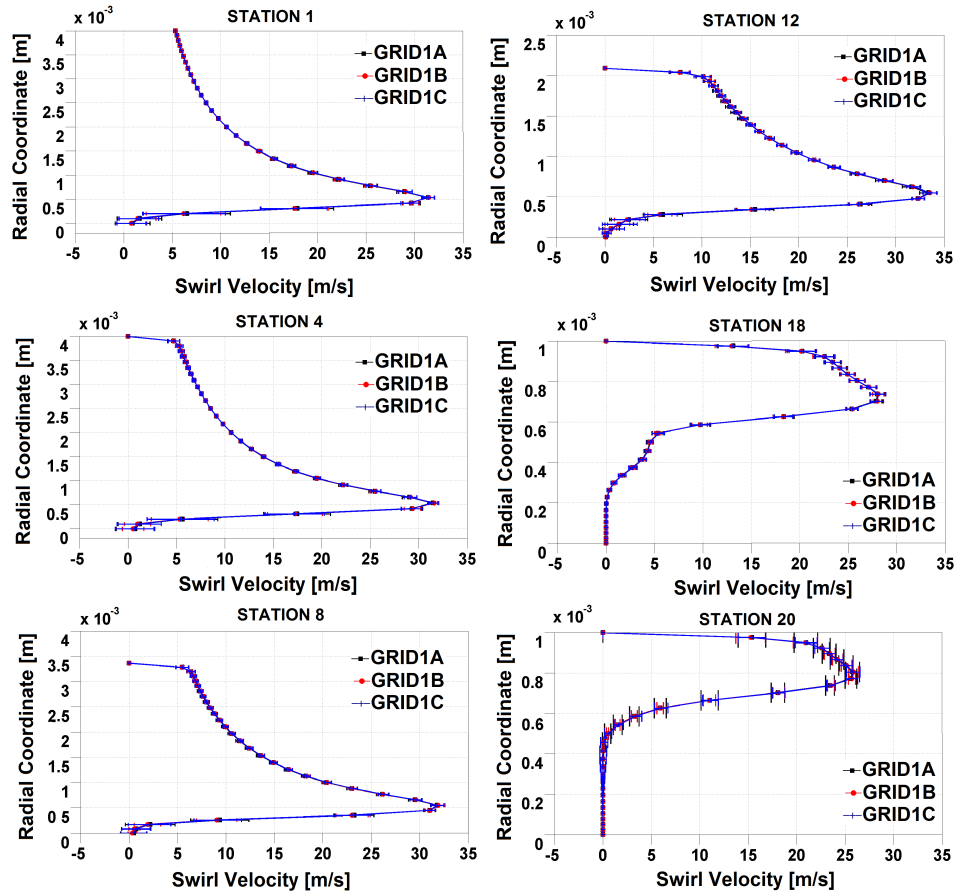


Figure 3.11: Mean swirl velocities and corresponding standard deviations along designated stations.

3.3.1.3 Conclusion

Three different computational domains are formed in order to study the effect of location of the pressure outlet boundary condition on the simulation results. The grids have the same grid topology inside the atomizer, which results in identical number of quadrilateral elements within the atomizer. The simulations with different computational domains shows that the mean quantities and the standard deviations from the mean are not affected by the size of the computational domain. Consequently, computational domain geometry of GRID1B, which was also used by Dash et. al. [26], is selected for further investigation.

3.3.2 Grid Sensitivity Study

3.3.2.1 Introduction

In order to investigate the effect of grid resolution on simulation results, four different computational domains are formed mainly by changing seed density of the vertical lines, which is used to construct the atomizer geometry. The grids, which are constructed for the sensitivity study, and the corresponding number of quadrilateral elements are shown together in Figure 3.12. The coarsest grid is the same as GRID1B (referred as GRID1 hereafter) which was used in computational domain sensitivity analysis.

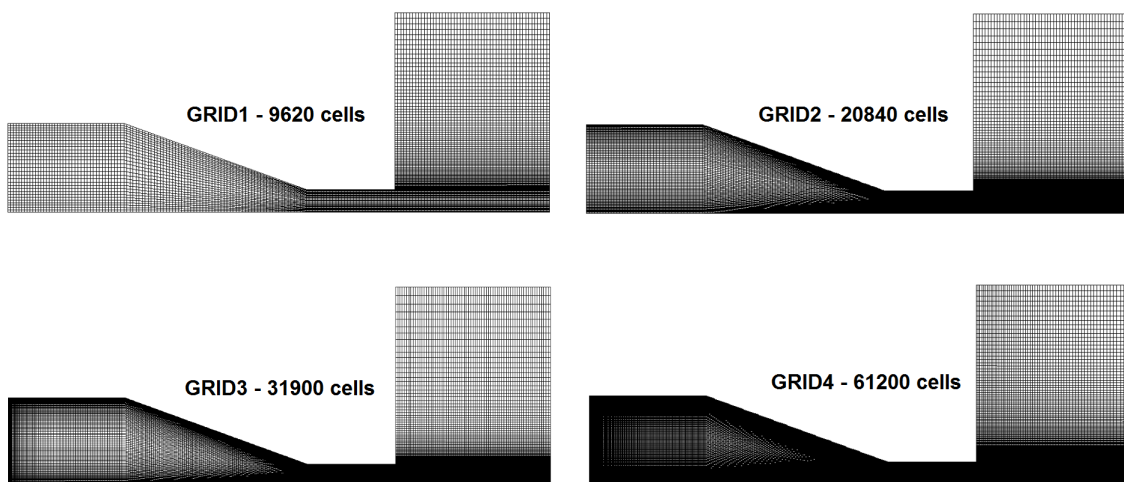


Figure 3.12: Computational domains used in grid sensitivity study.

The coarse grid and the fine grid that was used in simulations performed by Dash et. al. [26] contains 5910 and 23640 cells, respectively. GRID1 and GRID2, which consisted of 9620 and 20840 quadrilateral cells, respectively, has nearly the same number of cells as Dash et. al. [26]. GRID3 and GRID4 contains 31900 and 61200 quadrilateral cells, respectively.

3.3.2.2 Simulation Results

Unsteady, 2D-AXS, laminar flow simulations are performed with GRID1, GRID2, GRID3 and GRID4 using the pressure based solver. The solution methodology, which is explained in previous section is followed while performing the simulations with different grids. The main difference between the simulations with different grids is the time step size. A fixed time step size of $1 \mu s$ is used in simulations with GRID1 and GRID2, on the other hand fixed time step sizes of $0.5 \mu s$ and $0.25 \mu s$ are used in simulations with GRID3 and GRID4, respectively. Although implicit time integration is used for the unsteady solution of the Navier-Stokes equations, explicit time integration scheme is used for the solution of the VOF equation. In order to meet the stability criterion for the VOF calculations the CFL number is kept smaller than 2 by decreasing the time step accordingly. The evolution of the air volume fraction with time is given in Figure 3.13 for GRID2, GRID3 and GRID4 for the first 12 ms. The evolution of air volume fraction with time for GRID1 was given before in Figure 3.7.

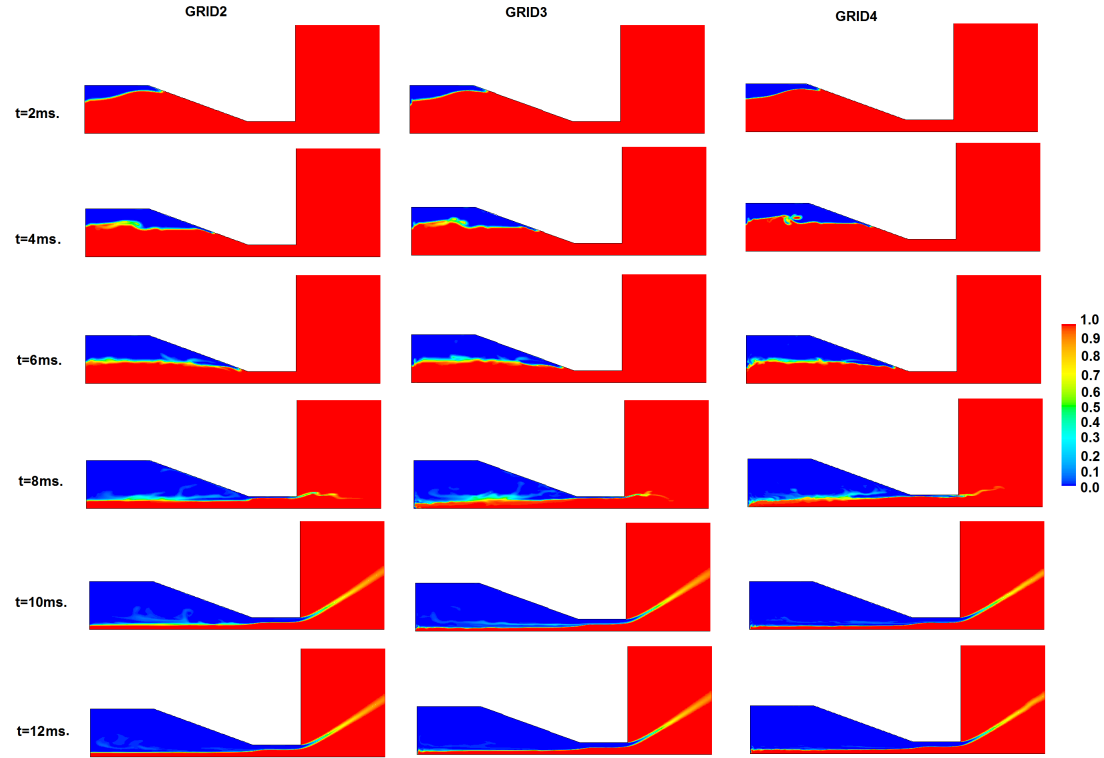


Figure 3.13: Evolution of air volume fraction contours for GRID2, GRID3 and GRID4.

Water flows out of the atomizer at about 8 ms for all grids. Surface waves are identified along the air core with the simulations performed with GRID3 and GRID4, whereas the simulations with the coarse grids do not catch up the wave phenomena.

After 20 ms, the simulations are further continued for an additional 100 ms in order to obtain the statistical properties of the flow. The mean volume fraction contours are shown in Figure 3.14 for all grids.

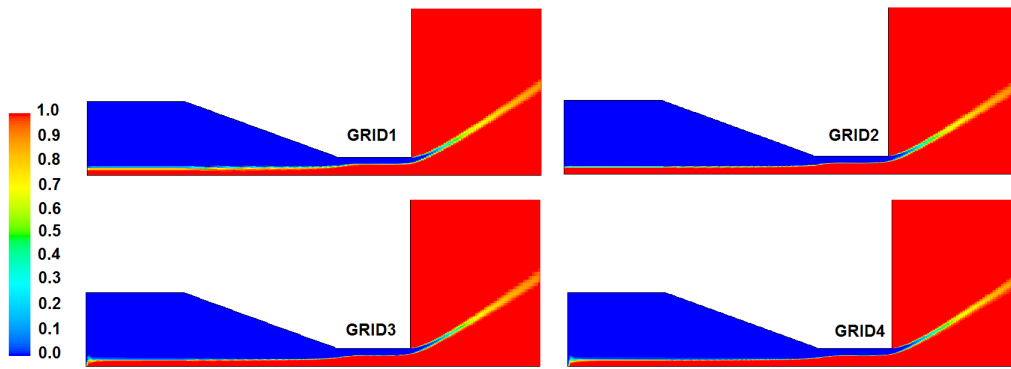


Figure 3.14: Mean volume fraction contours of air.

Investigation of the mean volume fraction contours reveals a major difference in the shape of the interface at the head end of the atomizer. Simulations with GRID1 and GRID2 predict a constant mean air core diameter all along the swirl chamber, whereas simulations with GRID3 and GRID4 predict a smaller mean air core diameter at the head end of the atomizer as shown in detail in Figure 3.15. The detection of such a phenomena at the depicted location is a result of increasing the grid density which results in capturing additional flow features at the water region, interface region and air core.

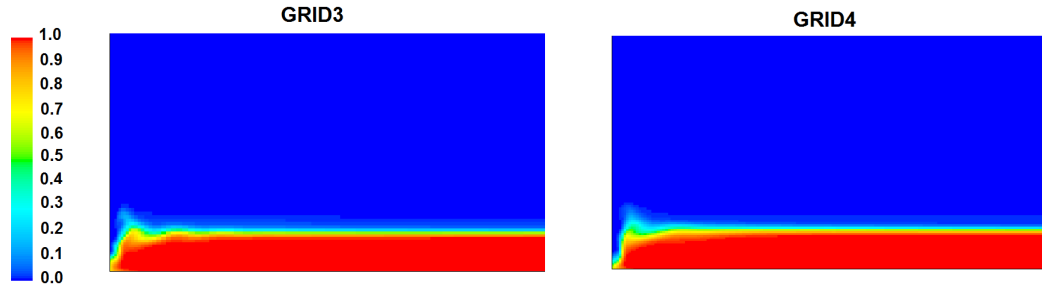


Figure 3.15: Mean volume fraction contours of air at the head end of the atomizer.

Although the shape of the interface differs at the head end of the atomizer for GRID3 and GRID4, the interface shape is the same for the rest of the atomizer for all grids. The calculated mean air core diameter at four different axial locations are given in Table 3.2 for all grids.

Table 3.2: Calculated mean air core diameters at four different axial locations.

GRID	Station4	Station12	Station18	Station20 (exit)
GRID1	0.618	0.687	1.170	1.328
GRID2	0.753	0.795	1.197	1.368
GRID3	0.660	0.753	1.193	1.374
GRID4	0.690	0.744	1.193	1.370

The calculated mean air core diameters for GRID3 and GRID4 are same at Station18 and very close to each other at other stations.

The mean static pressure contours for GRID1, GRID2, GRID3 and GRID4 are shown together in Figure 3.16. The mean static pressure is maximum at the upper head end of the atomizer and it is minimum at the air core for all four grids. The flow solver predicts a maximum static pressure value of 10.13 bars for GRID1, 10.08 bars for GRID2 9.8 bars for GRID3 and 9.7 bars for GRID4. The minimum mean static pressures are predicted at the air core for all grids and they are below the ambient pressure. The minimum mean static pressure values for GRID3 and GRID4 are 0.88 bars and 0.60 bars below the ambient pressure, respectively, but these values are localized at

the head end of the atomizer near the air core.

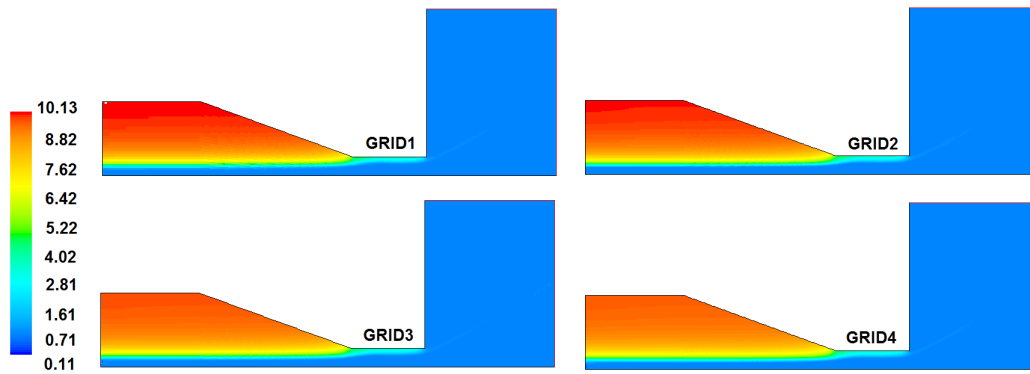


Figure 3.16: Mean static pressure contours [bars].

The mean axial velocity contours for GRID1, GRID2, GRID3 and GRID4 are shown together in Figure 3.17. The maximum mean axial velocity is predicted at the exit of the atomizer for all grids. The values for the maximum mean axial velocities are 36.15 m/s, 36.55 m/s, 35.50 m/s and 35.42 m/s for GRID1, GRID2, GRID3 and GRID4, respectively.

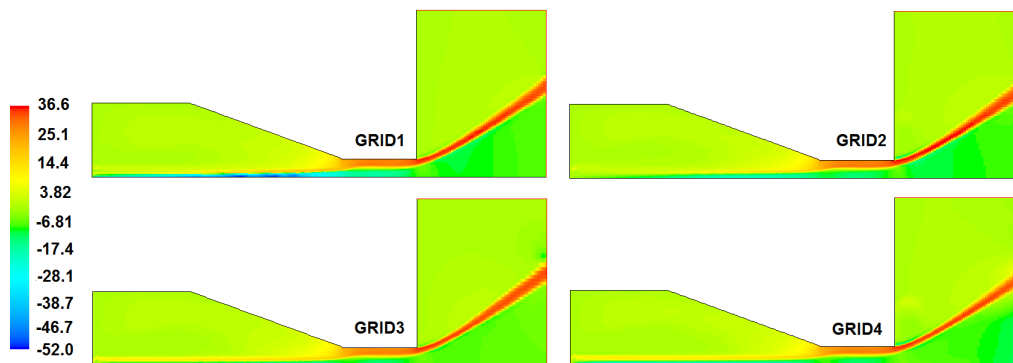


Figure 3.17: Mean axial velocity contours [m/s].

Minimum mean axial velocity is predicted as -51.3 m/s at an axial location of about 8-10.5 mm away from the head end for GRID1. This is due to coarse grid resolution as explained before in the previous section. For GRID2 the minimum mean axial

velocity is predicted as -18 m/s at the air core near the convergence section of the atomizer. The minimum mean axial velocities for GRID3 and GRID4 are predicted as -26.3 m/s and -23.3 m/s, respectively, at the air core near the head end of the atomizer.

The mean swirl velocity for GRID1, GRID2, GRID3 and GRID4 are shown together in Figure 3.18. The maximum mean swirl velocity is predicted near the air core for all grids. The values for the maximum mean swirl velocities are 34.1 m/s, 35.5 m/s, 38.5 m/s and 37 m/s for GRID1, GRID2, GRID3 and GRID4, respectively.

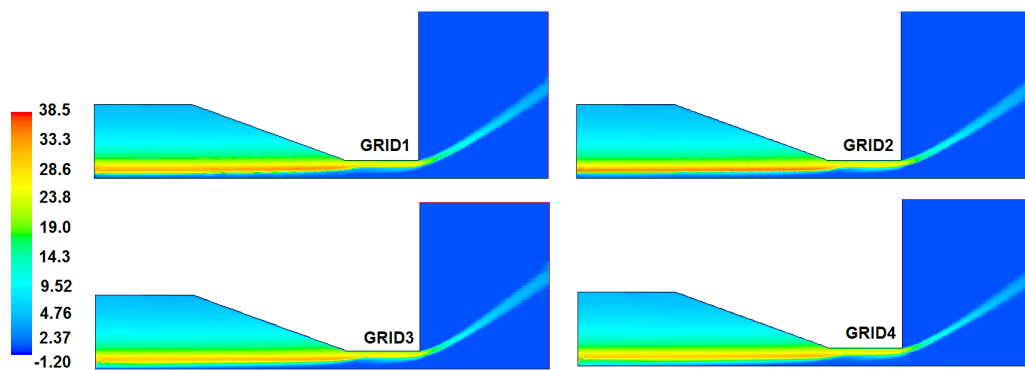


Figure 3.18: Mean swirl velocity contours [m/s].

The numerical simulations with GRID3 and GRID4 captures the oscillating free surface phenomena at the head end of the atomizer, which results in a reduced air core diameter at the head end of the atomizer. This phenomena was also observed in the High Speed Shadowgraphy Experiments as given in Chapter3. In order to make a selection between GRID3 and GRID4, the axial and swirl velocity distributions at stations close to the head end of the atomizer are investigated.

The mean axial velocity distributions for GRID3 and GRID4 are shown together in Figure 3.19 for four different stations. The error bars in Figure 3.19 represents the standard deviation from the mean axial velocity for each grid.

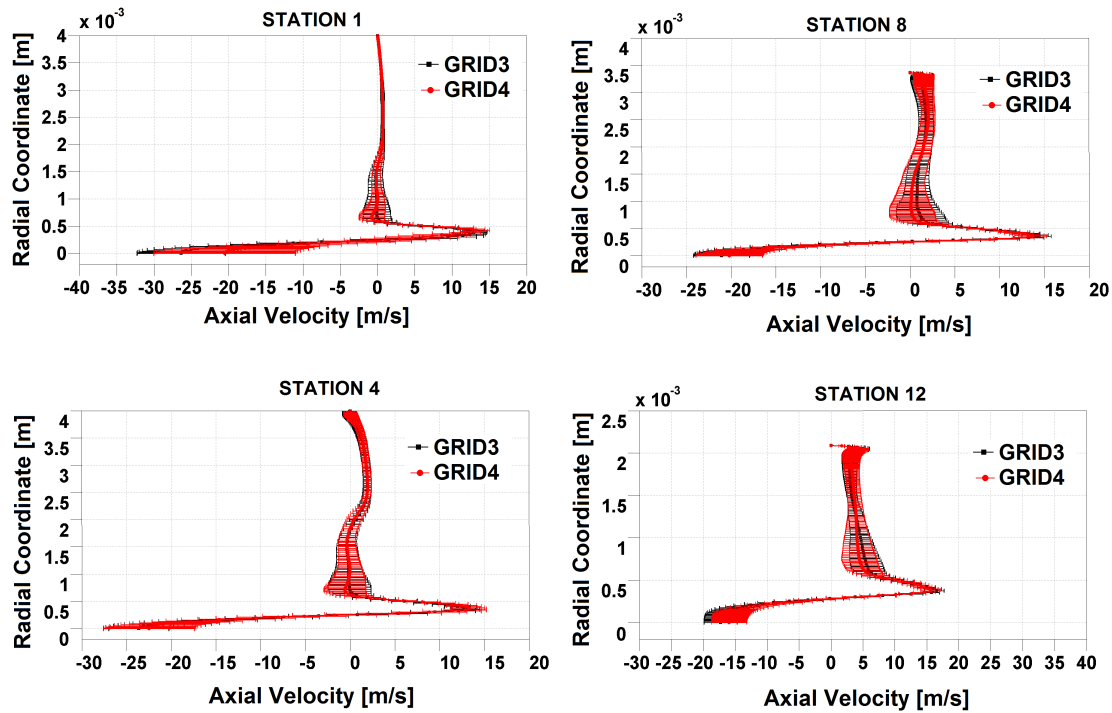


Figure 3.19: Mean axial velocities and corresponding standard deviations along designated stations.

The standard deviation from the mean axial velocity is maximum in radial locations inside the air core for all Stations. The standard deviation from the mean predicted by GRID4 is slightly higher than the that predicted by GRID3.

The mean swirl velocity distributions for GRID3 and GRID4 are shown together in Figure 3.20 for four different stations. The error bars in Figure 3.20 represents the standard deviation from the mean swirl velocity for each grid. The standard deviation from the mean swirl velocity is maximum in radial locations inside the air core for all Stations. The standard deviation from the mean swirl velocity predicted by GRID4 is slightly higher than the standard deviation from the mean swirl velocity predicted by GRID3.

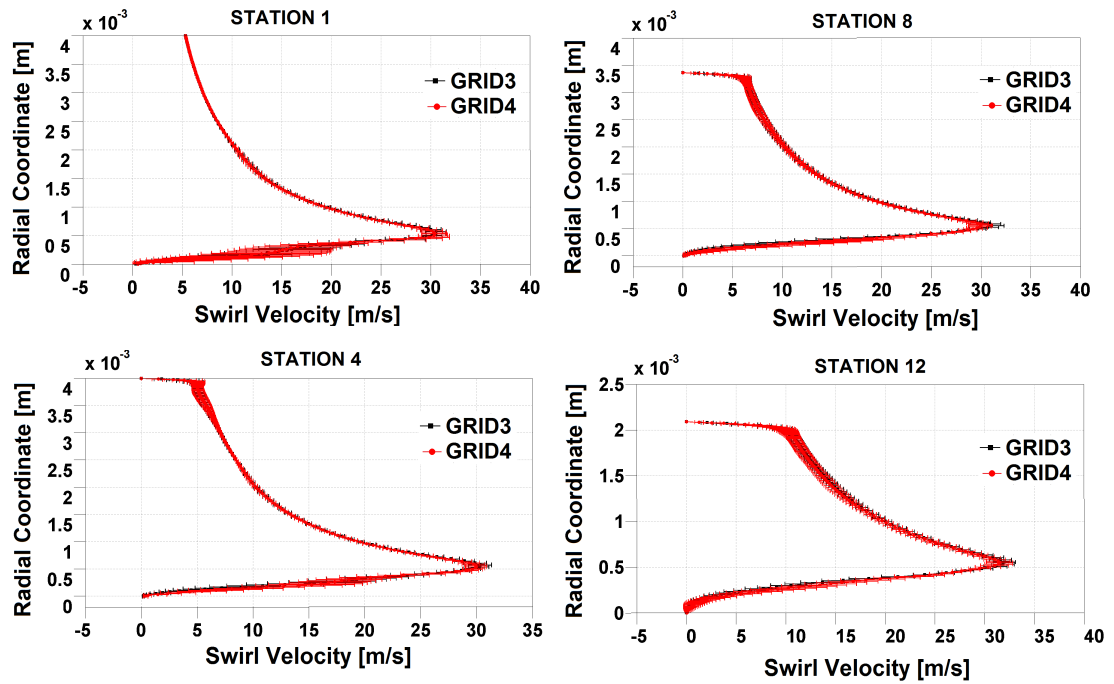


Figure 3.20: Mean swirl velocities and corresponding standard deviations along designated stations.

3.3.2.3 Conclusion

Four different grids are formed and simulations are performed in order to see the effect of grid resolution on the simulation results. The simulations show that the grid resolution is important to catch the flow features inside the atomizer. As the grid resolution increases oscillations of the interface are identified at the head end of the atomizer. The oscillations of the interface at the head end of the atomizer can not identified with GRID1 and GRID2, however, oscillations of the interface are captured with GRID3 and GRID4. Despite of the oscillations, which are identified at the head end for GRID3 and GRID4, the mean values do not differ significantly with the grid resolution. The standard deviation from the mean axial velocity and mean swirl velocity, which are predicted with simulations performed with GRID3 and GRID4, differs slightly in the air region. However, the computation time of simulations with GRID4 is about twice much of the computation time of simulations with GRID3. As a result GRID3 was selected for further investigation.

3.4 Two Dimensional Axis-Symmetric Swirl Simulation Results

3.4.1 Introduction

In this section the results of the AXS simulations performed with GRID3 is investigated in detail. The bottom cause of the oscillations, which are identified at the head end of the atomizer, are explored and the waves on the air core are identified. The Taylor-Görtler vortices, which were reported by several researchers ([20], [22], [29], [87]) are assessed. The unsteady air core diameter is calculated at several axial locations and the frequency domain representation of the air core diameter data is obtained.

3.4.2 Flow Through the Pressure Swirl Atomizer

The flow through the pressure swirl atomizer can be divided into two main regions based on the volume fractions and a region of transition between two regions. In the first region, the volume fraction of air is zero, so it depicts a water region. In the second region the volume fraction of air is one, so it depicts an air region. There is a transition region between the two regions where the volume fraction can have any value between zero and one. The mean volume fraction contours obtained from the unsteady simulations are shown in Figure 3.21.

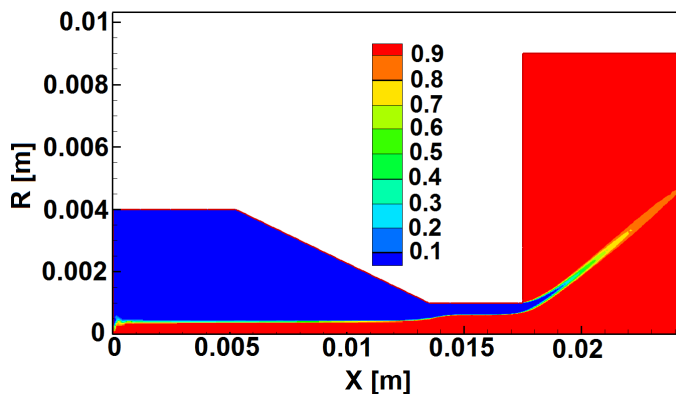


Figure 3.21: Mean Volume fraction contours of air.

The flow of water through the atomizer is associated with the water region, while the flow of air in to the atomizer is associated with the air core region. The mean flow quantities are obtained by taking time average of the instantaneous quantities between 20 ms and 120 ms.

The mean volume fraction values are shown in Figure 3.22 at six different stations along the atomizer. The mean values of volume fraction of air are zero for the water region, one for the air region, and in between for the transition region.

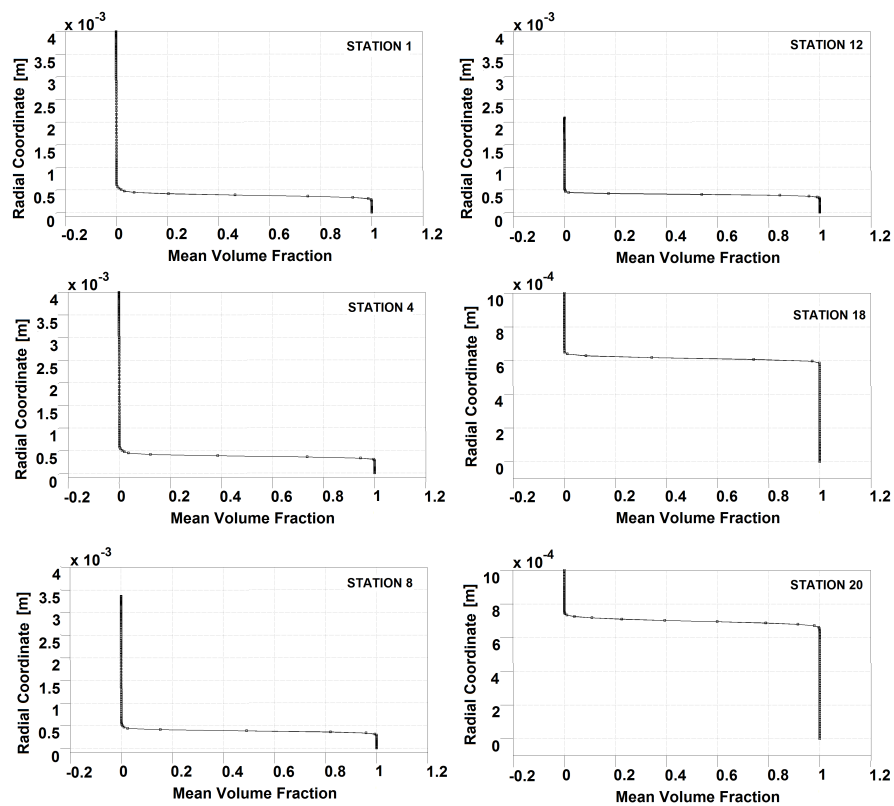


Figure 3.22: Mean volume fractions at designated stations.

Instantaneous in plane velocity vectors are shown together with the instantaneous volume fraction contours of air at the nozzle of the atomizer in Figure 3.23 in order to illustrate the water and air flows more clearly.

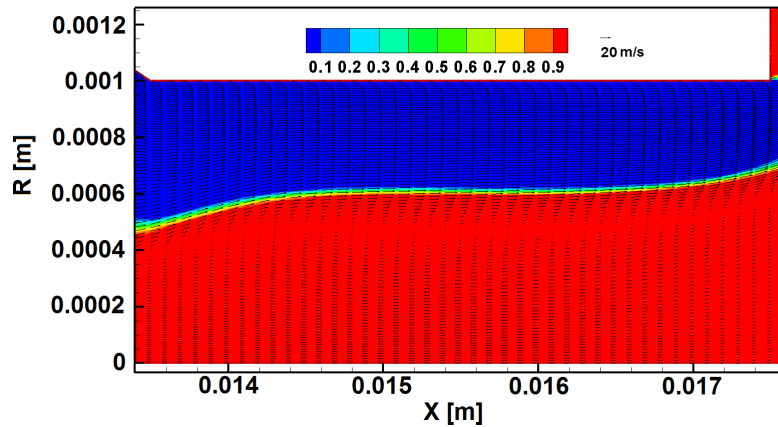


Figure 3.23: Contours of volume fraction of air together with in plane velocity vectors.

The water flows out of the atomizer above the transition region. Below the transition region, air flow into the atomizer is identified at radial locations close to the axis, and air flow out of the atomizer is identified at radial locations close to the transition region. As a result, there are inflation points at the air region at which the in plane velocity of air is zero. The locations at which the in plane velocity is zero can be identified from Figure 3.22 at the nozzle of the atomizer. The inflation point of the in plane velocity is always at the air region along the axis of the atomizer.

The mean axial velocity contours, which are obtained from the unsteady simulations, are shown in Figure 3.24.

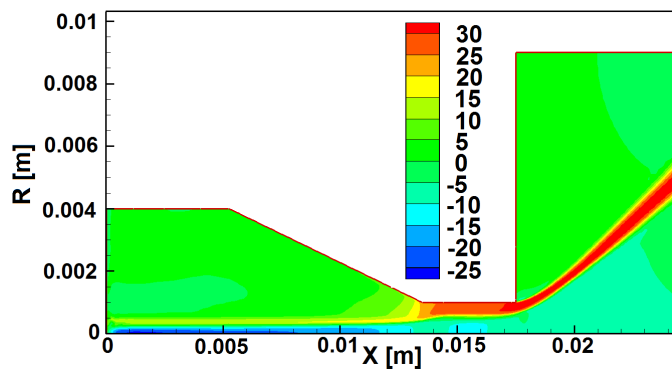


Figure 3.24: Mean axial velocity contours [m/s].

The mean axial velocity is small all along the swirl chamber above the interface and increases to the nozzle and maximum at the nozzle exit. The negative mean axial velocities are associated with the air core. The magnitude of the negative axial velocities increases from the exit of the atomizer to the head end of the atomizer. Regions of high negative mean axial velocities are identified close to the head end of the atomizer at the air core.

The mean axial velocities and the corresponding standard deviations are given in Figure 3.25 at six different stations along the atomizer. The horizontal red lines, which shown on each graph in the Figure 3.25, designates the boundaries of the interface region. The upper part of the interface region is the water region and the lower part of the interface region is the air core.

The mean axial velocity is zero at the outermost radial location of each station. This is due to the no-slip boundary condition for Stations 4, 8, 12, 18 and 20 and mass flow inlet boundary condition at Station 1. The mean axial velocity is small along Station 1 down to a certain radial coordinate close to the interface region. It then increases, attains its maximum value within the interface region, decreases to zero within the air core, changes direction and has its maximum value at the axis. The fluctuations in the axial velocity is maximum within the air core for Station 1. Similar arguments are true for Stations 4, 8 and 12, in addition, the mean axial velocity as well as the standard deviation from the mean in the water region increases as one goes in axial direction from Station 1 to Station 12. At Station 18 (mid nozzle) and Station 20 (nozzle exit), the mean axial velocity in the water region is higher than the other stations and the mean axial velocity attains its maximum value at the nozzle exit.

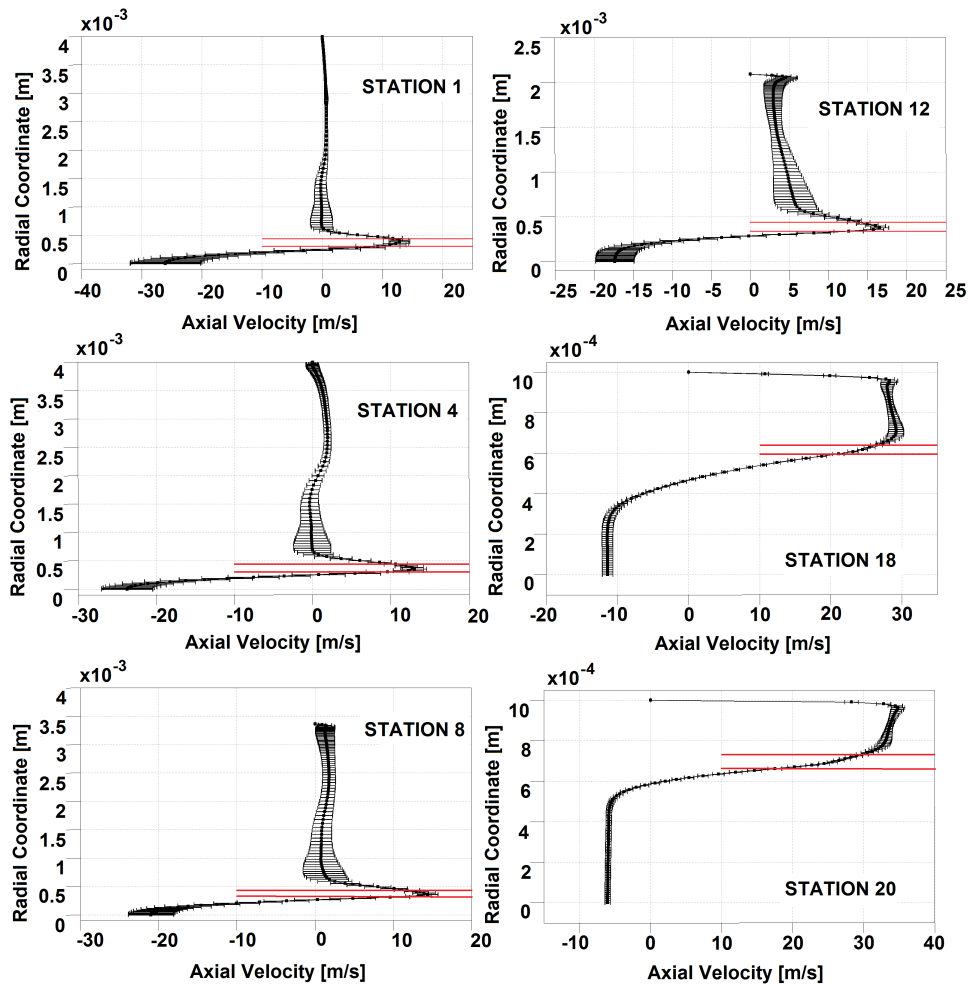


Figure 3.25: Mean axial velocities and corresponding standard deviations along designated stations.

The standard deviation in the mean axial velocity within the water region increases up to Station 12 and decreases along stations at the nozzle. The air, which is sucked into the atomizer, does not have the information about the flow physics inside the atomizer. The standard deviation from the mean axial velocity, thus, minimum at the exit of the atomizer (Station 20). As the air goes in to the atomizer, it is effected by the unsteady phenomena inside the atomizer and the standard deviation in the mean axial velocity within the air core starts to increase (Station 18). The standard deviation from the mean axial velocity increases as air goes further into the atomizer and it is maximum at Station 1.

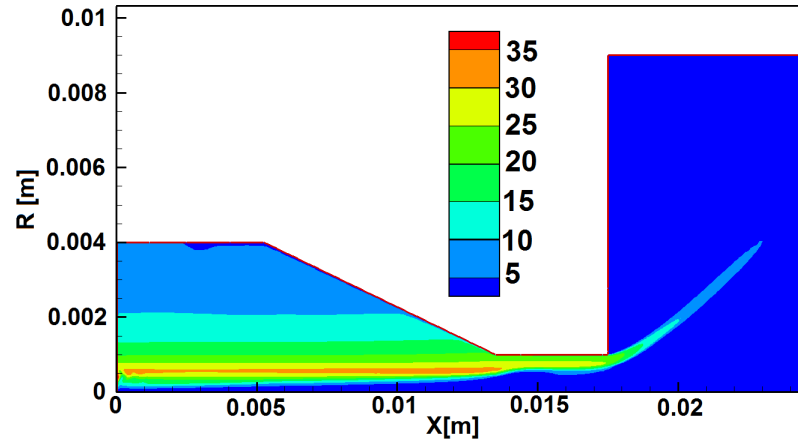


Figure 3.26: Mean swirl velocity contours [m/s].

The mean swirl velocity contours obtained from the unsteady simulations are shown in Figure 3.26. The mean swirl velocity is minimum near the walls of the swirl chamber and at the mass flow inlet boundary, it gradually increases and attain its maximum value near the interface and then decreases to zero at the axis. This behavior of the swirl velocity resembles a bounded free vortex from the walls of the swirl chamber to the interface and a forced vortex from the interface to the axis boundary along the air core.

The mean swirl velocities and the corresponding standard deviations are given in Figure 3.27 at six different stations along the atomizer. The horizontal red lines, which shown on each graph in the figure designates the boundaries of the interface region. The upper part of the interface region is the water region and the lower part of the interface region is the air core.

The mean swirl velocity is zero at the outermost radial location for all Stations except Station 1. This is due to the no-slip boundary condition for Stations 4, 8, 12, 18 and 20 and mass flow inlet boundary condition at Station 1. As the radial coordinate decreases, the mean swirl velocity increases and attains its maximum value within the water region for all stations. Then it decreases with decreasing radial coordinate at the interface and air core regions.

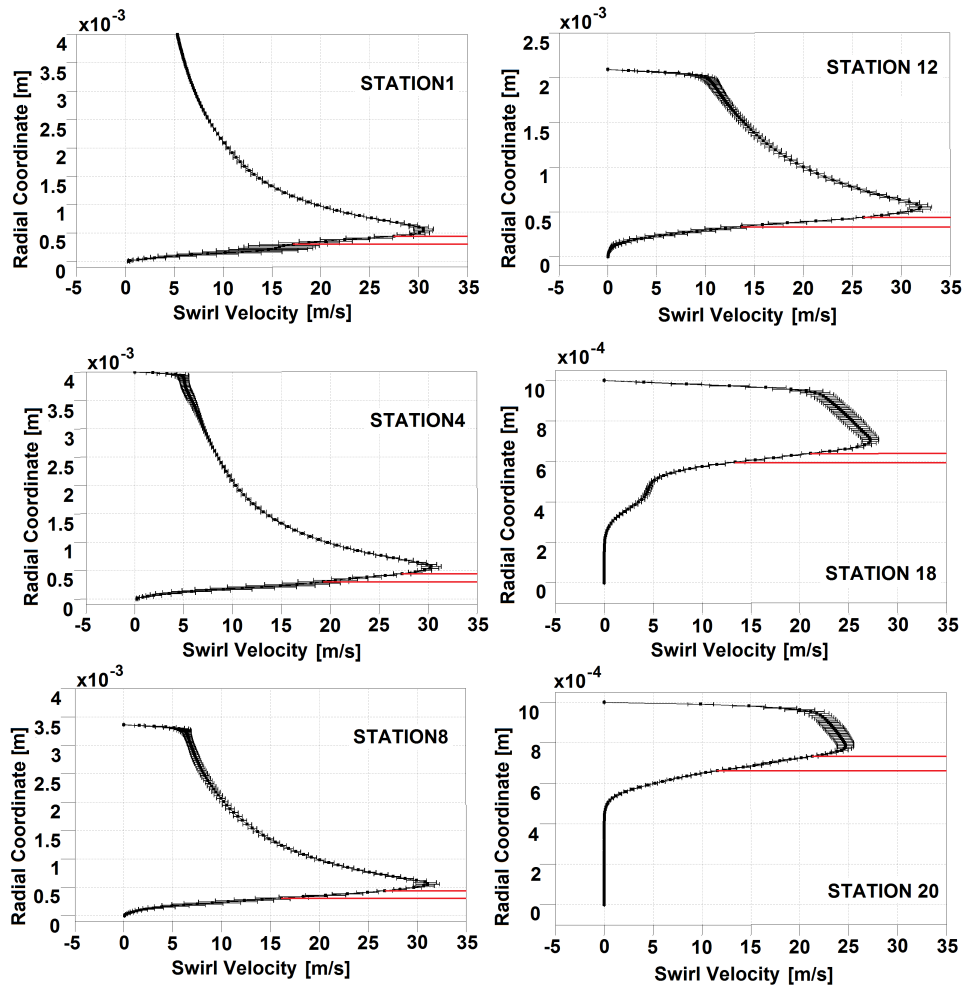


Figure 3.27: Mean swirl velocities and corresponding standard deviations along designated stations.

The standard deviations from the mean swirl velocity is maximum at the air core region for Station 1. For Stations 4, 8 and 12, relatively high standard deviations from the mean swirl velocity are observed at radial locations close to the wall in the water region. However, the standard deviation from the mean swirl velocity is maximum at the air core regions for Station 4 and Station 8, and it is maximum at the interface region for Station 12. The deviation from the mean was maximum at the water region for Stations 18 and 20 and it decreases with decreasing radial coordinate. At station 20 (nozzle exit) the deviations from the mean swirl velocity is minimum at the air core region.

The air, which is sucked into the atomizer, does not have a swirl velocity component at the exit of the nozzle (Station 20) as can be seen from Figure 3.27. As the air goes in to the atomizer it attains a swirl velocity component starting from the radial locations close to the interface region (Station 18).

The mean radial velocity contours obtained from the unsteady simulations are shown in Figure 3.28. Discrete regions of high mean radial velocity are identified close to the interface.

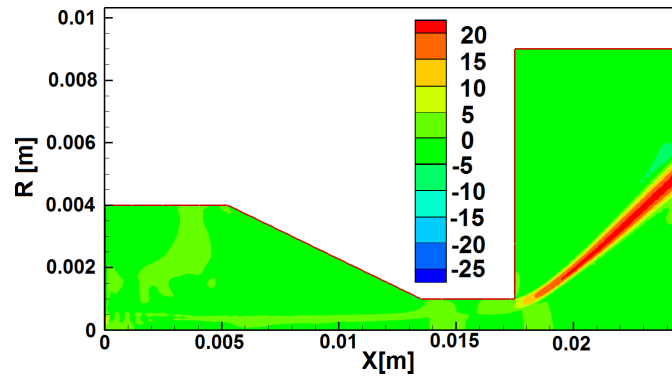


Figure 3.28: Mean radial velocity contours [m/s].

3.4.3 Vortex Dynamics

The unsteady AXS numerical simulations reveal vortex structures both in the water region and in the air core. The vortex structures, that are identified inside the pressure swirl atomizer at 41.5 ms, are given in Figure 3.29 as visualized by the axial velocity contours/volume fraction contours and streamlines originated both from the mass flow inlet and pressure outlet boundaries.

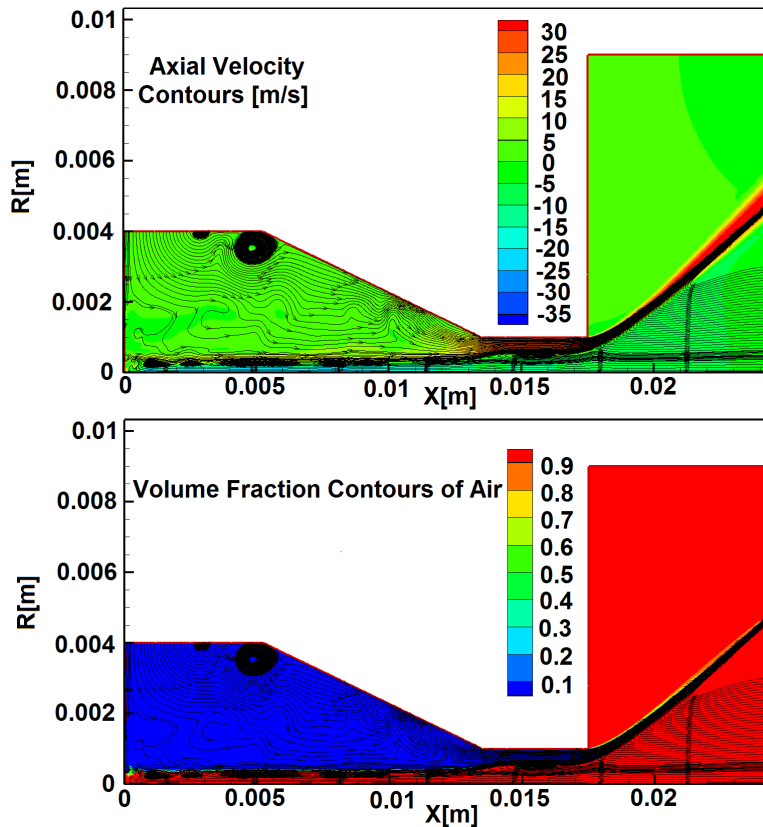


Figure 3.29: Vortex structures inside the pressure swirl atomizer.

It is figured out that at the head end of the atomizer there exist a stagnation region for both the incoming water flow from the mass flow inlet boundary and the incoming air from outside of the atomizer, which makes this region highly unsteady. In the water region the main unsteady vortex structures are identified just after the mass flow inlet boundary near the wall as shown in Figure 3.29. Vortex structures within the air core just below the transition region are also identified as seen in Figure 3.29.

The vortices in the water region (upper part of the swirl chamber, adjacent to wall) was reported by Xue [87], as steady recirculating regions, location of which affects the axial velocity variations in the swirl chamber and consequently at the exit orifice. Chinn et.al. [20] and Cooper et.al. [22] identified similar vortices within the swirl chamber adjacent to wall and they commented that these vortices are similar to Taylor-Görtler vortices that are present in the Taylor-Couette flow, between two concentric cylinders. They also pointed out that the vortices undergo a slight change in shape and position even the flow is not turbulent. Later Lavante et. al. [29] figured out similar vortices, and commented that these vortices are Taylor-Görtler type which are due to the hydrodynamic instability of the liquid passes the concave wall. On the other hand the vortices on the air core has not been identified yet.

The waves on the air core was reported by several researchers, yet the bottom cause of these oscillations have not been understand yet. The only work that came close to a reasonable explanation to the mechanism that creates the surface waves is the work of Lavante et. al. [29]. They pointed out the small amplitude oscillations at the surface of the air core originates from the head end of the atomizer. However they stated that the phenomena of cyclic expansion/contraction of the air core needs further investigation.

The unsteady vortex structures at the water region, the stagnation region at the head end of the atomizer and vortices in the air core will be investigated in detail in the following sections.

3.4.3.1 Vortex Structures in the Water Region

Time dependency of the vortex structures in the water region close to the wall boundary are shown in Figure 3.30 as visualized by the axial velocity contours and streamlines originated from the mass flow inlet boundary. The time difference between each snapshot is constant and is equal to 1 ms. This vortex structures was seen on the original work of Dash et. al. [26] on the same atomizer, but they were not investigated by the authors.

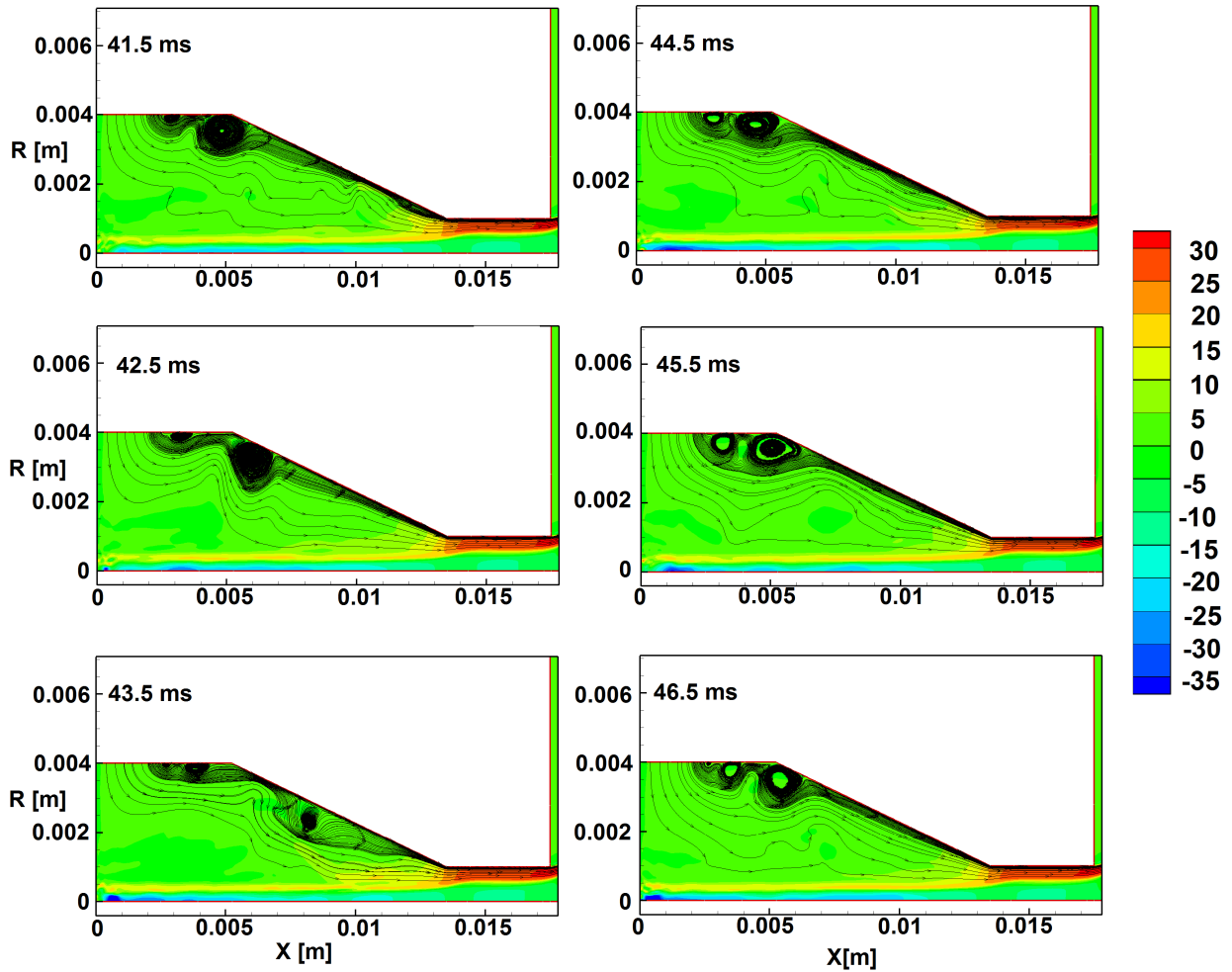


Figure 3.30: Evolution of the corner vortices near the swirl chamber wall.

Each vortex in the water region originates from the end of the mass flow inlet boundary, which is the main reason for the formation of vortices near the wall. At the inlet boundary the velocity vector has no axial component. The axial velocity of the water inside the atomizer develops so that the flow adjusts itself to go out from the nozzle. A corner vortex forms at the edge of the inlet boundary and grows in magnitude as it approaches to the concave region at the upper part of the swirl chamber. It is seen from Figure 3.30 that, at 41.5 ms, a small vortex near the mass flow inlet boundary is followed by a big vortex just below the concave part of the wall boundary. As time passes the big vortex below concave part of the wall moves downstream to the nozzle exit ($t=42.5$ ms) and loose its shape as it gains axial velocity with the flow ($t=43.5$

ms). Meanwhile the size of the small vortex near the mass flow boundary increases in time as it moves to the concave part of the swirl chamber ($t=44.5$). At this time an additional small vortex is identified again near the inlet boundary. The size of each vortex increases as it approaches to the concave part of the swirl chamber, which supports the idea that the vortices are affected by the instabilities in the boundary layer.

The time history of axial velocity at Probe2 ($x=5.25$ mm, $r=3.5$ mm) is given in Figure 3.31 together the frequency domain representation of the axial velocity signal.

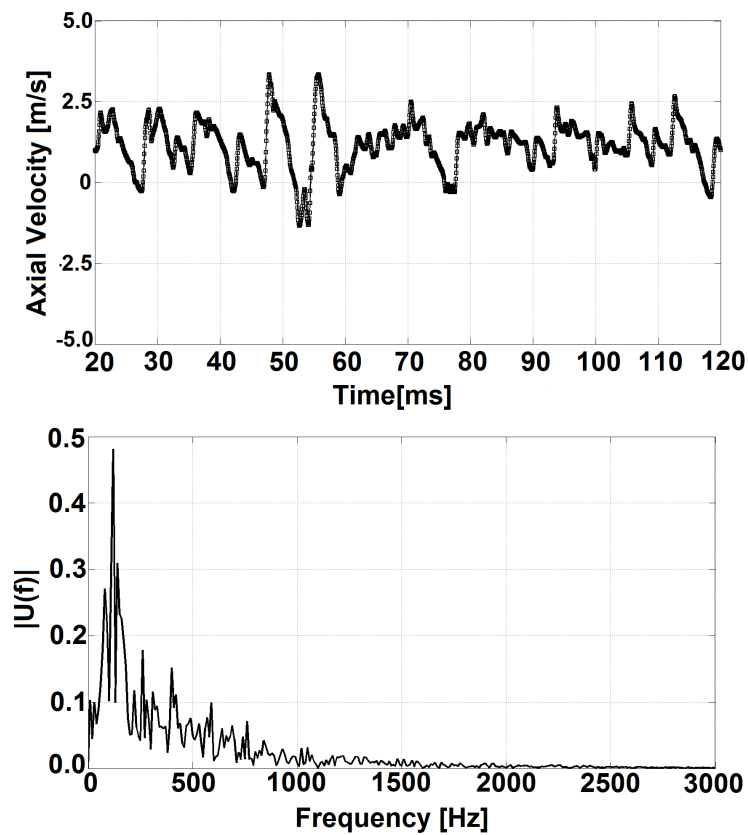


Figure 3.31: Time history of axial velocity and frequency domain representation of axial velocity signal.

The mean velocity at the probe is calculated as 1.17 m/s with a standard deviation of 0.73 m/s. The frequency spectrum of the axial velocity data at the probe reveals a dominant frequency at 120 Hz, which represents the frequency for the motion of corner vortices.

3.4.3.2 The Stagnation Region at the Head End of the Atomizer

In the present study, the 2D-AXS numerical predictions reveal an unsteady phenomena at the head end of the swirl chamber near the air core interface. The unsteady phenomena is attributed to the the stagnation region at the head end. The representation of the stagnation region is shown in Figure 3.32 as visualized by the volume fraction contours of air and in plane velocity vectors. The big arrow in the water region shows the water flow coming from the upper part of the swirl chamber, while the big arrow in the air core shows the air flow coming from outside of the atomizer. As the radial water flow meets the air core it tends to change its direction towards the nozzle of the atomizer. Similarly as the airflow meets the atomizer head end it tends to change its direction so that it flows out of the nozzle of the atomizer. Therefore a stagnation region is formed at the head end of the atomizer which leads to oscillations in the free surface at this region.

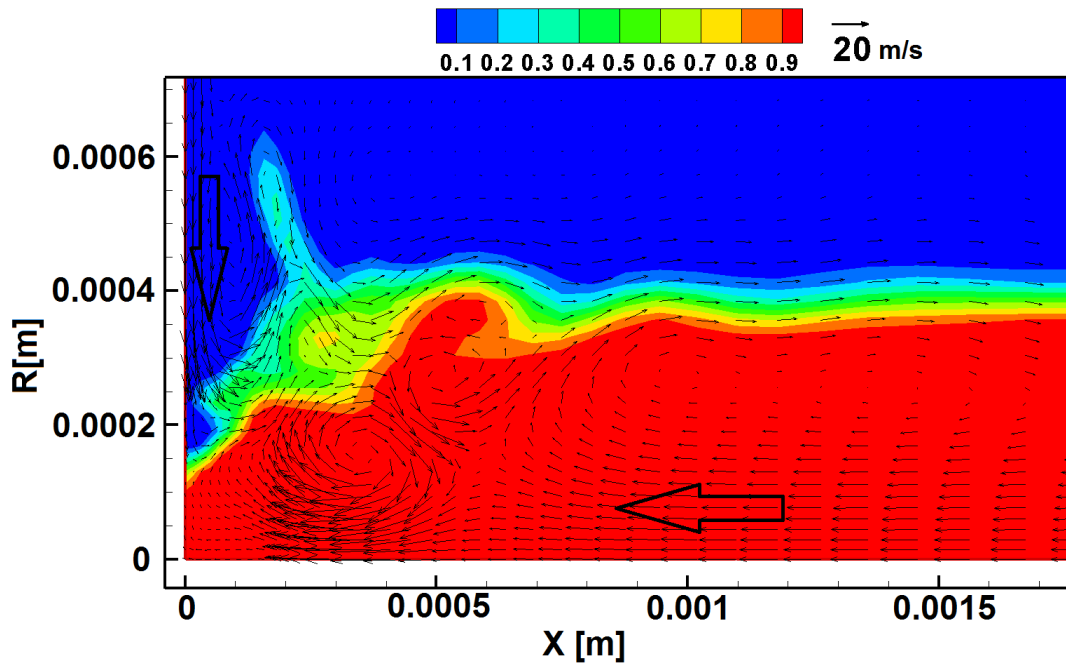


Figure 3.32: Stagnation region, water and air flows.

In order to have an idea about the frequency and amplitude of the oscillations of the free surface and the underlying flow physics, the volume fraction contours of air are shown together with the in plane velocity vectors in Figure 3.33. The time difference between each snapshot is constant and 0.1ms.

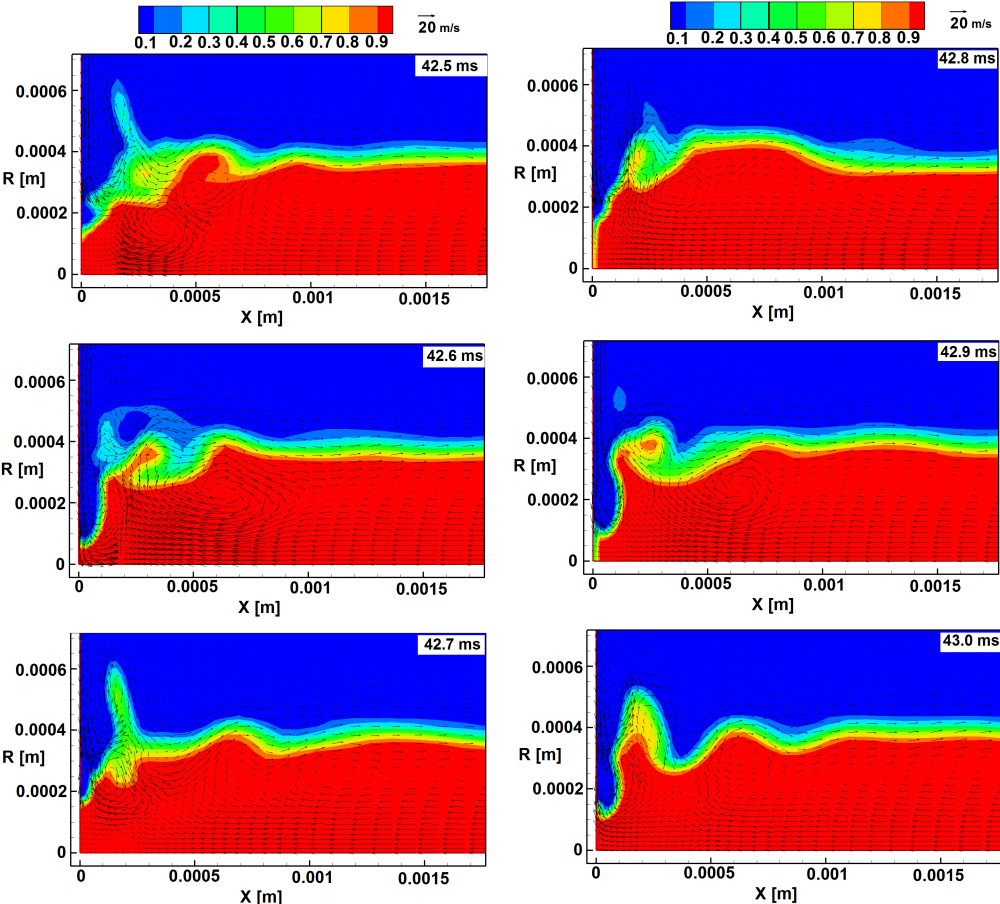


Figure 3.33: Stagnation region, volume fraction contours of air and in plane velocity vectors.

The time history of air core diameter can be calculated along a station at $x=0.2$ mm using the predicted volume fraction data. The time history of air core diameter along the station at $x=0.2$ mm is given in Figure 3.34 together with the frequency domain representation of the air core diameter signal.

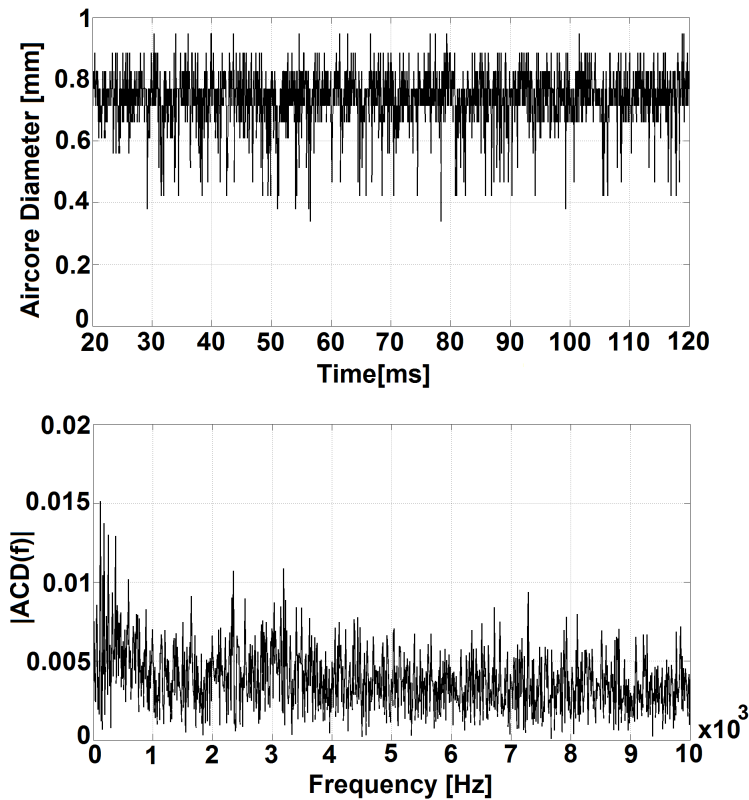


Figure 3.34: Time history of air core diameter and frequency domain representation of air core diameter signal along a station at $x=0.2$ mm.

The frequency domain representation of the air core diameter data reveals high frequency peaks at 2350 and 3190 Hz. In addition some low frequency peaks detected and the most dominant peak is at 120 Hz, which is the same dominant frequency that was found for the corner vortices in the previous section.

The time history of axial, radial and swirl velocity at Probe3 ($x=0.2$ mm, $r=0.15$ mm) within the air core close to the stagnation region are given in Figure 3.35 together with the frequency domain representation of the velocity signals. The mean axial velocity at the probe is calculated as -5.31 m/s with a standard deviation of 7.55 m/s, the mean radial velocity is calculated as 3.5 m/s with a standard deviation of 6.3 m/s and the mean swirl velocity is calculated as 8.2 m/s with a standard deviation of 6.96 m/s.

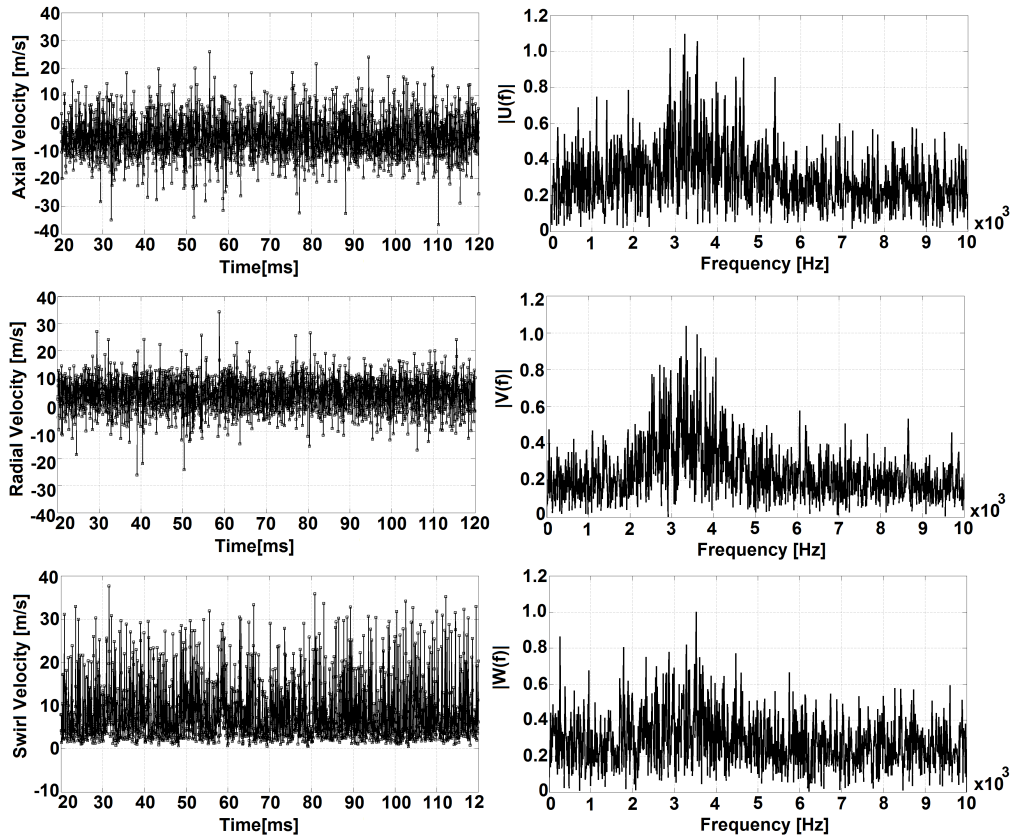


Figure 3.35: Time history of axial, radial and swirl velocity and frequency domain representation of velocity signals.

The frequency spectrum of the axial velocity and radial velocity data at Probe3 reveal several high frequency peaks between 2870 Hz and 5380 Hz and between 2520 and 4050 Hz, respectively. On the other hand, the frequency spectrum of the swirl velocity data at Probe3 reveals several high frequency peaks between 1780 Hz and 5750 Hz and a low frequency peak at 260 Hz. The high frequency peaks, which are identified using the frequency domain representation of the air core diameter along the station at $x=0.2$ mm, falls within the region at which the high frequency peaks are identified using the frequency domain representation of axial, radial and swirl velocity at Probe3.

The fluctuations of the air core interface are closely related to the unsteady flow phenomena occurring in the stagnation region at the head end of the atomizer.

3.4.3.3 Vortex Structures in the Air Core

General view of the vortex structures in the air core is presented in Figure 3.36 as visualized by volume fraction contours of air and streamlines originated from pressure outlet boundaries. There are several small vortices in the air core at the swirl chamber and convergence section of the atomizer. There is one relatively big vortex structure in the air core at the nozzle of the atomizer.

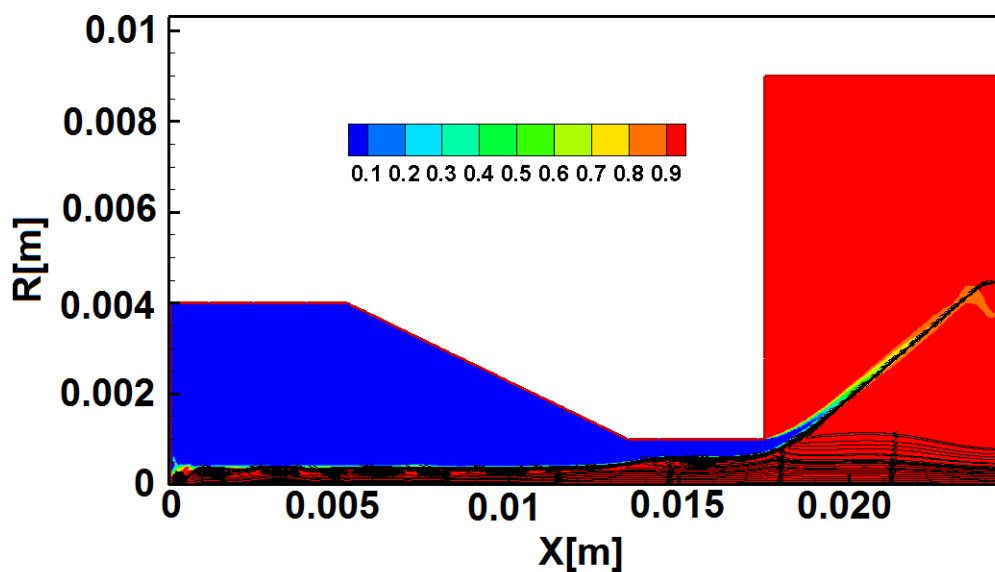


Figure 3.36: Vortex structures in the air core.

In order to present the vortices in detail, the air core region is zoomed in and the vortices in four different region of the air core are presented together in Figure 3.37. In the first region, the vortices in the air core region at the swirl chamber of the atomizer are presented. In the second and third regions the vortices in the convergence section are shown and in the fourth region the vortex in the air core at the nozzle section is shown.

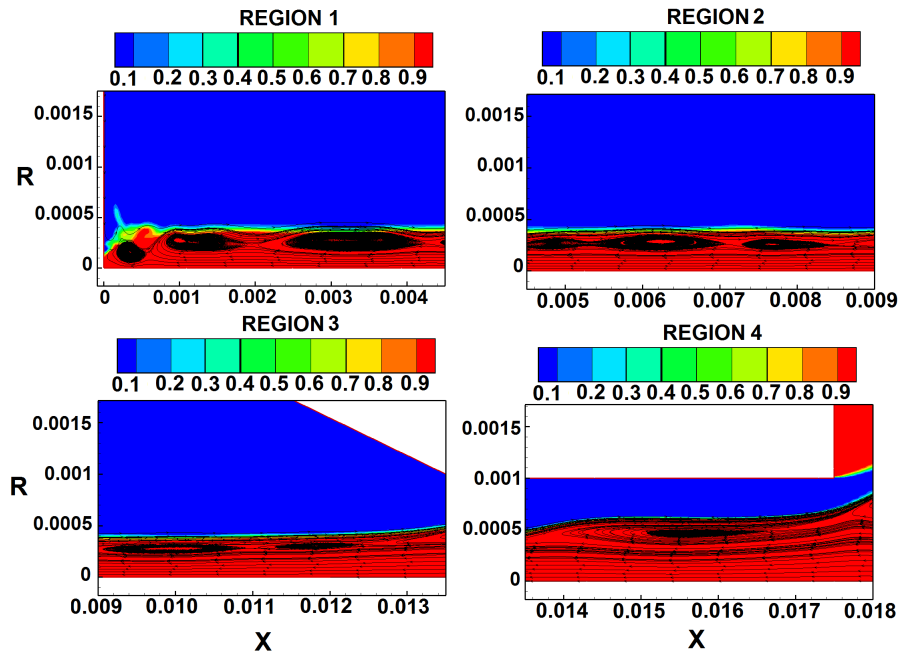


Figure 3.37: Vortex structures at four different regions of the air core.

As explained in Section 4.4.2, below the transition region, air flow into the atomizer is identified at radial locations close to the axis, and air flow out of the atomizer is identified at radial locations close to the transition region. As a result, there are inflation points at the air region at which the in plane velocity of air is zero. This behavior of the velocity field in the air core region favors the formation of the vortices in the air core. The evolution of the vortices in the air core is presented in Figure 3.38. The size of the vortices are big close to the head end region and their effect on the shape of the air core are discernible. As one moves from head end of the atomizer to the nozzle, the vortex stretching occurs and the effect of vortices on the shape of the air core becomes small.

Although, the formation of the vortices in the air core away from the stagnation region does not depend on the flow physics at the head end, their instationary nature seems to be due to the disturbances created at the head end.

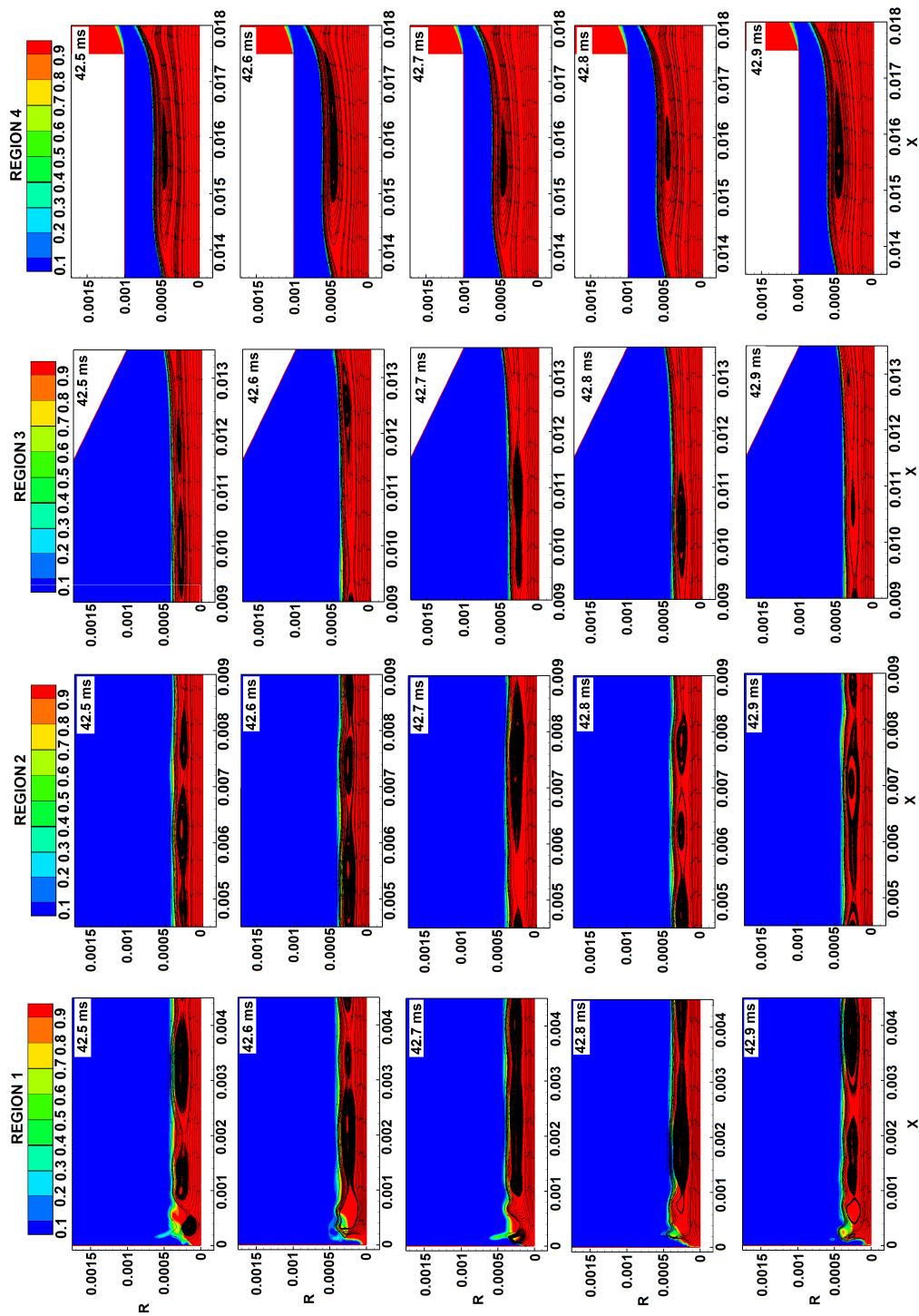


Figure 3.38: Evolution of the vortices in the air core.

The time history of axial velocity at Probe4 ($x=1.109$ mm, $r=0.275$ mm), Probe5 ($x=3.5$ mm, $y=0.275$ mm) Probe6 ($x=17.5$ mm, $r=0.55$ mm) are given in Figure 3.39 together with the frequency domain representation the axial velocity signal at each probe point. The probe points in the air core are selected such that they are in the vicinity of a vortex at an instant of time.

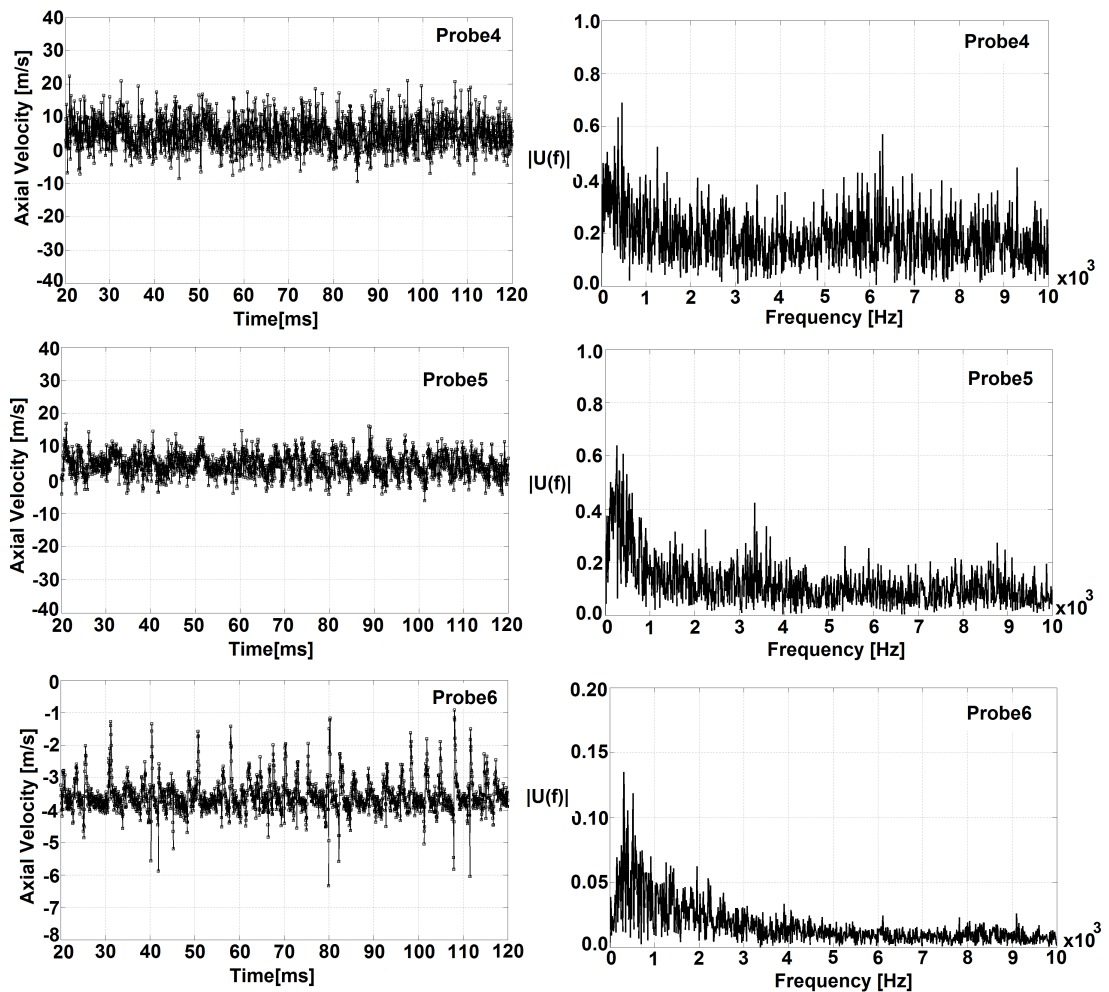


Figure 3.39: Time history of axial velocity and frequency domain representation of axial velocity signal.

The mean axial velocities and the corresponding standard deviations and the frequencies at which the amplitude peaks are detected are tabulated in Table 3.3.

Table 3.3: Predicted mean axial velocities, corresponding standard deviations and the frequency peaks at designated probe points .

	Probe Number		
	4	5	6
x coordinate [mm]	1.1	3.5	17.5
r coordinate [mm]	0.275	0.275	0.550
Mean axial velocity [m/s]	4.94	4.48	-3.52
Standard deviation [m/s]	4.54	3.26	0.505
Low frequency peaks [Hz]	370-460	260-400	310-520
High Frequency peaks [Hz]	6290	3340	None

Investigation of Figure 3.39 and Table 3.3 shows that the standard deviation from the mean axial velocity decreases from the head end of the atomizer to the nozzle exit. Low frequency amplitude peaks as well as high frequency amplitude peaks are identified at probe points close to the head end, but the amplitude of the high frequency oscillations diminishes rapidly starting with Probe3. At the exit of the atomizer high amplitude peaks are no longer present in the frequency domain representation of the axial velocity signal. The low frequency amplitude peaks are between 260-520 Hz and the high frequency peaks are between 3340-6290 Hz depending on the axial location.

3.4.4 Analysis of the Air Core Diameter

The time history of air core diameter is calculated along different stations using the predicted volume fraction data. The time history of air core diameter data is given in Figure 3.40 for six different stations. The time history of air core diameter at other stations are given in Appendix D.

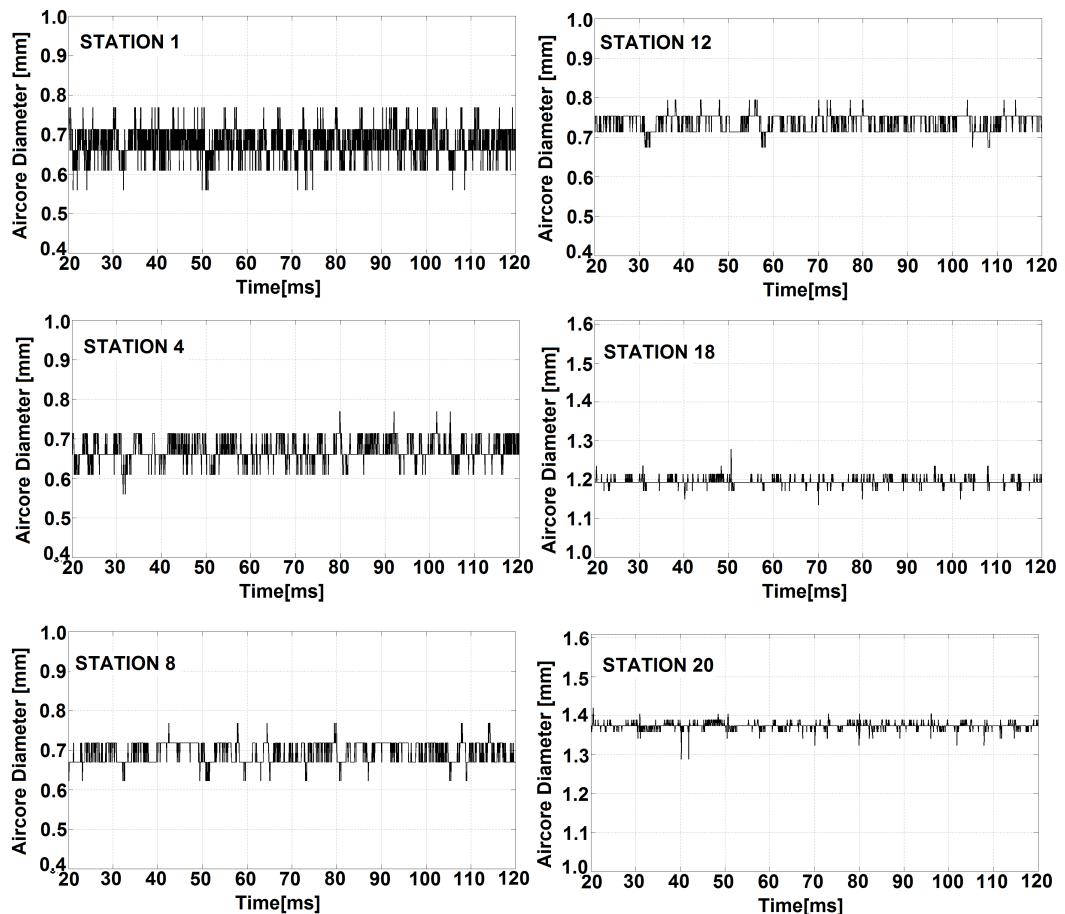


Figure 3.40: Time history of air core diameter at designated stations.

The amplitude of oscillations of the air core diameter data is maximum close to the head end of the atomizer (Station 1 and Station 4). As one moves from the head end of the atomizer to the nozzle, the amplitude of the oscillations decreases (Station 8, 12, 18 and 20).

The frequency domain representation of the air core diameter data are given in Figure

3.41 for the stations whose time domain representations are given previously in Figure 3.40. The frequency spectrum plots of diameter at all stations are given in Appendix E. The frequency spectrum of the air core diameter signal reveals that the dominant frequency ranges depend on the axial location of the Station along which the air core diameter is calculated.

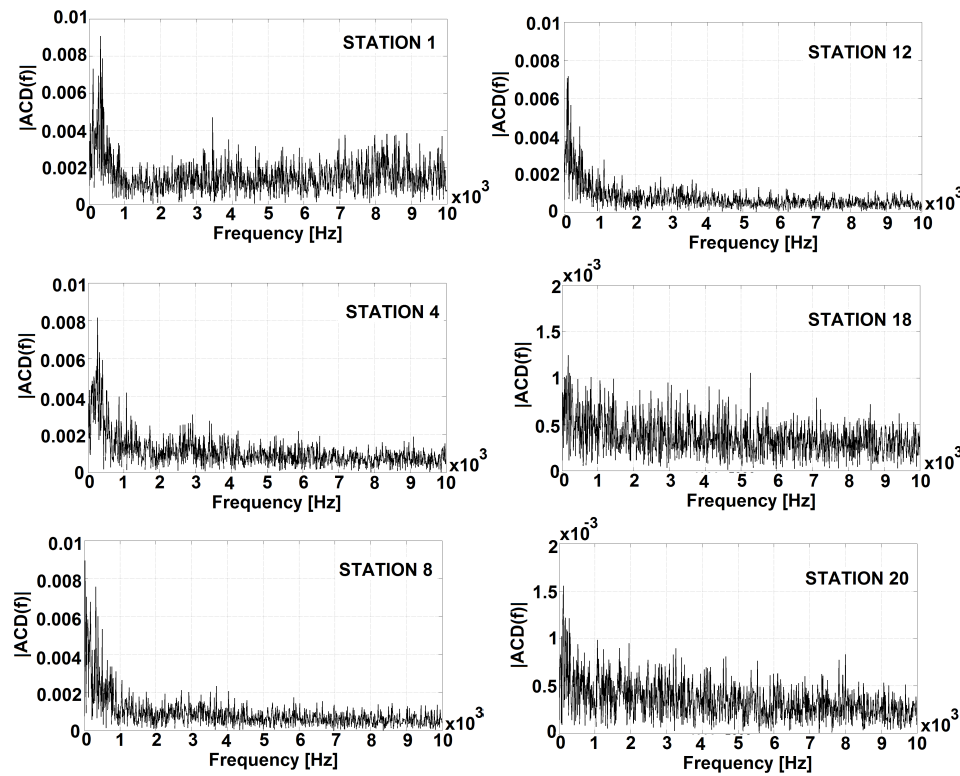


Figure 3.41: Frequency spectrum of air core diameter.

At stations close to the head end of the atomizer (Station 1 and Station 4), dominant low frequency peaks are detected, together with relatively low amplitude high frequency peaks. At Station 1 dominant low frequency peaks are detected at 120 Hz, 320 Hz and 370 Hz, and relatively low amplitude high frequency peaks are detected between 3450 Hz and 8320 Hz. At Station 4 dominant low frequency peaks are detected at 260 Hz and 320 Hz and no discernible high frequency peaks are detected. At Station 8 and Station 12 there is no dominant high frequency peaks. Dominant low frequency peaks are detected at 320 and 380 Hz at Station 8. The decrease in amplitude of the oscillations at the nozzle section reveals itself in the frequency amplitude

plots at Station 18 and Station 20. At station 18 and at the exit several amplitude peaks are detected between 0-5260 Hz with comparable amplitude as in the case of experiments.

3.4.5 Comparison of Results

The comparison of the predicted mean air core diameter from AXS numerical simulations with the measured mean air core diameter data using High Speed Shadowgraphy System are given in Figure 3.42. The error bars in Figure 3.42 represents the standard deviation from the mean for each mean air core diameter data.

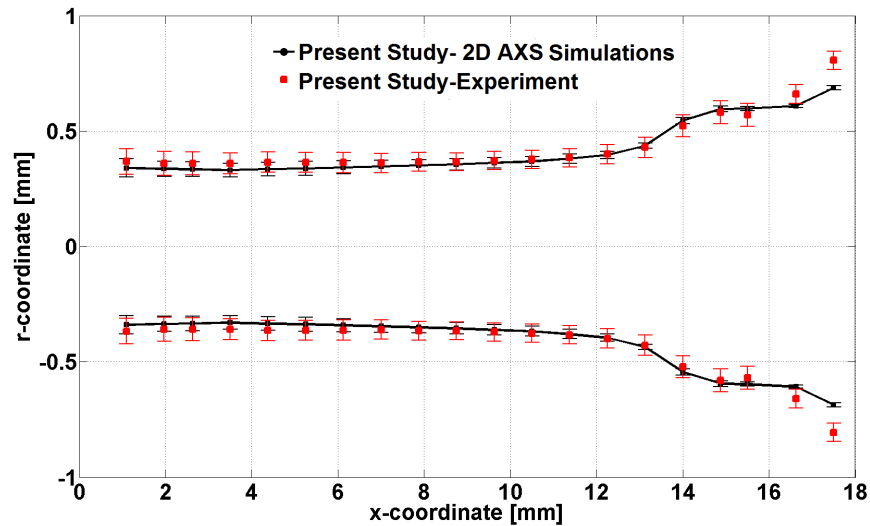


Figure 3.42: Mean air core diameter and standard deviations.

The shape of the air core predicted by the 2D-AXS simulations is similar to that obtained from the High Speed Shadowgraphy Experiments. The calculated mean air core diameters are almost constant between Station1 ($x=1.09$ mm) and Station 12 ($x=10.5$ mm). The mean air core diameters predicted by the 2D-AXS numerical simulations are lower along the swirl chamber and the convergence section up to Station 14 when compared to air core diameters obtained from the experiment. At Station 14 the air core diameters predicted by both the 2D-AXS numerical simulations and the experiments are the same and is equal to 0.79 mm. Starting from Station

15 up to Station 19 the air core diameter predicted by the 2D-AXS simulations are slightly higher than the experimental values. At Station 19 and Station 20 the air core obtained from the experiments are higher than those predicted by the 2D-AXS numerical simulations.

The standard deviation from the mean air core diameter is maximum at Station 1 for both air core diameter data obtained from the experiments and predicted by 2D-AXS numerical simulations. The standard deviation from the mean air core diameter data, which is obtained from the experiment is higher than the one that is predicted by the 2D-AXS numerical simulations at all stations. The standard deviations from the mean air core diameter, predicted by the simulations and measured with the experiments, decrease up to Station 12. The standard deviation from the mean air core diameter as obtained from the experiment increases up to mid nozzle and decreases to a minimum at the exit of the atomizer. However, the standard deviations from the mean air core diameter, which is predicted by the 2D-AXS numerical simulations, decreases with increasing axial coordinate all the way down to the atomizer exit.

The comparison of numerically obtained mean air core diameter values and mean air core values obtained from the High Speed Shadowgraphy Experiments are given in Table 3.4 at six different stations.

Table 3.4: Comparison of air core diameters at designated stations .

	Present Study Air Core Diameter [mm]		
	2D AXS	Experiment	% Difference
Station 1	0.67	0.73	7.7
Station 4	0.66	0.72	8.1
Station 8	0.69	0.72	3.8
Station 12	0.73	0.75	2.3
Station 18	1.19	1.14	4.7
Station 20	1.37	1.61	14.7

The comparison of the frequency domain representations of the air core diameter data, which are obtained from the experiments and predicted by the 2D-AXS numerical simulations, are given together in Figure 3.43.

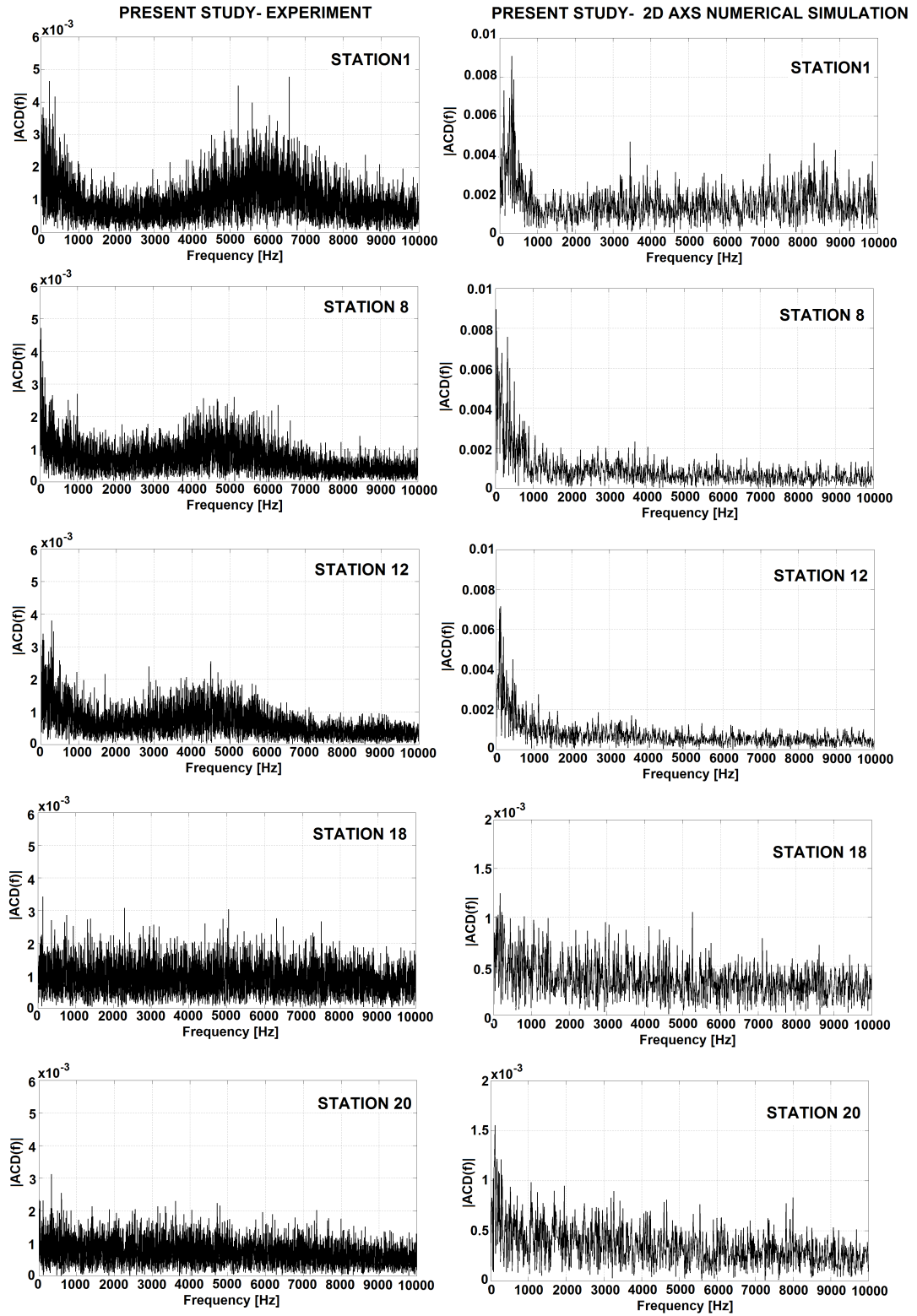


Figure 3.43: Comparison of frequency spectrum of air core diameter at designated stations, experiment and AXS numerical simulations.

At stations close to the head end, both dominant low frequency peaks and dominant high frequency peaks are identified from the frequency spectrum of the experimental data. The amplitude of the high frequency oscillations are comparable that of the low frequency oscillations up to Station 8. However the frequency spectrum of the air core diameter data, which is predicted by the 2D-AXS numerical simulations, has some high frequency peaks with small amplitude only at Station1. The frequency peak at 3450 Hz is within the high frequency range measured by the experiments. The oscillations at the interface seems to localize to the stagnation region and it is barely perceived at locations away from the head end. The fact that the high frequency peaks are identified only at two stations close to the head end in 2D-AXS numerical simulations may be due to the inefficiency of the axis-symmetric simulations together with the VOF method to handle the high frequency low amplitude oscillations.

The frequency spectrum of air core diameter data obtained from the experiments, and 2D-AXS numerical simulations both have low frequency peaks at all stations. The low frequency peaks, which are identified on the frequency spectrum of the air core diameter data predicted by the 2D-AXS numerical simulations are all within the low frequency range, which is found from the frequency spectrum of the experimental data.

At the exit of the atomizer a low frequency amplitude peak is identified at 280 Hz, which is close to the experimentally obtained low frequency peak of 332 Hz.

3.5 Three Dimensional Flow Simulations

3.5.1 Introduction

In this section the results of the three dimensional (3D) numerical simulations, performed with the ANSYS-FLUENT software, are presented. The major characteristics of the GRID3, which was used in AXS numerical simulations, are extended to third dimension in 3D numerical simulations.

The geometry of the solution domain and computational grid used in 3D flow simulations are given together in Figure 3.44. Using the advantage of periodicity of the flow, only one half of the atomizer is modeled and the periodic boundary condition is applied to the boundary shown in dark blue in Figure 3.44. The mass flow inlet boundary condition is applied at the tangential inlet. Pressure outlet boundary conditions are applied at the outer boundaries. No slip boundary condition is applied at the wall boundaries.

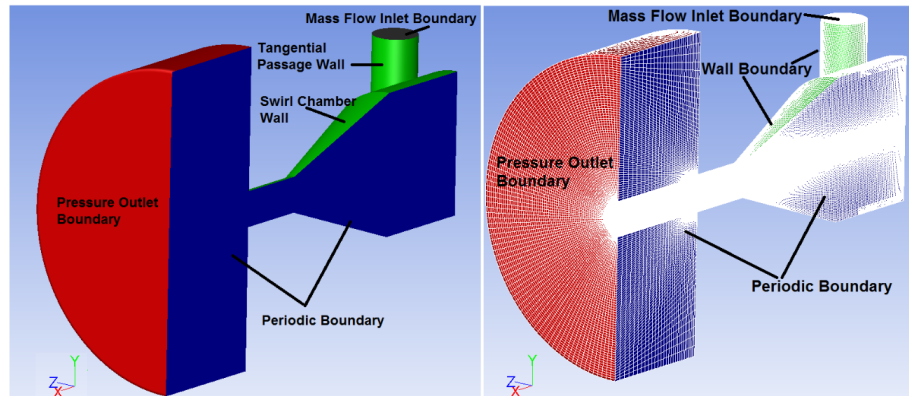


Figure 3.44: The geometry of the solution domain and computational grid for 3D flow simulations.

The computational grid is hybrid; it contains tetrahedral elements at the tangential passage and at a small volume on swirl chamber adjacent to the tangential passage. In the remaining parts the grid contains hexahedral elements. The computational grid contains 1.800.000 elements in total.

Unsteady, three dimensional, laminar flow simulations are performed with the com-

putational grid shown in Figure 3.44 using the pressure based solver. Mass flow rate of water is defined as 0.0265 kg/s at the mass flow inlet boundary, the total mass flow into the atomizer is 0.053 kg/s due periodicity. Implicit time integration is used for the unsteady solution of the Navier-Stokes equations and explicit time integration scheme is used for the solution of the VOF equation. In order to meet the stability criterion for the VOF calculations the CFL number is kept smaller than 2 by decreasing the time step accordingly.

3.5.2 Flow Through the Pressure Swirl Atomizer

The flow through the pressure swirl atomizer is solved using ANSYS-FLUENT software. The solution is initialized such that the air is present inside the computational domain ($\alpha_a=1$) except for the mass flow inlet boundary at which the volume fraction of the air is always 0. Initial volume fraction contours of air is shown in Figure 3.45.

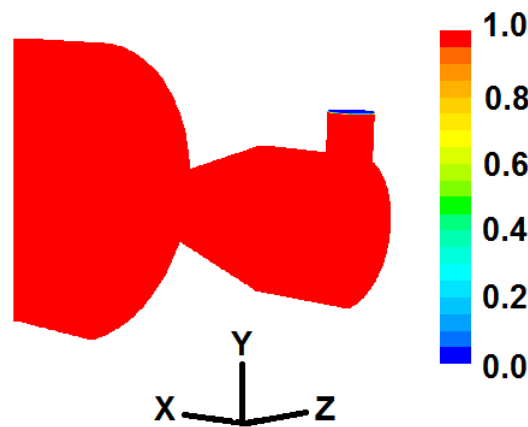


Figure 3.45: Initial volume fractions contours of air.

A fixed time step size of $0.5 \mu s$ is used in 3D numerical simulations and the total simulation time is 71 ms. The solutions are second order accurate in space and first order accurate in time. The iterative time advancement scheme of ANSYS-FLUENT is used to solve the unsteady flow. In the iterative time advancement scheme, all the equations are solved iteratively for a given time step until the convergence criteria are met. Therefore, in order to advance the solution for one time step, it is necessary to

perform a number of outer iterations. The number of outer iterations performed in the present study is kept constant at 20 for performed numerical simulations.

The evolution of air volume fraction with time is given in Figure 3.46 starting from 1ms up to 13ms. At about 7 ms water jet goes out of the atomizer and at 13 ms a hollow cone liquid jet is formed.

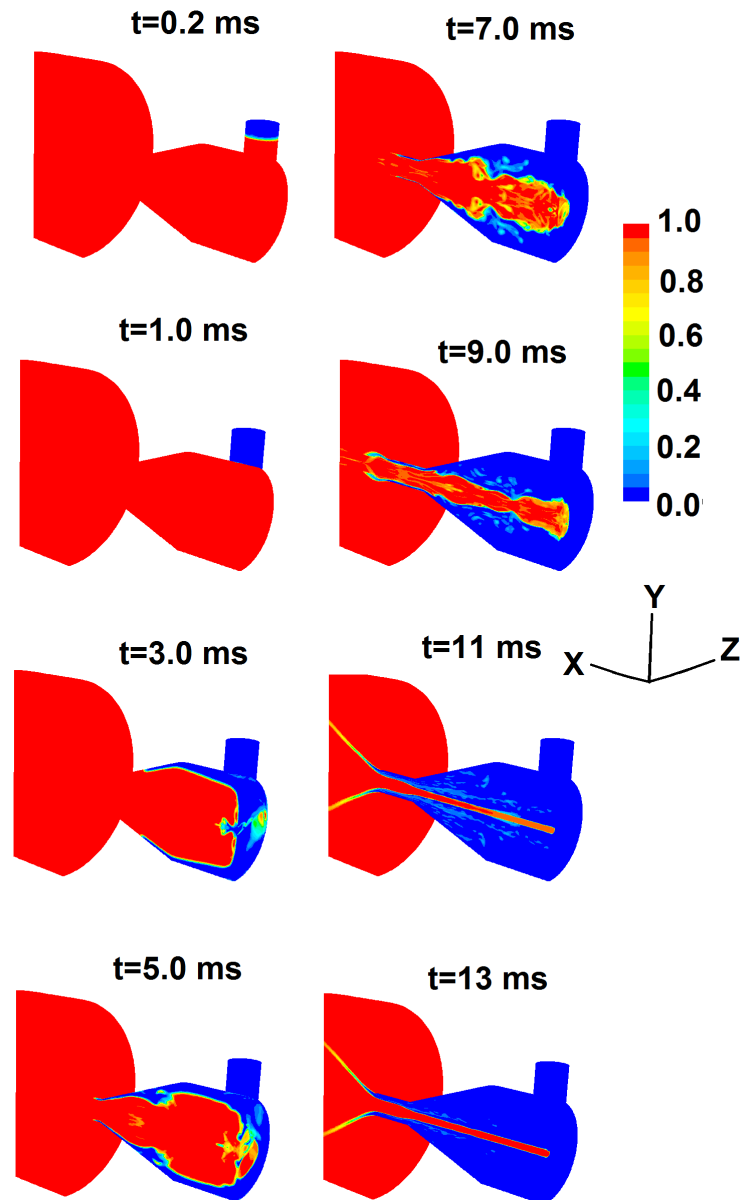


Figure 3.46: Evolution of the volume fractions contours of air.

The simulations are continued up to 71 ms and the statistical results that will be presented in the following sections are obtained using the simulation data obtained between 25 ms and 71 ms. It takes about one month to have the results of a 50 ms unsteady simulation with 64 high end cores in parallel.

The mean volume fraction contours of air are given in Figure 3.47 at different slides along the axis of the atomizer and at a slide in x-z plane.

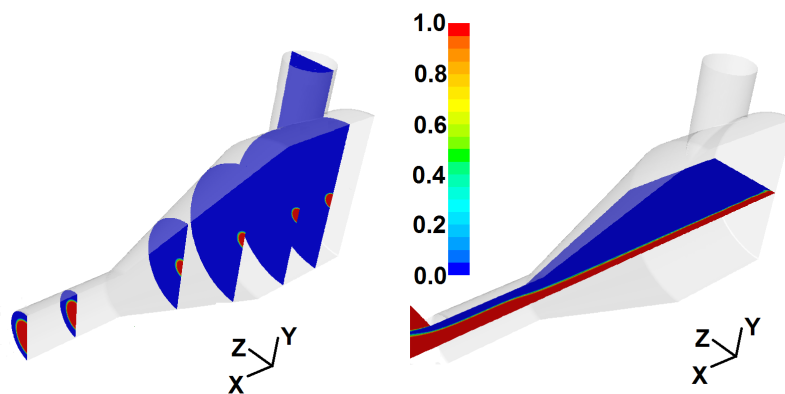


Figure 3.47: Mean volume fraction contours of air.

The mean air core diameter is minimum at the head end of the atomizer and almost constant along the swirl chamber. The air core diameter starts to increase at convergence part of the atomizer and have its maximum value at the exit of the nozzle.

The mean axial velocity contours are given in Figure 3.48 at different slides along the axis of the atomizer and at a slide in x-z plane.

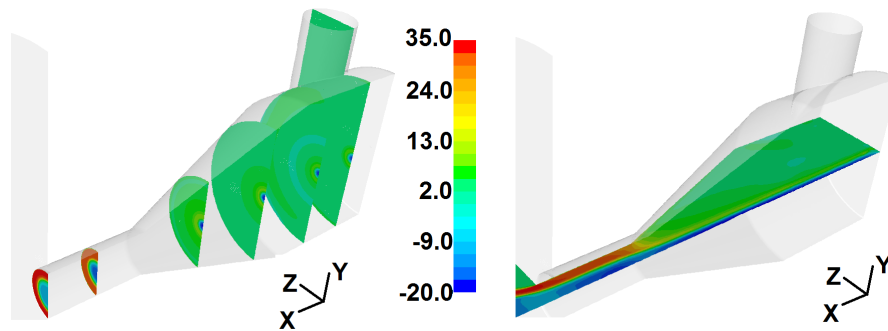


Figure 3.48: Mean axial velocity contours.

The maximum mean velocity is predicted at the exit of the atomizer and the maximum value for the mean axial velocity is 35.8 m/s. The minimum mean axial velocity is predicted at the air core and the minimum velocity for the mean axial velocity is -20 m/s. The axial velocity distributions are further investigated along six different stations at three different planes. The orientations of the planes ($\theta=45^\circ$, $\theta=90^\circ$ and $\theta=135^\circ$) are shown in Figure 3.49 along with the plane that periodic boundary condition is applied.

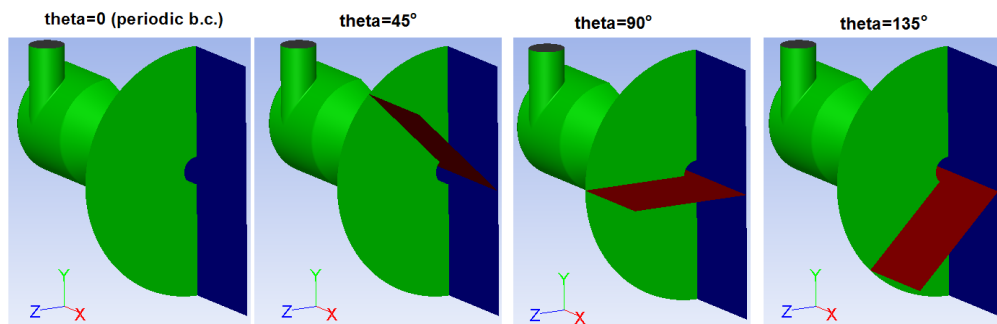


Figure 3.49: Periodic boundaries and three different planes.

The mean axial velocity distributions along different stations are shown together in Figure 3.50 at three different planes. Minor differences in the mean axial velocity present at stations close to the head end of the atomizer. This is due to the presence of the tangential inlet through which the water goes in to the atomizer.

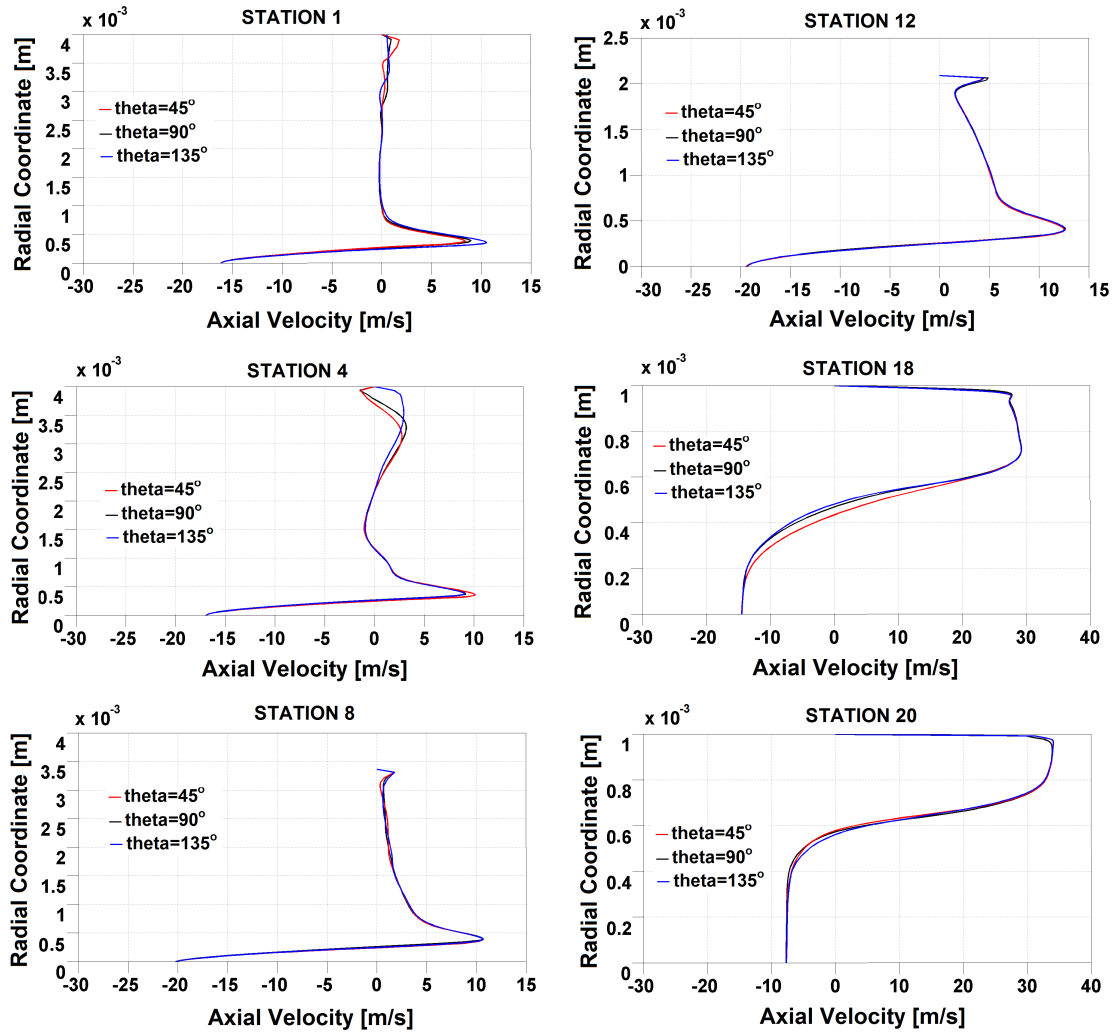


Figure 3.50: Comparison of mean axial velocities at three different planes .

The mean axial velocity distributions and the corresponding standard deviations, which are obtained from the 3D numerical simulations along stations at $\theta=90^\circ$ plane, are compared with the mean axial velocities and standard deviations, which are obtained from the 2D-AXS numerical simulations in Figure 3.51.

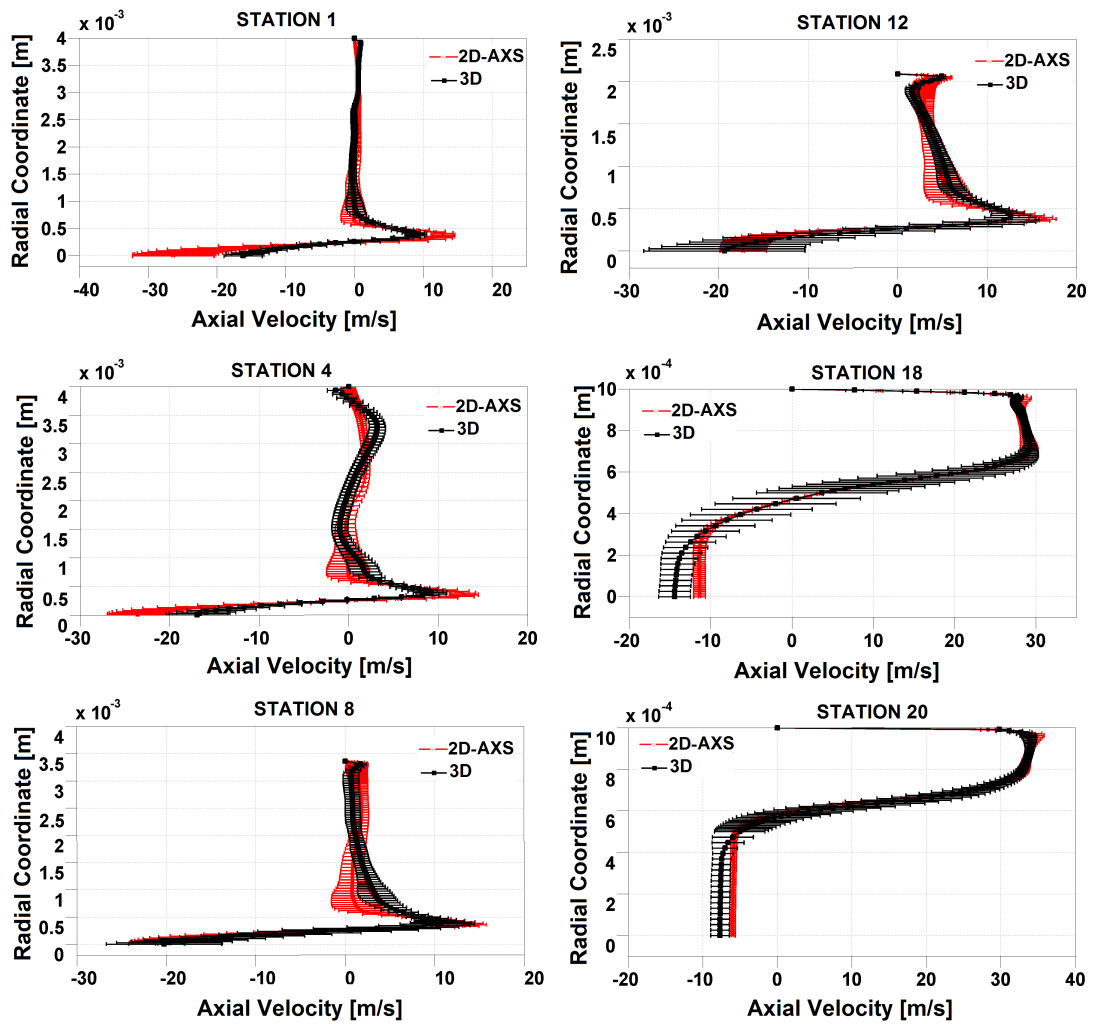


Figure 3.51: Comparison of 3D mean axial velocities and the corresponding standard deviations (theta=90 plane) and 2D-AXS mean axial velocities and the corresponding standard deviations.

The mean axial velocity distributions are similar in all stations. The minimum mean axial velocity predicted by the AXS numerical simulations are higher at stations close to the head end of the atomizer (Station 1 and Station 4). This is mainly due to the fact that, in 3D numerical simulations and water goes into the atomizer from a discrete number of tangential ports. Sufficiently away from the head end (Station 8), the predicted minimum mean axial velocities are differed only 1 m/s. The predicted maximum mean axial velocities are close to each other at all Stations. At the exit of the atomizer the maximum mean axial velocity differs only 0.5 m/s. The standard

deviation from the mean axial velocity, predicted by 2D-AXS simulations, is higher for stations close to the head end of the atomizer. Starting with Station 8 up to the exit of the atomizer (Station 20) standard deviation from the mean axial velocity predicted by 3D numerical simulations is higher than that predicted by 2D-AXS simulations.

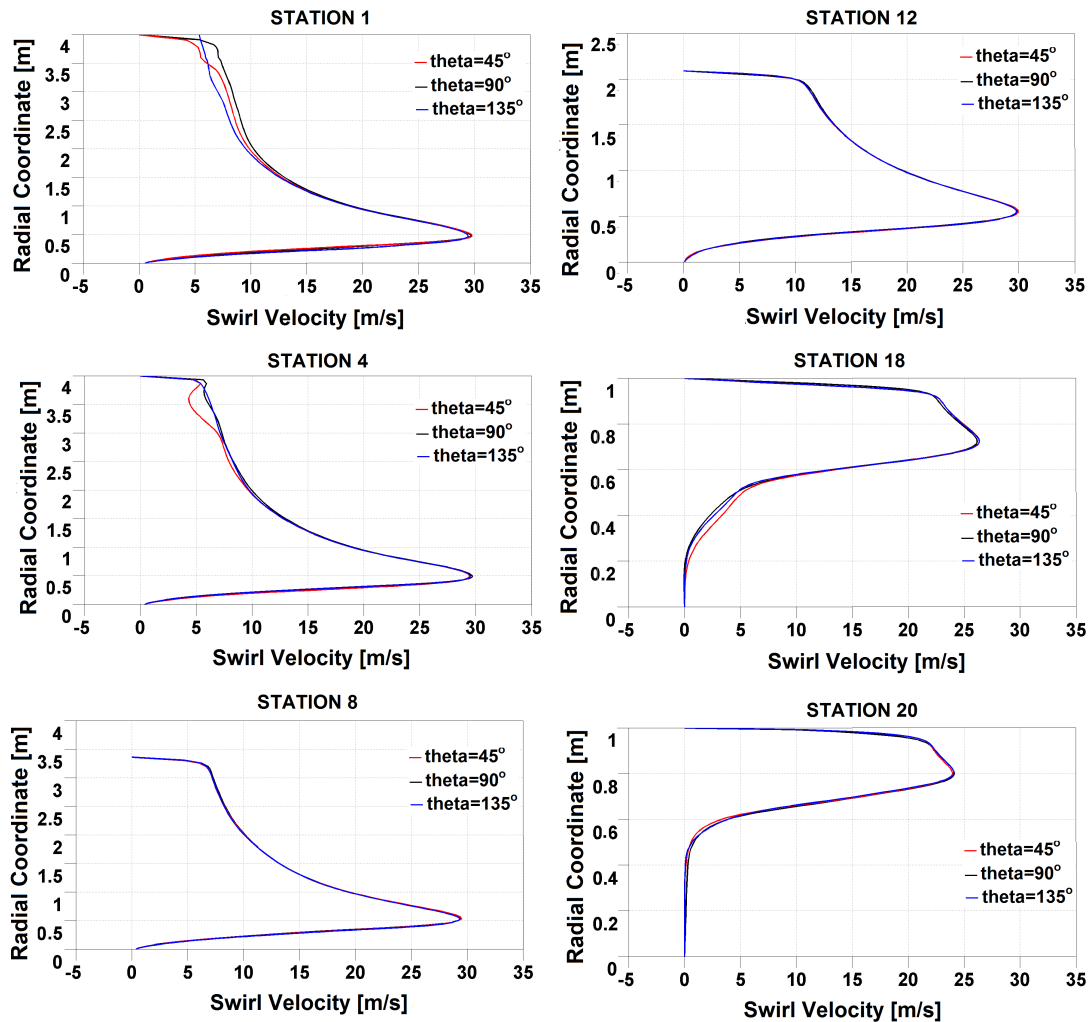


Figure 3.52: Comparison of mean swirl velocities at three different planes.

The mean swirl velocity distributions along different stations are shown together in Figure 3.52 at three different planes. The effect of the tangential inlet passage on the swirl velocity distribution along Station 1 is obvious. There is no swirl velocity component of the flow at $r=4$ mm on planes $\theta=45^\circ$ and $\theta=90^\circ$ but the swirl velocity is 5.4 m/s at $r=4$ mm on plane $\theta=135^\circ$. At the depicted location the flow has a

swirl velocity component due to the tangential inlet passage and the swirl velocity component is the same as the mean flow velocity in the tangential inlet passage. The swirl velocity distributions along other stations are similar for all planes.

The mean swirl velocities and the corresponding standard deviations, which are obtained from the 3D numerical simulations along stations at theta=90 plane, are compared with the mean swirl velocities and standard deviations, which are obtained from the AXS numerical simulations in Figure 3.53.

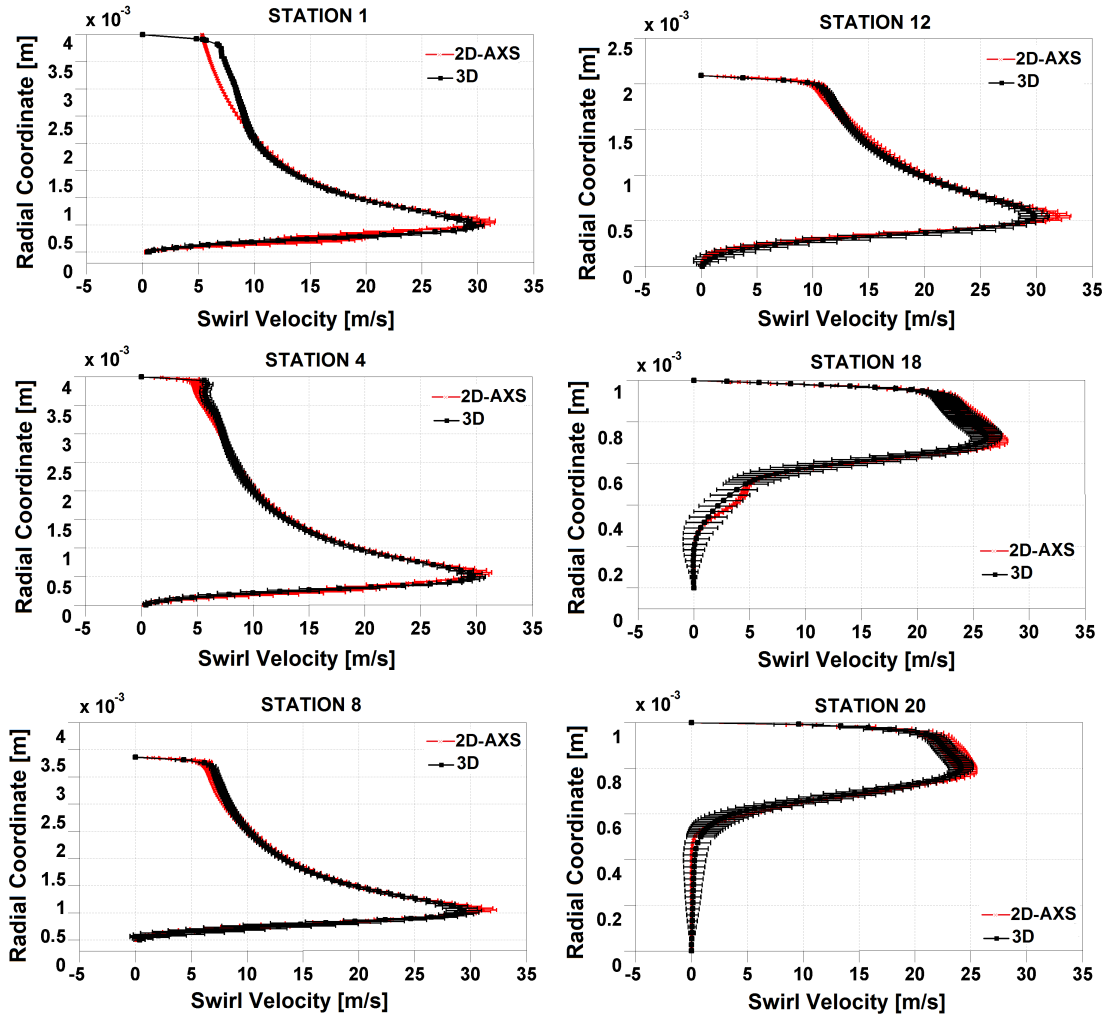


Figure 3.53: Comparison of 3D mean swirl velocities and the corresponding standard deviations (theta=90 plane) and AXS mean swirl velocities and the corresponding standard deviations.

There is a major difference in the mean swirl velocity distribution along Station 1.

The 2D-AXS numerical simulations predicts a finite velocity at $r=4$ mm, whereas the 3D numerical simulations give zero velocity at the same location. This due to the implementation of the mass flow inlet boundary condition in 2D-AXS numerical simulations, in which a finite swirl velocity is defined at mass flow inlet boundaries. Whereas in 3D numerical simulations mass flow of water is defined perpendicular to the mass flow inlet boundary at the specified mass flow rate. The mean swirl velocity distributions is similar away from the head end for all stations. On the other hand, standard deviations from the mean differs considerably starting from Station 12 up to the exit of the nozzle, with the standard deviations from the mean swirl velocity predicted by the 3D numerical simulations higher than that of AXS numerical simulations.

3.5.3 Vortex Dynamics

In this section the 3D numerical simulations are further investigated for the vortex structures that has been identified before with AXS numerical simulations. The time history of vortex structures in the water region is visualized using the Q-criterion, which is defined as follows;

$$Q = \frac{1}{2}(\|\Omega\|^2 - \|S\|^2) > 0 \quad (3.10)$$

where Ω is the vorticity magnitude and S is the strain rate magnitude. Flow inside the pressure swirl atomizer is dominated by the shear region near the air core vortex. As a result it is hard to identify the vortex structures in the water region by only considering the vorticity magnitude. The Q-criterion represents the locations inside the pressure swirl atomizer where rotation dominates the shear.

The vortices in the water region and the air core vortex, as visualized by Q-isosurfaces with a threshold value of 2×10^7 , are given in Figure 3.54 at six instants of time.

Two different vortices are identified in the water region. There are some helical vortices close to the wall of the swirl chamber which rotates and travels along the axial coordinate ($t=45$ - $t=46.5$ ms). As they travel down to the nozzle of the atomizer, the vortices near wall stretches and join to the air core vortex ($t=47$ - $t=48$ ms). In addition there are several small helical vortices in the swirl chamber which effects the air core vortex locally.

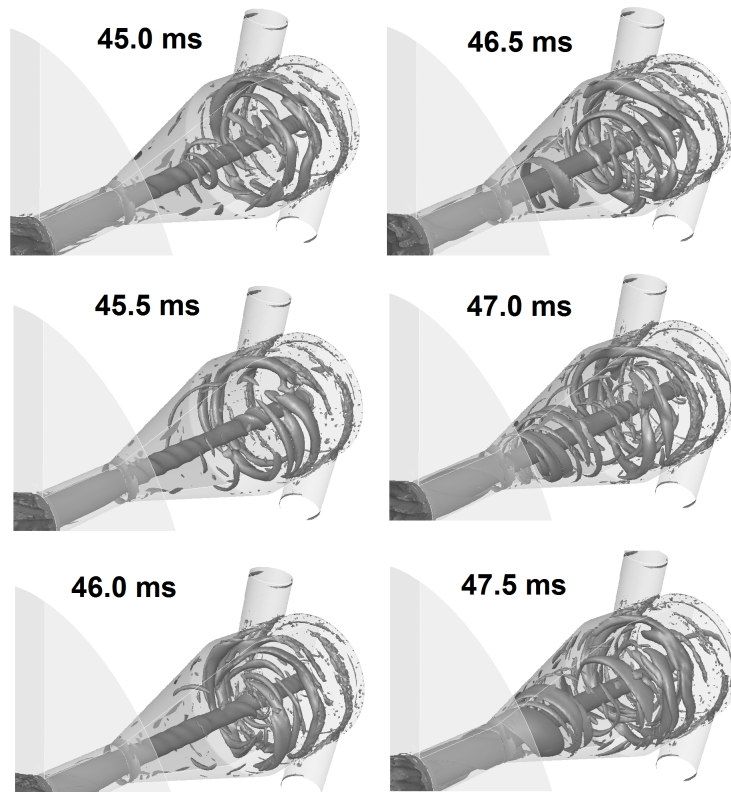


Figure 3.54: Vortices in the water region and air core vortex as visualized by Q-isosurfaces.

The contours of volume fraction together with the in plane velocity vectors in $\theta=90$ plane are given together in Figure 3.55 for five different simulation time. The velocity vectors shows the air is being sucked in to the atomizer and there is an inflation point within the air core at which the in plane velocity is zero. This behavior is in agreement with the results of the 2D-AXS numerical simulations. There exist small vortices within the air core which results in squeezing and swelling of the air core.

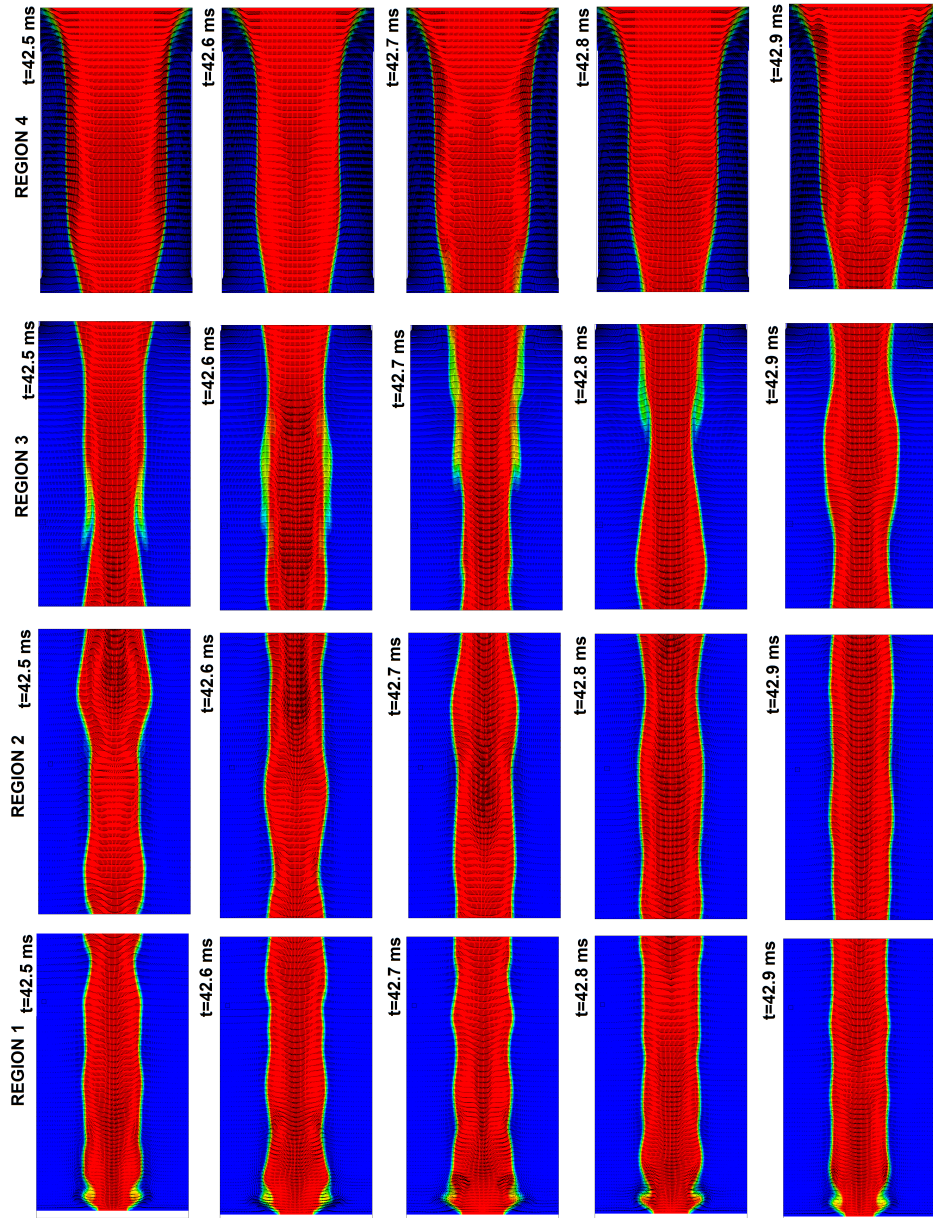


Figure 3.55: Contours of volume fraction and in plane velocity vectors ($\theta=90^\circ$).

Contrary to the results of 2D-AXS numerical simulations the effect of the vortices within the air core to the shape of the interface is discernible even at axial locations away from the head end.

The shape of the air core is illustrated in Figure 3.56 for two instants of time as visualized by the isosurfaces of volume fraction of air. The squeezing and swelling of the air core at the inlet of the nozzle can be identified by comparing the two images. The rotational waves on the air core are discernible in both images given in Figure 3.56.

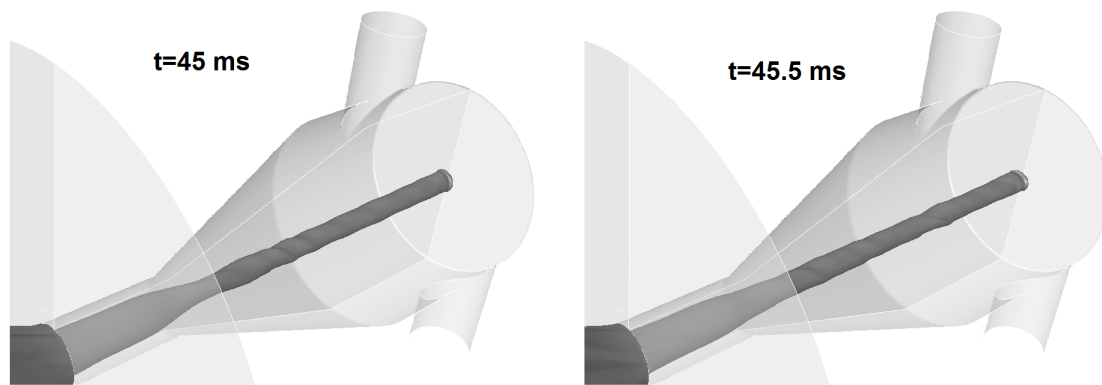


Figure 3.56: Isosurfaces of volume fraction of air .

3.5.4 Analysis of the Air Core Diameter

The time history of air core diameter is calculated along different stations at plane $\theta=90$ using the predicted volume fraction data. The time history of air core diameter data is given in Figure 3.57 for four different stations.

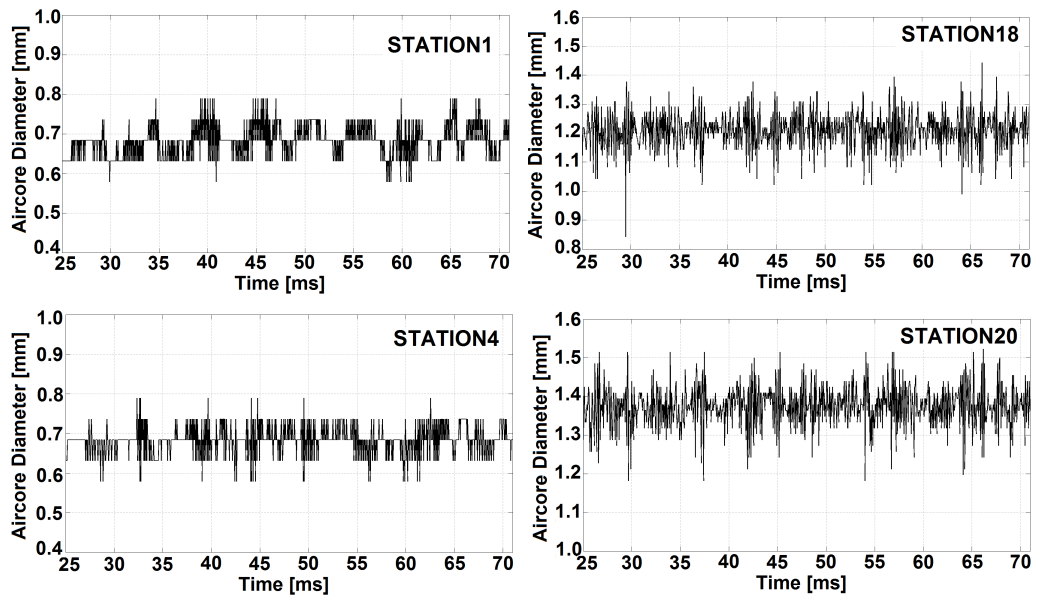


Figure 3.57: Time history of air core diameter at designated stations ($\theta=90$).

As one moves from the head end of the atomizer (Station1, Station4) to the nozzle (Station18, Station20), the amplitude of the oscillations do not decrease in contrary to the results of the AXS numerical simulations. The frequency domain representation of the air core diameter data are given in Figure 3.58 for the stations whose time domain representations are given previously in Figure 3.57. The frequency spectrum of the air core diameter signal reveals that the dominant frequency ranges depends on the axial location of the Station along which the air core diameter is calculated.

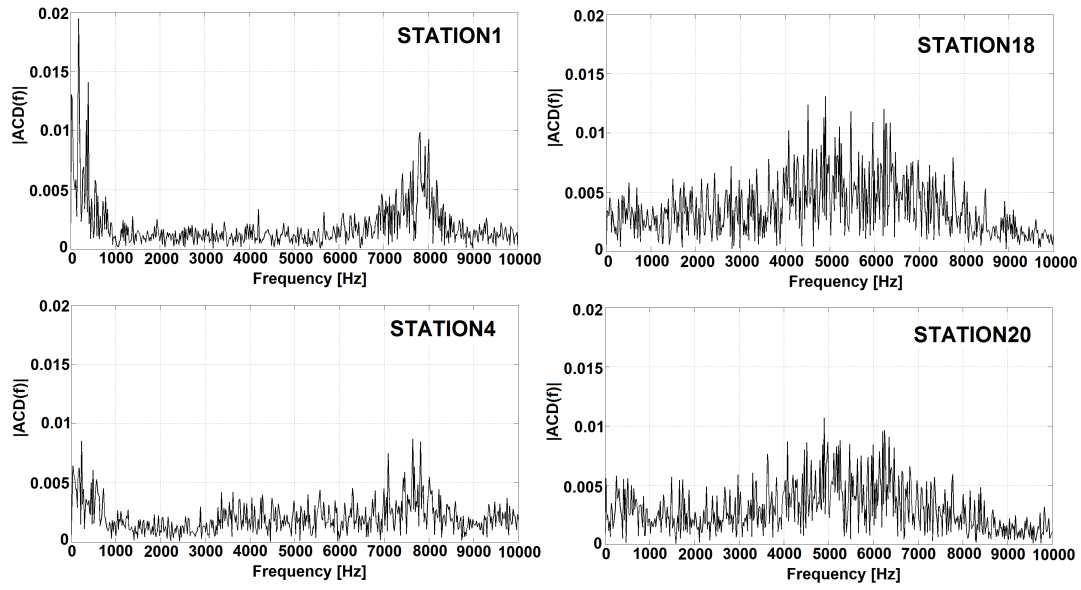


Figure 3.58: Frequency domain representation of air core diameter at designated stations ($\theta=90$).

3.5.5 Comparison of Results

The comparison of the predicted mean air core diameter from 3D numerical simulations with the predicted mean air core diameter from 2D- AXS numerical simulations are given in Figure 3.59. The error bars in Figure 3.59 represents the standard deviation from the mean for each mean air core diameter data.

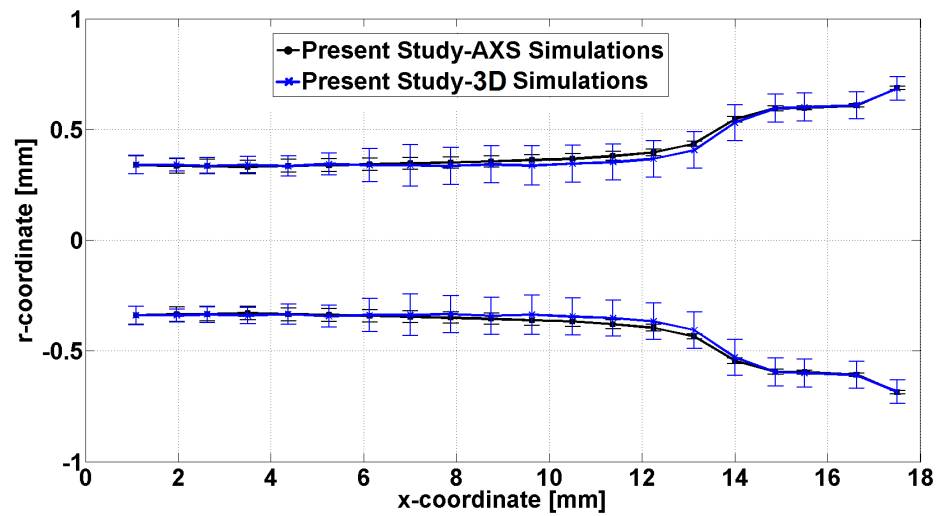


Figure 3.59: Mean air core diameter and standard deviations predicted by numerical simulations.

The mean air core diameter predicted by both simulations differs slightly between $x=8$ mm and $x=14$ mm and nearly the same at the other stations. The standard deviations from the mean aircore diameter, predicted by the 3D numerical simulations, are greater than that predicted by the 2D-AXS simulations at each station.

The comparison of the predicted mean air core diameter from 3D numerical simulations with the measured mean air core diameter data using High Speed Shadowgraphy System are given in Figure 3.60.

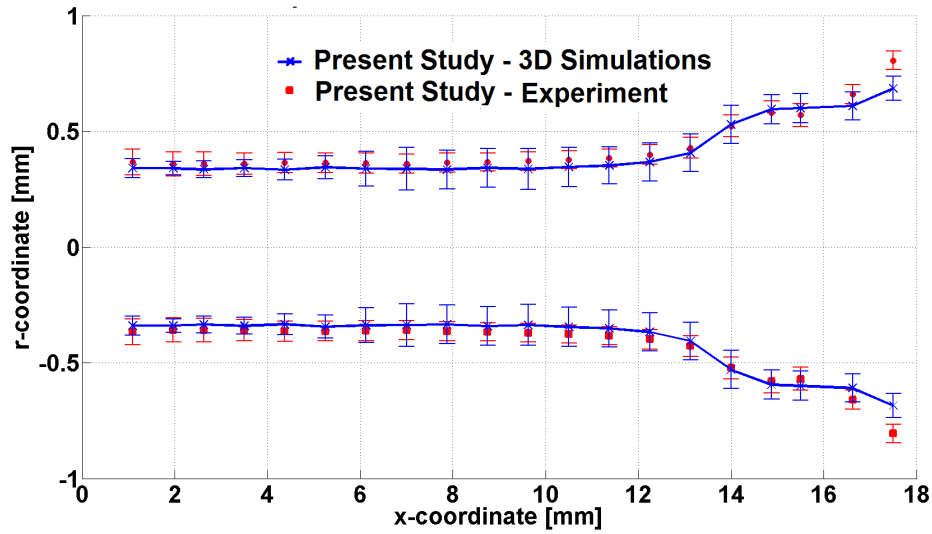


Figure 3.60: Comparison of mean air core diameter data-3D numerical simulations and experiment.

The mean air core diameter predicted by the 3D numerical simulations are slightly below the ones that are measured during the experiments at all Stations except Station 16-18. The difference between the predicted and measured mean air core diameter values is maximum at the exit of the atomizer. This discrepancy may be attributed to the inefficiency of the numerical method in adapting the flow to the sudden change in the boundary conditions at the exit of the atomizer.

CHAPTER 4

CONCLUSIONS AND RECOMMENDATIONS

In this study the unsteady flows through a pressure swirl atomizer and the resulting hollow cone spray formation is studied using experimental and numerical methods. The water flow inside the pressure swirl atomizer and the resulting hollow cone water spray are visualized using the High Speed Shadowgraphy System. The system utilizes two high speed cameras, which work in synchronous mode and sample images at 20 kHz. The formation of the air core inside the atomizer and the development of the hollow cone spray are visualized simultaneously.

At low mass flow rates the pressure swirl atomizer runs full and a straight liquid jet forms at the exit of the atomizer. As the flow rate through the atomizer increases an air core appears inside the atomizer and a hollow cone spray is formed. The formation of the air core inside the atomizer is rather rapid and the mass flow rate at which an air core presents in the atomizer is less than 1 lt/min.

The images, which are obtained using the high speed cameras, are processed using the developed image processing tool. The image processing tool uses the high density gradients at the edge of the interfaces to gather information about the air core and the hollow cone spray. The air core diameter at different locations inside the atomizer and the spray cone angle are quantified using the developed image processing tool at different operating points of the atomizer. In addition the microscopic properties of the resulting hollow cone spray are studied using the two component PDPA for three different operating points.

The experimental investigation of the pressure swirl atomizer shows that the air core

inside the pressure swirl atomizer has a dynamic character. The visual investigation of the captured images reveals vortical structures and surface waves. The quantitative analysis of the air core diameter is performed at four different flow rates of the atomizer using the developed image processing tool. The air core diameter is estimated at twenty stations along the axis of the atomizer. For the 3.18 lt/min flow rate, the air core diameter values obtained agree well with the results of Dash et. al. [26]. The mean air core diameter at 2.0 lt/min flow rate is smaller than the air core diameter observed for the larger flow rates at all stations. As the water flow rate increases, the mean air core diameter increases and reaches to an asymptote with increasing water mass flow rate. The shape of the mean air core is almost identical for all operating conditions. The standard deviation of the air core diameter decreases with the increasing water mass flow rate. At low water flow rates, the standard deviation of the air core diameter is minimum, which is a result of the low flow velocities and high residence time of the water inside the atomizer.

The frequency domain representation of the air core diameter reveals dominant low and high frequency content. The amplitude of the dominant low frequency peaks and dominant high frequency peaks are comparable at stations close to the head end of the atomizer. In all cases, the amplitude of the high frequency peaks decreases as one moves from the head end of the atomizer to the inlet of the atomizer, which shows that the high frequency phenomena is specific to locations close to the head end of the atomizer.

The Proper Orthogonal Decomposition is applied to the time variation of the air core diameter along the axis. The first mode shape has the highest reconstruction information and represents the main shape of the air core along the axis of the atomizer. The first mode shape along the axis has almost a constant thickness and without any contractions or nodal points, which indicates the presence of traveling wave along the air core. The remaining modes have several expansions/contractions separated with nodal points, which indicate the presence of standing/stationary waves.

The developed image processing tool is also used to evaluate the spray cone angle. The spray cone angles obtained differ only slightly with the increasing water flow rate through the atomizer.

The experimental methodology that is used in the present study, together with the developed image processing tool, constitutes a powerful analysis tool for investigating the behavior of the air core inside the pressure swirl atomizer and the macroscopic properties of the hollow cone spray. Although photographic techniques are applied to visualize the flow features inside the pressure swirl atomizer by several other researcher, the application of an edge detection algorithms to quantify the air core and the spray features is a new approach implemented in this study.

The two component PDPA is used to gather information about the microscopic properties of the hollow cone spray at three different flow rates. The Sauter Mean Diameter distributions show that the small droplets are located near the axis of the spray, while the large droplets are present near the spray boundaries for all flow rates. It is observed that the SMD values differ only slightly with the mass flow rate through the atomizer. The axial and radial velocity distributions of two droplet size classes are investigated. The first size class contains the droplets whose diameters are smaller than $10\ \mu\text{m}$, and the second size class contains the droplets whose diameters are greater than $100\ \mu\text{m}$. The streamlines, associated with the mean axial velocity of droplets smaller than $10\ \mu\text{m}$, reveals a vortex formation close to the axis of the atomizer and the vortex tends to move towards the atomizer exit as water mass flow rate increases.

The unsteady, two-phase flow through the pressure swirl atomizer is also investigated numerically with ANSYS-FLUENT software. 2D axisymmetric swirl and 3D unsteady, laminar flow simulations are performed. The numerical simulations reveal several vortex formations within the water in addition to the air core vorticies. One of these vortex structures appears at the inlet boundary and moves within the swirl chamber as it grows in size and stretches as it approaches the inlet of the nozzle before it disappears. These vortex structures are convected with the flow and has a spiral path. Another vortex structure is identified at the stagnation region near the head end of the atomizer. These vorticies are localized at the head end of the atomizer and make the air core interface to oscillate at this region. The third vortex structure is identified inside the air core which is favored by the presence of an inflation point in the air velocity field. These vortex structures within the air core are stationary but they oscillate with the air core at the head end. The high resolution simulation of the two-phase flow within the swirl chamber and the identification of the vortical

structures are the main contributions of the present study.

The mean air core diameters obtained numerically at the different stations along the axis of the atomizer agree well with the experimental values. In addition, the mean quantities obtained in the 2D-axisymmetric swirl simulations agree quite well with the 3D numerical simulations. The main vortex structures in the water region as well as within the air core are identified in both 2D-axisymmetric swirl and 3D numerical simulations. It is concluded that the 2D-axisymmetric swirl numerical solutions can be employed in the investigation of general flow features in a pressure swirl atomizer. Although the computational cost of 3D numerical simulations is high, an accurate information is obtained in regard to the unsteady vortical features of the flow within the swirl chamber.

Based on the experimental and numerical studies performed it may also be concluded that the low frequency oscillations observed in the pressure/velocity field are associated with the dynamics of the vortical structures within the water region, while the high frequency oscillations are associated with the dynamics of the vortical structures at the head end of the air core.

In a future study, the tools developed in this study may be used in investigating the effect of geometrical parameters of the atomizer and the effect external periodic disturbances on the air core diameter and on the spray cone angle.

REFERENCES

- [1] A. Lefebvre. *Atomization and Sprays*. Taylor & Francis, 1989.
- [2] L. Bavyel and Z. Orzechowsk. *Liquid Atomization*. Taylor & Francis, 1993.
- [3] I.J. Ito. Propellant Injection Systems and Processes. In V. Yang, Habiballah M., Hulka J., and Popp M., editors, *Liquid Rocket Thrust Chambers: Aspects of Modeling, Analysis and Design*, chapter 1, pages 1–18. 2004.
- [4] E. Cha, D. Kim, B.S. Kim, Yoon Y., and Bazarov V. Analysis of Swirl Coaxial Injector with Backhole as an Acoustic Damper in Liquid Rocket Engines. In *41st AIAA/ASME/SAE/ASEE Joint Propulsion Conference & Exhibit*, number July, Tuscon, Arizona, 2005.
- [5] H.W. Douglass. *Liquid Rocket Engine Injectors*. NASA SP-8089, 1976.
- [6] R. Biggs. Robert Biggs Rocketdyne - F-1 Saturn V First Stage Engine. In Steven C. Fisher and Shamim A. Rahman, editors, *Remembering the Giants : Apollo Rocket propulsion Development*, chapter 1, pages 15–26. NASA, Washington D.C., 2009.
- [7] V.R. Rubinsky. Combustion Instability in the RD-0110 Engine. In Vigor Yang and William Anderson, editors, *Liquid Rocket Engine Combustion Instability*, chapter 4, pages 89–112. AIAA, 1995.
- [8] V. Bazarov, V. Yang, and Puri P. Design and Dynamics of Jet and Swirl Injectors. In V Yang, Habiballah M, Hulka J, and Popp M, editors, *Liquid Rocket Thrust Chambers: Aspects of Modeling, Analysis and Design*, pages 19–103. 2004.
- [9] G. N. Abramovich. *The Theory of Swirl Atomizer*. 1944.
- [10] G.I. Taylor. The Mechanics of Swirl Atomizers. In *International Congress of Applied Mechanics*, London, 1948.
- [11] E. Giffen and A. Muraszew. *Atomization of Liquid Fuels*. Chapman and Hall, London, 1953.
- [12] J.J. Chinn. An Appraisal of Swirl Atomizer Inviscid Flow Analysis, Part 1: The Principle of Maximum Flow for a Swirl Atomizer and Its Use in the Exposition and Comparison of Early Flow Analyses. *Atomization and Sprays*, 19(3):263–282, 2009.

- [13] Y. I. Khavkin. *Theory and Practice of Swirl Atomizers*. Taylor&Francis, New York, 2004.
- [14] S.K. Som. Theoretical and Experimental Investigations on the Formation of Air Core in a Spray Atomizing Nozzle. *Applied Scientific Research*, 36:173–196, 1980.
- [15] S.K. Som. Theoretical and Experimental Studies on the Formation of an Air Core in a Swirl Spray Pressure Nozzle Using a Power Law Non-Newtonian Liquid. *Applied Scientific Research*, 40:71–91, 1983.
- [16] S.K. Som and G.W. Biswas. Initiation of Air Core in a Swift Nozzle Using Time-Independent Power-Law Fluids. *Acta Mechanica*, 51:179–197, 1984.
- [17] N. K. Rizk and A.H. Lefebvre. Internal flow characteristics of simplex swirl atomizers. *Journal of Propulsion and Power*, 1(3):193–199, May 1985.
- [18] A.H. Lefebvre and M Suyari. Film thickness measurements in a simplex swirl atomizer. *Journal of Propulsion and Power*, 2(6):528–533, 1986.
- [19] J. Ballester and C. Dopazo. Discharge Coefficient and Spray Angle Measurements for Small Pressure-Swirl Atomizers. *Atomization and Sprays*, 4:351–367, 1994.
- [20] J.J. Chinn, A.J. Yule, and H.J.K. De Keukelaere. Swirl Atomizer Internal Flow: A Computational and Experimental Study. In *12th Annual Conference of ILASS-Europe*, pages 41–46, Lund, Sweden, 1996.
- [21] S.M. Jeng, M.A. Jog, and M.A. Benjamin. Computational and Experimental Study of Liquid Sheet Emanating from Simplex Fuel Nozzle. *AIAA Journal*, 36(2):201–207, 1998.
- [22] D. Cooper, J. J. Chinn, and A. J. Yule. Experimental Measurements and Computational Predictions of the Internal Flow Field in a Pressure Swirl Atomizer. In *15th Annual Conference of ILASS-Europe*, number July, pages 1–6, Toulouse, France, 1999.
- [23] A. Datta and S. K. Som. Numerical prediction of air core diameter , coefficient of discharge and spray cone angle of a swirl spray pressure nozzle. *International Journal of Heat and Fluid Flow*, 21:412–419, 2000.
- [24] A.T. Sakman, M.A. Jog, S.M. Jeng, and M.A. Benjamin. Parametric study of simplex fuel nozzle internal flow and performance. *AIAA journal*, 38(7):1214–1218, 2000.
- [25] S. Nonnenmacher and M. Piesche. Design of hollow cone pressure swirl nozzles to atomize Newtonian fluids. *Chemical engineering science*, 55:4339–4348, 2000.

- [26] S. K. Dash, M. R. Halder, M. Peric, and S. K. Som. Formation of Air Core in Nozzles With Tangential Entry. *Journal of Fluids Engineering*, 123(4):829, 2001.
- [27] U. Maatje, E. Von Lavante, F. Albina, and M. Peric. Experimental and Numerical Study of Simplex Nozzles. In *17th Annual Conference of ILASS-Europe*, number September, Zurich, Switzerland, 2001.
- [28] D. Cooper and A.J. Yule. Waves on the air core/liquid interface of a pressure swirl atomizer. In *17th Annual Conference of ILASS-Europe*, number September, Zurich, Switzerland, 2001.
- [29] E. von Lavante and U. Maatje. Investigation of unsteady effects in pressure swirl atomizers. In *18th Annual Conference of ILASS-Europe*, number September, Zaragoza, Spain, 2002.
- [30] M.R. Halder, S.K. Dash, and S.K. Som. Initiation of air core in a simplex nozzle and the effects of operating and geometrical parameters on its shape and size. *Experimental thermal and fluid science*, 26:871–878, 2002.
- [31] D. Donjat, J.L. Estivalezes, M. Michau, and G. Lavergne. Phenomenological study of the pressure swirl atomizer internal flow. In *9th International Conference on Liquid Atomization and Spray Systems*, Sorrento, Italy, 2003.
- [32] S. Shaikh, U. Banaszak, E Von Lavante, D. Cooper, and A. J. Yule. CFD prediction of the Effects of Viscosity on the Internal Flow of a Scale Pressure-swirl Atomiser. In *19th Annual Conference of ILASS-Europe*, number September, Nottingham, U.K., 2004.
- [33] J. Madsen, B.H. Hjertager, and T. Solberg. Numerical simulation of internal flow in a large-scale pressure-swirl atomizer. In *19th Annual Conference of ILASS-Europe*, Nottingham, U.K., 2004.
- [34] Nan Zong and Vigor Yang. Dynamics of simplex swirl injectors for cryogenic propellants at supercritical conditions. In *42nd AIAA Aerospace Sciences Meeting and Exhibit*, volume 1, pages 1–13, Reno, Nevada, 2004.
- [35] Hongbok Park and Stephen D. Heister. Nonlinear simulation of free surfaces and atomization in pressure swirl atomizers. *Physics of Fluids*, 18(5):052103, 2006.
- [36] MR Halder and SK Som. Numerical and experimental study on cylindrical swirl atomizers. *Atomization and Sprays*, 16:223–236, 2006.
- [37] M.R. Morad and E. Eslami. Numerical and experimental study on aircore formation in a liquid-liquid coaxial swirl injector. In *10th International Conference on Liquid Atomization and Spray Systems*, Kyoto, Japan, 2006.

- [38] J.N. Hinckel, H.F. Villa Nova, and V. Bazarov. CFD Analysis of Swirl Atomizers. In *44th AIAA/ASME/SAE/ASEE Joint Propulsion Conference and Exhibit*, number July, pages 1–11, Hatford, CT, 2008.
- [39] Sunghyuk Kim, Taeock Khil, Dongjun Kim, and Youngbin Yoon. Effect of geometric parameters on the liquid film thickness and air core formation in a swirl injector. *Measurement Science and Technology*, 20(1):015403, January 2009.
- [40] S. Moon, E. Abo-Serie, and C. Bae. Liquid film thickness inside the high pressure swirl injectors: Real scale measurement and evaluation of analytical equations. *Experimental Thermal and Fluid Science*, 34(2):113–121, February 2010.
- [41] Qing-fei Fu, Li-jun Yang, and Yuan-yuan Qu. Measurement of annular liquid film thickness in an open-end swirl injector. *Aerospace Science and Technology*, 15(2):117–124, March 2011.
- [42] H.F. Huo, N. Zong, and V. Yang. Cryogenic fluid dynamic response of swirl injector to external forcing at supercritical conditions. In *47th AIAA Aerospace Sciences Meeting*, number January, pages 1–17, 2009.
- [43] V. Bazarov. *Liquid Injector Dynamics*. Mashinostroenie, 1979.
- [44] Ismailov Maksud. *Modeling of Classical Swirl Injector Dynamics*. PhD thesis, Purdue, 2010.
- [45] T. Khil, S. Kim, S. Cho, and Y. Yoon. Quantifying the Variation of the Mass Flow Rate Generated in a Simplex Swirl Injector by Pressure Fluctuation. Number July, page 92407, 2008.
- [46] B. Ahn, M. Ismailov, and S.D. Heister. Forced excitation of swirl injectors using a hydro-mechanical pulsator. In *45th AIAA/ASME/SAE/ASEE Joint Propulsion Conference and Exhibit*, number August, pages 1–11, 2009.
- [47] W.D. Bachalo. Spray Diagnostics for the Twenty-First Century. *Atomization and Sprays*, 10:439–474, 2000.
- [48] J. Ortman and A.H. Lefebvre. Fuel distributions from pressure-swirl atomizers. *AIAA Journal of Propulsion and Power*, 1(1), 1985.
- [49] X.F. Wang and A.H. Lefebvre. Mean drop sizes from pressure-swirl nozzles. *Journal of Propulsion Power*, 3(1):11–18, 1987.
- [50] X. Li, L.P. Chin, R.S. Tankin, and T. Jackson. Comparison between experiments and predictions based on maximum entropy for sprays from a pressure atomizer. *Combustion and Flame*, 86:73–89, 1991.
- [51] D.J. Hautman. Spray characterization of liquid/gas coaxial injectors with the center liquid swirled. *Atomization and Sprays*, 3:373–387, 1993.

- [52] V. Dorfner, J. Dmnick, F. Durst, and R. Köhler. Viscosity and Surface Tension Effects in Pressure Swirl Atomization. *Atomization and Sprays*, 5:261–285, 1995.
- [53] K. Ramamurthi and T. J. Tharakan. Flow Transition in Swirled Liquid Sheets. *AIAA Journal*, 36(3):420–427, March 1998.
- [54] K. Ramamurthi and R. Patnaik. Uniformity of Swirled Sprays formed with Nozzles of Varying Surface Roughness. *Atomization and Sprays*, 9:483–796, 1999.
- [55] J.L. Santolaya, L.A. Aísa, J.A. García, I.G. Palacín, and E. Calvo. Dynamic Characterization of a Pressure Swirl Hollow Cone Spray. In *18th Annual Conference of ILASS-Europe*, number September, Zaragoza, Spain, 2002.
- [56] Y. Khavkin. Secondary drop breakup in swirl atomizers. *Atomization and Sprays*, 12:615–627, 2002.
- [57] P.G. Han, J. Seol, S. Hwang, and Y. Yoon. The spray characteristics of swirl coaxial injectors. In *41st AIAA Aerospace Sciences Meeting and Exhibition*, number January, pages 1–14, Reno, Nevada, 2003.
- [58] B.S. Park, H.Y. Kim, and Y. Kim. Effects of Fuel Temperature on the Spray Characteristics of a Dual-orifice Type Swirl Injektor. In *9th International Conference on Liquid Atomization and Spray Systems*, Sorrento, Italy, 2003.
- [59] J Yon and JB Blaisot. Spray sizing by imaging: Focusing and droplet image superposition. ... *Liquid Atomization and Spray Systems, ILASS Europe ...*, 2004.
- [60] D. Kim, S. Kim, P. Han, and Yoon Y. The Atomization Characteristics of a Liquid-Liquid Swirl Coaxial Injector. In *10th International Conference on Liquid Atomization and Spray Systems*, 2006.
- [61] Byung-Sung Park, Ho Young Kim, and Sam S. Yoon. Transitional Instability of a Pressure-Swirl Atomizer Due To Air-Core Eruption At Low Temperature. *Atomization and Sprays*, 17(6):551–568, 2007.
- [62] Dongjun Kim, Poonggyoo Han, Ji-Hyuk Im, Youngbin Yoon, and Vladimir G. Bazarov. Effect of Recess on the Spray Characteristics of Liquid/Liquid Swirl Coaxial Injectors. *Journal of Propulsion and Power*, 23(6):1194–1203, November 2007.
- [63] T. Marchione, C. Allouis, a. Amoresano, and F. Beretta. Experimental Investigation of a Pressure Swirl Atomizer Spray. *Journal of Propulsion and Power*, 23(5):1096–1101, September 2007.

- [64] Li-jun Yang, Ming-he Ge, Meng-zheng Zhang, Qing-fei Fu, and Guo-biao Cai. Spray Characteristics of a Recessed Gas/Liquid Coaxial Swirl Injector. *Journal of Propulsion and Power*, 24(6):1332–1339, November 2008.
- [65] K. U. Reddy and D. P. Mishra. Studies on Spray Behavior of a Pressure Swirl Atomizer in Transition Regime. *Journal of Propulsion and Power*, 24(1):74–80, January 2008.
- [66] J. Karnawat and a. Kushari. Spray Evolution in a Twin-Fluid Swirl Atomizer. *Atomization and Sprays*, 18(5):449–470, 2008.
- [67] JH Im and Youngbin Yoon. The Effects of the Ambient Pressure on Self-Pulsation Characteristics of a Gas/Liquid Swirl Coaxial Injector. In *44th AIAA/ASME/SAE/ASEE Joint Propulsion Conference and Exhibit*, number July, pages 1–11, Hartford,CT, 2008.
- [68] R. J. Kenny, James R. Hulka, Marlow D. Moser, and Noah O. Rhys. Effect of Chamber Backpressure on Swirl Injector Fluid Mechanics. *Journal of Propulsion and Power*, 25(4):902–913, July 2009.
- [69] CJ Eberhart, DM Lineberry, and MD Moser. Experimental Cold Flow Characterization of a Swirl Coaxial Injector Element. In *45 th AIAA/ASME/SAE/ASEE Joint Propulsion Conference and Exhibit*, number August, pages 1–14, Denver,Colorado, 2009.
- [70] J.L. Santolaya, L.a. Aísa, E. Calvo, I. García, and J.a. García. Analysis by droplet size classes of the liquid flow structure in a pressure swirl hollow cone spray. *Chemical Engineering and Processing: Process Intensification*, 49(1):125–131, January 2010.
- [71] A. Belhadef, A. Vallet, M. Amielh, and F. Anselmet. Pressure-swirl atomization: Modeling and experimental approaches. *International Journal of Multiphase Flow*, 39:13–20, March 2012.
- [72] Saket Bhardwaj and Ajay Mittal. A Survey on Various Edge Detector Techniques. *Procedia Technology*, 4:220–226, 2012.
- [73] F. Durst and M. Zare. Laser Doppler measurements in two-phase flows. In *Proc of the LDA-Symposium*, pages 403–429, Copenhagen,Denmark, 1975.
- [74] W.D. Bachalo and Houser M.J. Development of the phase Doppler spray analyzer for liquid drop size and velocity characterization. In *AIAA/SAE/ASME 20th Joint Propulsion Conference*, Cincinnati,Ohio.
- [75] G. Kerschen and J.C. Golinval. Physical Interpretation of the Proper Orthogonal Modes Using the Singular Value Decomposition. *Journal of Sound and Vibration*, 249(5):849–865, January 2002.

- [76] Gal Berkooz, Philip Holmes, and JL Lumley. The proper orthogonal decomposition in the analysis of turbulent flows. *Annual review of fluid ...*, (25):539–575, 1993.
- [77] L Sirovich. Chaotic Dynamics of Coherent Structures. *Physica D*, 37:126–145, 1989.
- [78] L Sirovich. Turbulence and the dynamics of coherent structures. *Quart. Appl. Math.*, 45:561–590, 1987.
- [79] A Rosenfeld and Kak A.C. *Digital Picture Processing*. Academic Press Inc., Orlando, 2 edition, 1982.
- [80] Alejandro Marquez, JJE Oviedo, and Darci Odloak. Model Reduction Using Proper Orthogonal Decomposition and Predictive Control of Distributed Reactor System. ... *Control Science and Engineering*, 2013:1–19, 2013.
- [81] Y.C. Liang, H.P. Lee, S.P. Lim, W.Z. Lin, K.H. Lee, and C.G. Wu. Proper Orthogonal Decomposition and Its Applications Part I Theory. *Journal of Sound and Vibration*, 252(3):527–544, May 2002.
- [82] Anindya Chatterjee. An introduction to the proper orthogonal decomposition. *Current science*, 78(7), 2000.
- [83] B.F. Feeny. A complex orthogonal decomposition for wave motion analysis. *Journal of Sound and Vibration*, 310(1-2):77–90, February 2008.
- [84] C.W. Hirt and Nichols B.D. Volume of Fluid (VOF) Method for the Dynamics of Free Boundaries. *Journal of Computational Physics*, 39:201–225, 1981.
- [85] S Muzaferija, M Peric, P Sames, and T Schellin. A two-fluid Navier-Stokes solver to simulate water entry. In *Proc 22nd Symposium on Naval Hydrodynamics*, pages 277–289, Washington D.C., 1998.
- [86] JU Brackbill, DB Kothe, and C Zemach. A continuum method for modeling surface tension. *Journal of computational physics*, 100:335–354, 1992.
- [87] Jianqing X. *Computation of Flow Inside Pressure Swirl Atomizers*. Phd, University of Cincinnati, 2004.

APPENDIX A

TIME HISTORY OF AIRCORE DIAMETER FOR DIFFERENT OPERATING POINTS

A.1 $Q=2.0$ lt/min

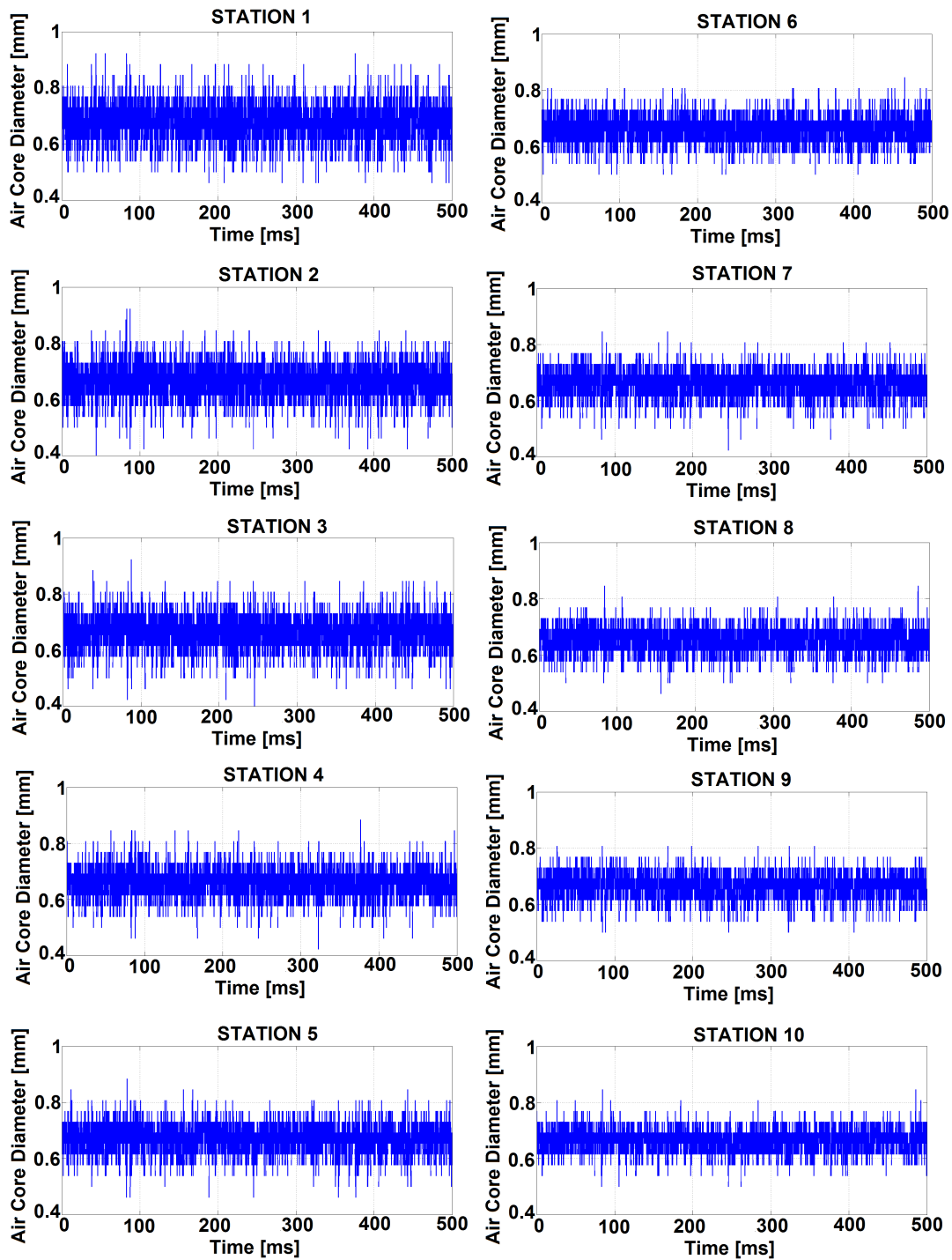


Figure A.1: Time history of the aircore diameter, Stations 1-10.

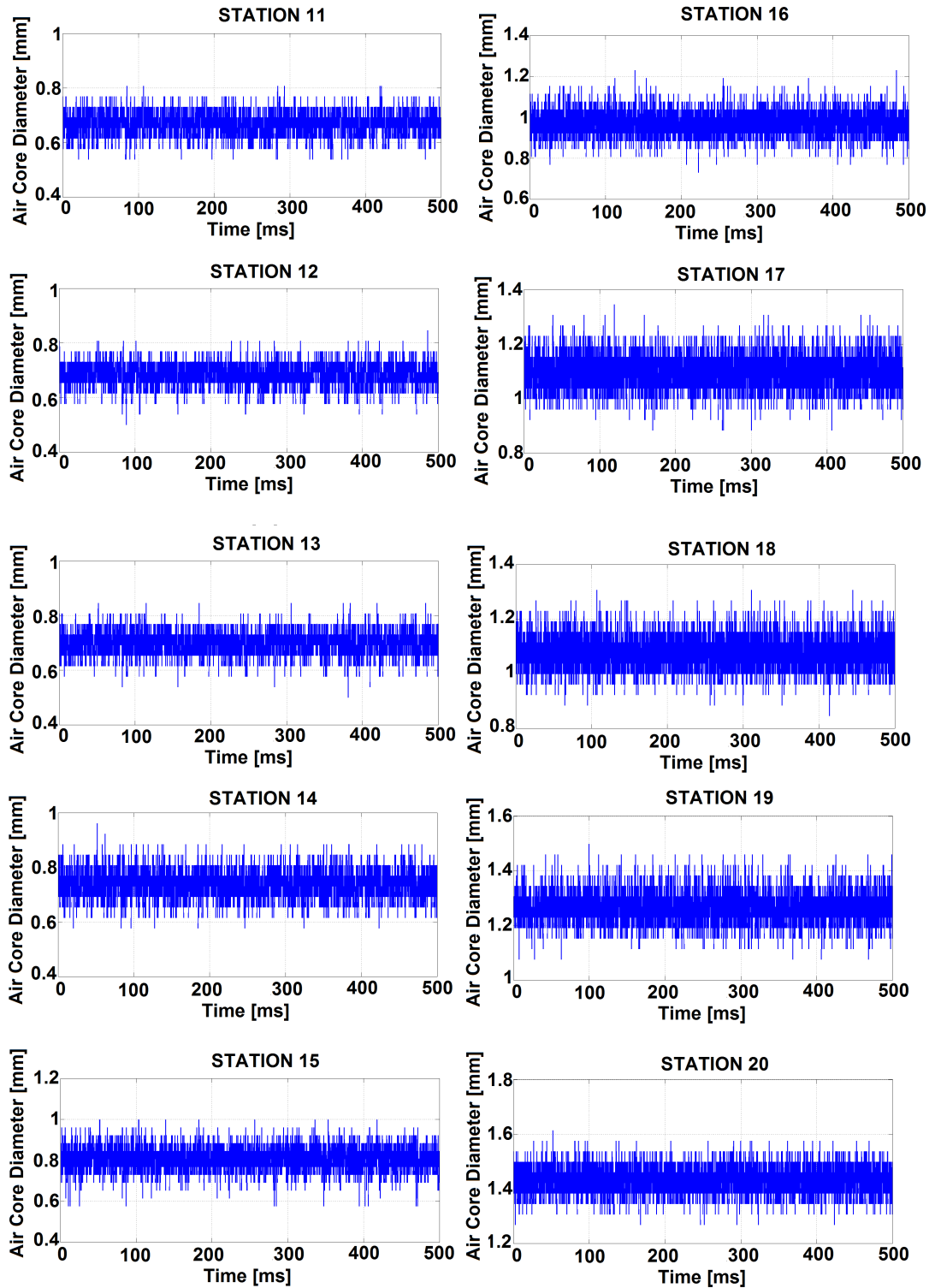


Figure A.2: Time history of the aircore diameter, Stations 11-20.

A.2 $Q=3.18$ lt/min

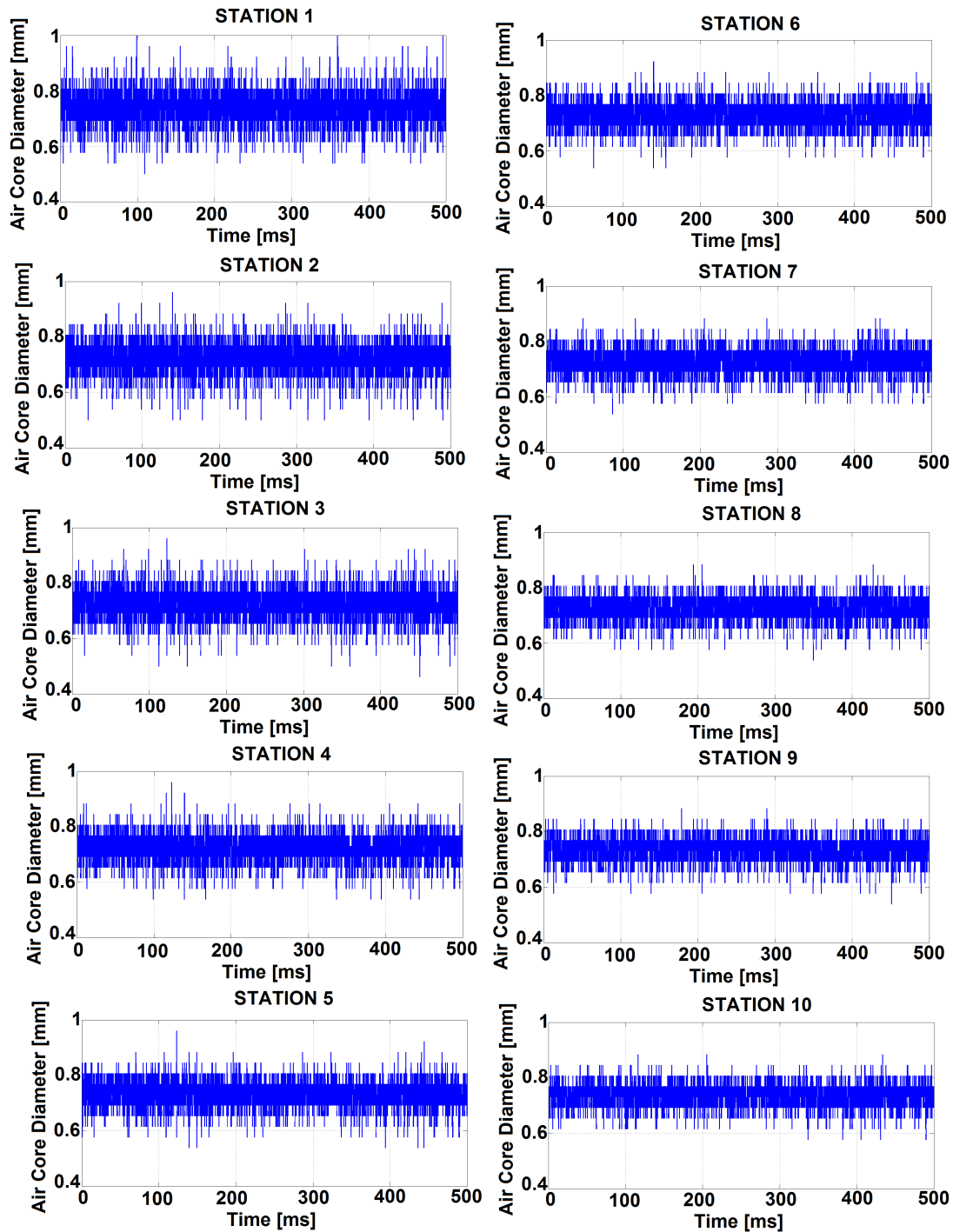


Figure A.3: Time history of the aircore diameter, Stations 1-10.

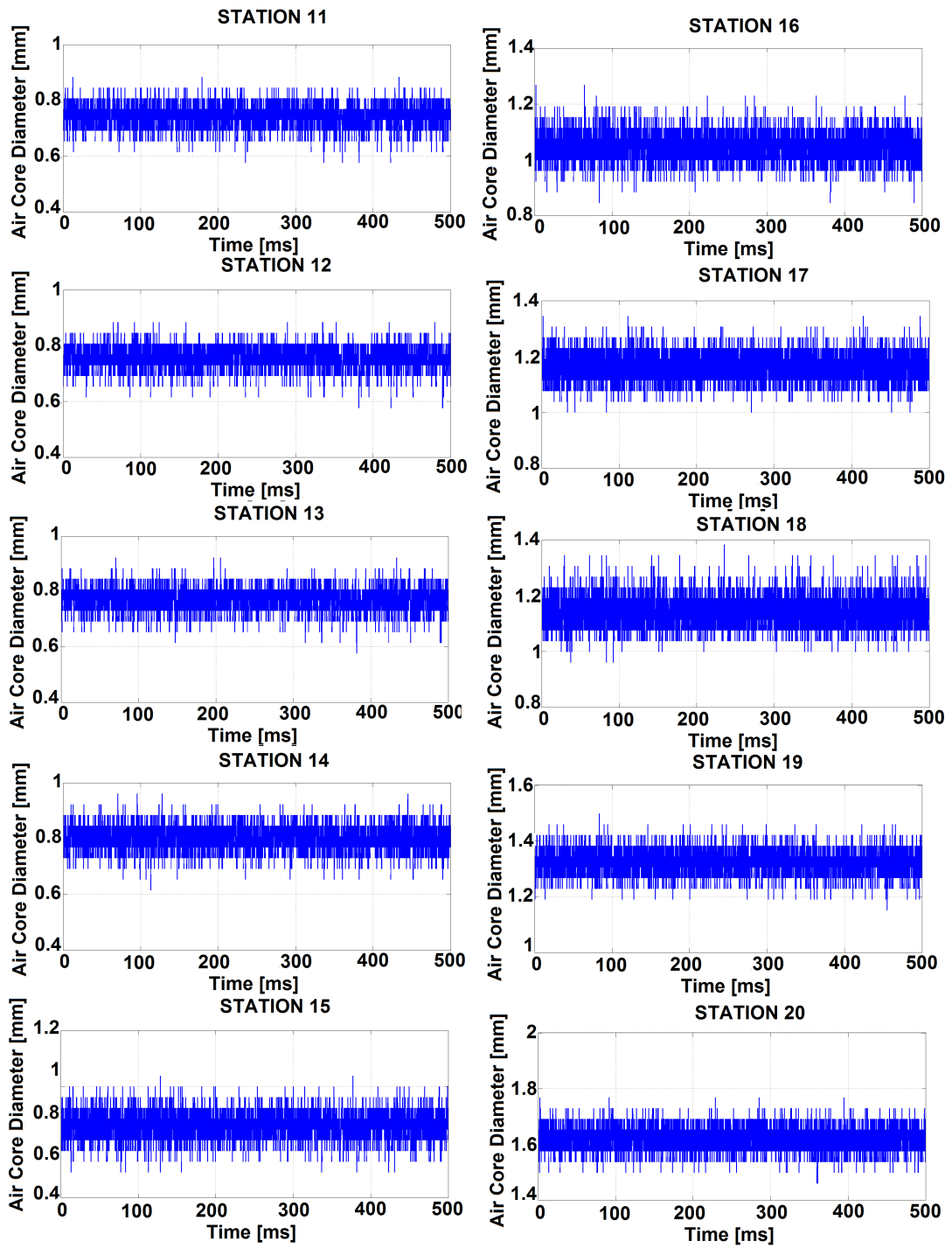


Figure A.4: Time history of the aircore diameter, Stations 11-20.

A.3 $Q=4.0$ lt/min

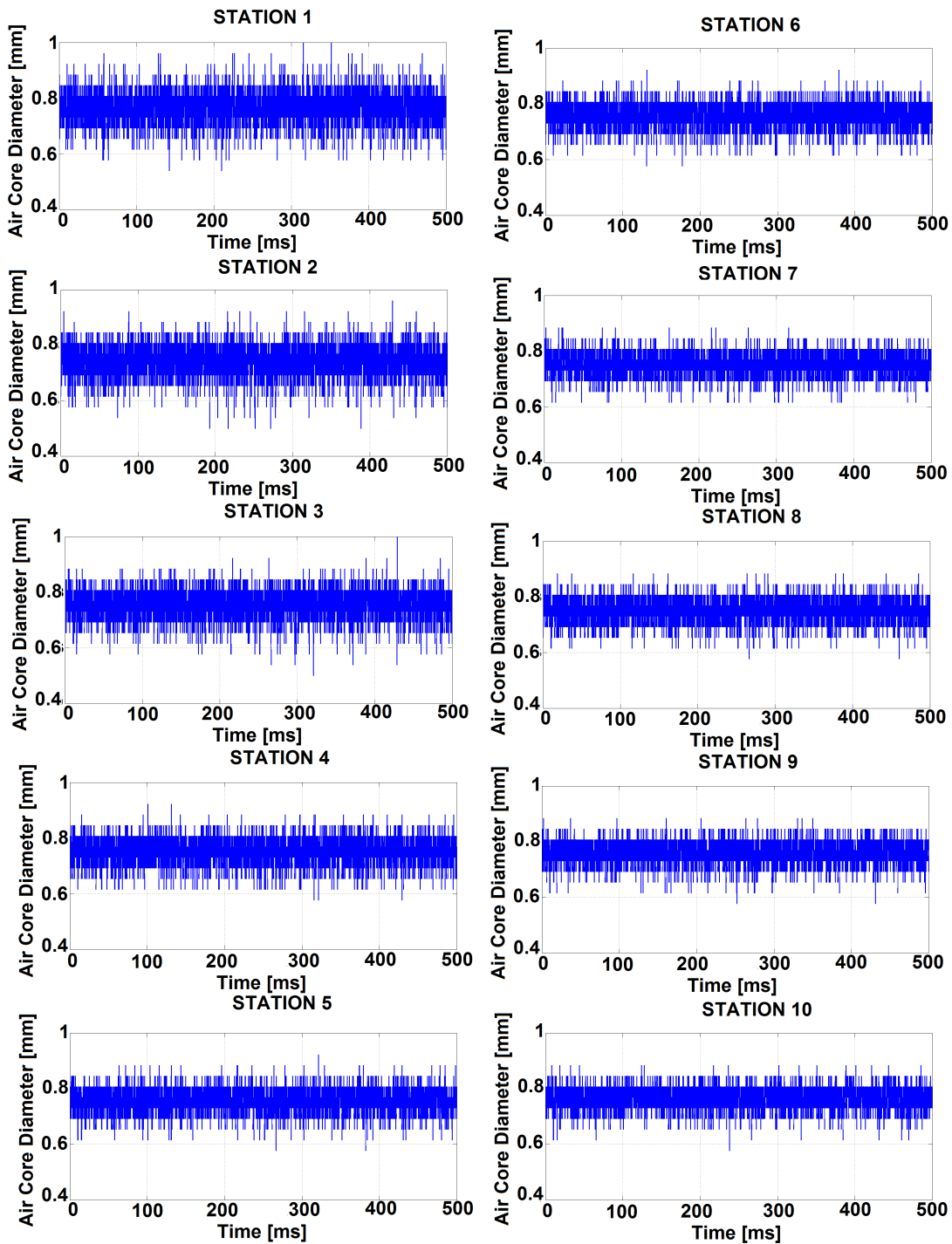


Figure A.5: Time history of the aircore diameter, Stations 1-10.

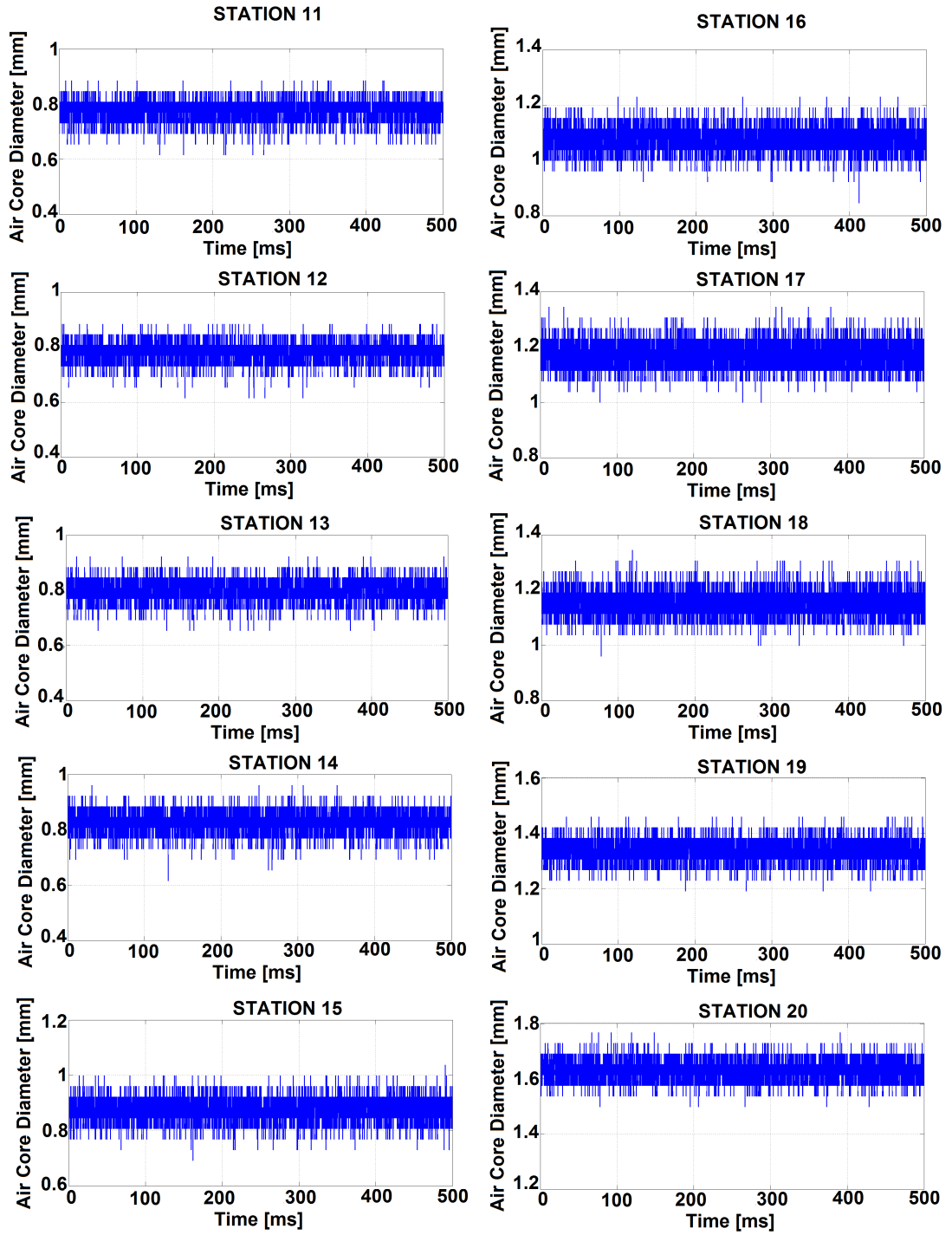


Figure A.6: Time history of the aircore diameter, Stations 11-20.

A.4 $Q=5.0$ lt/min

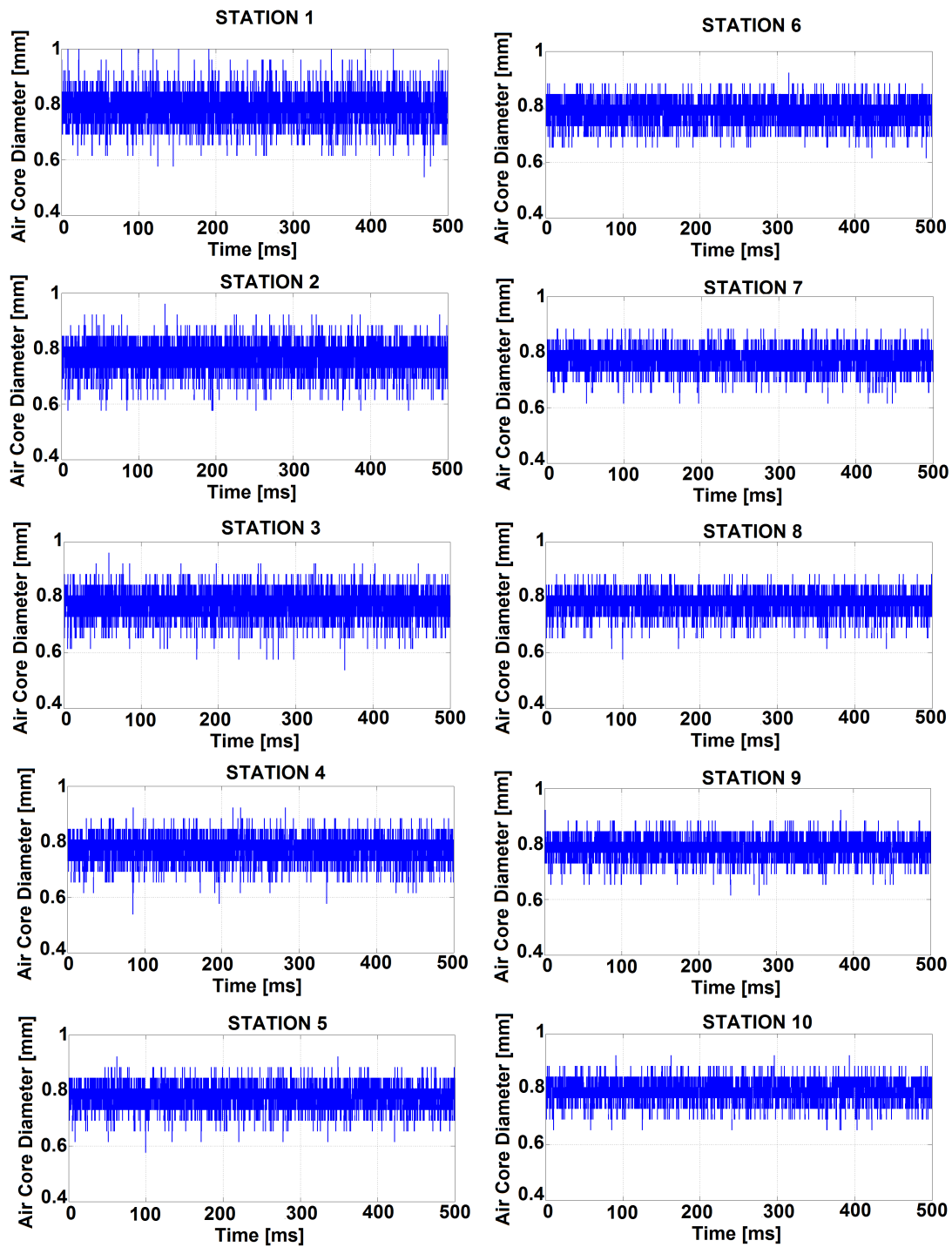


Figure A.7: Time history of the aircore diameter, Stations 1-10.

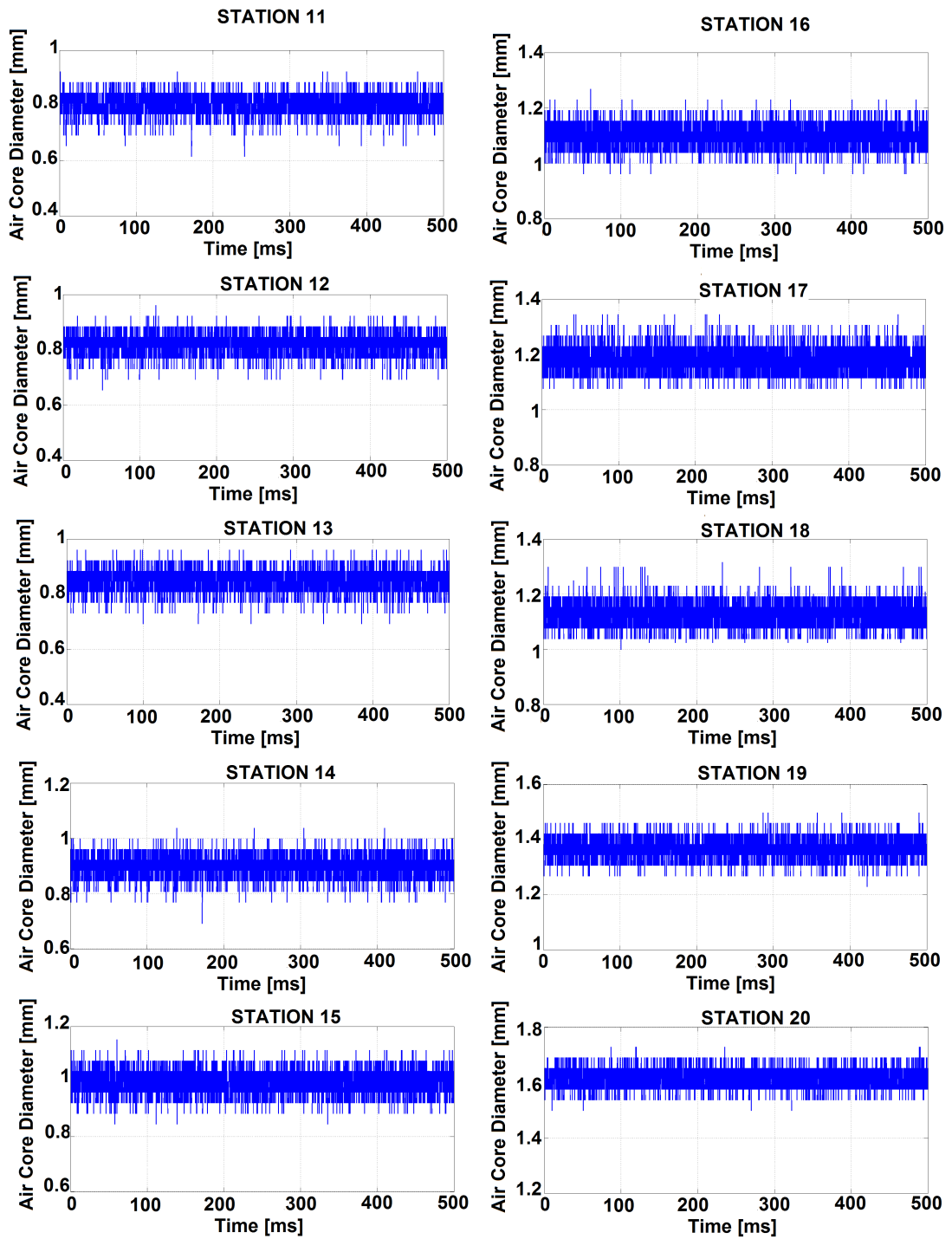


Figure A.8: Time history of the aircore diameter, Stations 11-20.

APPENDIX B

FREQUENCY SPECTRUM OF AIRCORE DIAMETER FOR DIFFERENT OPERATING POINTS

B.1 Q=2.0 lt/min

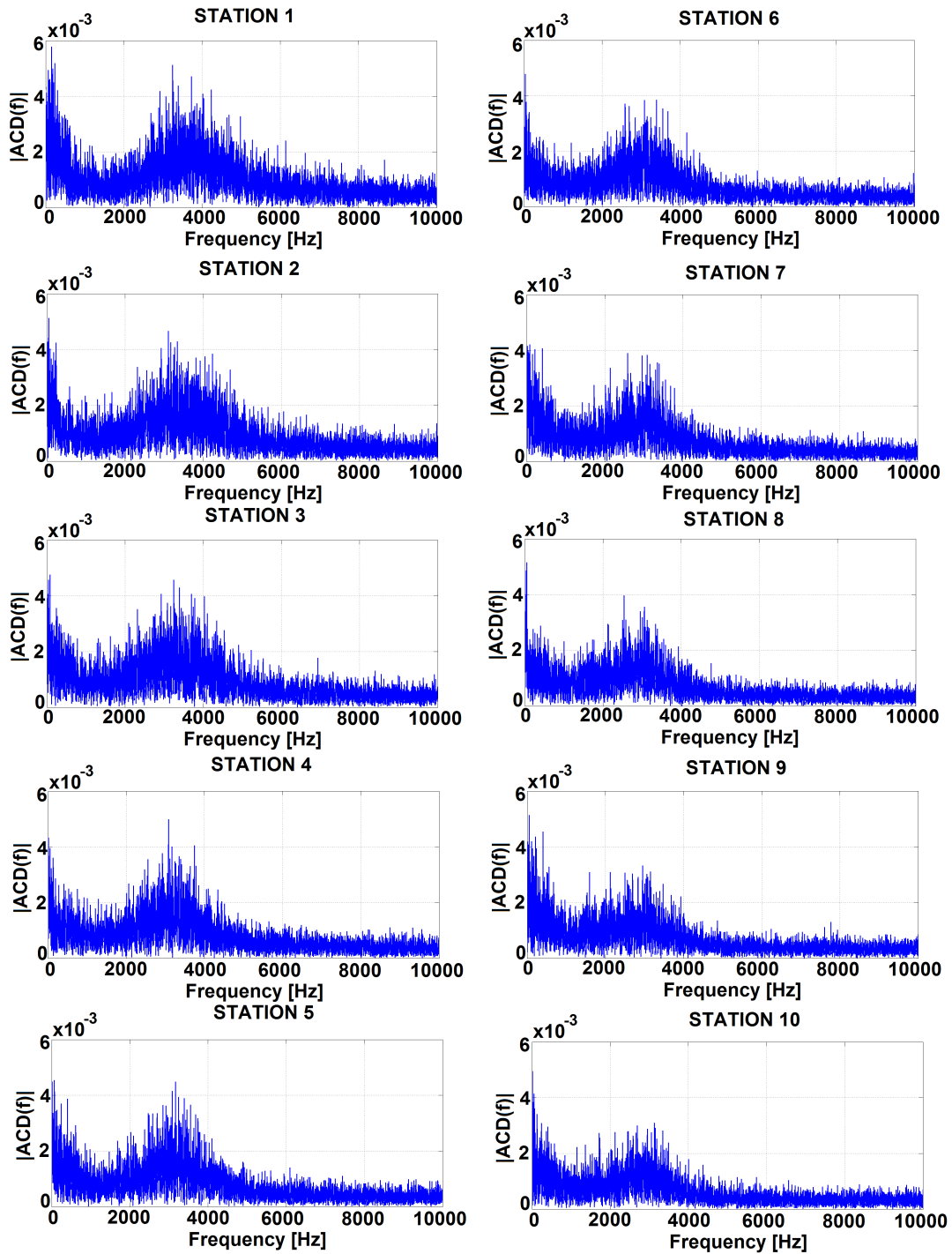


Figure B.1: Frequency spectrum of the aircore diameter, Stations 1-10.

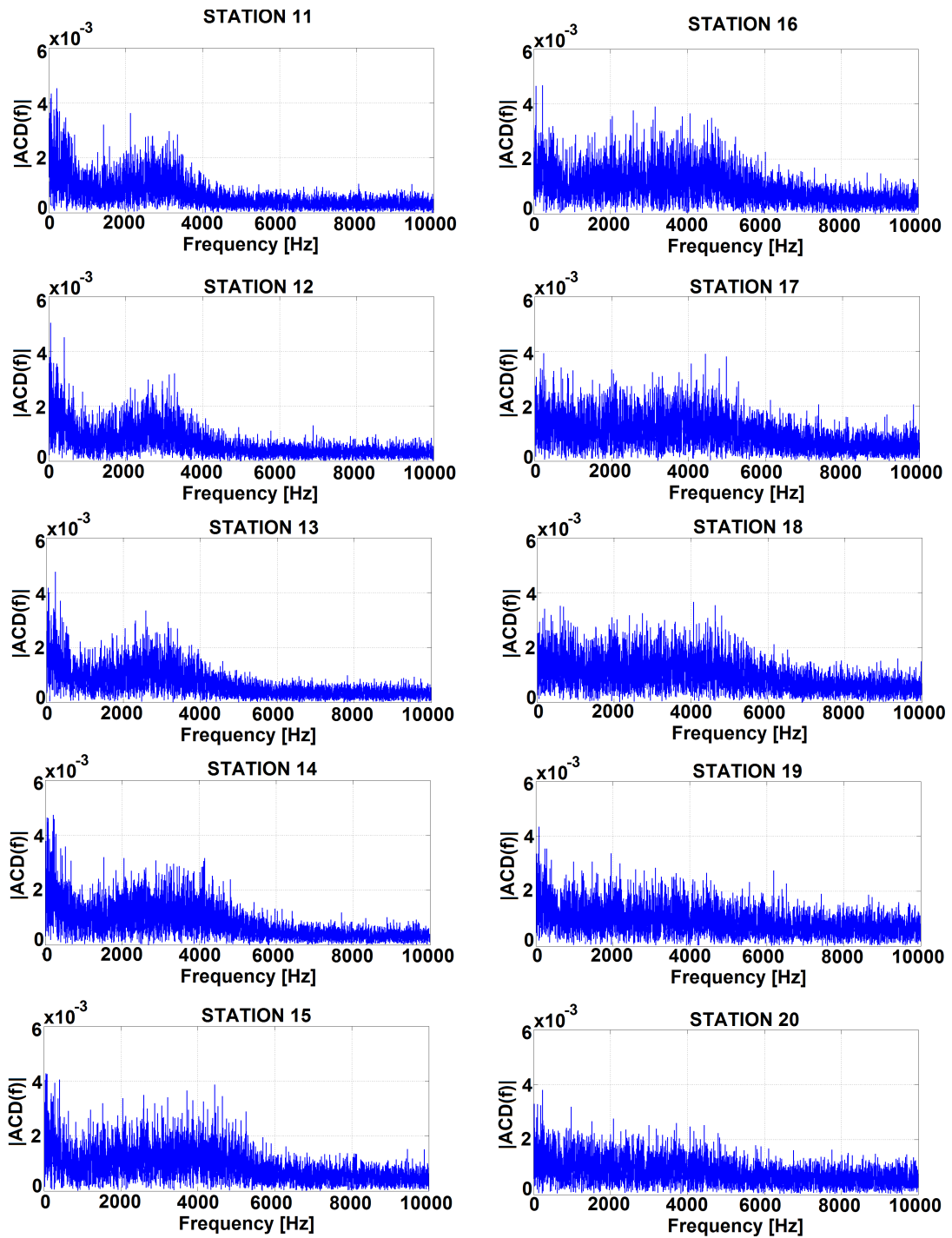


Figure B.2: Frequency spectrum of the aircore diameter, Stations 11-20.

B.2 Q=3.18 lt/min

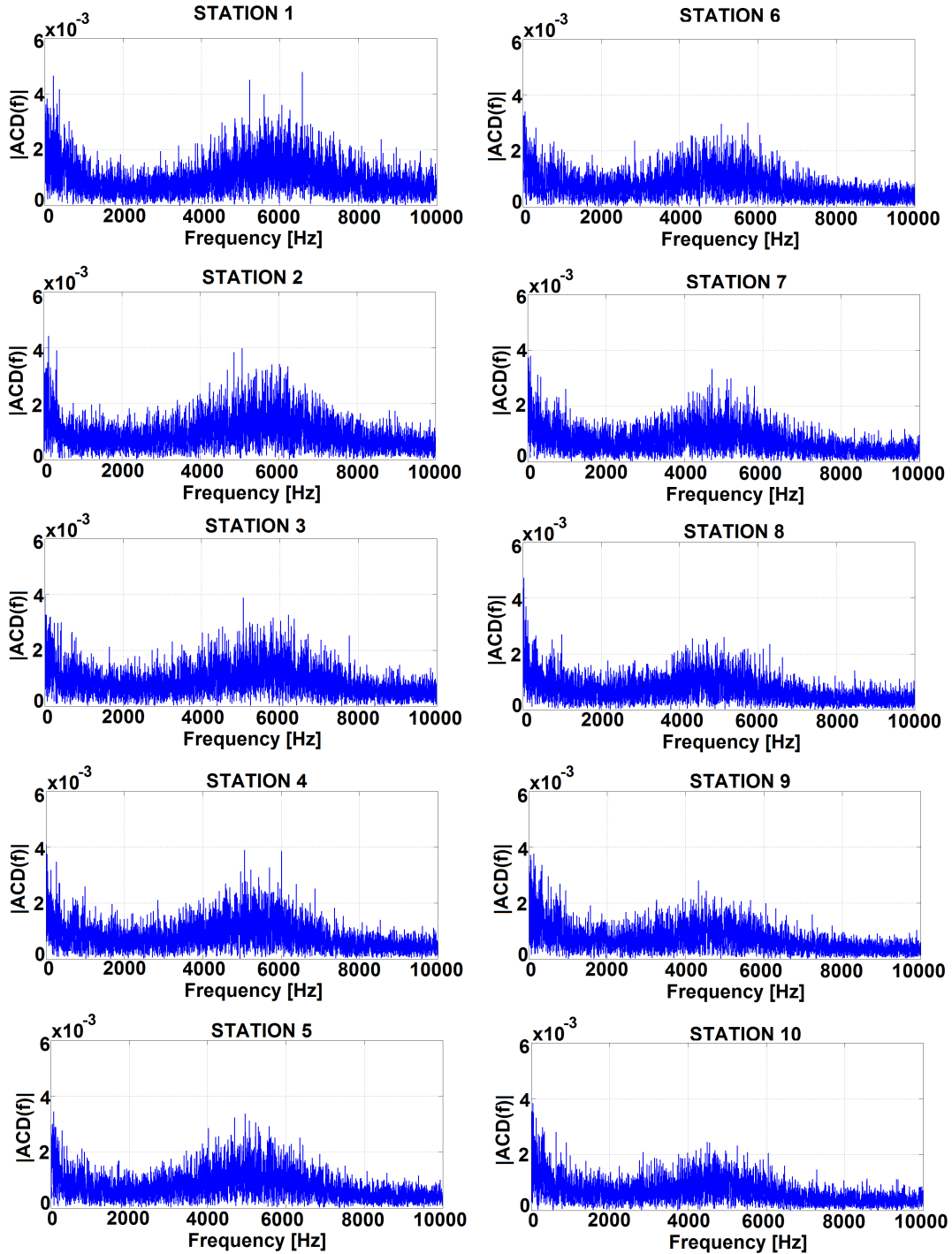


Figure B.3: Frequency spectrum of the aircore diameter, Stations 1-10.

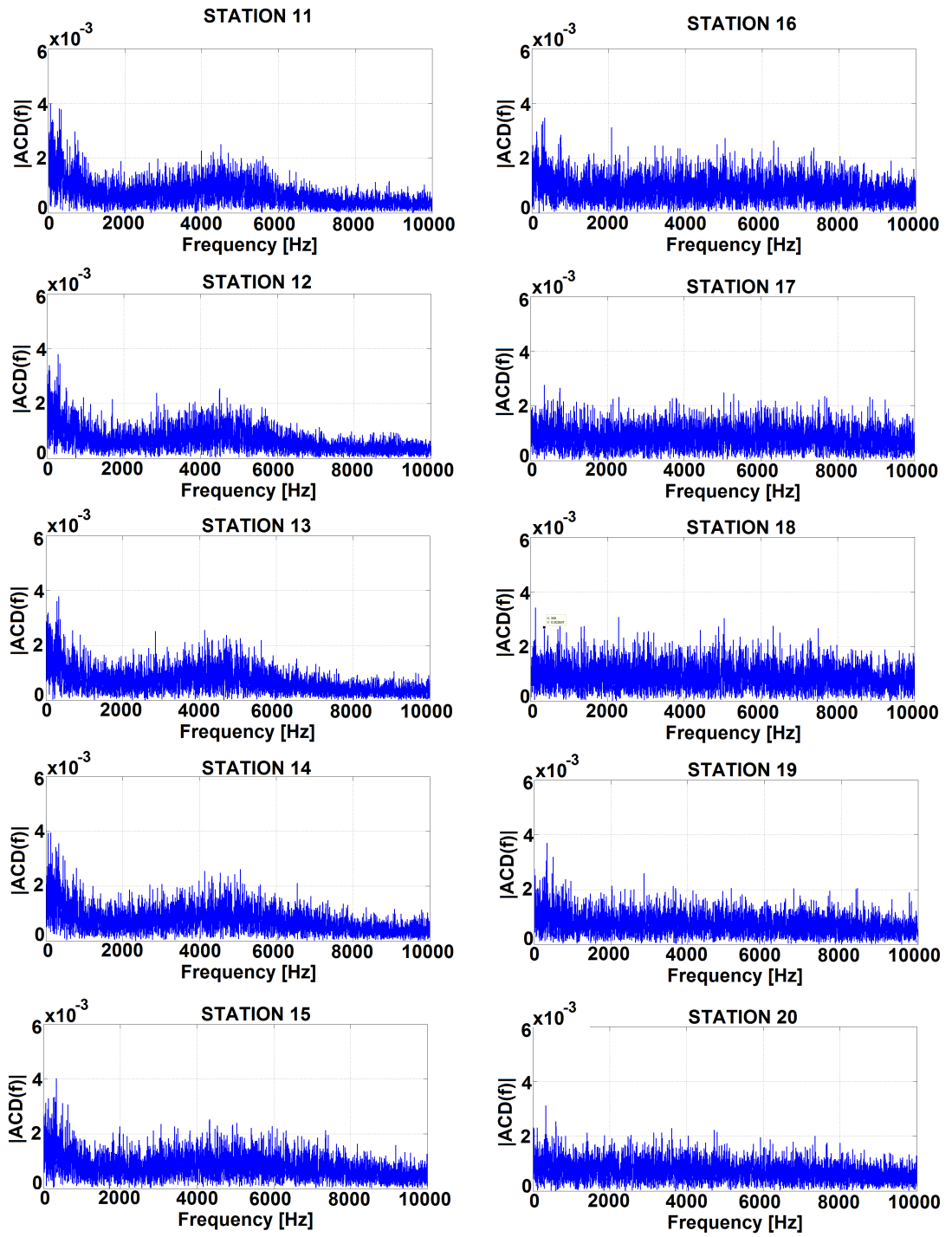


Figure B.4: Frequency spectrum of the aircore diameter, Stations 11-20.

B.3 Q=4.0 lt/min

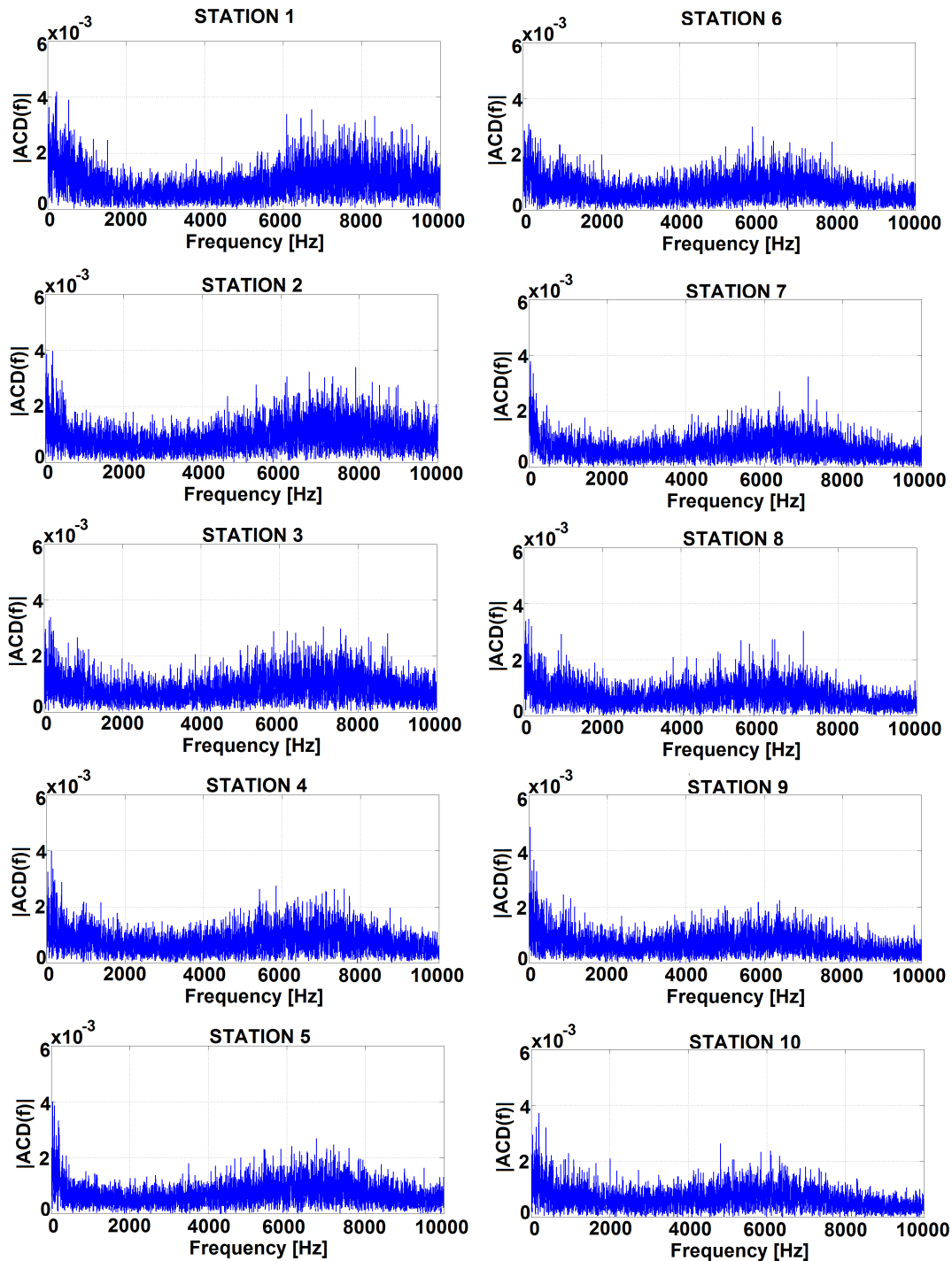


Figure B.5: Frequency spectrum of the aircore diameter, Stations 1-10.

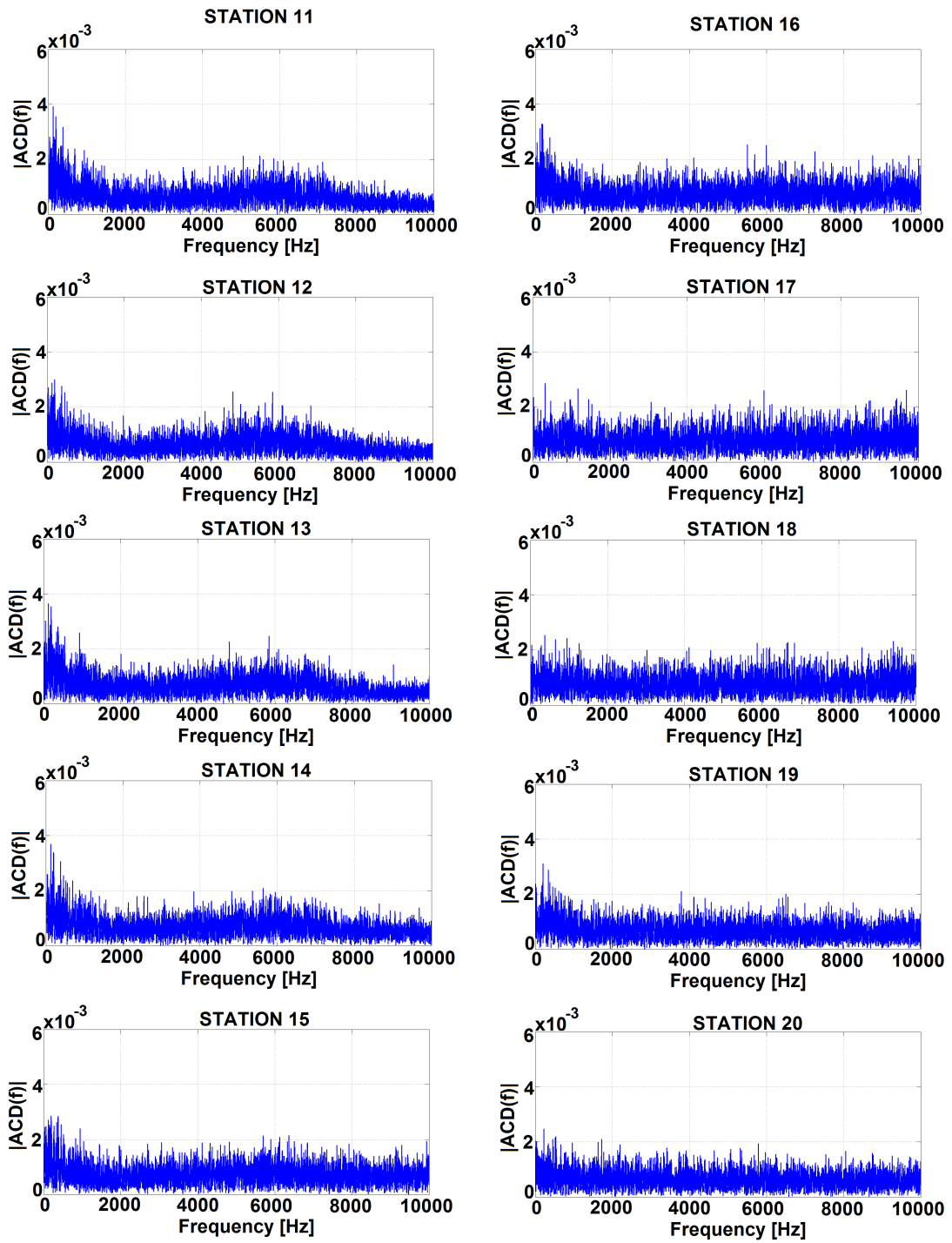


Figure B.6: Frequency spectrum of the aircore diameter, Stations 11-20.

B.4 Q=5.0 lt/min

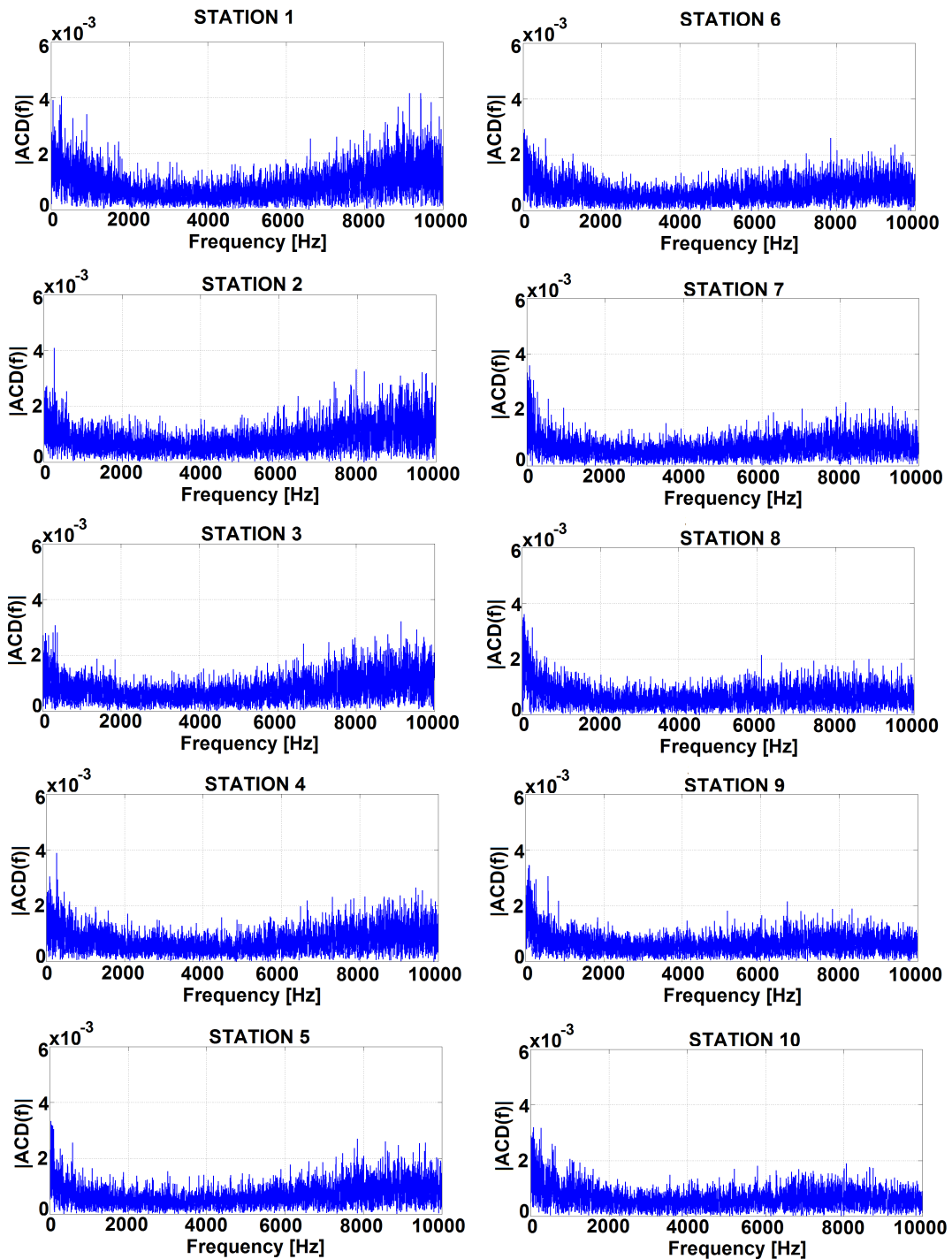


Figure B.7: Frequency spectrum of the aircore diameter, Stations 1-10.

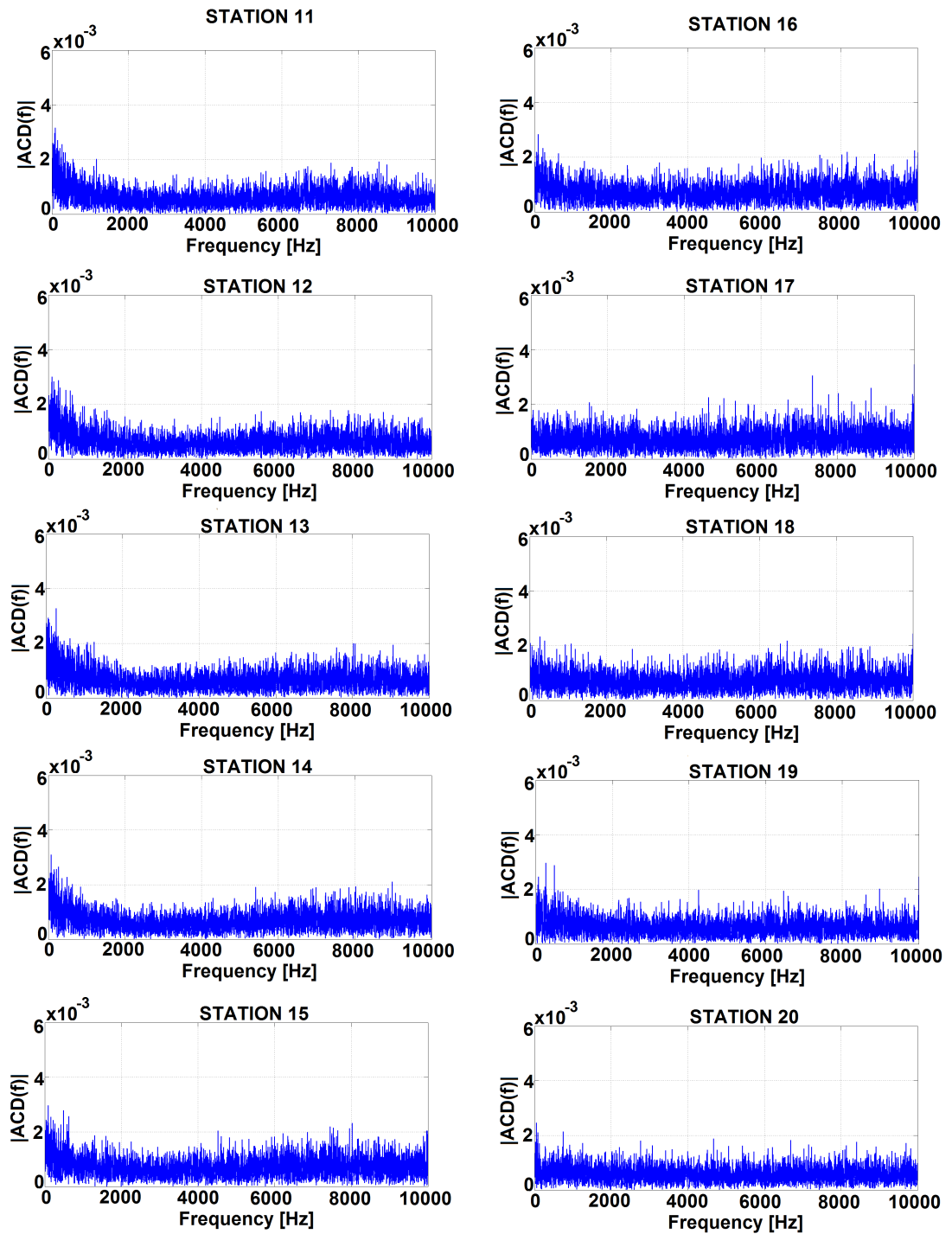


Figure B.8: Frequency spectrum of the aircore diameter, Stations 11-20.

APPENDIX C

MODE SHAPES OF AIRCORE FOR DIFFERENT OPERATING POINTS

C.1 $Q=2.0$ lt/min

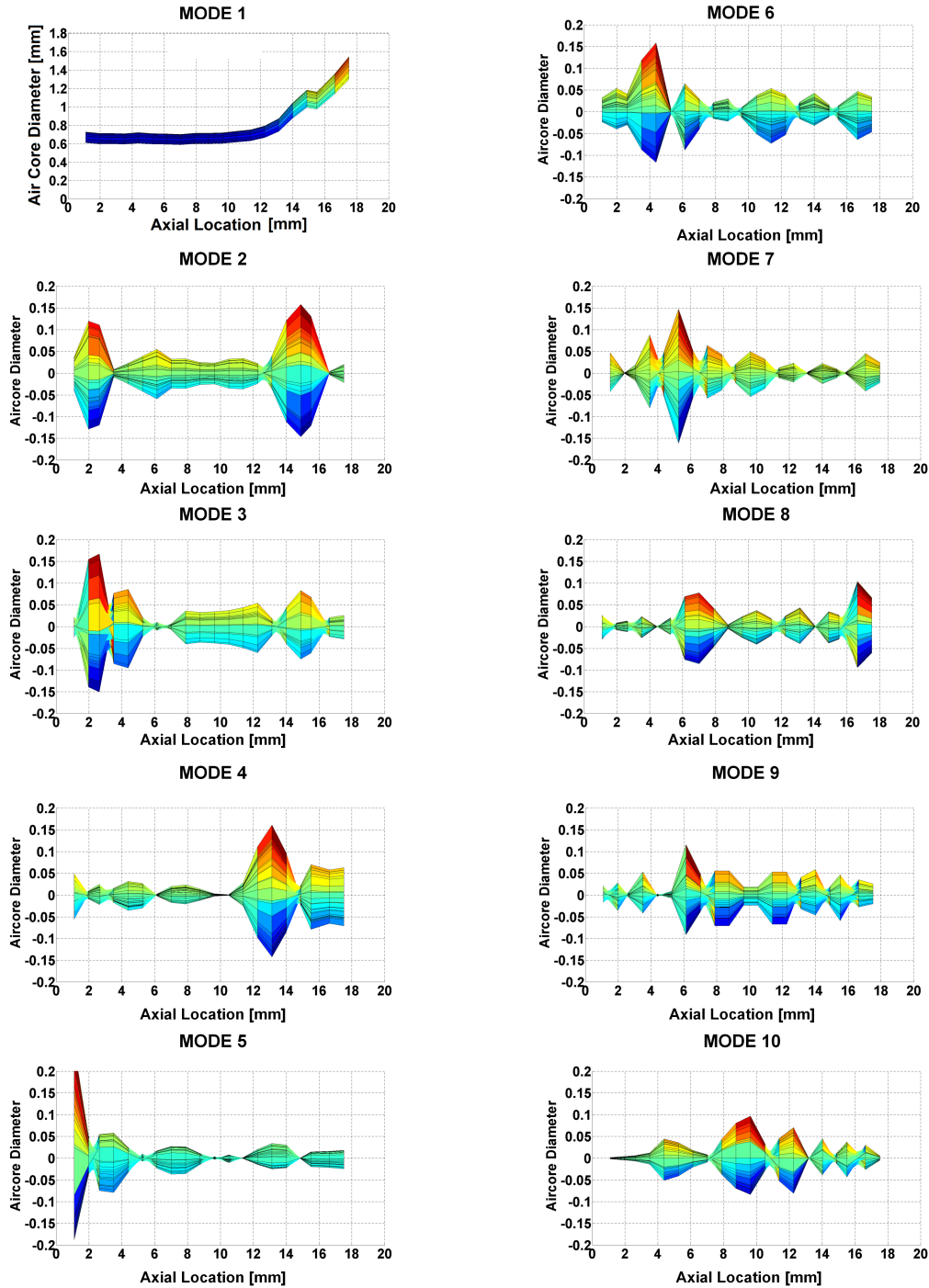


Figure C.1: Mode shapes of the aircore, Modes1-10.

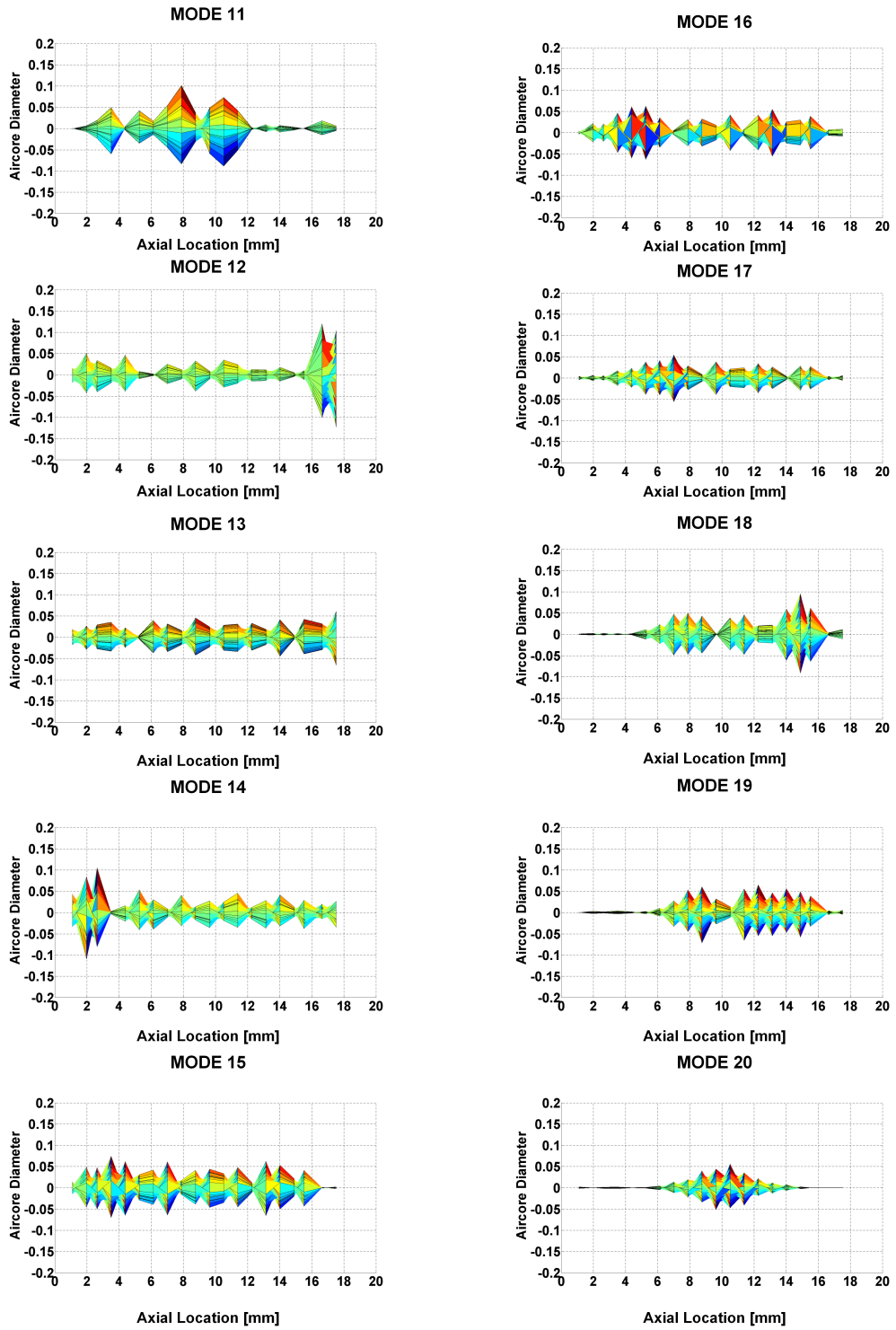


Figure C.2: Mode shapes of the aircore, Modes 11-20.

C.2 $Q=3.18$ lt/min

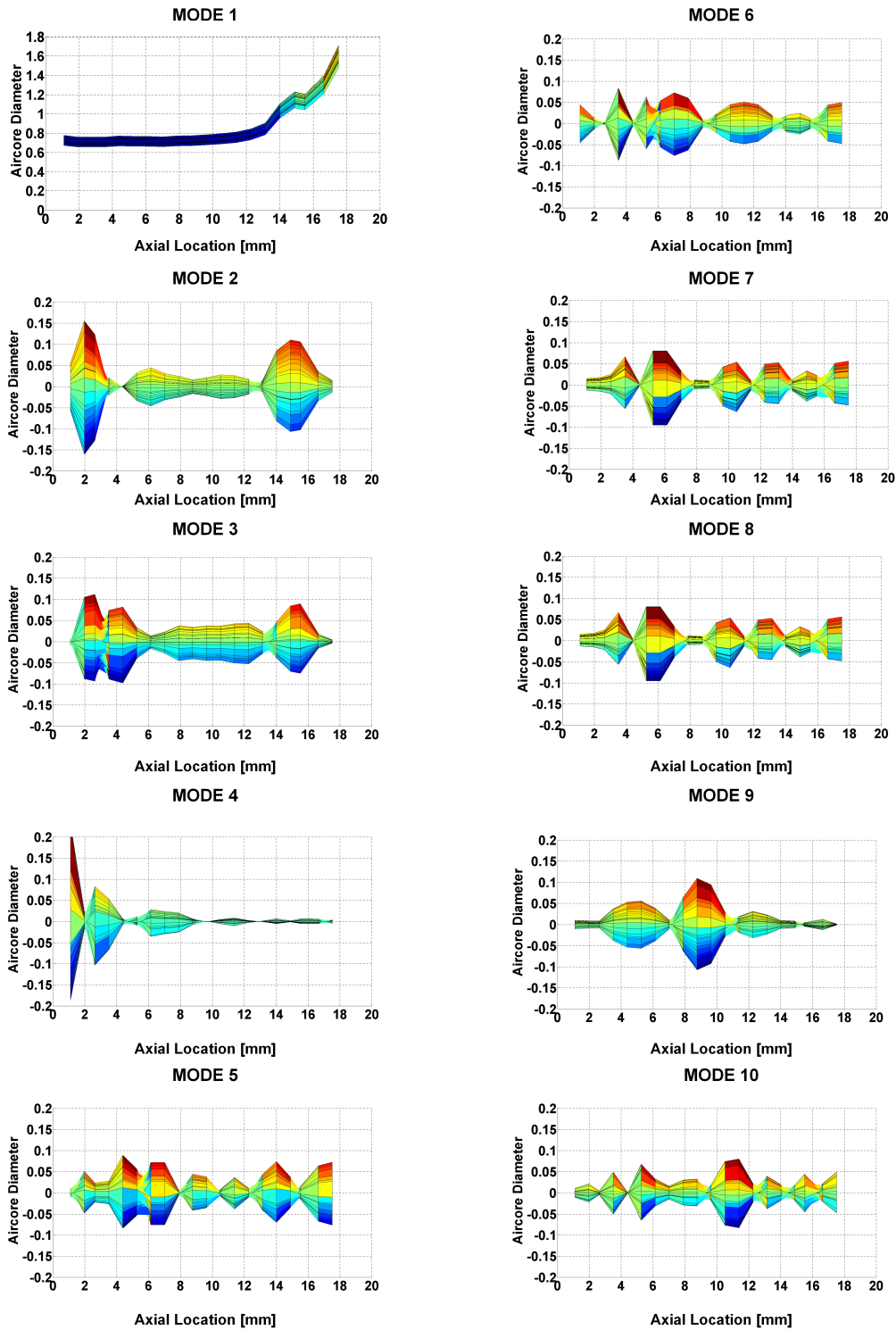


Figure C.3: Mode shapes of the aircore, Modes1-10.

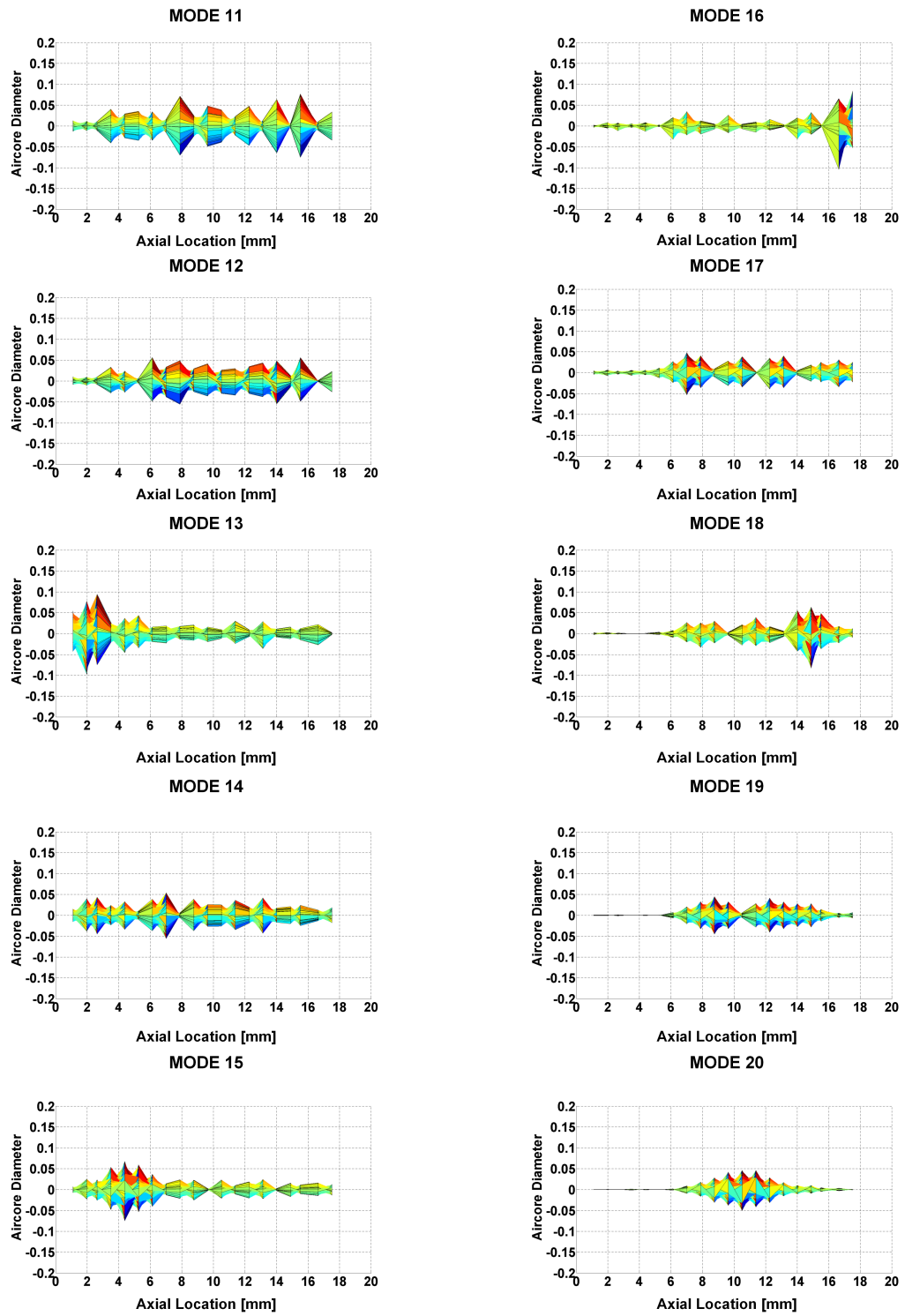


Figure C.4: Mode shapes of the aircore, Modes11-20.

C.3 Q=4.0 lt/min

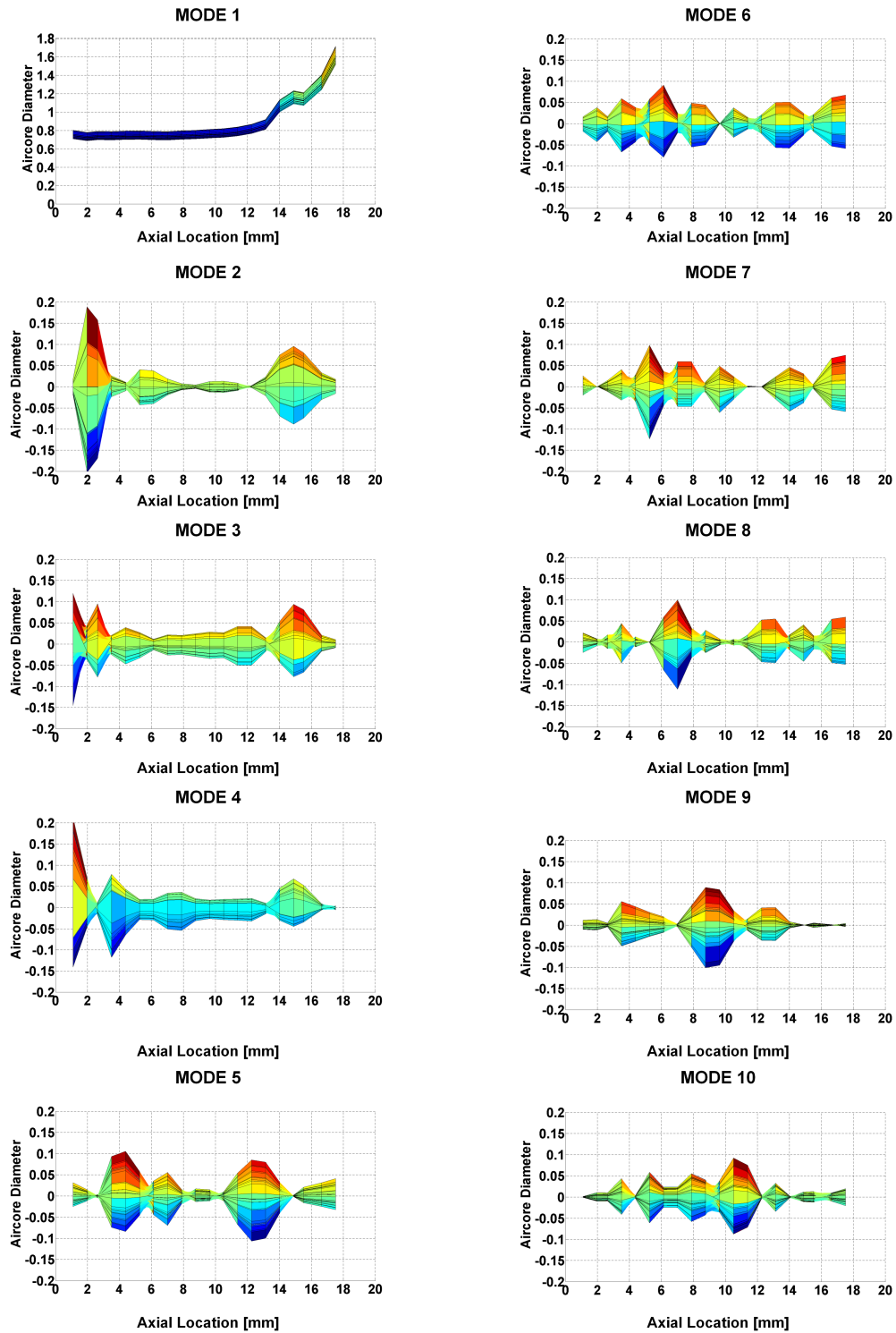


Figure C.5: Mode shapes of the aircore, Modes1-10.

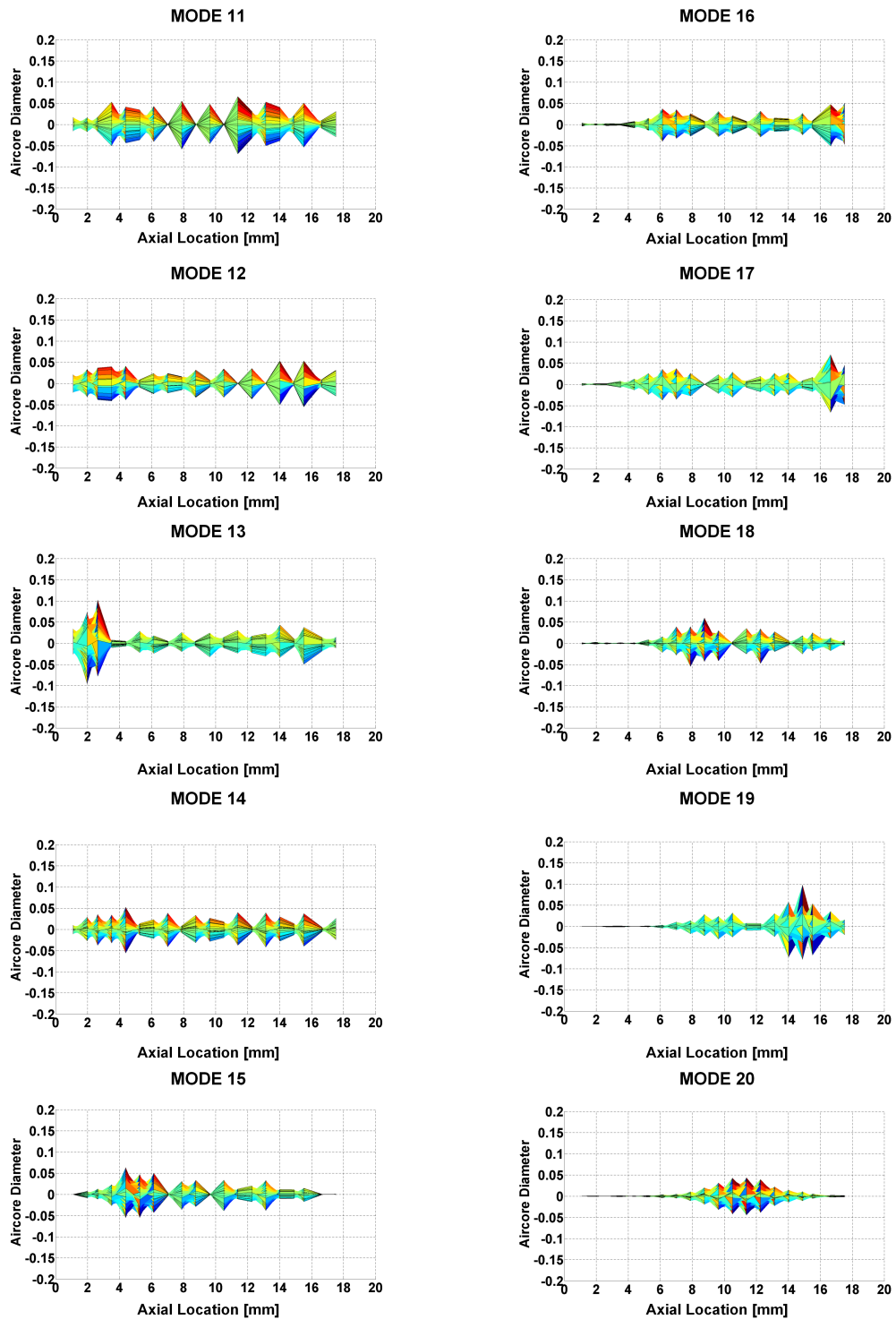


Figure C.6: Mode shapes of the aircore, Modes 11-20.

C.4 Q=5.0 lt/min

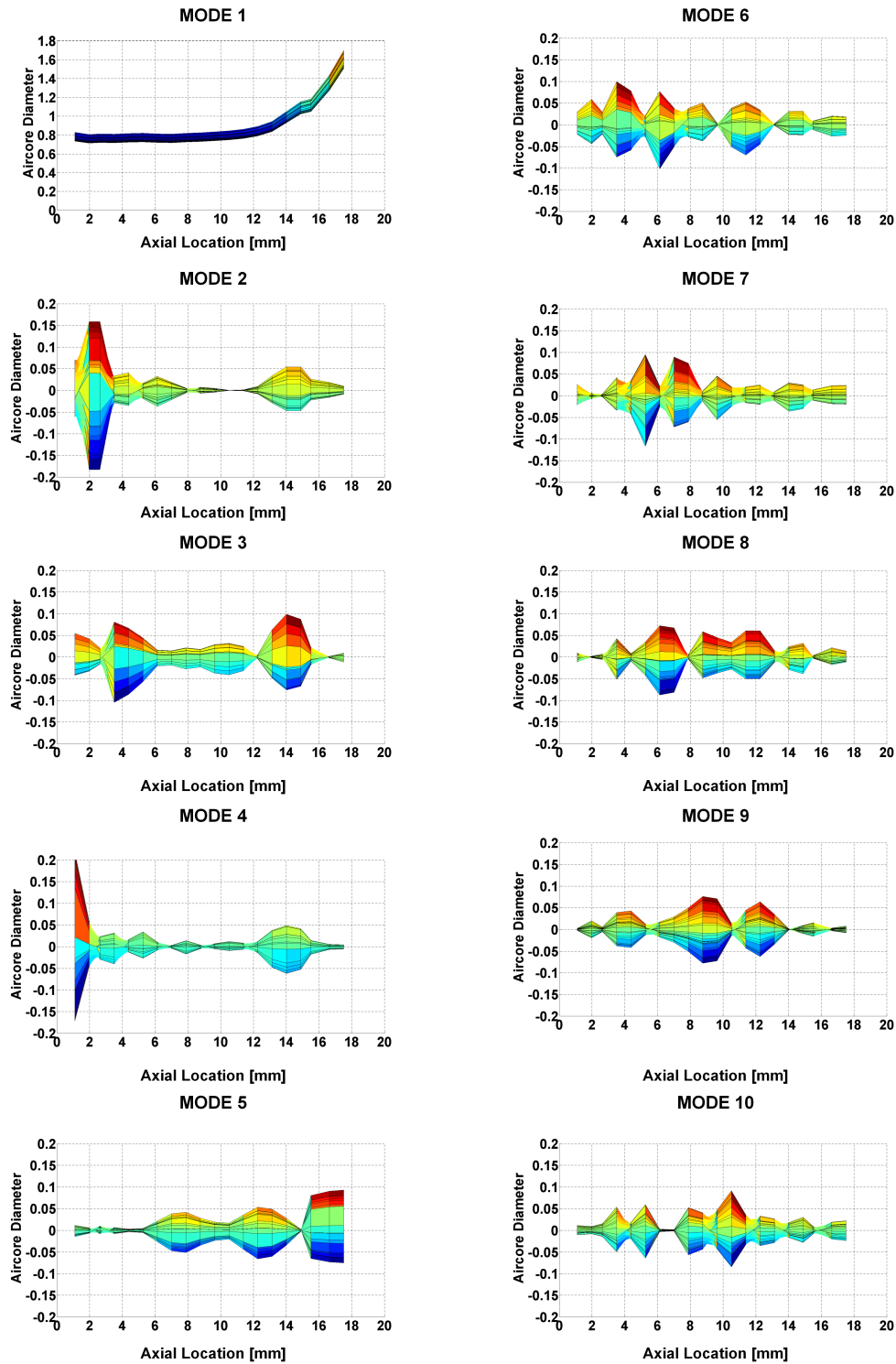


Figure C.7: Mode shapes of the aircore, Modes1-10.

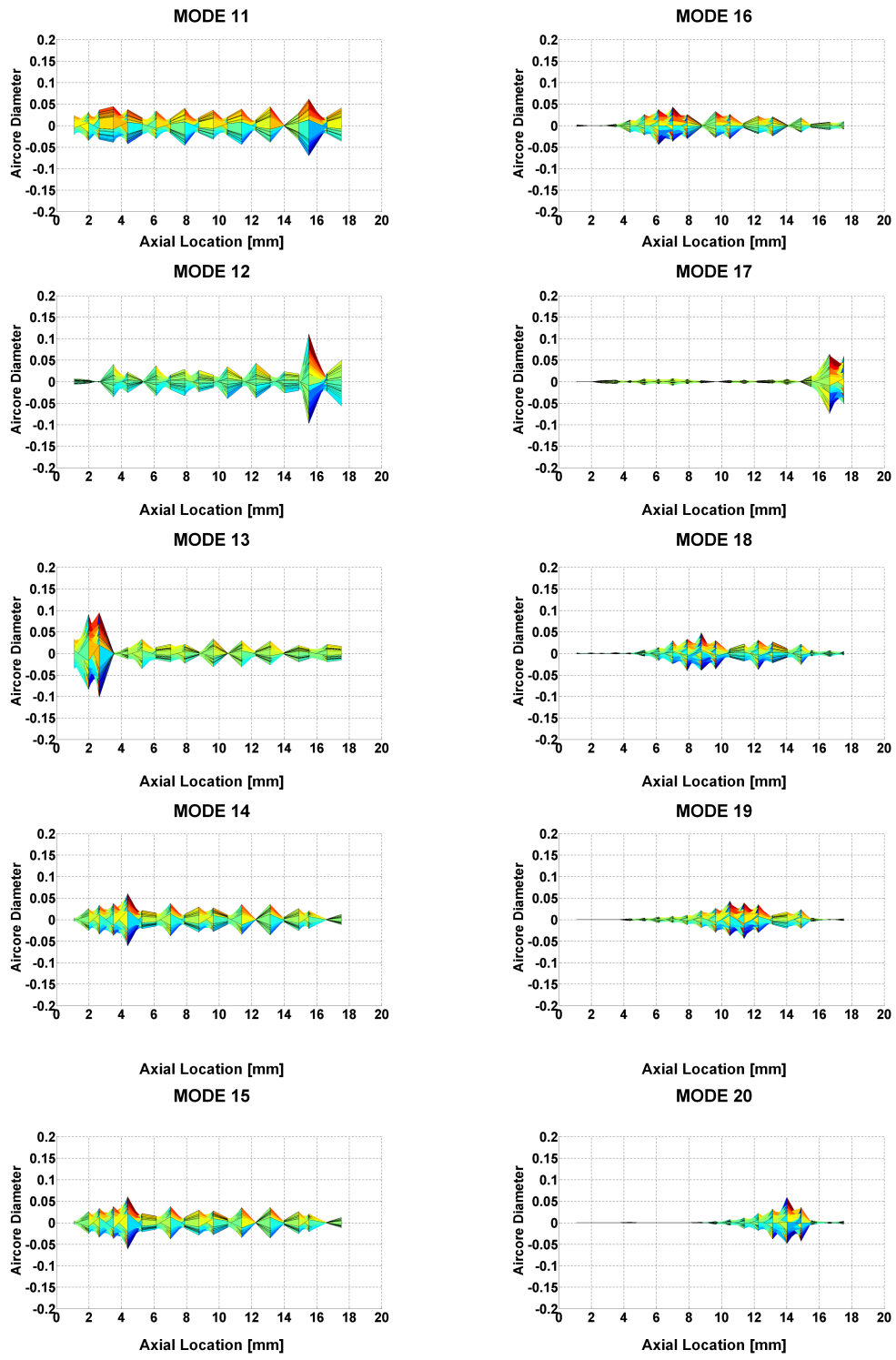


Figure C.8: Mode shapes of the aircore, Modes11-20.

APPENDIX D

TIME HISTORY OF AIRCORE DIAMETER- 2D AXISYMMETRIC SWIRL NUMERICAL SIMULATIONS

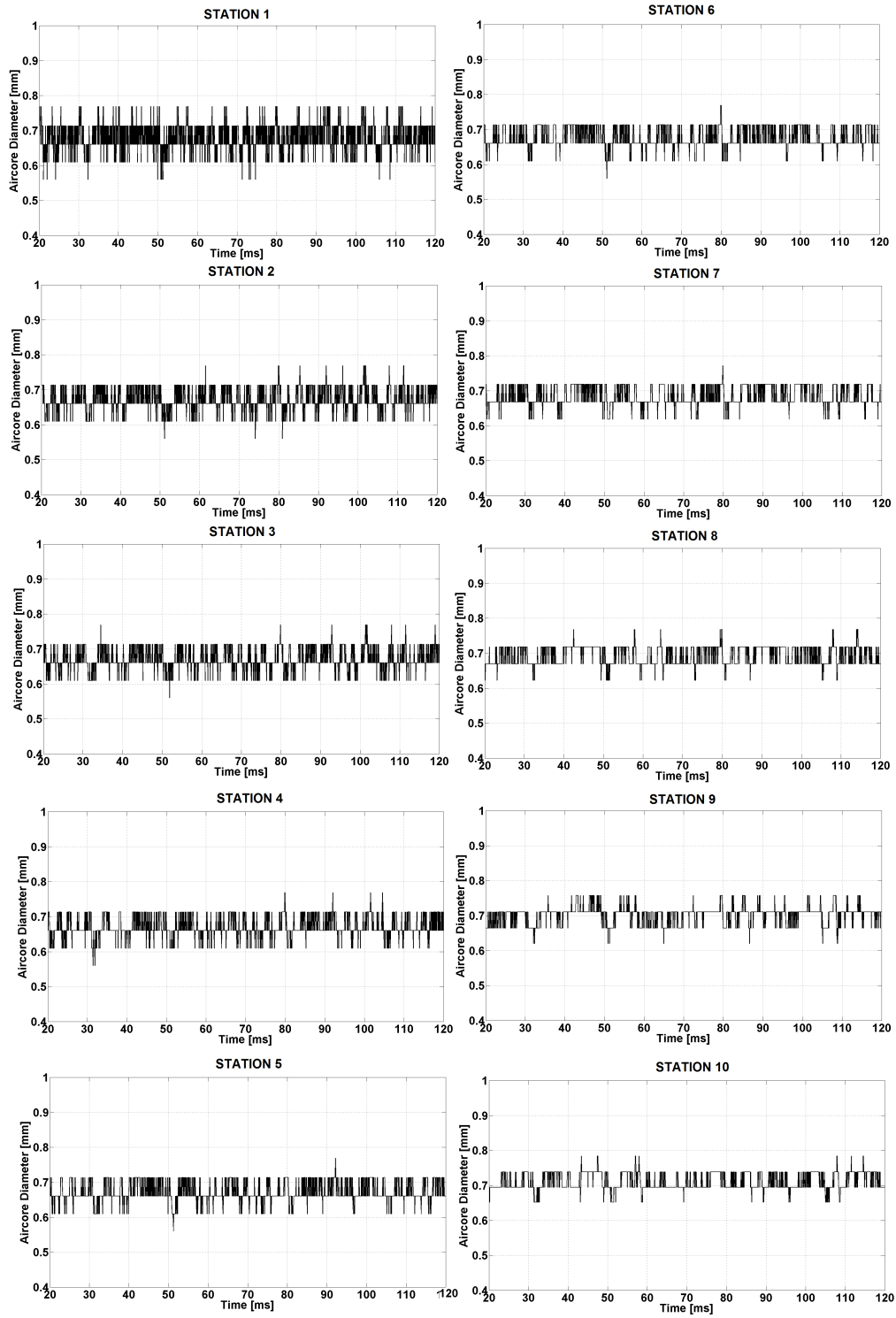


Figure D.1: Time history of the aircore diameter, Stations 1-10.

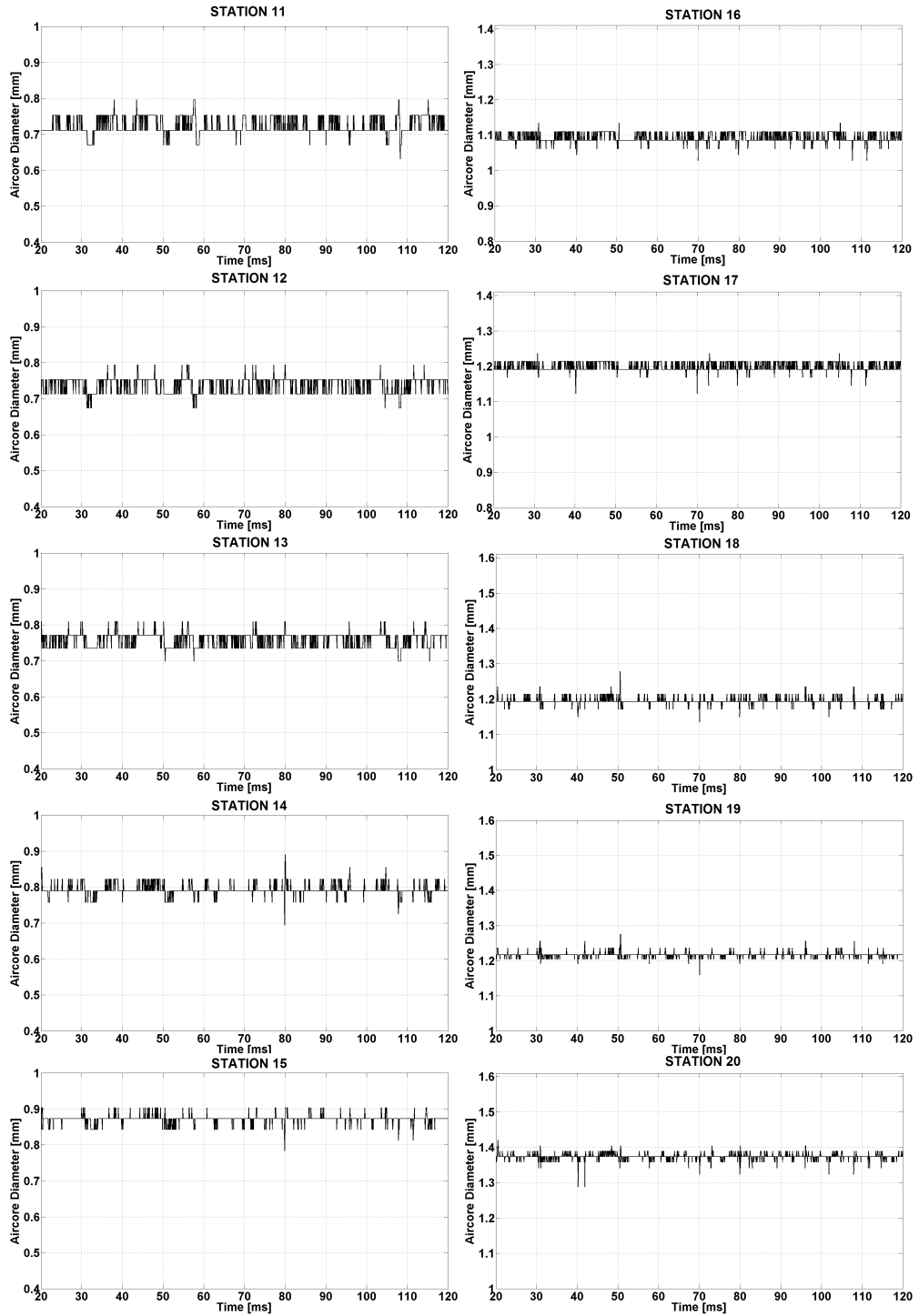


Figure D.2: Time history of the aircore diameter, Stations 11-20.

APPENDIX E

FREQUENCY SPECTRUM OF AIRCORE DIAMETER- 2D AXISYMMETRIC SWIRL NUMERICAL SIMULATIONS

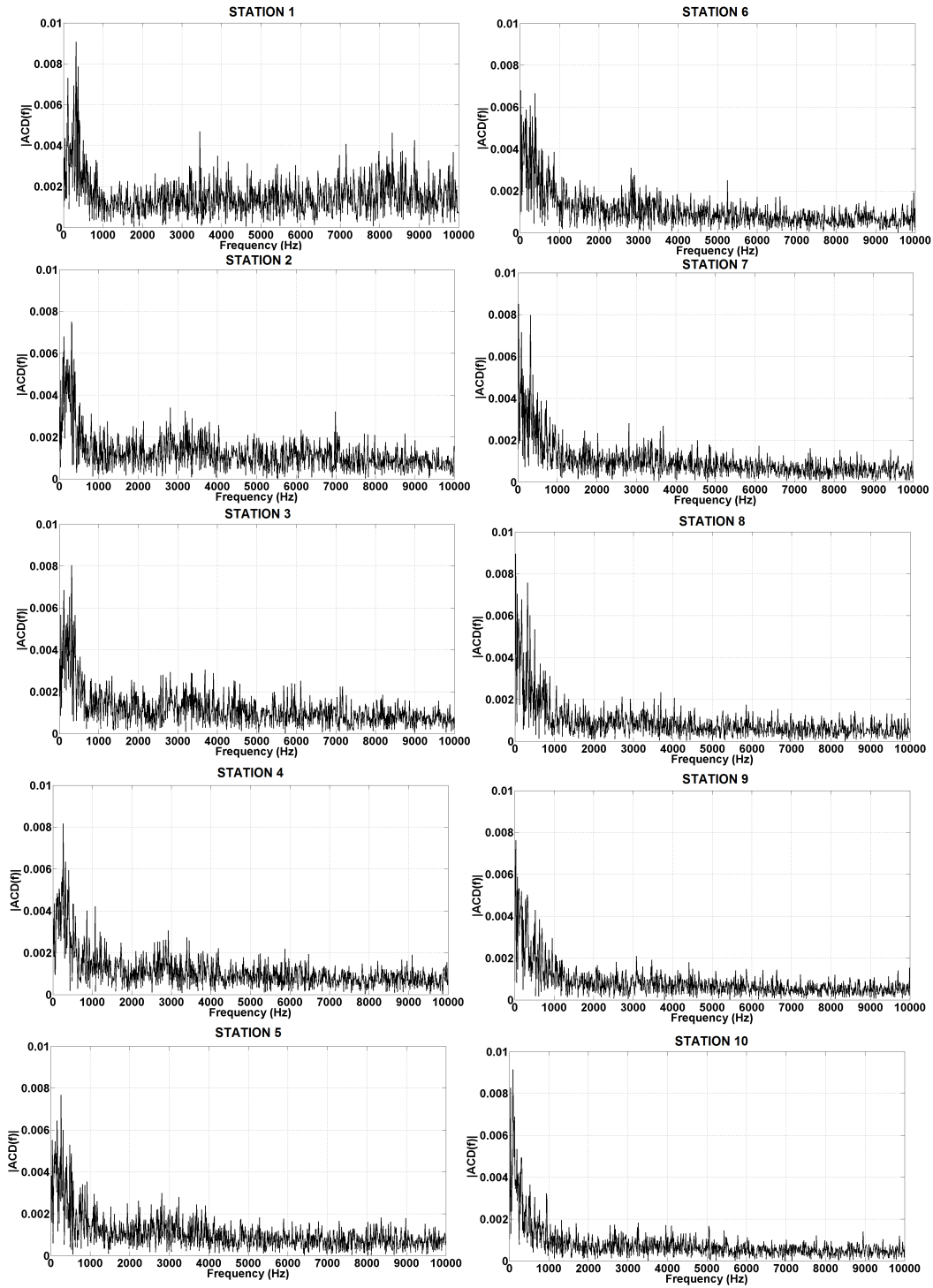


Figure E.1: Frequency spectrum of the aircore diameter, Stations 1-10.

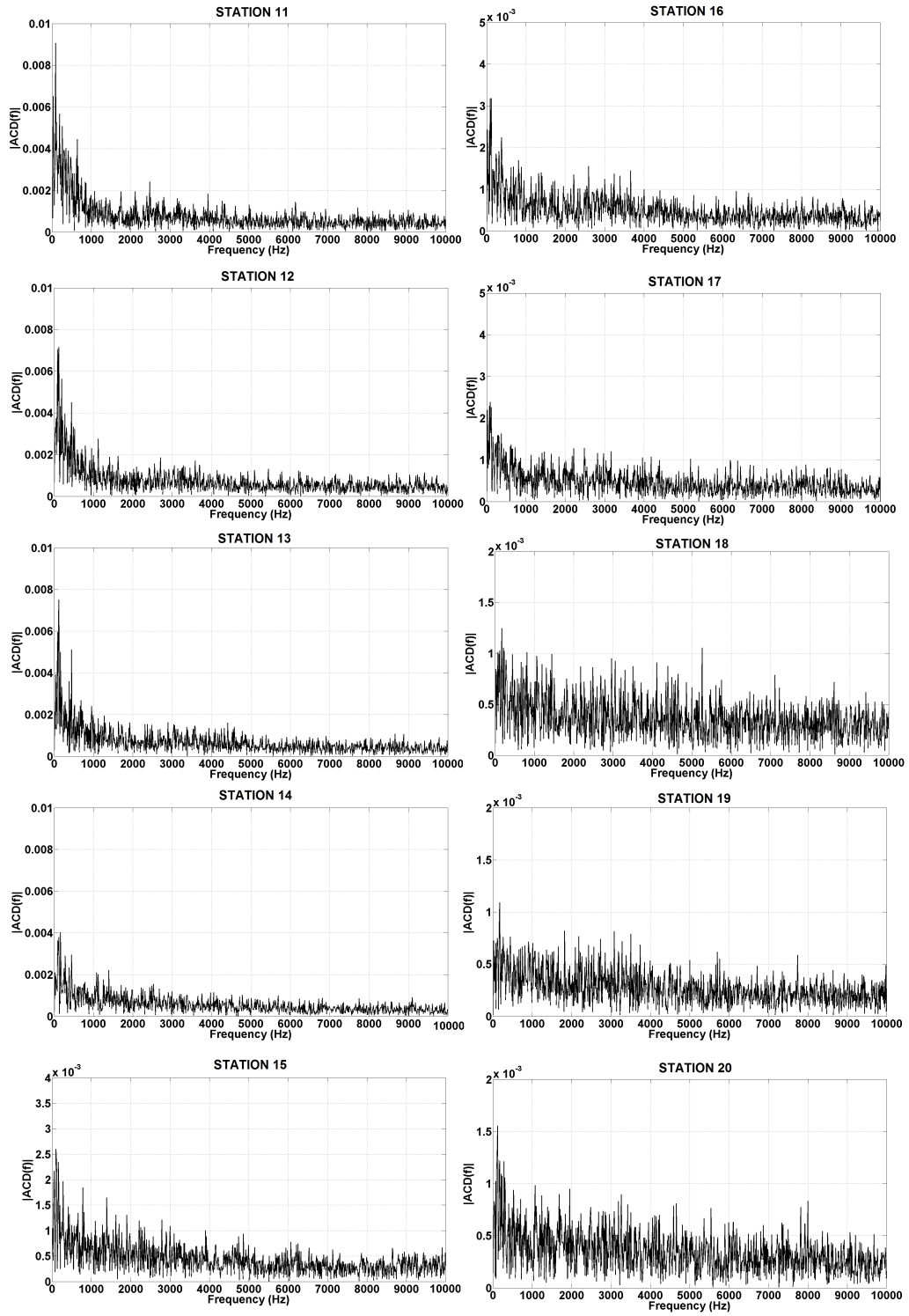


Figure E.2: Frequency spectrum of the aircore diameter, Stations 11-20.

CURRICULUM VITAE

PERSONAL INFORMATION

Surname, Name: Sümer, Bülent

Nationality: Turkish (TC)

Date and Place of Birth: 1977, Samsun

Marital Status: Married

Phone: +905334024056

Fax: +903125909148

EDUCATION

Degree	Institution	Year of Graduation
M.S.	Aerospace Engineering Dept., METU	2004
B.S.	Aerospace Engineering Dept., METU	2001
High School	Mehmet Emin Resulzade Anatolian, Ankara	1995

PROFESSIONAL EXPERIENCE

Year	Place	Enrollment
2002-2005	TÜBİTAK-SAGE	Research Engineer, Propulsion Syst. Div.
2005-2010	TÜBİTAK-SAGE	Senior Research Engineer, Propulsion Syst. Div.
2010-present	TÜBİTAK-SAGE	Chief Research Engineer, Propulsion Syst Div.

PUBLICATIONS

Journal Publications

1. M.A. Ak, A. Ulas, B. Sümer, B. Yazıcı, C. Yıldırım, L.O. Gönc, F.E. Orhan, "An experimental study on the hypergolic ignition of hydrogen peroxide and ethanolamine", *Fuels*, Vol.90, Issue 1, pp.395-398, January 2011.

International Conference Publications

1. K. Bozkaya, B. Sümer, B. Kuran, M.A. Ak, "Reliability Analysis of a Solid Rocket Motor Based on Response Surface Method and Monte Carlo Simulation, 41st AIAA/ASME/SAE/ASEE Joint Propulsion Conference and Exhibit, AIAA-2005-3598, 2005.
2. B.Sümer, N.Erkan, O. Uzol, Ismail H. Tuncer "Experimental and Numerical Investigation of a Pressure Swirl Atomizer" ICLASS 2012, 02-06 September, Heidelberg, Germany.
3. B.Sümer, N.Erkan, O. Uzol, Ismail H. Tuncer "Experimental Investigation of Flow Through a Pressure Swirl Atomizer and the Resulting Hollow Cone Spray at Different Operating Conditions", 7. Ankara International Aerospace Conference, 11-13 September, Ankara, Turkey.

National Conference Publications

1. G. Püskülcü , B. Sümer, D.E. Gündüz, B. Yazıcı, C. Yıldırım, F.E. Orhan, M.A. Ak "Ground Testing of a Liquid Propellant Rocket Motor", *Recent Advances in Space Technologies*, 2005.
2. D.E. Gündüz, D. DüNDAR, M.A. Ak, G. Püskülcü, B. Sümer, C. Yıldırım, B. Yazıcı, F.E. Orhan, L.O. Gönc "Hypergolic Ignition of Liquid Fuel and Liquid Oxidizer in a Rocket Motor ",*Recent Advances in Space Technologies*, 2005.
3. B. Yazıcı, D.E. Gündüz, G. Püskülcü, C. Yıldırım, B. Sümer, M.A. Ak, F.E. Orhan, L.O. Gönc, M.A.Ak "Passive Flow Rate Control of the Fuel and the Ox-

idizer in Liquid Propellant Rocket Motors“, Recent Advances in Space Technologies, 2005.

4. B. Sümer, M.A. Akgün, İ.H. Tuncer “A Computational Static Aeroelastic Analysis Procedure for Aircraft Wings”, Ankara International Aerospace Conference, 2005.
5. A. Ulaş, M.A. Ak, F.E. Orhan, D.E. Gündüz, L.O.Gönç, B. Sümer, G. Püskülcü, C. Yıldırım “Design and Testing of a Hydrogen Peroxide-Kerosene Liquid Propellant Rocket Motor”, Istanbul Space Propulsion Workshop, 10-12 June 2004.